High Temperature Deformation and Fracture Assessment of Similar Steel Welds

Dissertation

zur Erlangung des Grades eines Doktors
der Ingenieurwissenschaften

vorgelegt von

Dipl.-Ing. Ümit Ceyhan

aus Ankara, Türkei

genehmigt von der

Fakultät für Natur- und Materialwissenschaften

der Technischen Universität Clausthal

Tag der mündlichen Prüfung

14.12.2006

Die vorliegende Arbeit wurde am Institut für Werkstoffforschung des GKSS-Forschungszentrums, Geesthacht und am Institut für Werkstoffkunde und Werktofftechnik der Technischen Universität Clausthal durchgeführt.

Vorsitzender der Promotionskommission
Prof. Dr. Wolfgang Schade

Hauptberichterstatter
Prof. Dr. Bilal Dogan (GKSS)

Berichterstatter
Prof. Dr. Lothar Wagner

Berichterstatter
Prof. Dr. Volker Wesling

Acknowledgment

I would like to express my sincere gratitude to Prof. B. Dogan for giving me the opportunity to conduct this work in GKSS Research Centre, Geesthacht, Germany, and for his invaluable guidance, support and supervision of this work. I am also grateful to Prof. L. Wagner for his interest in this work and for taking over the co-referee of the thesis in Technical University of Clausthal, Germany.

I wish to thank to Prof. K.-H. Schwalbe for his support and invaluable discussions during the conduction of this work. I am also thankful to Dr. B. Petrovski and Prof. X.Zheng for their constructive comments and guidance during the experimental and metallographic studies. I also would like to thank to partners of the European Project CRETE and VAMAS TWA31 for fruitful discussions which have contributed a lot to the present work.

Thanks are due to A.C. Cruz from ISQ, Portugal, and A. Chowdhury from ERA, UK, for providing the test material.

I wish to thank to my colleagues in Materials Research Institute of GKSS Research Centre for their technical support, Ms. P. Fischer in metallography, Mr. K. Erdmann, Mr. M. Horstmann, Mr. Tek in materials testing.

Finally, I wish to express my deepest gratitude to my lovely wife Zeynep and my newly born daughter Elif who gave me the strength during the entire time of conduction of this work have made my life rewarding.

This work was carried out at the GKSS Research Centre, Geesthacht, Germany between 2002 and 2006.

Ümit Ceyhan
Geesthacht, June, 20th 2006

Summary

The structural integrity assessment of welded components is of industrial interest which requires well characterised material behaviour and data obtained at service temperatures. The functionally graded microstructure of weldments in weldment zones of base metal (BM), heat affected zone (HAZ) and weld metal (WM) affects the stress and strain distribution at the tip of a crack in a component made of these materials. The ferritic P22 and bainitic-martensitic P91 steels similar welds were chosen to study the deformation and fracture behaviour in high temperature tensile and fracture mechanics tests at 550 °C and 600 °C, respectively. Micromechanisms of deformation were studied on microtensile tests on both materials, which served as basis for fracture mechanical studies of crack initiation and growth. Creep crack initiation and creep crack growth studies were carried out on specimen geometries of C(T), CS(T), SEN(B) and RNB(T) which are of industrial importance due to the similarity of loading to components. The data obtained from high temperature crack initiation and growth tests were analysed following the recently drafted Code of Practice (CoP). The data were used for two most widely used defect assessment methods, the British TDFAD of R5 and German 2CD methods. The assessment methods, developed originally for base metals, predict well the failure in weldments of the studied materials. The prospects of applicability of the assessment methods and weaknesses are reported. Sensitivity analyses were carried out to study the effects of input parameter variations on the assessment method and life predictions. Both deterministic and probabilistic sensitivity analyses were applied to determine the extent of possible error in defect assessment. The present work has contributed to the recently drafted CoP for high temperature testing and analysis of weldments, as well as the European assessment methods, extending their use into assessment of weldments.

Zusammenfassung

Die Bewertung von Bauteilen industrieller Anlagen auf Sicherheit und strukturelle Integrität setzt Materialkennwerte sowie Bruchmechanikdaten bei Einsatztemperaturen voraus. In dieser Arbeit wurden Daten an Grundmaterial (BM), Wärmebeinflusszone (HAZ) und Schweissgut (WM) von artgleichen Schweissverbindungen von ferritischem Stahl P22 bei 550°C sowie martensitischem Stahl P91 bei 600°C ermittelt. Die Gefüge und Abmessung der Schweissgutzone beeinflussen die Spannungs- und Dehnungsfelder an der Rissspitze eines Bauteils. Mikroskopische Untersuchungen zum Verformungsverhalten und Bruchmechanismen wurden an Zug- und Bruchmechanikversuchsproben durchgeführt mit dem Ziel die Wechselwirkung zwischen dem Gefüge und der ermittelten Materialdaten zu korrelieren. Dabei eignet sich insbesondere das neu-entwickelte Mikrozugversuchsverfahren zur Untersuchung der Vervormungs - und Bruchmechanismen in der schmalen Schweissmaterialzone. Die Hochtemperaturbruchmechanikversuche wurden an Bruchmechanikproben industrieller Bedeutung (C(T), CS(T), SEN(B) und RNB(T)) durchgeführt. Die ermittelten Daten wurden durch Anwendung der europäischen Fehlerbewertungsmethoden, der britischen TDFAD von R5 sowie der deutschen 2CD bewertet. Die beiden Methoden, die zur Bewertung von Bauteilen aus Grundmaterial entwickelt worden sind, können zur Bewertung von Bauteilen mit Schweissverbindungen angewandt werden. Sensitivitätanalysen der Änderung der Eingangsparameter durch Anwendung der deterministischen und probabilistischen Methode wurden durchgeführt.

CONTENTS

1. INTRODUCTION

Failures of high temperature components in power generation and petrochemical plants account a substantial portion of the direct costs of operation along with environmental damage and even costing human lives. Historically, the manufacturer's experience has been the basis for the safe design of critical engineering components. However, in recent times crack initiation, growth and failure analyses based on the assumption of the existence of defects in the structure have become more accepted for design and as remaining life prediction methodology.

The operational and plant assessment experience indicates that in the majority of cases where failure occurs in components, defects predominate in the vicinity of weldments. Therefore, time dependent failure at high temperatures by creep crack initiation (CCI) and creep crack growth (CCG) in structural joints imposes a limit on component service life in plants. Although the concepts used for time dependent fracture analysis of homogeneous bodies are commonly applied for defect assessment of weldments, complex structure of weldments having various weldment zones which exhibit particular interactions, requires novel aspects in testing and defect assessment. Recent collaborative efforts of European Creep Collaborative Committee (ECCC) [1] and Creep Group of European Thematic Network FITNET [2] indicate the need for novel methods in defect assessment of weldments and harmonise the existing know-how in the industry and academia for a unified defect assessment method for weldments.

The most widely used standard for creep crack growth testing of metallic materials, ASTM E 1457-00 [3], is mainly addressing testing homogeneous materials in compact tension, C(T), type specimens. However, complexity of stress conditions due to geometrical factors and heterogeneous microstructure in welded industrial components requires harmonised testing and assessment methods. Therefore, the outstanding need for high temperature characterisation of CCI and CCG behaviour of weldments in alternative industrial type specimens has been the subject of collaborative efforts of ESIS TC11 [4] and European project CRETE [5], which had the objective of harmonising testing procedures in order to obtain data for use in defect assessment of weldments. A European Code of Practice (CoP) [6] has become the output of these efforts which provides guidelines for specimen selection, testing and data analysis for weldments that include novel aspects such as testing of industrial type specimen geometries for creep crack initiation and growth testing.

The main purpose of this study is to contribute to the current knowledge and to developing methodology in high temperature defect assessment of weldments. This includes improvement of current testing methods by introducing novel aspects of industrial specimens and the peculiarities of weldments. It is commonly accepted that improvement of the reliability of defect assessment procedures requires profound testing and data assessment methods in which microstructural and geometrical aspects are of primary importance. Therefore, present work aims at contributing to improve a) testing methods, b) data assessment methods, c) understanding of damage and fracture (CCI and CCG) behaviour, d) utilisation of test data in defect assessment methods, e) treatment of data scatter in defect assessment of weldments at high temperatures.

In this thesis, high temperature damage and fracture behaviour of similar weldments of most commonly used low alloy ferritic 2.25CrMo (P22) and newly developed high strength martensitic Mod-9CrMo (P91) steels are characterised at 550 °C and 600 °C, respectively. Firstly, microtensile (MT) tests are conducted on specimens machined out of different weldment zones of P22 and P91 steels. MT tests facilitate the determination of local tensile and damage properties of each weldment zone without any constraint effect of adjacent zones. The finding of MT test aids understanding local material behaviour and deformation mechanisms in defect assessment. Fracture mechanics tests are conducted by use of the guidelines given in the CoP [6] for high temperature testing of weldments. The CCI and CCG properties of different weldment zones (BM, HAZ, WM) are correlated by fracture mechanics crack tip loading parameters that provided input for eventual defect assessment in components. The scatter in correlations are studied and related to microstructural aspects. Different constraints imposed by different specimen geometries are studied. The defect assessment methods, namely British Time Dependent Failure Assessment Diagram (TDFAD) and German Two-Criteria-Diagram (2CD) are reviewed for the applicability of these methods in weldments of P22 and P91. The assessment data may exhibit high scatter due to welding process and functionally graded microstructure of weldments. Two methods are compared and scatter in data are related to specimen geometry effects and microstructural differences. Sensitivity analysis is performed in order to study the effect of scatter introduced into fracture mechanical correlations and defect assessment methods during testing and evaluation of data. All results are interpreted concerning their consequences in life assessment of defects in weldments of components operated at high temperatures, which is the novel aspect of the present reported work.

2. STATE OF THE ART

2.1 FRACTURE MECHANICS CONCEPTS

2.1.1 Linear Elastic Fracture Mechanics Concepts

Continuum mechanics concept of loading a component considers a crack in a two-dimensional body as illustrated in Figure 2.1. For an embedded defect with crack length 2a, conditions of either plane stress or plane strain are assumed to apply. For simplicity, consideration is limited to mode I loading, where normal separation of the crack faces are assumed. The shear modes II and III which lead to the sliding of crack faces, are of less concern as cracks, in practice, tend to grow normal to the applied loads.

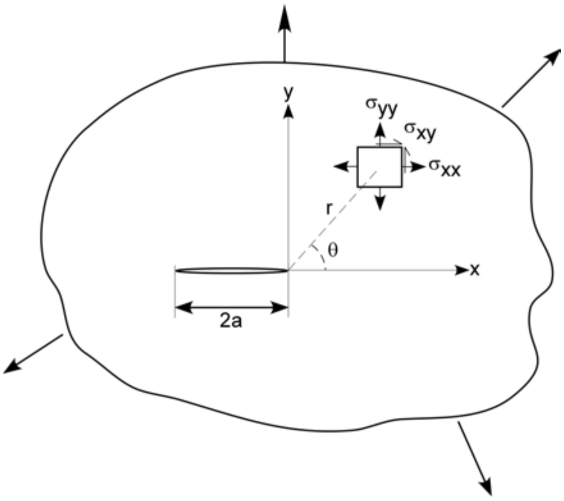

Figure 2.1. Coordinate system describing a crack in an arbitrary body

The basic principle of fracture mechanics is that in the vicinity of the crack tip, the stress and stress fields vary with coordinates in a manner which depends only on material properties apart from single scaling parameter, the stress intensity factor K. The local variations with positions are determined by the solution of the equilibrium and compatibility equations in conjunction with the boundary conditions on the crack surface. The effects of remote loading, geometry and crack size are all included in the single scaling parameter, K.

2.1.1.1 Stress Function Methods

For elastic material behaviour, the stresses close to the crack tip are given in terms of the coordinates in Figure 2.1 as [7]

$$\sigma_{xx} = \frac{K}{\sqrt{2\pi r}}\cos\frac{\theta}{2}\left(1-\sin\frac{\theta}{2}\sin\frac{3\theta}{2}\right)+T$$

$$\sigma_{yy} = \frac{K}{\sqrt{2\pi r}}\cos\frac{\theta}{2}\left(1+\sin\frac{\theta}{2}\sin\frac{3\theta}{2}\right) \qquad (2.1)$$

$$\sigma_{xy} = \frac{K}{\sqrt{2\pi r}}\cos\frac{\theta}{2}\left(\sin\frac{\theta}{2}\cos\frac{3\theta}{2}\right)$$

The form of these equations is irrelevant to the remote boundary conditions but these affect the parameter K, which defines the amplitude of the crack tip singularity. The remote boundary conditions also affect the higher order terms but these are negligible unless far from the crack tip region when r is not small compared with the crack size, a, or any other dimension such as remaining ligament. The second order term, the T stress depends on geometry, crack size and the tractions parallel to the crack plane in the x-direction and is sometimes used in two parameter descriptions of fracture. In present approach only the single parameter description involving K is considered. Then Equations 2.1 may be written in tensor notation as

$$\sigma_{ij} = Kr^{-1/2} f_{ij}(\theta) \tag{2.2}$$

As the body is linear elastic, the strains local to the crack tip obey a similar equation, namely

$$\varepsilon_{ij}^{e} = \left(\frac{K}{E}\right) r^{-1/2} g_{ij}(\theta, \nu) \tag{2.3}$$

where the functions g_{ij} depend on Poisson's ratio ν and on whether conditions of plane stress or plane strain apply. The functions g_{ij} can readily be derived from Equation 2.1 by noting that out-of-plane stress $\sigma_{zz} = 0$ in plane stress, and $\sigma_{zz} = \nu(\sigma_{xx} + \sigma_{yy})$ in plane strain.

As the body is linear elastic K must be directly proportional to the applied load. K also depends on geometry and crack size, a, and solutions are widely available in handbooks [7]. For infinite plate loaded by a uniform tensile stress, σ, normal to a crack size of 2a,

$$K = \sigma\sqrt{\pi a} \tag{2.4}$$

Hence the solution for a crack in a finite body is written as

$$K = Y\sigma\sqrt{a} \tag{2.5}$$

where Y is a non-dimensional function of crack size and component dimensions. Stress intensity factors for a number of common test specimen geometries can be found in different books [7].

An important consequence of Equations 2.2 and 2.3 is that the strain energy density varies as (1/r) when the crack tip is approached. Using the summation convention for tensor notation involving repeated indices, the strain energy density is

$$\frac{1}{2}\sigma_{ij}\varepsilon_{ij}^{e} = \left(\frac{K^2}{E}\right) r^{-1} f(\theta, \nu) \tag{2.6}$$

where the function $f(\theta,\nu)$ depends on whether conditions of plane stress or plane strain apply. By integrating Equation 2.6 over a small circular region at the crack tip, it is possible to demonstrate that the energy stored within a finite region is finite. However, if the singularity is any stronger, the $r^{-1/2}$ singularity in stress and strain is the strongest singularity possible at the crack tip for an elastic material [8].

2.1.2 Small Scale Yielding

Equations yielding the stresses at the vicinity of the crack tip predict that the stresses tend to infinity as the crack tip is approached. In elastic-plastic materials, yielding at the crack tip reduces the stresses. However, in the case of small scale yielding (SSY) the plastic deformation is contained within a small zone around the crack tip. Provided the plastic zone is sufficiently small, the surrounding elastic region can still be characterised by Equations 2.1. However, K must be increased to K′ to describe the higher elastic stresses away from the crack tip required to balance the reduced stresses in the plastic zone. This is depicted in Figure 2.2.

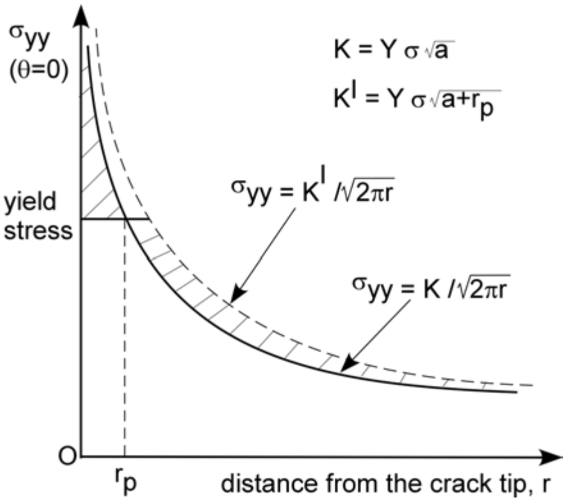

Figure 2.2. Schematic stress field ahead of a crack in small-scale yielding [8]

An approximate estimate of K′ for SSY can be made by evaluating the stress intensity factor for a crack of size $(a+r_p)$, where r_p is the plastic zone size correction shown in Figure 2.2. The value of r_p is chosen to make the two shaded areas equal so that the equilibrium is maintained. This is achieved by making r_p approximately equal to the distance over which the elastic stresses exceed yield stress.

In plane stress, the stress σ_{yy}, directly ahead of the crack (θ=0) is equal to yield stress σ_Y, when

$$r_p = \frac{K^2}{2\pi\sigma_Y^{\,2}} \tag{2.7}$$

This follows from the σ_{yy} component of Equation 2.1 provided the plastic zone is buried within the region where the terms in $r^{-1/2}$ are dominant. In plane-strain SSY multi-axial constraint leads to yielding occurring when the stress, σ_{yy}, directly ahead of the crack is approximately equal to $\sqrt{3\sigma_Y}$ i.e.

$$r_p = \frac{K^2}{6\pi\sigma_Y^{\,2}} \tag{2.8}$$

Equations 2.7 and 2.8 may be written in more general form

$$r_p = \frac{\beta K^2}{\sigma_Y^2} \tag{2.9}$$

where β is influenced not only by whether conditions of plane stress or plane strain, but also by the remote tractions geometry, the multi-axial yield condition, and materials strain hardening properties. It is also a function of angular position [9-11].

Within the plastic zone K′ characterises the product of stress and strain which retains the (1/r) singularity of Equation 2.6. This equation is modified to

$$\sigma_{ij}\varepsilon_{ij} = \left(\frac{(K')^2}{E'}\right) r^{-1} f(\theta, \text{material}) \tag{2.10}$$

where the angular function depends on strain hardening properties of the material and on condition of plane stress or plane strain. However, both stress and strain have an $r^{-1/2}$ singularity in the elastic case. In the plastic case the stresses are lower and strains higher so that they correspond to a point on the material stress-strain curve with combined r^{-1} singularity.

2.1.3 Elastic-Plastic Fracture Mechanics

Linear elastic fracture mechanics (LEFM) is valid only as long as non-linear material deformation is confined to a small region surrounding the crack tip. In many materials it is virtually impossible to characterise the fracture behaviour with LEFM.

Elastic-plastic fracture mechanics applies to materials that exhibit time-independent, non-linear behaviour. (i.e. plastic deformation). Mainly two elastic plastic parameters are adopted: the crack tip opening displacement (CTOD) and the J contour integral. Critical values of J or CTOD give nearly size-independent measures of fracture toughness even for relatively large amount of crack tip plasticity. In this section main emphasis is put on J contour integral, as the time dependent fracture parameter, C^*, is defined based on J integral.

2.1.3.1 J Integral

The J integral has gained a great success as a fracture characterising parameter for non-linear materials. Rice [12] provided the basis for extending fracture mechanics methodology well beyond the validity limits of LEFM, by idealising elastic-plastic deformation as non-linear elastic. Figure 2.3 illustrates the uniaxial stress-strain behaviour of elastic-plastic and non-linear elastic materials.

The loading behaviour of two materials is identical, but the material responses differ when each is unloaded. The elastic-plastic material follows a linear unloading path with the slope equal to Young’s modulus, while the non-linear elastic material unloads along the same path as it was loaded. There is a unique relationship between stress and strain in an elastic material, but a given strain in an elastic-plastic material can corresponds to more than one stress value if the material is unloaded or cyclically loaded. Consequently, it is much easier to deal with an elastic material than a material that exhibits irreversible plasticity.

As long as the stresses in both materials increase monotonically, the mechanical response of the two materials are identical. When the problem is generalised to three dimensions, non-linear elastic material does not necessarily follow the loading behaviour of the elastic-plastic material. However, there are good examples proving that this assumption is satisfactory. Thus, an analysis which assumes non-linear elastic behaviour may be valid for an elastic-plastic material, provided that no unloading occurs. The deformation theory of plasticity, which relates total strains to stresses in a material, is considered equivalent to non-linear elasticity.

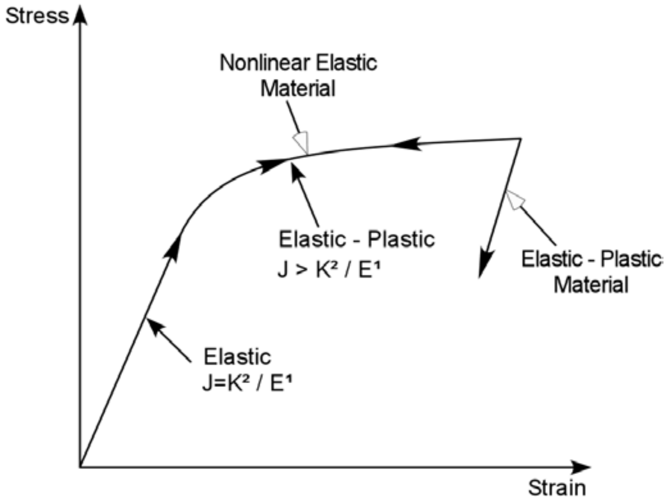

Figure 2.3. Stress-strain behaviour of an elastic-plastic material

Rice [12] applied deformation plasticity (i.e. nonlinear elasticity) to the analysis of a crack in a non-linear material. He showed that the non-linear energy release rate J, could be written as a path-independent line integral. Hutchinson [13] and Rice and Rosengren [14] also showed that J uniquely characterises the crack tip stresses and strains in non-linear materials. Thus the J integral can be viewed as both an energy parameter and a stress intensity parameter.

In a similar manner to the use of the stress intensity factor in LEFM, J integral can be used to describe the variations of stress and strain local to a crack tip under elastic-plastic conditions. This is defined such that the amplitude of the (1/r) singularity in the product of stress and strain in Equations 2.6 and 2.8 becomes

$$\sigma_{ij}\varepsilon_{ij} = Jr^{-1}f(\theta, \text{material}) \tag{2.11}$$

In small scale yielding $J = (K')^2 / E'$. When more widespread conditions of plasticity occur in a structure, J integral is increased above these elastic values. This is depicted schematically in Figure 2.3.

The J integral can be constructed as a line integral defined on a contour surrounding a crack tip, as in Figure 2.4.

$$J = \int_{\Gamma} \left[W_s dy - T_i \left(\frac{\partial u_i}{\partial x} \right) ds \right] \tag{2.12}$$

where W_s is the strain energy density given by

$$W_s = \int_0^{\varepsilon_{ij}} \sigma_{ij} d\varepsilon_{ij} \tag{2.13}$$

with σ_{ij} and ε_{ij} the stress and strain tensors, respectively. T_i and u_i components of the traction and displacement vectors, and s is arc length along Γ. The contour Γ is a path traversed anticlockwise which surrounds the crack tip as shown in Figure 2.4. For non-linear elastic material, J is path-independent and can be evaluated on any convenient contour when computations are performed. For linear elastic materials J is equal to the energy release rate, G.

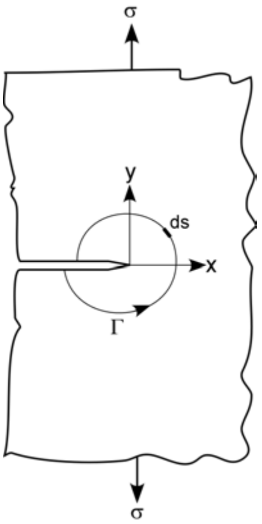

Figure 2.4. Integration contour for J around a crack tip

T_i would define the normal stresses acting at the boundaries. The components of the traction vector are given by

$$T_i = \sigma_{ij} n_j \tag{2.14}$$

where n_j are the components of the unit vector normal to Γ.

The Equation 2.11 has been examined for materials which deform according to the idealised power law hardening expression

$$\varepsilon = \alpha \varepsilon_y \left(\frac{\sigma}{\sigma_y} \right)^N \tag{2.15}$$

where N, α, σ_y, ε_y are constants. The constants σ_y, ε_y are usually chosen as the yield stress and strain as σ_y/E when fitting Equation 2.15 to actual stress-strain data. As the product of stress and strain varies with (1/r) by Equation 2.11, for the material law of Equation 2.15 the stress near the crack tip must vary as $(1/r)^{1/(N+1)}$. The stress tensor in Equation 2.11 may then be written as

$$\sigma_{ij} = \sigma_Y \left(\frac{J}{\alpha I_N \sigma_Y \varepsilon_Y r} \right)^{1/(N+1)} \tilde{\sigma}_{ij}(\theta, N) \tag{2.16}$$

where I_N is a non-dimensional function of N and σ_{ij} is non-dimensional function of θ and N.

The strain field near the crack tip corresponding to the stress field of Equation 2.16 is rewritten by using the Equation 2.15 as

$$\varepsilon_{ij} = \alpha\varepsilon_Y \left(\frac{J}{\alpha I_N \sigma_Y \varepsilon_Y r} \right)^{N/(N+1)} \tilde{\varepsilon}_{ij}(\theta, N) \tag{2.17}$$

where $\tilde{\varepsilon}_{ij}(\theta, N)$ is another non-dimensional function of θ and N. The stress and strain fields of Equations 2.16 and 2.17 are usually referred to as HRR fields after Hutchinson [13], Rice and Rosengren [14] who first solved the near crack tip field problem for power law hardening materials.

In fracture assessment using J integral, it is postulated that crack extension takes place when J reaches a critical value, J_c. In mode I loading, the critical value of J for plane strain conditions is denoted by J_{Ic}. The stress-strain fields at the crack tip inside the plastic zone are uniquely defined by J integral independently of the size of the plastic zone. Therefore the critical value must be independent of the extent of the yielding if it is truly a material property. Hence, J_{Ic} may be related to the fracture toughness, K_{Ic}, by $J_{Ic} = K_{Ic} / E'$ in view of Equations 2.10 and 2.11. In practice, J_{Ic} is often evaluated from test specimens which exhibit significant plasticity.

2.1.4 Time Dependent Fracture Mechanics

2.1.4.1 Creep Crack Growth

The primary aim of high temperature crack growth study stems from the need for assessing the remaining life of components that have been in service under creep conditions and are approaching their originally predicted design life. More system operators such as in naval and aviation sectors, energy utility and petrochemical companies are turning to a retirement-for-cause (RFC) philosophy rather than rely on life predictions made decades ago that were based on concepts that are now out-dated [15].

Components that operate at high temperatures relative to the melting point of the material may fail by slow, stable extension of macroscopic crack in creeping material. Traditional approaches to design in the creep regime apply only when creep failure is controlled by a dominant crack in the structure. Figure 2.5 illustrates the typical creep response of a material subject to constant stress.

Deformation at high temperatures can be divided into 4 regimes: instantaneous (elastic) strain, ε_o, primary creep, secondary (steady state) creep, and tertiary creep. The elastic strain occurs immediately upon application of the load. It is already known that the elastic stress-strain response of a material is not instantaneous; it is limited to the speed of sound in the material. It can, however, be viewed as instantaneous in such creep problems, where the time scale is usually measured in hours. Primary creep dominates at short times after the load is applied where the strain rate decreases with time as the material strain hardens. In the secondary creep stage, the deformation reaches a steady state, where the strain hardening and softening are balanced. The creep rate is constant in the secondary stage. In the tertiary stage, the creep rate accelerates, as the material approaches ultimate failure. Microscopic failure mechanisms such as grain boundary cavitation, nucleate in this final stage of creep.

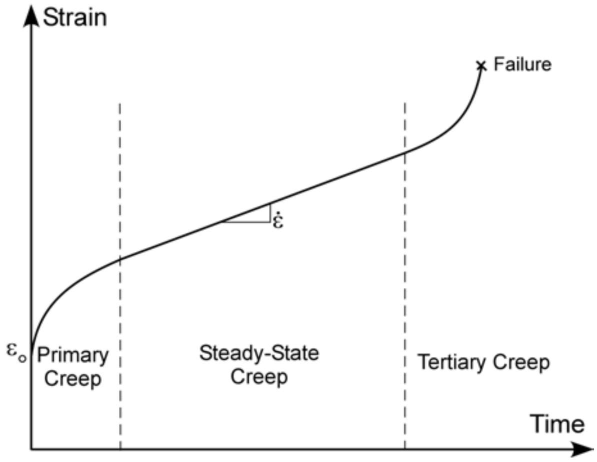

Figure 2.5. Typical creep response of a material under constant load

During growth of microscopic crack at high temperatures, all four type of creep response can occur simultaneously in the most general case as it is seen in Figure 2.6. The material at the tip of the growing crack is in the tertiary stage of creep, since the material is failing obviously locally. The material may be elastic remote from the crack tip, and in the primary and secondary stages of creep at moderate distances from the tip.

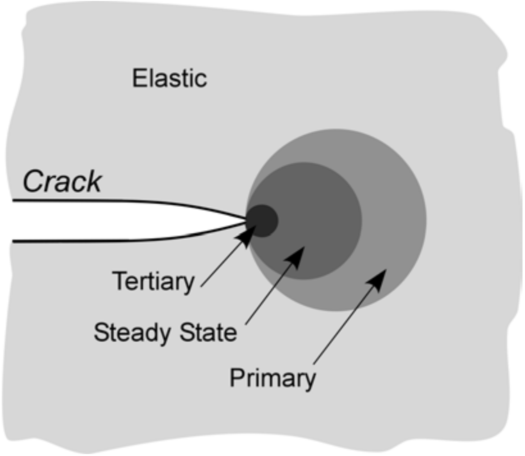

Figure 2.6. Creep response zones at a crack tip

Most analytical treatments of creep crack growth assume limiting cases, where one or more of these regimes are not present or confined to a small portion of the component. If, for example, the component deformation is predominantly elastic, and the creep zone is confined to small region, near the crack tip, the crack growth can be characterised by the stress intensity factor, K. In the other extreme, when the component deforms globally in steady state extensive creep, elastic strains and tertiary creep can be disregarded [8]. A parameter that applies to the latter case is described below, followed by a brief discussion of approaches that consider the transition from elastic to steady state creep behaviour.

There are two competing mechanisms involved in creep crack growth. The creep deformation is characterised by crack-tip blunting in the material ahead of the crack tip. This relaxes the crack-tip stress field and tends to retard crack growth. The other mechanism results in an accumulation of creep damage in the form of microcracks and voids that enhance crack growth as they coalesce. Whichever phenomenon dominates determines whether or not creep crack growth takes place. Steady state crack growth will occur when equilibrium between these two effects is attained [15].

Time dependent crack growth can result from creep effects as well as environmental effects or from combination of both. An oxidising environment can accelerate the creep crack growth rate by an order of magnitude or more. In many tests no attempt was made to separate the effects. This has made the interpretation and comparison of data difficult. Efforts have concentrated on trying to identify the loading parameter with which the crack growth rate correlates regarding the operating conditions of the material. The most commonly employed loading parameters are the elastic stress intensity factor, K, the energy rate integral, $C^*(t)$ [16], and the reference stress σ_{ref}, depending on the loading conditions and the crack tip deformation regimes. If a particular loading parameter is applicable, the crack growth rate should correlate with it regardless the specimen's/component's geometry.

The CCG behaviour under steady state (SS) or extensive creep for which the stress field becomes time-independent or stationary, where creep deformation dominates, is correlated with the path independent integral, $C^*(t)$ [16]. If the size of the creep zone at the crack tip is very small compared to the crack length and other pertinent dimensions, the material is under small-scale creep (SSC) and the stress intensity factor, K, is expected to be a valid parameter. The intermediate region is represented by transition (or non-steady state) creep where the C_t parameter introduced appears to correlate crack growth [17]. Although, there is no parameter, at present, that is widely accepted for the correlation of CCG over the entire range of SSC, non-steady state and transition creep regimes, attempts have been made to extend the applicability of C^*.

2.1.4.2 C^* Integral

A formal fracture mechanics approach to creep crack growth was developed soon after the J integral was established as an elastic-plastic fracture mechanics parameter. Landes and Begley [16] Ohji et.al.[18] and later Nikbin et.al [19] independently proposed what became known as the C^* integral to characterise crack growth in a material undergoing steady state creep. They applied Hoff's analogy which states that if there exists a non-linear elastic body that obeys the relationship $\varepsilon_{ij} = f(\sigma_{ij})$, a viscous body may be characterised by $\dot{\varepsilon}_{ij} = f(\sigma_{ij})$. The function of stress are the same for both bodies that develop identical stress distributions when the same load is applied. Hoff's analogy can be applied to steady state creep, since the creep rate is only a function of the applied stress.

The C^* integral is defined by replacing strains with strain rates and displacements with displacement rates in the J contour integral as in 2.17 [8]

$$C^* = \int_\Gamma \left(\dot{W}_s dy - \sigma_{ij} n_j \frac{\partial \dot{u}_i}{\partial x} \partial s \right) \tag{2.18}$$

where $\dot{W}_s$ is the strain energy density rate, defined as

$$\dot{W}_s = \int_0^{\varepsilon_{kl}} \sigma_{ij} d\dot{\varepsilon}_{ij} \tag{2.19}$$

Hoff's analogy implies that the C^* integral is path-independent, because J is path-independent. Also if secondary creep follows a power law

$$\dot{\varepsilon}_{ij} = A\sigma_{ij}^{n} \tag{2.20}$$

where A and n are material constants. It is possible then to define an HRR-type singularity for stresses and strain rates at the crack tip

$$\sigma_{ij} = \left(\frac{C^*}{AI_n r}\right)^{\frac{1}{n+1}} \tilde{\sigma}_{ij}(n,\theta) \tag{2.21}$$

and

$$\dot{\varepsilon}_{ij} = \left(\frac{C^*}{AI_n r}\right)^{\frac{n}{n+1}} \tilde{\varepsilon}_{ij}(n,\theta) \tag{2.22}$$

where the constants I_n, $\tilde{\sigma}_{ij}$ and $\tilde{\varepsilon}_{ij}$ are identical to the corresponding parameters in HRR relationship. Note that, here, n is creep exponent rather than strain hardening exponent.

Just as the J integral characterises the crack tip fields in an elastic or elastic-plastic material, the C^* integral uniquely defines crack tip conditions in a viscous material. Thus the time dependent crack growth rate in a viscous material should only depend on the value of C^*. Experimental studies [16, 18-21] have shown that creep crack growth rates correlate very well with C^*, provided steady state creep is the dominant deformation mechanism in the specimen. The crack growth rate follows the power law

$$\dot{a} = D_o C^{*\phi} \tag{2.23}$$

where D_o and ϕ are material constants. In many materials, $\phi = n/(n+1)$, a result predicted by grain boundary cavitation models.

Experimental measurement of C^* is done in analogy to the J-integral. J is usually measured by invoking the energy release rate definition

$$J = -\frac{1}{B}\left(\frac{\partial}{\partial a}\int_0^{\Delta} F d\Delta\right)_{\Delta} \tag{2.24}$$

where F is the applied load and Δ is the load line displacement. Similarly, C^* can be defined in terms of a power release

$$C^* = -\frac{1}{B}\left(\frac{\partial}{\partial a}\int_0^{\dot{\Delta}} F d\dot{\Delta}\right)_{\dot{\Delta}} \tag{2.25}$$

The J integral can be related to the energy absorbed by a laboratory specimen, divided by the ligament area, that is energy per unit ligament area

$$J = \frac{\eta}{Bb}\int_0^{\Delta} F d\Delta \tag{2.26}$$

where η is a dimensionless constant that depends on geometry. Therefore, C^* is given by [8]

$$C^* = \frac{\eta}{Bb}\int_0^{\dot{\Delta}} F d\dot{\Delta} \qquad (2.27)$$

For a material that creeps according to a power law, the displacement rate is proportional to F^n, assuming global creep in the specimen. In this case, Equation 2.27 reduces to

$$C^* = \frac{n}{n+1}\frac{\eta}{Bb}F\dot{\Delta} \qquad (2.28)$$

The geometry factor η is determined for a variety of test specimens.

All of the approaches currently available for the calculation of the C^* parameter by means of algebraic formulae are based on two assumptions on material structure and behaviour [8]. The first assumption is that the crack under investigation is located in material with a homogeneous microstructure. The second assumption is that the crack growth path is confined to the same material in which crack growth initiated.

When a crack is present in a welded joint, one or both of these assumptions may be violated in three different ways all stemming from the fact that there are usually considerable differences in microstructure and properties between the weld metal (WM), the heat affected zone (HAZ) and the base material (BM). Firstly, the crack tip may be located in a region of heterogeneous microstructure, i.e. the weld metal or the heat affected zone. Secondly, crack growth may be controlled by the deformation behaviour of material with very different creep properties to those of the region of material in which the crack is located. For instance, a crack located in a weld metal or heat affected zone region, which is controlled by deformation in surrounding parent material. Thirdly, the crack growth path may traverse material regions with widely differing microstructures and properties, like weld metal, coarse and fine-grained heat affected zone and parent material.

2.1.4.3 Short Time Versus Long Time Behaviour

It is important to emphasise that C^* applies only to extensive creep (steady state behaviour) conditions. Extensive creep deformation does not occur immediately after loading, because it takes some time. At this moment the stresses and strains exhibit a $1/\sqrt{r}$ singularity near the crack tip and are uniquely defined by K_I. Crack tip conditions can be characterised by K_I as long as the creep zone is embedded in the singularity dominated zone. The creep zone grows with time, eventually invalidating K_I as a crack tip parameter. At long times, creep zone spreads throughout the entire structure [15].

When the crack grows with time, the behaviour of the structure depends on the crack growth rate relative to the creep rate. In brittle materials, the crack growth rate is so fast that it overtakes the creep zone. The crack growth can be characterised by K_I because the creep zone at the tip of the growing crack remains small. At the other extreme, if the crack growth is sufficiently slow that the creep zone spreads throughout the structure, C^* is the appropriate characterising parameter.

C(t) Parameter

The transition from short time elastic behaviour to long time viscous behaviour has been analysed [22]. If the load is suddenly applied and then held constant, a creep zone gradually develops in an elastic singularity zone where the stresses well within the creep zone can be described by

$$\sigma_{ij} = \left(\frac{C(t)}{AI_n r} \right)^{\frac{1}{n+1}} \tilde{\sigma}_{ij}(n,\theta) \tag{2.29}$$

where C(t) is a parameter that characterises the amplitude of the local stress singularity in the creep zone. C(t) varies with time and is equal to C^* in the limit of long time extensive creep behaviour which was formulated in Equation 2.21. For small scale creep (SSC) conditions, C(t) decays as 1/t according to the relationship

$$C(t) = \frac{K_I^2 (1-\nu)^2}{(n+1) E t} \tag{2.30}$$

After this formulation, it would just an easy fact to define a characteristic time for the translation from short time to long time behaviour

$$t_T = \frac{K_I^2 (1-\nu)^2}{(n+1) E C^*} \tag{2.31}$$

or

$$t_T = \frac{J}{(n+1) E C^*} \tag{2.32}$$

When significant crack growth occurs over time scales much less than t_T, the behaviour can be characterised by K_I, whereas C^* is the appropriate parameter when significant crack growth requires times t>> t_T.

C_t Parameter

Unlike K_I and C^*, direct experimental measurement of C(t) under transient conditions is usually not possible. As a result, C_t parameter is proposed to characterise crack growth over the range from SSC to extensive creep [17]. The advantage of C_t is that it can be measured relatively easily.

By separating global displacement into instantaneous elastic and time-dependent creep components

$$\Delta = \Delta_e + \Delta_c \tag{2.33}$$

The creep displacement, Δ_c, increases with time as the creep zone grows. Also, if load is fixed, $\dot{\Delta}_c = \dot{\Delta}$. The C_t parameter is defined as the creep component of the power release rate

$$C_t = -\frac{1}{B} \left(\frac{\partial}{\partial a} \int_0^{\dot{\Delta}_c} F d\dot{\Delta}_c \right)_{\dot{\Delta}_c} \tag{2.34}$$

which is similar to Equation 2.25.

It has been shown that the small scale creep limit for C_t can be expressed as follows [17]

$$(C_t)_{SSC} = \left(\frac{f'(a/W)}{f(a/W)} \right) \frac{F\dot{\Delta}_c}{BW} \tag{2.35}$$

where $f(a/W)$ is the geometry correction factor for Mode I stress intensity.

Although C_t was originally intended as an approximation of C(t), it has become clear that these two parameters are distinct from each other. The C(t) parameter characterises the stresses ahead of a stationary crack, while C_t is related to the rate of expansion of the creep zone. The latter quantity appears to be better suited to materials that experience relatively rapid creep crack growth. Both parameters approach C^* in the limit of steady-state creep.

2.1.4.4 NSW Creep Crack Growth Model

The experimental predictions on a large number of materials showed that the creep crack growth rate is most sensitive to multiaxial creep ductility, and crack growth rates can be predicted approximately within a factor about two by [23]

$$\dot{a} = \frac{3C^{*0.85}}{\varepsilon_f^*} \tag{2.36}$$

which is called the approximate NSW model [24].

The $\dot{a}$ and C^* have the units of mm/h and MPa m/h, respectively. ε_f^* is taken as the uniaxial failure strain, ε_f for plane stress conditions and $\varepsilon_f/30$ for plane strain conditions [23].

Yatomi et.al. [25, 26] have proposed a modified NSW model (NSW-MOD) which considers the dependence of creep strain and ductility on crack tip angle, creep strain exponent, n, and stress state using the stress and strain distributions given in Equations 2.21 and 2.22 and an appropriate model of multiaxial creep ductility is

$$\dot{a} = (n+1)(A\, r_c)^{\frac{1}{n+1}} \left[\frac{C^*}{I_n} \right]^{\frac{n}{n+1}} \frac{\overline{h}_n}{\varepsilon_f} \tag{2.37}$$

where r_c is the size of the creep process zone (usually related to grain size of the material) and factor $\overline{h}_n$ depends on the creep exponent, n, and the model used to relate the uniaxial and multiaxial creep ductility of the material [25, 26].

2.1.4.5 Creep Crack Initiation

A steady state case is considered at the crack tip after the build-up of the crack tip process zone of a creep deforming material. However, a gradient of damage exists during the crack growth. As the material which has just entered the process zone undergoes a little damage, the material which is very close to the crack tip is almost exhausted and has spent all of its ductility before it fails. This situation does not occur at the crack tip immediately after the loading, because material requires sufficient time for damage accumulation.

Damage accumulation in different materials depends on their creep properties. For ductile materials, an incubation period, which may reach to 40-80 percent of life of the specimen/component can be considered [8]. There will be a period of damage accumulation at the crack tip which causes crack tip blunting without any crack growth. Figure 2.7 illustrates stages of crack tip blunting and initiation.

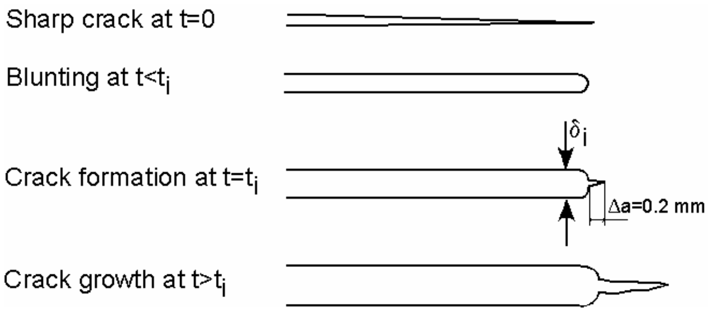

Figure 2.7. Stages of crack growth initiation from a sharp crack

The behaviour of components under creep loading conditions is described by load line displacement – time diagrams. On application of steady (constant) load to a pre-cracked component the load point displacement increases with time. The creep zone ahead of the crack tip is defined as the region in which creep strain exceeds the elastic strain, where the creep zone size increases with time according to,

$$r_c = K^2 (EBt)^{2/(n-1)} F_c(\theta)/2\pi \tag{2.38}$$

where $F_c(\theta)$ is a shape function as defined in [22]. The microstructural damage occurs as a consequence of accumulation of creep strain. Initiation of creep crack requires attainment of critical local strain at the crack tip. The magnitude of time to initiate a creep crack, t_i, depends on the increment of crack extension, Δa_i, determined for the definition of crack initiation, x_c [27]. Therefore, determination of Δa_i, by using either PD method or partial unloading compliance is of engineering importance as it directly affects the life of a structural component [28].

The time to generate critical displacement, therefore damage, to initiate a microcrack i.e. x_c=10 μm grain size, will be significantly less than a microcrack , i.e. x_c=0.2 or 0.5 mm as in engineering definition adopted in testing and assessment codes [29, 30]. In engineering terms, detection of a crack using non-destructive testing (NDT) is required in service components that correspond to the adopted engineering macro crack initiation size.

In component defect assessment, the data analysed to determine crack growth rate vs. crack tip parameter K or C^* that gives an initial “tail” with a decreasing growth rate prior to steady-state growth rate [19]. The tail represents the transition to steady state and depends on material properties and loading conditions. However, the data prior to steady state crack growth initiation, defined at crack extension, Δa, of 0.2 or 0.5 mm reflect the stress redistribution and development of damage. Therefore, it needs to be recorded and analysed as it may cover a large part of component life in service.

One method to predict the creep crack initiation time is modelled by Ainsworth [31, 32] to provide a relationship between the crack tip opening displacement rate and the parameter C(t) and C^*. The process of crack tip blunting continues until the plasticity of the material at the crack tip exhausted and a critical crack tip opening displacement, δ_i, is reached (Figure 2.7). This criterion is used to determine the creep crack initiation time, t_i. For ductile materials, when steady state creep conditions are established, the creep crack initiation time can be estimated as

$$t_i = \frac{1}{\varepsilon_0}\left(\frac{\sigma_0 \dot{\varepsilon}_0 \delta_i}{C^*}\right)^{\frac{n}{n+1}} \tag{2.39}$$

The incubation period can also be estimated by using the reference stress method where data are not available for the material used in the component [32]. The incubation time is calculated using

$$t_I = 0.0025\left[\frac{\sigma_{ref}\, t_{R(ref)}}{\left(K_a^p\right)^2}\right]^{0.85} \tag{2.40}$$

The incubation time for the component in secondary creep stage can be obtained from the following equations when incubation time data are available from test specimens.

$$\left(\frac{t_{Icomp}}{t_{Ispec}}\right) = \left(\frac{C^*_{spec}}{C^*_{comp}}\right)^{n/n+1} \tag{2.41}$$

where subscripts comp. refers to the component and spec. refers to the specimen.

Estimation of CCI time using NSW Creep Crack Growth Model

Upon the initial loading, before the steady state conditions achieved at the crack tip, the crack growth rate is often less than the steady state value by an order of 1/(n+1) [8]. Therefore, by using the NSW creep crack growth model, initial crack growth rate might be estimated as

$$\dot{a}_i \approx \frac{\dot{a}}{n+1} = \frac{3C^{*0.85}}{(n+1)\varepsilon_f^*} \tag{2.42}$$

Similarly, if the modified NSW model (Equation 2.37) can be used to estimate the initial crack growth rate

$$\dot{a}_i \approx \left(A\, r_c\right)^{\frac{1}{n+1}}\left[\frac{C^*}{I_n}\right]^{\frac{n}{n+1}}\frac{\bar{h}_n}{\varepsilon_f} \tag{2.43}$$

Austin and Webster [33] have proposed that CCI time can be calculated from

$$t_i = \frac{\Delta a}{\dot{a}} \tag{2.44}$$

where Δa is the minimum crack extension that can be measured reliably and a_i is assumed to be constant during the increment of the crack growth.

Therefore, upper and lower bounds of CCI time, t_i, can be obtained by using NSW model equations used to determine initial creep crack growth rate (Equation 2.42) and steady-state creep crack growth rate (Equation 2.36), respectively [34].

$$\frac{\Delta a\,\varepsilon_f^*}{3C^{*0.85}} \le t_i \le \frac{\Delta a(n+1)\varepsilon_f^*}{3C^{*0.85}} \tag{2.45}$$

Similarly, upper and lower bounds can be estimated using modified NSW (NSW-MOD) creep crack growth models:

$$\frac{\Delta a}{(n+1)(A\,r_c)^{\frac{1}{n+1}}}\left[\frac{I_n}{C^*}\right]^{\frac{n}{n+1}}\frac{\varepsilon_f}{\bar{h}_n} \le t_i \le \frac{\Delta a}{(A\,r_c)^{\frac{1}{n+1}}}\left[\frac{I_n}{C^*}\right]^{\frac{n}{n+1}}\frac{\varepsilon_f}{\bar{h}_n} \tag{2.46}$$

The experimental and analytical work is reported showing the applicability of the above modified model [26].

2.2 HIGH TEMPERATURE DEFECT ASSESSMENT OF WELDMENTS

2.2.1 Introduction

Failures of high temperature components, particularly with weldments, in power generation and petrochemical plants are a substantial portion of the direct costs of operation. Historically the manufacturer's experience has been the basis for the design of critical engineering components based on defect-free approach. However, crack initiation, growth and failure analyses have recently become more accepted for design and remaining life prediction methodology [29,35,36]. The history of the development of high temperature assessment codes and defect assessment codes are summarised as follows [37]

- 1950s – ASME – Design codes for uncracked structures culminating in a substantial reduction in pressure vessel failures.

- 1970s – Development of high temperature fracture mechanics methods.

- 1980s – Extending the high temperature testing, and life assessment techniques to include fracture mechanics methodologies, British Energy's R6, R5, PD6493.

- Setting up of Versailles Agreement on Materials and Standards (VAMAS) committee TWA11 (1988), TWA19 (1993) and TWA25 (1999), to make recommendation for testing methods and standards for engineering alloys.

- 1990s – ASTM E 1457 – First code of practice for high temperature testing and analysis. The French A16 defect assessment draft code.

- 1999 – BS7910, integrating low and high temperature fracture, British Energy's R5 Updated.

- 2000 – Development of a unified International CoP for high temperature defect assessment and inclusion into Knowledge-Based-System.

- 2005 – Dissemination of the European CoP for creep crack initiation and growth testing of industrially relevant specimens [38] and the CoP for high temperature crack initiation and growth testing of weldments, which has been submitted to IIW SC STAND for ISO standardisation [6].

The purpose of defect assessment procedures is to provide a methodology which summarises the best approach to structural assessment, at any given time of the flawed engineering structures. The key to the approach is the development of a suitable methodology to describe the fundamental degradation and failure processes in structures. It is inevitable that the recommended methods will be subjective as they will reflect the interpretations of those producing the document. However, it is essential that all approaches must be conservative in application because of safety concerns.

Defect assessment procedures based on fracture mechanics concepts, through which the time dependent effects of creep can be modelled, use experimental uniaxial and crack growth data from laboratory test specimens. The level of constraint, loading type, use of valid testing procedure would affect the experimental results. The failure and/or crack initiation times for an industrial component are predicted by using the experimental data, for which several levels of complexity need to be considered. This depends on the level of criticality of the problem.

Furthermore, the level of confidence or the scatter in the data will also play an important role in increasing confidence in the life predictions. The analyses [29,35,36] utilise non-linear fracture mechanics concepts and, therefore, the stress sensitivity and the non-linearity will magnify any errors that might exist in the original input information. Therefore, the inclusion of probabilistic methods into defect assessment for design and life assessment procedures is necessary to determine the confidence limits of the analysis.

2.2.2 Creep Failure in Plant Weld Components

The operational structural assessment indicates that high temperature failures occur from defects predominate in the vicinity of welds in components. Therefore, high temperature component performance is generally limited by the performance of the weldments under service conditions [39-42]. Weldments are functionally graded materials with complex microstructure due to the welding process. Furthermore, the components of the weldment vary containing a range of interfaces possessing different local properties as in similar and dissimilar welds with or without filler metal as shown in Figure 2.8.

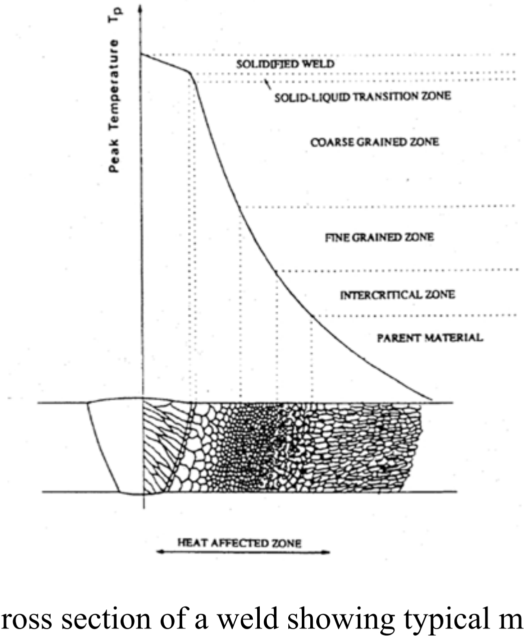

Figure 2.8. Schematic cross section of a weld showing typical microstructural zones [43].

Four types of creep damage and cracking associated with weldments have been catalogued for both headers and piping by Chen et.al. [44]. Each of the four creep damage types are identified below and shown schematically in Figure 2.9:

Type I – Longitudinal or transverse damage in the weld metal and remains entirely within the weld metal.

Type II – Longitudinal or transverse damage in the weld metal, but grows into the surrounding HAZ

Type III – Damage in the coarse grained HAZ region

Type IV – Damage initiated or growing in the intercritical zone of the HAZ. The transition region between the fully-transformed, fine grained HAZ, and partially-transformed base metal.

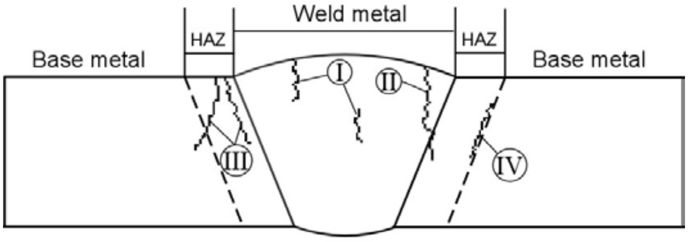

Figure 2.9. Four types of damage in welds in relation to microstructure [44].

Comprehensive reviews were published recently on high temperature performance of weldments [39,41]. The functionally graded microstructure of weldments has different mechanical and creep properties which in turn directly influence the stress redistribution and damage accumulation within the weld. Allen [39] has shown the effect of interaction of different weldment zones on the performance of welded structure, including for dissimilar weldments, i.e. P91-P22, P91-1CrMoV, with and without filler material. He has also reported that creep failure in uniaxial cross weld tests involves complex interactions between zones as on P22 and P91 steel welds. His conclusion on P22 WM/P22 HAZ conjoint failure mechanism by ductile strain interaction and necking is a peculiarity of plain bar specimen geometry is remarkable. Parker [45] has shown that real circumferential pipe butt welds differ from uniaxial test bars in constraint, loading conditions, and stress state. Thin weak zones are highly constrained in both uniaxial test bars and real welds. Hence, uniaxial thin zone test failures should be quite representative of real welds. This issue is addressed in present study by MT testing approach (Section 5.1). However, thick weak zones such as P22 weld metal are unconstrained in test bars, but quite constrained in real welds with high wall thickness/weld width ratio and circumferential geometry. Therefore, creep deformation in thick weak weld zones may proceed only slowly in real welds, but can cause rapid failure in uniaxial test bars. It follows that while low ductility uniaxial rupture data may predict real weld failure quite accurately, high ductility uniaxial data are liable to underpredict life in real welds. A separate consideration which reinforces these conclusions is the effect of loading condition. Uniaxial test loads are unaffected by creep strain, but plant system loading may be relaxed by creep deformation. A thick weak zone is thus likely to absorb strain and relax its loading, but a thin weak zone show low macroscopic ductility, negligible system stress relaxation, and hence potential early creep failure.

Williams et.al. [46] have attempted to find a correlation between creep performance of uniaxial cross-weld specimens and heavy section ferritic welds. Because this specimen geometry cannot represent all expected practical weldment loading conditions. They have attempted to correlate the life expectancy of a uniaxial cross-weld specimen with a range of possible loading conditions of a thick-section pipe. Their approach was based on an initial comparison between the calculated life of a cross-weld specimen and pipe weld specimen, subjected only to axial loading. The approach taken in present study involves both standard uniaxial and local tension properties from MT tests, along with time dependent fracture mechanical data used in assessment procedures TDFAD and 2CD in a unified form. Special care is taken for the evaluation of scatter in data by use of deterministic and probabilistic approaches, which may have big influence on outputs of defect assessment.

2.2.3 Choice of Fracture Mechanics Parameter

In defect assessment of components in service under creep conditions, the material's ductility and extent of constraint play an important role in the type of analysis to be used. Therefore, the choice of fracture mechanics parameter is an important issue for the reliability of the assessment.

The parameters which are used to correlate the crack growth rate, $\dot{a}$, are the stress intensity factor K, the reference stress σ_{ref} and the creep parameter C^*-integral. They are correlated with crack growth rate, $\dot{a}$ as in the following,

$$\dot{a} = A' K^{m'} \tag{2.47}$$

$$\dot{a} = H \sigma_{ref}{}^{p} \tag{2.48}$$

$$\dot{a} = D_o C^{*\phi} \tag{2.49}$$

where A', D_o, H, m', ϕ and p are material constants. While the Equation 2.47 is appropriate for creep-brittle conditions, Equation 2.48 is used to correlate when failure is mainly by net-section rupture. Equation 2.49 is relevant for most engineering applications where steady state creep crack growth occurs.

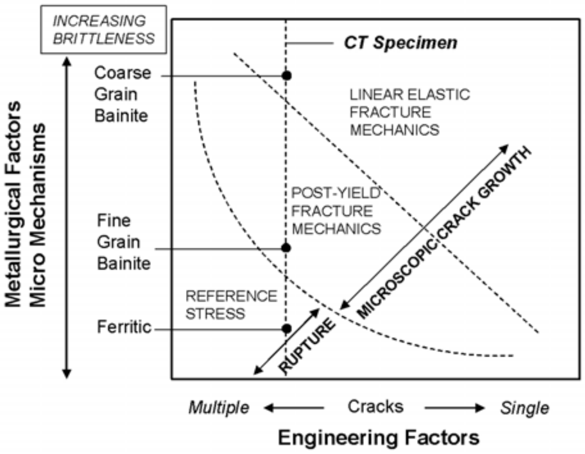

Figure 2.10. Schematic view of the regimes of fracture ranging from elastic to fully ductile behaviour [37].

A schematic description of the relevant range of applicability of the parameters, K, C^* and σ_{ref} are shown in Figure 2.10 [37]. The vertical line corresponds to a fixed size compact-tension, C(T), specimen, which suggests that the relevant fracture mechanics parameter could vary depending on the metallurgical factors.

Two-parameter failure assessment methods which are able to consider both fracture and/or ligament rupture controlled failure at the same time, are available [29,46]. The time dependent failure assessment diagram (TDFAD) of the assessment procedure R5 [29] is a two-parameter failure assessment method. It is used to predict failure by creep crack initiation at some stainless steels and developed by British Energy (UK). The two criteria diagram (2CD) [47], which has been developed by Siemens AG (DE) is also a dual parameter failure assessment method. It is used to predict creep crack initiation in ferritic steels. Comparison of both methods and their application to various materials (P22, P91) and their weldments have recently been reported. [28,48,49].

2.2.4 Design and Assessment Procedures

A number of design and assessment procedures exist worldwide. The main difference between assessment and design procedures is that while an assessment procedure aims to predict accurately in-service component behaviour, a design procedure provides guidelines to design a safe system. While assessment procedures are more detailed in-house company procedures, the design procedures are public/standard approaches which has to be inherently less detailed and more conservative. Dogan [50,51] and Auerkari et.al. [52] have independently summarised the available current assessment and design procedures which are currently used to assess the time to rupture and defect growth in pressure equipment. Maskell [53] has compiled a complete list giving all details of the assessment procedures used and the users. Each procedure was assigned an abbreviation as seen in Figure 2.11.

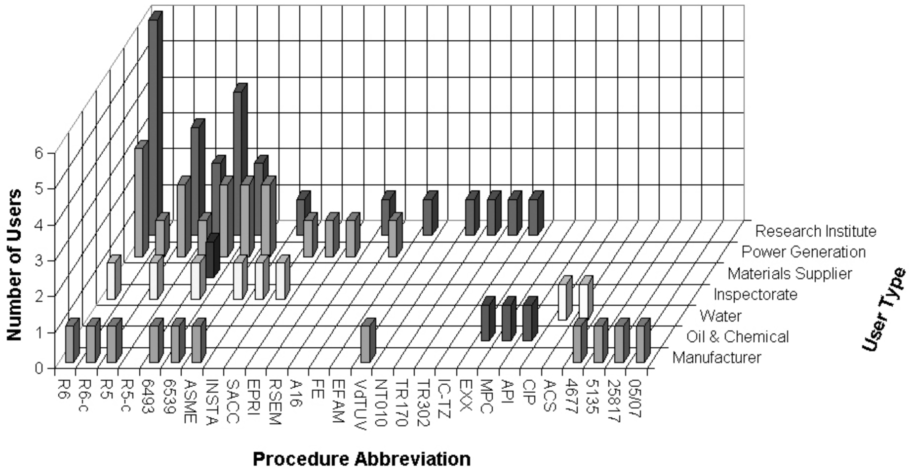

Figure 2.11. Assessment and design procedures by user type [53].

The development of high temperature codes in different countries has moved in similar directions and in many cases the methodology has been borrowed from a previously available code in another country [54]. The early approaches to high temperature life assessment were methodologies based on defect-free assessment codes, i.e. ASME Code Case N-47 [55] and the French code RCC-MR [36]. However, in RCC-MR, the behaviour of a small region ahead of a crack or notch is later addressed in an additional appendix, A16. Strain amplification and design curves are included in the document [56]. These have many similarities, and are based on lifetime assessment of uncracked structures.

The R5 Code [29] had the intention of augmenting or replacing certain sections of N-47 and RCC-MR, and provides in-service assessment rules for mechanical components operating at high temperature. One part of the R5 approach is that a notional defect may be postulated and subsequent behaviour predicted for likely service cycles. Indeed, together with the defect assessment code R6 [57] it may be used in any of the three modes [58]: 'safe life' (no degradation of properties), 'damage tolerant' (life extension) or 'fail safe' (leak-before break).

The objective of the A16 code [59] is to propose methods for determining the detrimental effects of defects on the life of a component. As the background to A16 was based on the high temperature fracture mechanics aspects of the liquid metal fast reactor industry, it is a suitable code for the creep regime of failure and is comparable in that sense to Volumes 4 and 5 of the R5 document.

Dogan and Ainsworth [50] have classified the defect assessment procedures in three groups according to the approach they use: (a) assessment procedures based on failure assessment diagram (FAD) techniques, (b) assessment procedures based on crack driving force (CDF) techniques and (c) others. The methodology based on FAD techniques is an integrated graphical representation where fracture failure and ligament collapse are simultaneously evaluated in time dependent failure assessment (TDFAD) [29] method of British Energy (UK). Similar approach is taken in two criteria diagram (2CD) of Siemens AG (DE). The assessment methodology of the procedures based on the use of crack driving force (CDF) diagrams is different from the philosophy of FAD based ones. The evaluation of fracture failure and ligament collapse is not calculated simultaneously in the CDF approach. Therefore, first of all a direct comparison between the applied load and limit load of the component is needed. Then, a diagram should be plotted where the applied fracture mechanics parameter (K, J, C^* or CTOD rate) is compared with the corresponding toughness values. Other defect assessment procedures i.e. ASME Section XI code [60] is similar to fitness-for-service guides but, concerning the assessment procedures, it does not use FAD's. It uses figures and tables, which the real situation can be compared to.

2.2.4.1 The R5 Procedure

The objective of the R5 development was to provide a comprehensive creep assessment document which is easily used by practitioner. It is based on "expert knowledge" in structural mechanics and materials science and it is intended to augment and replace, where necessary, the provisions of ASME Code [61] and French Code RCC-MR [36]. It also extends the rules of these codes to facilitate the assessment of defects and weldments, including dissimilar metal welds. In contrast to design codes, R5 is an assessment procedure and therefore, generally does not contain the margins or factors inherent in design codes.

2.2.4.2 The British Standard BS 7910

This method of assessing the significance of flaws when time dependent creep effects have to be taken into account, is based on the R5 Procedure [29], but simplified where appropriate [35]. It is intended for use when assessing components made in ferritic and austenitic steel since most information is available on these materials. The assessment procedure may be applied at the design stage as well as to flaws that are actually detected during pre-service or in-service inspection is subject to restrictions given in the standard [35].

The first objective is to decide whether the flaw is innocuous and will never affect the integrity of the plant, whether remedial action can be deferred until some time in the future or repairs are needed immediately. For plant operating at high temperatures, the first factor to be established is whether the component will operate in the creep regime. Initially, creep exemption criteria are established to determine the lowest temperature at which creep effects need to be considered. If the component/temperature/service life combination fulfils the exemption criteria, no further considerations need to be given to creep. If the exemption criteria are not met, the possibility of creep failure cannot be ruled out. For situations where creep crack propagation is possible the creep crack growth assessment procedures should be applied. If cyclic loading is involved, consideration should be given to the possibility of creep-fatigue interaction.

2.2.4.3 The French Design Code RCC-MR – A16

RCC-MR, French fast reactor design code, addresses the design and construction rules for defect free structures. Loading types include internal and external pressure. The weight of the equipment and its content, thermal expansion pressure and dynamic loads, temperature effects are taken either as constant or transient [36]. The purpose of the analyses is to demonstrate that a component does not undergo certain types of damage when subjected to loadings. Analyses consist in verifying compliance with criteria selected on the basis of the method of analysis and the level of criteria and temperature.

In the RCC-MR code, a somewhat different approach to the creep design of weldments is adopted. The allowable stresses of the welded joint depend on the quality of the weld and its mechanical characteristics. When elastic analysis methods are used it is acceptable to calculate the response of the structure without considering the variation of mechanical properties within the joint. The weldment is then assessed by using the allowable stresses specific to the joint. These are obtained by multiplying the efficiency coefficient, $n \le 1$, where n takes account of type of joint and the extent of the inspections, by allowable stresses in the joint. The stresses are either tabulated or deduced by using factors on the base material's stresses. These factors are denoted by J_t and J_r, for creep deformation and creep rupture, respectively. The allowable stresses in the joint then become nJ_tS_t for the creep deformation properties, and nJ_rS_r for the creep rupture properties, where S denotes the corresponding allowable stress in the base material.

The non-mandatory document A16 of the RCC-MR provides methods to perform defect assessment as well as methods for leak-before-break analysis. When the initial geometry of the defect is determined the defect assessment may proceed in two stages:

a) Calculation of the defect evolution when the structure is subjected to loading. If creep is insignificant in the area of the defect, fatigue analysis is made for the initiation and propagation phases. If creep is significant, creep-fatigue analysis is made to describe initiation and propagation.

b) Verification that the presence of the final defect when it is subjected to the specified loading does not induce any risk of rupture and instability during the life of the structure. If creep is insignificant in the area of the defect, fast rupture and instability assessment is done. Tear initiation is assumed to occur when propagation under specified loads exceeds 0.2 mm.

σ_d Method for Creep and Creep-Fatigue Initiation

Calculation with Creager–Neuber procedure provides estimation of the real stress σ_d that accounts for plasticity. The σ_d stress is obtained in the plane of the crack with Creager formulae which provide analytical solutions for a singular elastic field σ_{de} as a function of the crack tip distance r, the angle θ and the stress intensity factors K_I, K_{II} and K_{III} [59]. With the

Neuber procedure [59] using the average material tensile curve at the temperature and the point under investigation the elastoplastic stress σ_d is obtained.

For the creep – fatigue calculations following the Creager- Neuber approach, the real strain range and the stress σ_{kd} at distance d during the holding time is estimated based on the results of an elastic analysis [59].

C_s^* Method

The simplified method, referred to as the C_s^* method, accounts for stresses and strains including creep. The C_s^* calculation is modelled based on J_s, which is the analytical estimate of J-integral. C_s^* solutions are given for loading conditions of mechanical, thermal gradient, combined thermal and mechanical loading. For mechanical loading [59]

$$C_s^* = J_{el} E \dot{\varepsilon}_{ref} / \sigma_{ref} \tag{2.50}$$

where the crack tip parameter C^*_s is used for estimating crack initiation time, t_i, and crack growth correlation for structural assessment.

2.2.4.4 The ASME III Approach

Subsection NH of ASME III [61] contains rules for the design of Class 1 nuclear components operating at elevated temperatures, which is 371 °C for ferritic steels and 427 °C for austenitic steels. The procedure allows design assessments to be performed for defect-free components operating in the creep regime. Limits on primary and secondary stresses are provided to demonstrate

(a) margins against plastic collapse

(b) margins against creep rupture

(c) that the component is operating within shakedown

Rules are then given to assess whether creep-fatigue initiation will occur during the component lifetime. Creep damage, D_c, is evaluated using a life fraction rule as

$$D_c = \sum (t / t_r)_j \tag{2.51}$$

and the fatigue damage, D_f, is evaluated using a Miner's rule as

$$D_f = \sum (n / N)_k \tag{2.52}$$

Creep rupture and fatigue endurance properties used to evaluate damage are design values, which incorporate inherent conservatisms. The total damage, D, is taken as the sum of the creep and fatigue components

$$D = D_c + D_f \tag{2.53}$$

For weldments, weld strength reduction factors are used to account for the inferior creep rupture strength of the weldment compared to the parent material. Similarly, a Fatigue Strength Reduction Factor (FSRF) of 2.0 is used to account for the inferior fatigue strength of the weldment compared to the parent material. It is also required that creep-fatigue initiation calculations for weldments use stress and strain concentration factors appropriate to the worst surface geometry.

2.3 CREEP CRACK INITIATION: INVESTIGATION AND ASSESSMENT

2.3.1 Introduction

The process of high temperature crack extension from pre-existing defects was considered only in terms of creep crack propagation. However, the period of incubation prior to the onset of creep crack growth can represent a significant portion of specimen or component life. For ductile materials, an incubation period prior to onset of crack growth may take up to 40% of the total life of the specimen [8].

The behaviour of specimens under creep loading conditions is described by load line displacement – time diagrams. On application of a constant force to a pre-cracked component the load point displacement increases with time. The creep zone ahead of the crack tip is defined as the region in which creep strain exceeds the elastic strain, the creep zone size increases with time according to,

$$r_c = K^2 (EBt)^{2/(n-1)} F_c(\theta) / 2\pi \tag{2.54}$$

where $F_c(\theta)$ is a shape function as defined in [22], K is the stress intensity factor, E is the Young's modulus, B is the specimen thickness and n is the Norton's creep exponent. Microstructural damage occurs as a consequence of accumulation of creep strain. Initiation of creep crack requires attainment of critical local strain at the crack tip. The magnitude of time to initiate a creep crack, t_i, depends on the increment of crack extension, Δa_i, determined for the definition of crack initiation, x_c [27]. Therefore, determination of Δa_i, by using either the potential drop (PD) method or partial unloading compliance is of engineering importance as it directly affects the life of a structural component [28].

The time to generate a critical displacement, therefore damage, to initiate a microcrack i.e. x_c=10 µm at the order of grain size, will be significantly less than a macrocrack defined at x_c=0.2 or 0.5 mm, which is also the engineering definition as adopted in testing and assessment codes [29]. In engineering terms, detection of a crack using non-destructive testing (NDT) is required in service components that correspond to the adopted engineering macro crack initiation size. In component defect assessment, the data analysed to determine crack growth rate vs. crack tip parameter K or C^* usually give an initial "tail" with a decreasing growth rate prior to steady-state growth rate. The tail represents the "transition" to steady state and depends on material properties and loading conditions. However, the data prior to steady state crack growth initiation, defined at crack extension, Δa, of 0.2 or 0.5 mm reflect the stress redistribution and development of damage. Therefore, it needs to be recorded and analysed as it may cover a large portion of component life in service.

Although it is not standardised yet, testing to obtain creep crack initiation data and determination of CCI fracture mechanics parameters are reported in European Creep Collaborative Committee (ECCC) documentation, Volume 3, Part 4 [62]. Crack tip opening displacement, CTOD or δ, creep crack initiation toughness, K^c_{mat}, C^*-Integral, stress intensity factor, K, J-Integral and nominal stress, σ_d, are given as potential CCI correlation parameters.

The Time Dependent Failure Assessment Diagram (TDFAD) method of British assessment procedure R5 [29] and German Two Criteria Diagram (2CD) [47] are two-parameter CCI assessment methods. They are used to predict crack initiation by taking the crack tip damage and ligament damage into account at the same time. The crack tip damage is evaluated by using fracture mechanics approach, whereas the ligament damage is calculated using limit load approach.

2.3.2 Determination of Creep Crack Initiation Parameters

2.3.2.1 Definition of creep crack initiation

The creep crack initiation is defined by a technical creep crack initiation length $\Delta a_i = a_i - a_0$. It is also possible to use a creep crack initiation length which is dependent on the geometry and size of specimens i.e. $a_i = 0.004$ W for C(T) or $a_i = 0.01$ W for DEN(T)-specimens. For C(T) specimens of W=25 mm and larger, it is recommended to use a constant creep crack initiation length of $\Delta a_i = 0.5$ mm independent of geometry and size of specimens [27,31]. The definition of a fixed crack length at initiation is advantageous in order to avoid the influence of spurious factors not related to crack advance. Dependent on the degree of brittleness and the grain size of the material investigated a constant creep crack initiation length of $\Delta a_i = 0.2$ mm can be chosen.

2.3.2.2 Stress Intensity Factor K

Stress Intensity Factor K represents the magnitude of the ideal crack tip stress field for mode I in a homogeneous, linear-elastic body [63]. As the body is linear elastic K must be directly proportional to the applied load. K also depends on geometry and crack size, a, and solutions are widely available in handbooks. For infinite plate loaded under a uniform tensile stress, σ, normal to a crack size of 2a,

$$K = \sigma\sqrt{\pi a} \tag{2.55}$$

The solution for a crack in a finite body is often written

$$K = Y\sigma\sqrt{a} \tag{2.56}$$

where Y is a non-dimensional function of crack size and component dimensions. Stress intensity factors for a number of common test specimen geometries are available in the literature [7].

2.3.2.3. C^* Integral

C^*-Integral is defined as a line integral that encloses the crack front from one crack surface to the other, used to characterise the local stress-strain rate field at any instant from in a body subjected to extensive creep conditions. The details are given in Section 2.1.4.2. C^* integral can be determined experimentally from

$$C^* = \frac{F\dot{\Delta}}{B(W-a)}H\eta \tag{2.57}$$

where H and η are the geometry factors of the specimen used and they are available in Appendix A for a variety of test specimens. The determination of C^* integral using experimental methods is given in detail in Section 4.2.7.2.

2.3.2.4 Crack Tip Opening Displacement (CTOD)

During the early part of test, the crack tip opening displacement (CTOD or δ) increases in direct proportion to the load line displacement with elastic, plastic and creep components, i.e.

$$\delta_{tot} = \delta_e + \delta_p + \delta_c \tag{2.58}$$

Creep crack initiation is assumed to stem from a pre-existing defect, which occurs on the attainment of a critical crack tip opening displacement, $\delta_{i,x}$. The creep crack initiation criterion defined at x=Δa=0.5mm [27,31]. Following creep crack initiation, the development of total displacement δ_{tot} no longer reflects the development of Δ_{total}^{LLD} and can decrease in magnitude [27]. $\delta_{i,x}$ for a growing crack is usually less than that for a non-growing crack. The parameter may be used to determine the crack initiation time using the equation [27]:

$$t_{i,x} = \left\{\frac{\delta_{i,x}}{C^*}\right\}^{\frac{n}{n+1}} D^{\frac{-1}{n+1}} - \frac{1}{E \cdot D \cdot \left(\sigma_{ref}\right)^{n-1}} \tag{2.59}$$

There are two approaches described to determine the crack tip opening displacement. Both approaches rely to some extent on knowledge of the position of the deformation hinge-point of the specimen. Therefore, they are only applicable up to the development of early crack extension (i.e. $0.15 \cdot \Delta a_f$, [64]) since the position of the hinge-point will shift with crack extension. The first approach involves determination of the deformation hinge point and its use to analytically convert load line displacement to δ_c [65]. The second is local CTOD approach which involves an analytical prediction based on direct metallographic measurement of δ on specimen side surfaces [66].

Hinge Point Method

In high temperature fracture mechanics tests, it is usual only to continuously monitor load line displacement. However a proven technique to determine $\delta_c(t)$ from $\Delta_c(t)$ is available [65]. The approach requires a series of hardness indent pairs to be placed on either side of the notch and pre-crack of the specimen. The spacing between each pair of indents is measured prior to the start and at the end of a test. The test is interrupted prior to or ideally close to crack initiation. These measurements are then used to establish the position of the hinge point with respect to the crack tip (i.e. $W - D' - a_o$) and to confirm that the relationship between displacement and distance from the load line is linear (Figure 2.12). The position of the hinge point is dependent on geometrical constraint and material ductility.

The crack opening displacement is determined from the load line displacement based on the gained information from

$$\delta_c(t) = \Delta_c(t) \frac{\left(W - D' - a_0\right)}{W - D'} \tag{2.60}$$

The critical crack tip opening displacement is determined from the record at the onset of cracking, as defined by the crack initiation criterion, x.

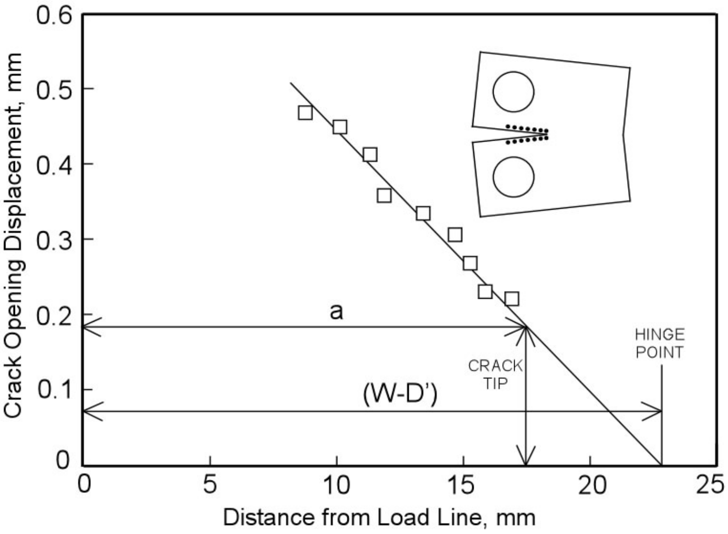

Figure 2.12. Variation of crack opening displacement with distance from the load line

Local CTOD Approach to Creep Crack Initiation

The alternative approach involves analytical determination of local crack tip displacement supported by metallographic measurement on the specimen side-surfaces. Crack Tip Opening Displacement (CTOD), as depicted in Figure 2.13(a) is used for creep crack initiation. Experimental evidence for the applicability of the local CTOD approach is shown in Figure 2.13(b).

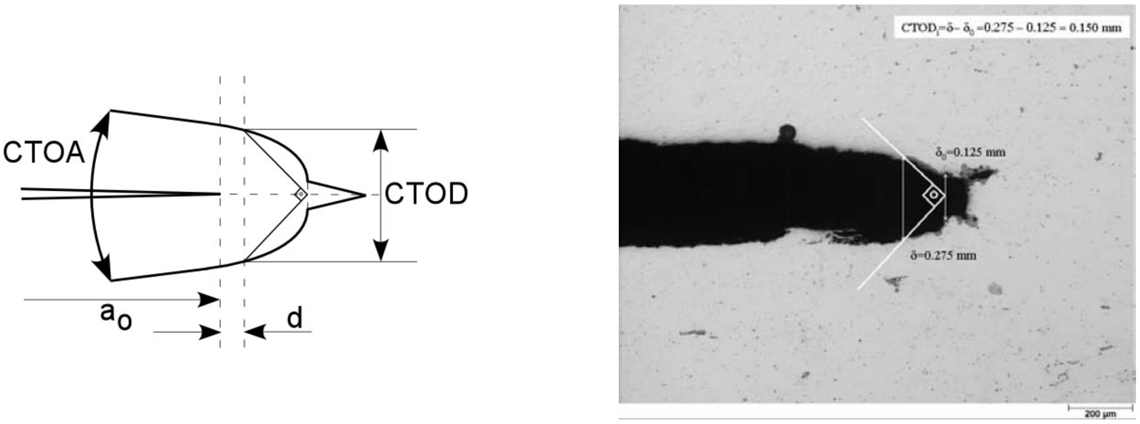

(a) (b)

Figure 2.13. (a) Illustration of CTOD and CTOA at crack initiation, (b) Metallographic of CTOD on a DEN(T) specimen

The application of this procedure in off-line inspection during testing is only possible with specimens without side grooves. For specimens with side grooves the metallographic examination is required to be done on the mid-plane section of the specimen. After unloading and withdrawal from the furnace, one of the sectioned test specimen side-face is ground and polished. The opening at the crack tip is then measured optically.

In order to minimise the subjectivity, the measurement of d is made at standard distance from the origin of the radius of curvature formed by the initial crack opening on loading. The standard measurement distance is determined by constructing lines from the origin of the radius of curvature at 45° to the centre line through the crack as depicted in Figure 2.13 (b).

The analytical approach to CTOD at crack initiation is illustrated in Figure 2.14. The CTOD is measured during time dependent fracture mechanics tests by measuring δ_{ts} at crack tip on the side surface of a specimen (t: tip, s: surface) following

$$X(t) = \frac{\delta_L(t)\cdot a_o}{\delta_L(t) - \delta_{ts}(t)} - a_i \tag{2.61}$$

Thus, Δ(t) can be calculated again by using triangular similarities from

$$\delta(t) = \frac{\delta_{ts}\cdot X(t)}{X(t) + d} \tag{2.62}$$

where

$$\mathrm{CTOD}(t) = \delta(t) \tag{2.63}$$

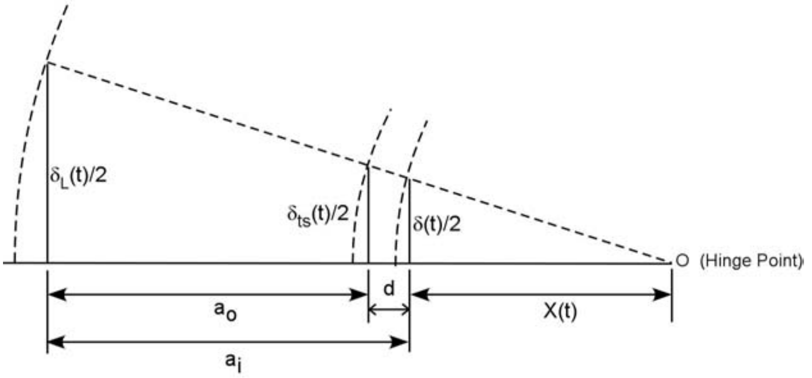

Figure 2.14. Dimensional relationship between δ_L, δ_{ts} and $\delta(t)$ for the determination of local CTOD at crack initiation.

2.3.2.5 Creep Crack Initiation Toughness K^c_{mat}

Creep crack initiation toughness K^c_{mat} is a generic term of resistance to crack initiation. It is the main concept of Time Dependent Failure Assessment Diagram (TDFAD) method of British R5 approach [29], which is used as control parameter for crack tip deformation leading to CCI. A central feature of the TDFAD approach is the definition of an appropriate CCI toughness which, when used in conjunction with the failure assessment diagram, ensures that crack growth in the assessment period is less than a value Δa. The CCI toughness values may be estimated indirectly from conventional creep crack initiation and growth data or evaluated directly from experimental load versus displacement information [28]. This section describes the latter direct approach for evaluating CCI toughness values.

Direct approaches for determining CCI toughness from experimental load vs. displacement data are based on methods used to derive critical J-integral. Therefore, the material toughness, K_{mat}, defined for low temperature fracture toughness standards [67-69] is adopted for creep conditions, denoted as K^c_{mat}.

Similarly, the total area under the load-displacement curve, U_T, may be conveniently partitioned into elastic, plastic and creep components, denoted U_e, U_p and U_c, respectively where

$$U_T = U_e + U_p + U_c \tag{2.64}$$

The following expression for direct evaluation of creep toughness from experimental load vs. displacement information has, therefore, been proposed

$$K_{mat}^{c} = \left[K^2 + \frac{E' \cdot \eta}{B_N \left(W - a_0\right)} \cdot \left(U_P + \frac{n}{n+1} U_c \right) \right]^{1/2} \tag{2.65}$$

where the factor n/(n+1) is required for consistency with standard creep crack growth testing procedures [3] as U_c is defined here as

$$U_c = F\Delta_c \tag{2.66}$$

where F is the applied load. Therefore, Equation 2.65 can alternatively be expressed as

$$K_{mat}^{c} = \left[K^2 + \frac{E' \cdot \eta \cdot U_P}{B_N \left(W - a_0\right)} \cdot \left(\frac{n}{n+1} \cdot \frac{E' \cdot \eta \cdot F \cdot \Delta_c}{B_N \cdot \left(W - a_0\right)} \right) \right]^{1/2} \tag{2.67}$$

which only differs from the Equation (A8.4) of Appendix A8 of R5 Volume 4 [29] in the use of $E' = E/\left(1-\nu^2\right)$ rather than E and the inclusion of an additional second term in equation 2.67 to incorporate the effects of plasticity during loading. Equation 2.67 is the recommended expression for determining the CCI toughness, K_{mat}^{c}. In order to accurately determine CCI toughness values experimentally, it is necessary to monitor load-line displacement during the loading phase of tests to allow U_p to be evaluated.

2.3.3 Assessment Methods for Creep Crack Initiation

2.3.3.1 Time Dependent Failure Assessment Diagram Method

Conventional methods for assessing incubation and the early stages of creep crack growth are generally based on the evaluation of parameters including crack opening displacement, δ, and crack tip parameters C^* and C(t) together with experimental data describing creep crack incubation or growth [8]. For low temperature defect assessment, the simplified R6 procedure [57] has been developed, which uses the concept of a Failure Assessment Diagram (FAD) where the detailed calculations of crack tip parameters are avoided. The failure assessment diagram indicates whether fracture will be controlled by elastic response, by plastic collapse or by intermediate elastic-plastic behaviour.

The FAD approaches have been extended to the creep regime [70-73] and the high temperature Time Dependent Failure Assessment Diagram (TDFAD) method has been incorporated into the high temperature defect assessment procedure R5 [29]. The TDFAD is a two-parameter failure assessment diagram, which takes both ligament failure and crack propagation into account. In other words, TDFAD combines fracture mechanics, which describes crack tip failure and damage mechanics, which describes ligament failure. A key requirement of TDFAD approach is the evaluation of time dependent CCI toughness, denoted as K_{mat}^{c} [74-76].

The TDFAD procedure is used either to determine whether a specified crack extension will be achieved within the assessment time or to determine the time required for a limited crack extension to occur. Hence approximate initiation times can be obtained, by using a predefined crack length for initiation i.e. 0.2 or 0.5 mm. After the construction of TDFAD for the time of interest, the failure initiation time for a specimen/component can be estimated by intersecting the line constructed by joining the points obtained for assessment with the TDFAD. This method is limited to Mode I type of loading and applicable to crack sizes which are small compared to component sizes.

Application and Construction of TDFAD

The procedures and parameters used in a TDFAD analysis are similar to that of the R6 [57] Option 2 FAD except that fracture toughness is replaced by CCI toughness and time dependent stress and strain parameters are needed. The TDFAD involves a failure assessment curve relating the two parameters K_r and L_r, which is defined in Equation 2.68 and a cut-off L_r^{max}. defined in Equation 2.69 below.

The application of TDFAD can be summarised in 5 steps [70]:

1) Define the maximum tolerable crack extension Δa for the creep crack initiation (CCI) (i.e. $\Delta a=0.2$ mm or 0.5 mm)
2) Obtain uniaxial creep data (i.e. $\sigma^c_{0.2}$, σ_r)
3) Construct TDFAD for each time of interest (i.e. t = 100h – 50,000 h)
4) Determine values of material creep crack initiation toughness, K^c_{mat}, for each time of interest for the specified maximum tolerable crack extension distance, Δa.
5) Calculate values of TDFAD parameters, L_r and K_r, for the time for which the occurrence of CCI needed to be predicted. If the point obtained lies within the safer zone of TDFAD, crack is not initiated.

The application procedure of TDFAD is illustrated in Figure 2.15.

The failure assessment diagram is then defined by the equations [29]

$$K_r = \left[\frac{E\varepsilon_{ref}}{L_r\sigma^c_{0.2}} + \frac{L_r^3\sigma^c_{0.2}}{2E\varepsilon_{ref}}\right]^{-1/2} \qquad \text{for} \qquad L_r \le L_r^{max} \tag{2.68.a}$$

$$K_r = 0 \qquad \text{for} \qquad L_r > L_r^{max} \tag{2.68.b}$$

In Equation 2.68, E is Young's modulus and ε_{ref} is the total strain from the average isochronous stress-strain curve at the reference stress, $\sigma_{ref} = L_r\sigma^c_{0.2}$, for the appropriate time and temperature. $\sigma^c_{0.2}$ is obtained from the isochronous stress-strain curve for the time of interest. Thus, Equation 2.68 enables the TDFAD to be plotted with K_r as a function of L_r. The cut-off, L_r^{max}, is defined as

$$L_r^{max} = \sigma_R / \sigma^c_{0.2} \tag{2.69}$$

where σ_R is the rupture stress from creep tests for the time and temperature of interest. Figure 2.16 shows the constructed TDFAD's for times of interest, from t=0 to 50,000 h.

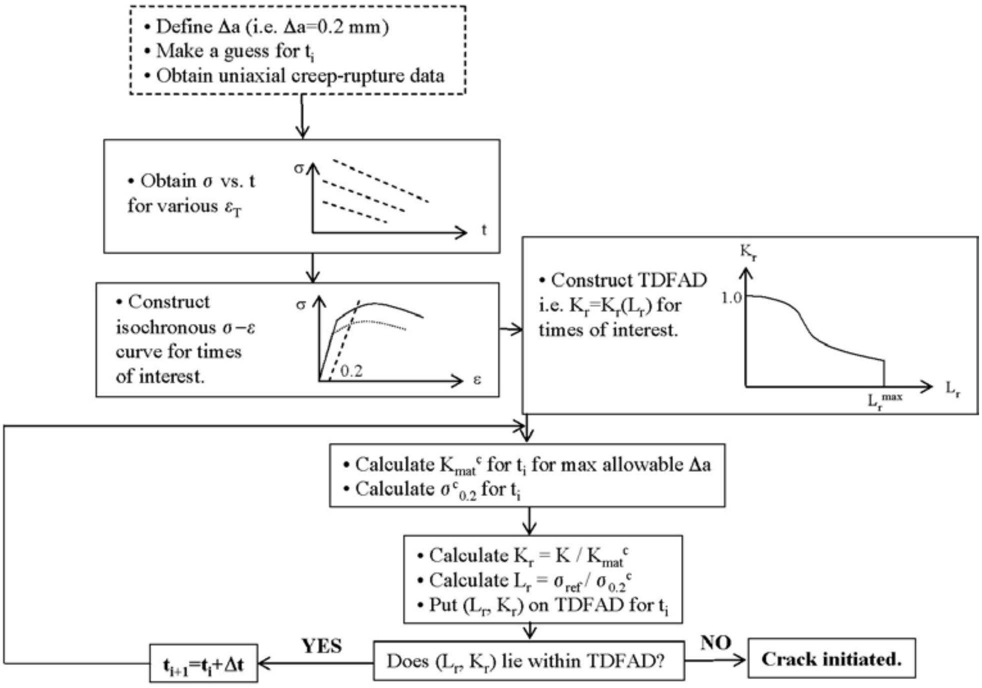

Figure 2.15. Flow diagram of the application of TDFAD

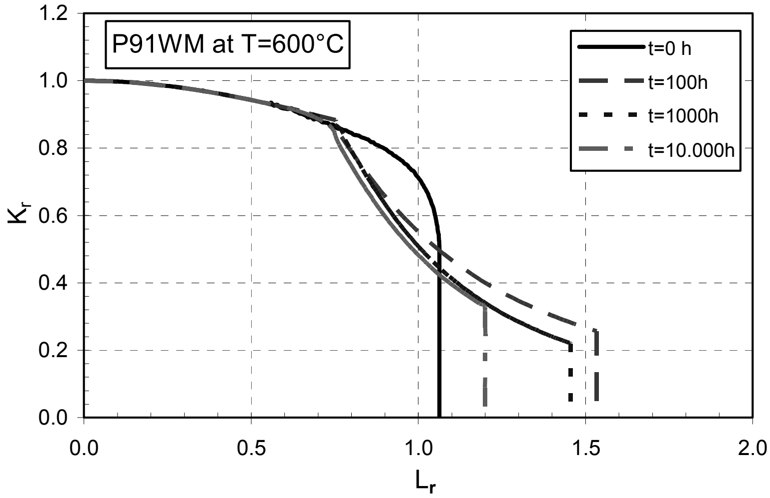

Figure 2.16. Time Dependent Failure Assessment Diagram (TDFAD) for different times of interest for P91 WM at 600 °C

TDFAD can be used either to estimate the time of initiation for a specimen/component or it can be used to determine if the crack is initiated at a certain time. The TDFAD parameters L_r and K_r have to be determined for the specimen/component for the times of interest. The parameter related to crack tip deformation, K_r, is defined as

$$K_r = K / K^c_{mat} \tag{2.70}$$

where K is the stress intensity factor and K^{c}_{mat} is the appropriate creep crack initiation toughness value [29] for a certain time and crack length. The TDFAD parameter related to ligament damage, L_r, is defined as

$$L_r = \sigma_{ref} / \sigma^{c}_{0.2} \tag{2.71}$$

where σ_{ref} is the reference stress and $\sigma^{c}_{0.2}$ is the stress corresponding to 0.2% inelastic (plastic plus creep) strain from the average isochronous stress-strain curve for the temperature and assessment time of interest [29].

2.3.3.2 Two-Criteria-Diagram Method

The Two-Criteria-Diagram (2CD) has been developed to assess creep crack initiation in ferritic steels [47]. The crack tip and ligament damage parameters, R_K and R_σ, respectively, are used in 2CD approach, which are similar to the TDFAD parameters K_r and L_r. The critical stress intensity factor, K_{Ii}, is used as a measure of crack initiation resistance rather than the creep crack initiation toughness, K^{c}_{mat}, which is used in TDFAD approach.

For the CCI and CCG, three different parameters have been proposed by Riedel and Rice [22]:

1) The stress intensity factor, K_I in Mode I loading case
2) The path independent integral C^*
3) The nominal stress in the farfield/ligament, which corresponds in a simplified manner to a general yield model in a creeping body.

Although it becomes invalid in inelastic crack tip conditions, the main advantage of using the linear elastic fracture mechanics crack tip parameter, stress intensity factor, K_I is that its application is well established for many different geometries and loading types. To calculate the stress intensity factors for components, numerous solutions for a wide variety of geometries and loading cases are available in the literature. Another advantage of using stress intensity factor, K, compared to the path-independent integral C^* is that, in application to components, It does not require measurement of creep displacement, Δ_c, on component's surface, like C^*-integral. Such measurement for real existing cracks in components loaded to a low stress level for a long service period is rather difficult or even impossible because of small displacement rates involved [77].

Therefore, stress intensity factor in Mode I loading, K_I, is chosen to be used in Two Criteria Diagram (2CD), which is designated as K_{Iid}. K_{Iid} is a fictitious, ideally elastic stress intensity parameter resulting from the commonly used linear elastic formulas. In 2CD method, K_{Iid} is used to characterise crack tip state.

However, for creeping bodies, in which both stress redistribution and damage accumulation occur in a time dependent manner, it is not sufficient to use only K_{Iid} as the only parameter to describe the crack tip behaviour. This means two different parameters are required in the creep range to define creep crack initiation and growth. For 2CD, these parameters are K_{Iid} for the description of crack tip situation and σ_n (nominal stress) for the consideration of the stress state description of farfield/ligament. Such a 2CD was first proposed by Ewald et al. in 1986 [47].

For the 2CD, the component loading parameters are normalised by time and temperature dependent data, which indicates material resistance

$$\begin{aligned} R_\sigma &= \sigma_{n0} / R_{mt} \\ R_K &= K_{Iid0} / K_{Ii} \end{aligned} \tag{2.72}$$

where R_σ is the farfield stress ratio and R_K is the crack tip stress intensity ratio. The σ_{n0} indicates the nominal stress in the farfield of the pre-cracked specimen or component. The R_{mt} is the creep rupture strength obtained from tensile specimens. In order to determine the R_{mt} for a time span, a series of tensile specimen must be tested to rupture at the temperature of interest.

K_{Iid0} is the fictitious elastic value at time zero at the crack tip of the component. K_{Ii} denotes the creep crack initiation value of the material, which is a material property. K_{Ii} depends on the shape and the size of the specimen as well as the temperature. Therefore it has to be determined from specimens with high K_{Iid} / σ_n ratio [77].

A typical 2CD can be seen in Figure 2.17. Similar to the TDFAD, the 2CD has two zones, namely, the "crack" zone and the "no crack" zone. The onset of crack initiation is determined by the position of the point, i.e. if it lays in the "crack" zone or in the "no crack" zone. The 2CD method also distinguishes the type of damage mechanism(s) affecting the initiation of the crack. Three different zones separated by R_σ / R_K lines define the type of damage zones. As depicted in Figure 2.17, CCI by pure ligament damage is assumed for $R_\sigma / R_K \geq 2$. CCI only by crack tip damage is assumed when $R_\sigma / R_K \leq 0.5$. The ratio $0.5 \leq R_\sigma / R_K \leq 2$ corresponds to the mixed damage zone, in which both ligament damage and crack tip damage are involved.

The validity of the ratio lines in Figure 2.17 is restricted to materials with sufficient high creep ductility. Only notch-weakening materials, i.e. materials with at least 7% rupture ductility are described by this type of diagram. For lower rupture ductility, i.e. brittle materials, the shape of the diagram changes [30]. However it is not included here, since it does not represent the materials studied in this thesis.

In order to apply the 2CD to a component, firstly, the creep strength data R_{mt} must be obtained by testing uniaxial specimens. Secondly, crack initiation data K_{Ii} referring to a specified Δa must be prepared in a time and temperature dependent manner [47].

After obtaining the data mentioned above, the 2CD for static loads can be applied to determine occurrence of crack initiation after a certain service time as follows:

1. the stress intensity factor for the initial flaw K_{Iid0} is determined

2. nominal stress in the farfield ligament behind the flaw, σ_{npl} is determined from

$$\sigma_{npl} = \frac{F}{B.(W-a)} \left(1 + 2 \frac{W+a}{W-a} \right) \tag{2.73}$$

After obtaining these values repeat the following steps for each service time

3. take or interpolate the creep strength R_{mt},
4. take or interpolate the stress intensity factor for crack initiation K_{Ii},
5. calculate the crack tip ratio $R_K = K_{Iid0} / K_{Ii}$
6. calculate the farfield stress ratio $R_\sigma = \sigma_{n0} / R_{mt}$

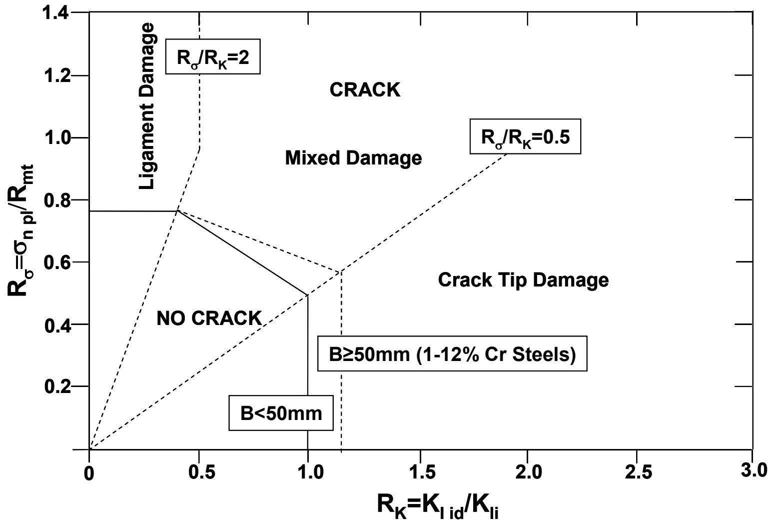

Figure 2.17. Two Criteria Diagram (2CD) for creep crack initiation

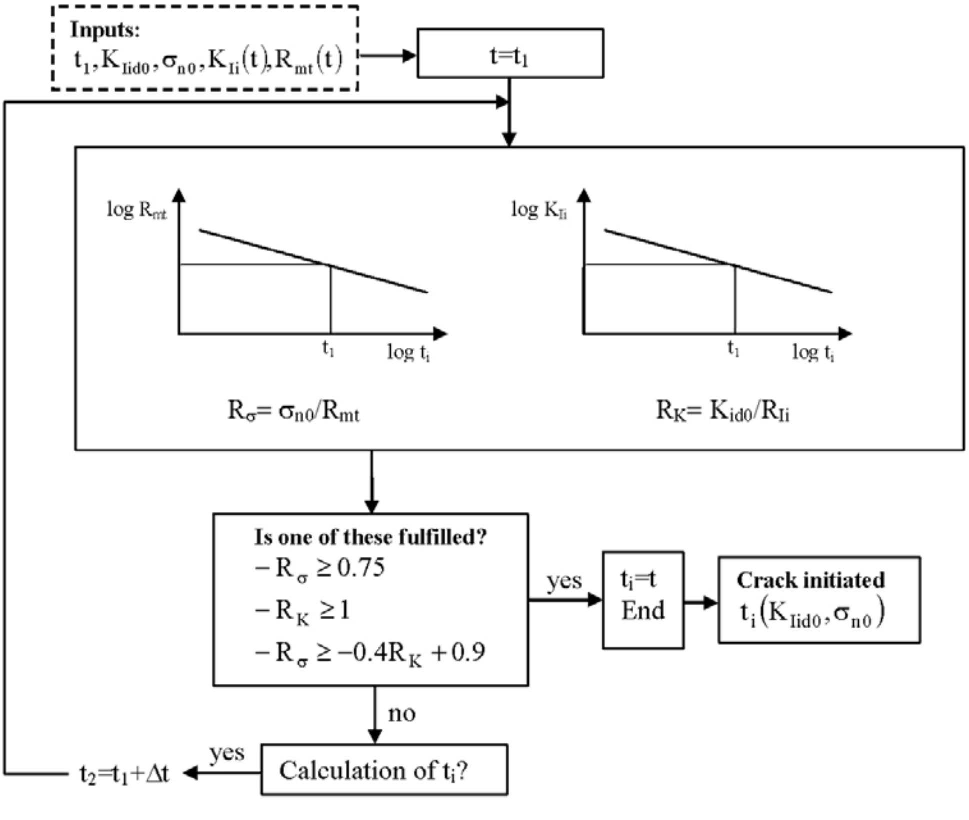

Figure 2.18. Flow chart for the application of 2CD to determine CCI time for static loading [77].

Data points R_σ and R_K for each service time are put into the 2CD. This yields the damage path of the component. The damage path is compared with the crack-no crack boundary line, so that the crack initiation time in the component can be obtained. The flowchart for application of 2CD for static loads is given in Figure 2.18.

Similar to TDFAD, 2CD can also be used to estimate the crack initiation time by plotting the crack growth path by calculating the R_σ and R_K values corresponding to different times i.e. t=10 to 10,000 h. The intersection point of the path with the "crack – no crack" boundary can be used to estimate the CCI time for the component or specimen.

This thesis aims to compare the two defect assessment methods for CCI, the TDFAD and 2CD, for test materials of 2.25CrMo (P22), 9CrMoV (P91) and their weldments. Sensitivity analyses of materials data, time and testing conditions are emphasised in this thesis. The sensitivity issue of high temperature data and defect assessment procedures which are mentioned here are discussed in detail in Section 2.4.

2.4 SCATTER ANALYSIS OF HIGH TEMPERATURE EXPERIMENTAL DATA

2.4.1 Introduction

Scatter is seen in any test data which might have many sources including noise in measurement systems or human error during testing [78]. Although some of these sources are unpredictable, scatter in data can be reduced significantly through use of proper testing methods and equipment that are calibrated following norms [6].

Most of the procedures used for high temperature plant assessment (See Sec. 2.2) are deterministic thus requiring appropriate, preferably specific data input to determine the crack behaviour and remaining life of components.

Furthermore, the prediction of life expectancy of a component containing a defect is strongly influenced by a wide range of parameters, which generally exhibit significant uncertainties and scatter. These include [79]

- The initial defect size, shape and location which may be subject to measurement errors,
- The component geometry which can also not be accurately identified (e.g. imprecise measurement of the pipe wall thickness),
- The operating conditions (e.g. load, temperature etc.) which may have variations with time,
- The materials properties, such as in weldments, which may not be precise [80].

Statistical analysis of experimental data is required in order to deal with the scatter in high temperature data. The statistical analysis allows determining the distribution of each parameter and their statistical properties. They will be used to estimate the sensitivity of calculated creep crack initiation and growth parameters. The statistical properties mentioned are standard deviation, mean, variance and error distribution of experimental data family [81]. The assessment of the experimental data to obtain crack growth parameters or failure assessment diagram parameters [29] requires dealing with the uncertainties of each input parameter. Given that there are more than one input parameter for an experimental dataset which goes into the assessment, combination of uncertainties of different input parameters may cause a significant uncertainty in the obtained results.

Therefore, a deterministic sensitivity analysis and/or a probabilistic analysis should be performed in order to evaluate the importance of the uncertainty of input parameters. These analysis methods deal with either individual or combined effect of variations of input parameters (experimental data) on output functions (assessment results).

The effect of each individual parameter on an output function are given in the form of a Tornado Diagram as well as being displayed in a table. A tornado diagram consists of a set of horizontal bars, one for each sensitivity input. The beginning and end of each bar represent value extremes, which are calculated based on the variations of the associated input.

When the uncertainty of the input can be modelled through the definition of a statistical distribution or when a set of measurements are available for the input from which a distribution can be evaluated that best fits those values, a probabilistic analysis [82] can be performed.

Probabilistic analysis is more complex compared to sensitivity analysis. In probabilistic analysis, regarding the distributions of input parameter families, a very high number of different combinations of input parameters are created and probabilistic distribution of output parameters are obtained. This condition requires methods like Monte Carlo Simulation, which depend on sampling of stochastic parameters (input parameters) and calculate output parameters.

2.4.2 Scatter in High Temperature Crack Growth Data

The scatter associated with test data reflects the uncertainty in confidence of a measurement of the real material property. Despite interaction of different factors which cause scatter in high temperature crack initiation and growth data, the sources of scatter can be classified as [78]

- Scatter due to test equipment,
- Scatter due to testing procedures,
- Scatter introduced during assessment of data.

2.4.2.1. Scatter due to Test Equipment

The scatter caused by testing equipment might be either due to measuring equipment or loading system. Although the test equipment should be calibrated and maintained periodically according to the instructions of the manufacturer, every system has a minimum capability to acquire the slightest changes. On the other hand, slight changes, which are allowable, occurring in the testing environment during the test might cause scatter in high temperature crack growth data.

The use of the testing equipment at its limits using very lower load levels than the maximum capacity of the servo-test machine, the test temperature that affects PD and LLD readings and alignment problem of the loading rig would lead to scatter in high temperature data.

Furthermore, improper alignment and installation of displacement gauges, friction at contact locations might cause scatter in data. The use of non-contact laser measurement system improves the quality of data, however, increases the sensitivity of the measuring equipment (Figure 2.19).

The PD method (ACPD or DCPD) used for crack size monitoring must be calibrated and maintained. The improper connection of current and voltage reading leads to scatter in PD data.

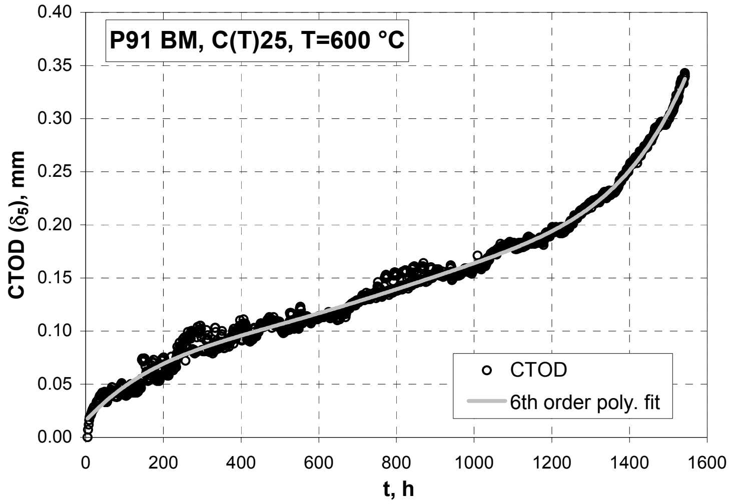

Figure 2.19. Scatter in local CTOD, measured crack tip opening displacement, vs. time plot of a P91 BM C(T) specimen tested at 600 °C.

2.4.2.2. Scatter due to Testing Procedures

Testing standards and codes [3,6] need to be strictly followed in obtaining reliable data. However, human error and insufficient training of personnel cause uncertainty in data. For the pin-loaded specimens, during the specimen installation, improper tolerances of the specimen and the loading pins may cause friction and lead to bad alignment.

During the initial loading of the specimen, an undesired shock loading may introduce a plastically deformed zone at the crack tip. This will change the material properties within the deformed zone as well as it will cause scatter at the very first portion of the data, which is very valuable for crack initiation studies.

2.4.2.3. Scatter Introduced During Assessment of Data

The assessment of high temperature data needs to follow the special procedures given in related standards and codes [3,6]. However, since these procedures are given in general terms, they usually do not mention the pitfalls of each individual step.

A typical dataset consists of load, temperature, potential drop and displacement data should be fitted using relevant regression methods which are available in commercial software programmes. However, using inadequate type of fitting method may affect the assessment procedure and cause kinks in the plots, which actually do not represent the real materials behaviour (Figure 2.20). Kinks usually appear at the junction points of the multiple fitting functions for PD vs. time or LLD vs. time.

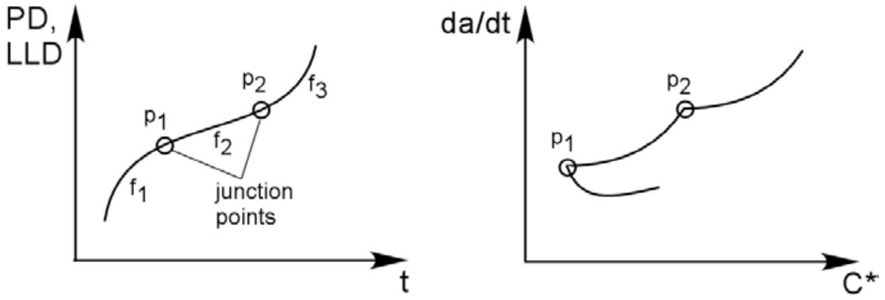

Figure 2.20. Schematic view of the possible effect of chosen fitting function to da/dt vs. C^* plot

The error introduced into the high temperature crack growth data through the use of incorrect materials properties and geometrical dimensions might affect the results drastically. Particularly, the incorrect use of Norton's creep exponent, n, and modulus of elasticity, E, lead to a high deviation of the results. For example, during the use of compliance method in determining the crack extension, the deviation of modulus of elasticity by 10% from the correct value will lead to a deviation in estimation of crack extension by 5%. Therefore, deterministic sensitivity analysis and/or probabilistic analysis requires that statistical distributions of input parameters should be performed in order to determine the individual and/or combined impact of the deviation of input parameters on the assessment of high temperature crack growth data.

2.4.3. Presentation of Scatter in Crack Growth Data

There are different approaches to define scatter bands of a set of crack growth data. One method involves construction of 95% or 90% confidence limits [79] as applied to the CCG data of P91WM in Figure 2.21. The other method uses ± 2σ standard deviation bands as seen in Figure 2.22.

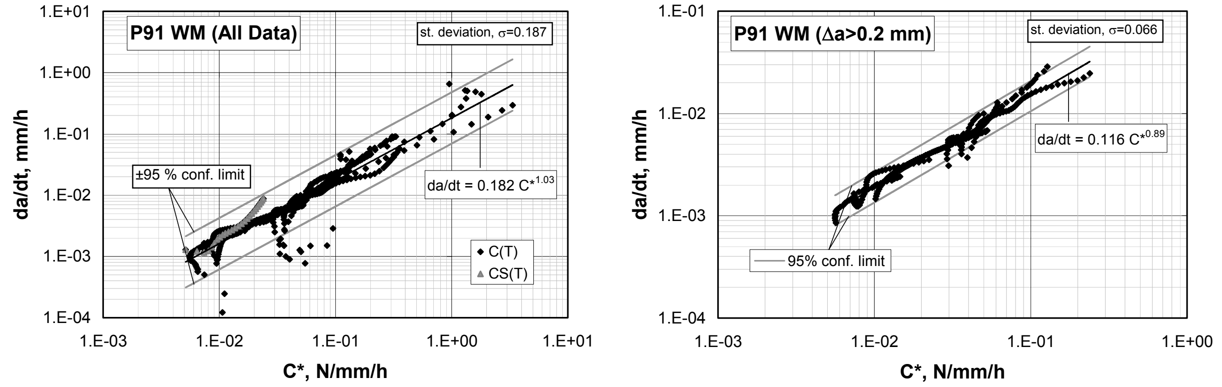

(a) (b)

Figure 2.21. CCG rate correlation with C^* for P91 WM, (a) all data without data reduction, (b) reduced data with data Δa>0.2 mm with scatter bands using 95% confidence limits.

For both of these methods, the wider the scatter band, less reliable is the defined data. For a normal distribution, the constructed ± 2σ lines cover a significant portion of the dataset. In fact, ± 2σ bounds and 95% confidence limits cover almost the same amount of data [79].

Putting scatter bands as in Figures 2.21 and 2.22, the group of data points which falls out of the representative material crack growth behaviour can be determined and later excluded from the dataset. Therefore, scatter bands such as 95% confidence limits can be used in decision-making as well. The collated data and proposed correlations may be compared with creep crack growth correlations given in defect assessment procedures such as BS PD6539 [83] or BS 7910 [35].

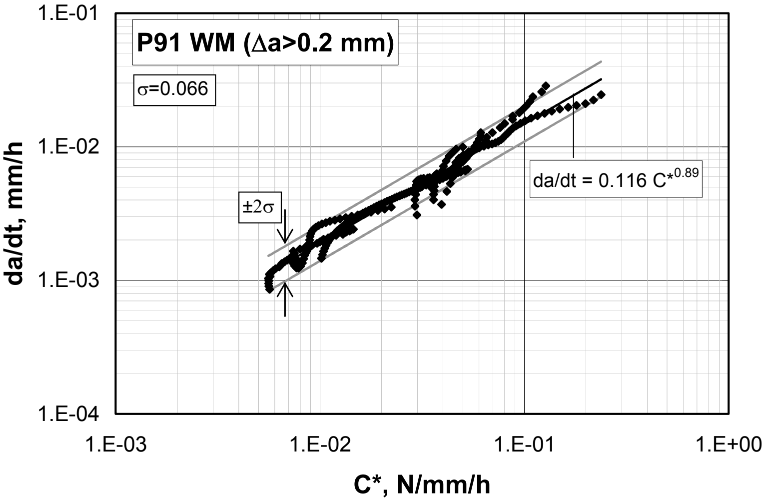

Figure 2.22. CCG rate correlation with C^* for P91 WM, data reduced to Δa>0.2 mm, with scatter band using ±2σ

2.4.4. Deterministic Sensitivity Analysis of Crack Growth Data

The principles of deterministic sensitivity analysis were described in the low temperature defect assessment procedure R6 [57]. The defect assessment procedure itself is deterministic and needs further sensitivity studies to address uncertainties in the various input parameters. As a general guide, deterministic sensitivity analyses are to be performed to demonstrate the realistic variations in input parameters that do not violate safety margins. The sensitivity analyses should also identify if the assessment is particularly sensitive to any of the input parameters.

There are a significant number of input parameters in the assessment of creep crack initiation (CCI) or creep crack growth (CCG) test data. In particular, materials data needed are creep strain, creep strain rate, creep ductility and modulus of elasticity, E. In addition, geometrical parameters of initial crack length, a_o, final crack length, a_f, geometrical dimensions of the specimen W, B, B_n, and distance between potential drop connections, Y, affect the test results. In evaluation where more than one type of specimens is used, each group of specimens geometry must be analysed separately, in order to compare their individual sensitivity to different parameters.

The number of input parameters contributing to sensitivity analysis is decided by examining the statistical distribution of each parameter, in case they are available. When they are not available, either these parameters can be discarded or analysed by inserting fictitious variation ranges for these parameters. Note that these fictitious ranges should be realistic and reflect the possible variation of parameter, such that based on the experience of the expert.

The R5 procedure [29] recommends for CCG assessment of components the following combinations of data for inclusion in the sensitivity studies [84]

- Best estimate-mean data
- Lower bound CCG data with upper bound creep strain data
- Upper bound CCG data with lower bound creep strain data

Implicit in these recommendations is that the input materials data are unlikely to be independent. Correlations between different material properties are difficult to assess quantitatively in the absence of a rigorous statistical treatment of data.

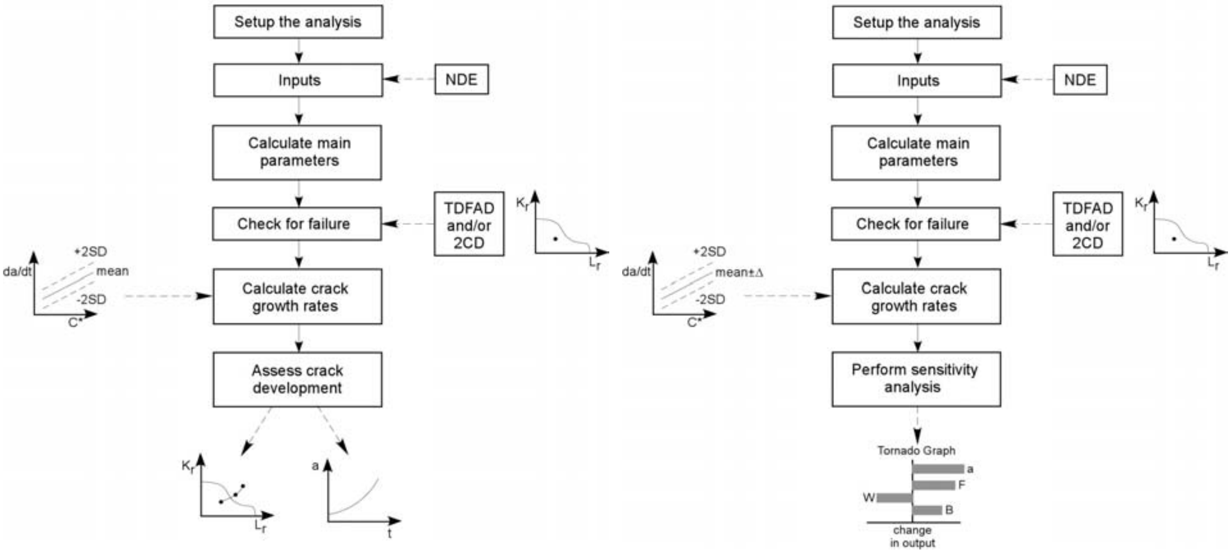

(a) (b)

Figure 2.23. Flow charts of (a) deterministic analysis and (b) deterministic sensitivity analysis [79]

Figure 2.23 depicts the difference between the deterministic analysis and deterministic sensitivity analysis of high temperature crack growth data in defect assessment procedures. Note the difference between two methods that in deterministic analysis, the input CCG data is the mean value. However, in deterministic sensitivity analysis it also consists of the variation of CCG data. The variation may depend on the real statistical data as well as it may depend on the range which is determined by the person assessing the data set. Therefore, the deterministic analysis yields merely the results of output parameters without any variations. The deterministic sensitivity analysis yields the effect of variations of input parameters as well as the output parameters depending on the mean values of the input parameters.

In deterministic sensitivity analysis, the sensitivity of each output parameter to the unit variation of each single input parameter is illustrated by tornado diagrams. The tornado diagram reveals the effect of variation of each single input parameter as well as the relativity of the effects of all parameter with respect to each other. Figure 2.24 shows the tornado diagram for the sensitivity of crack tip parameter, C^*, calculated at $\Delta a=0.5$ mm to unit variations of the following testing parameters, test load, F, specimen thickness, B, specimen net thickness, B_n, specimen width, W, initial and final crack lengths, a_o and a_f. In order to obtain individual effects of input parameters, regression coefficient of each input parameter is obtained by regression analysis of the dataset. The presentation of effects of various testing parameters on output parameter(s) by use of tornado diagrams serves as an effective tool for interpreting test results and facilitates proper use of test results in defect assessment procedures.

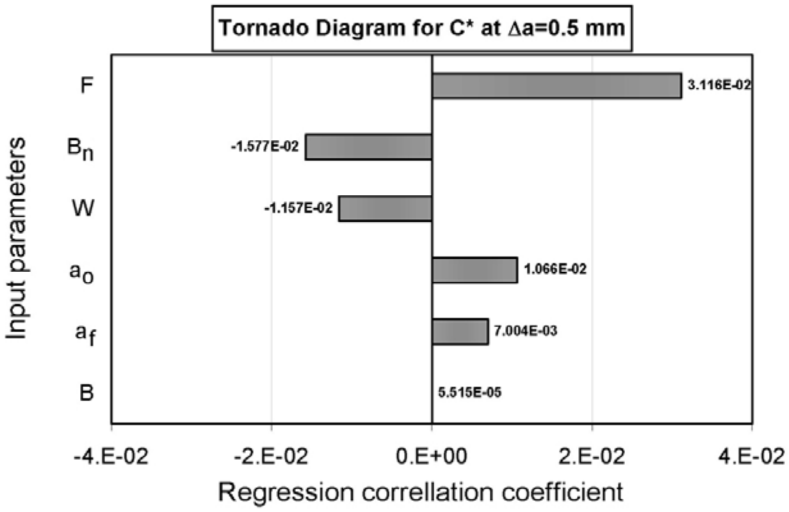

Figure 2.24. Tornado diagram of a CS(T) specimen of P22 BM tested at 550 °C for the sensitivity of C^* calculated at $\Delta a = 0.5$ mm.

2.4.5. Probabilistic Sensitivity Analysis of Crack Growth Data

An alternative to deterministic sensitivity studies is probabilistic sensitivity analysis. This method can either be used independently or it may be used together with deterministic approach. It provides a basis for deterministic sensitivity analyses since it helps to define acceptable margins of input parameters, i.e. contributions from variation of materials properties and geometrical effects are predicted more realistically. Figure 2.25 shows the flowchart for probabilistic sensitivity analysis.

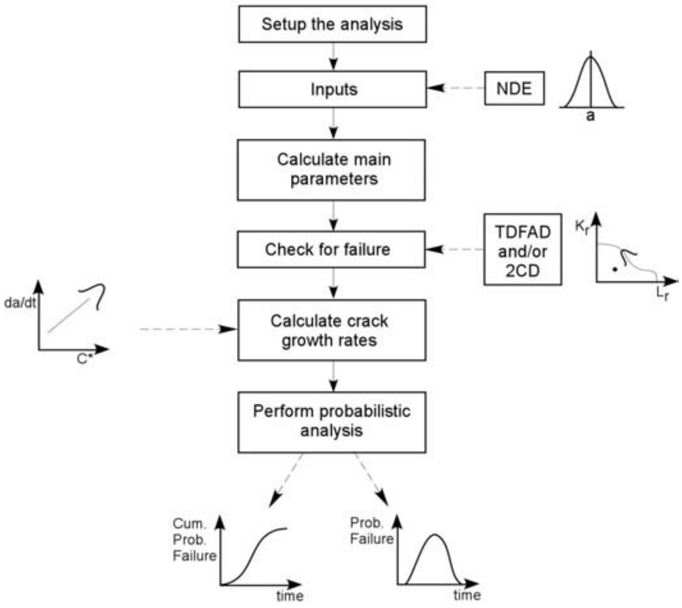

Figure 2.25. Flow chart of probabilistic sensitivity analysis [79]

The most important advantage of the probabilistic sensitivity analysis is that the probabilistic method reduces the degree of conservatism that is introduced by the deterministic sensitivity analysis by use of most pessimistic combinations of input parameters. On the contrary, the use of probabilistic sensitivity analysis facilitates the calculation of probability of large number of different combinations of input parameters. Therefore, the user may discard the cases with very low probability and obtain more reliable and less conservative results.

In this thesis, the probabilistic sensitivity analysis method used is based on Monte Carlo simulation technique [85]. It depends on creating families of input parameters with high numbers and calculating output parameters at high numbers, so that possible statistical distributions of output functions can be determined.

2.4.5.1. Monte Carlo Simulation

The Monte Carlo simulation [85] is an effective technique in performing probabilistic sensitivity analysis. It is a stochastic technique used to solve mathematical problems. It uses random numbers and probability statistics to obtain the aimed answer. The Monte Carlo simulation involves five steps

1) The selection of ranges and distribution for each input parameter,
2) Generation of a sample from the ranges and distributions specified in the first step,
3) Evaluation of the model for each element of the sample,
4) Uncertainty analysis,
5) Sensitivity analysis.

In Monte Carlo simulation, the random selection process is repeated many times to create multiple scenarios. Each time a value for each input parameter is randomly selected and it forms one possible scenario and solution to the problem. Added together, these scenarios give a range of possible solutions, where some of which are more probable and some less probable. When repeated for many scenarios (e.g. 10^4 times), the average solution will give an approximate answer to the problem. Accuracy of this answer can be improved by simulating more scenarios. In fact, the accuracy of a Monte Carlo simulation is proportional to the square root of the number of scenarios used [86]. Monte Carlo simulation is advantageous because it is a very direct approach which is able to solve problems for which no other solutions exist. However, this also means that it is computer intensive and requires high-capability computers and long runtimes.

3. MATERIALS

3.1. INTRODUCTION

Two materials were chosen for the experimental programme, namely P22 and P91 steels. The ASTM SA335 P22 (2.25 Cr1Mo) steel is the most commonly used low alloy ferritic steel in high temperature tubing and pipework in power generation and petro-chemical plants. The ASTM SA335 P91 (Mod-9Cr1Mo) steel is a newly developed high strength, high ductility bainitic-martensitic steel with possible applications in pressure parts in conventional and nuclear power plants and petrochemical reactor vessels and pipework.

Similar welded pipes of two materials were produced within the EC Project SOTA [87] by circumferential butt-welding using the shielded metal arc welding (SMAW) process. The test materials were taken from the welded pipes of 220 mm outer diameter and 48 mm wall thickness for P22 and 295 mm outer diameter and 58 mm wall thickness for P91. The P22 and P91 pipes were post-weld heat treated at 710 °C and 760 °C, respectively, prior to sectioning of blanks for machining of the specimens.

The chemical compositions of the material both BM and WM are given in Table 3.1. The materials tensile and creep properties at test temperatures for P22 and P91, both with BM and WM were determined in the EC Project SOTA [87] as seen in Table 3.2. The compositions of elements for BM fall in the designated material composition range. Uniaxial creep ductility values are taken from [88].

Table 3.1. Chemical compositions of materials [89]

Material	C	Mn	Si	P	S	Cr	Ni	Mo	V	Al	Nb
P22 BM	0.101	0.443	0.206	0.024	0.015	2.07	0.099	0.939	<0.01	<0.01	-
P22 WM	0.017	0.731	0.407	0.019	0.008	2.38	0.05	1.05	0.02	-	0.007
P91 BM	0.091	0.409	0.369	0.028	0.013	8.44	0.272	0.922	0.24	0.07	-
P91 WM	0.087	0.692	0.285	0.013	0.007	9.39	0.63	0.98	0.267	-	0.04

Table 3.2 Materials data determined in tensile and creep tests

Material	$R_{p0.2}$(MPa)	R_m(MPa)	E(GPa)	D_1	m	A_1	n	ε_f
P22 BM-550 °C	350	397	157	0.0024	16.91	2.80×10^{-43}	17.80	0.37
P91 BM-600 °C	441	463	164	0.0018	27.73	1.57×10^{-45}	18.51	0.13
P22 WM-550 °C	327	369	136	0.0016	19.17	7.64×10^{-21}	7.40	0.07
P91 WM-600 °C	362	385	125	0.0015	23.86	5.99×10^{-24}	8.55	0.02
P22 SIM. HAZ-550 °C Type IV	241	345	108.3	0.0017	8.51	1.09×10^{-22}	8.48	0.37*
P22 SIM. HAZ-550 °C Centre	320	381	144.8	0.0016	12.20	9.55×10^{-17}	5.99	0.37*
P91 SIM. HAZ-600 °C Type IV	320	333	155	0.0016	17.38	7.16×10^{-35}	14.35	0.13*
P91 SIM. HAZ-600 °C Centre	293	317	139	0.0016	20.74	7.16×10^{-35}	14.09	0.13*

(*) Due to lack of data, BM uniaxial creep ductility is taken.

The stress strain curves of materials P22 and P91 and their weldment zones are shown in Figures 3.1 and 3.2, respectively. The yield strength data at test temperature show a decrease in WM and particularly HAZ, where the welds are undermatched in terms of strength values.

Figure 3.3 depicts the creep rupture strength of P22 and P91 steels at 10^5 hours for a temperature range at which these materials are mostly operated. It is seen that the magnitude of the rupture strength of P22 is almost the half of the P91's and it decreases more rapidly with increasing temperature.

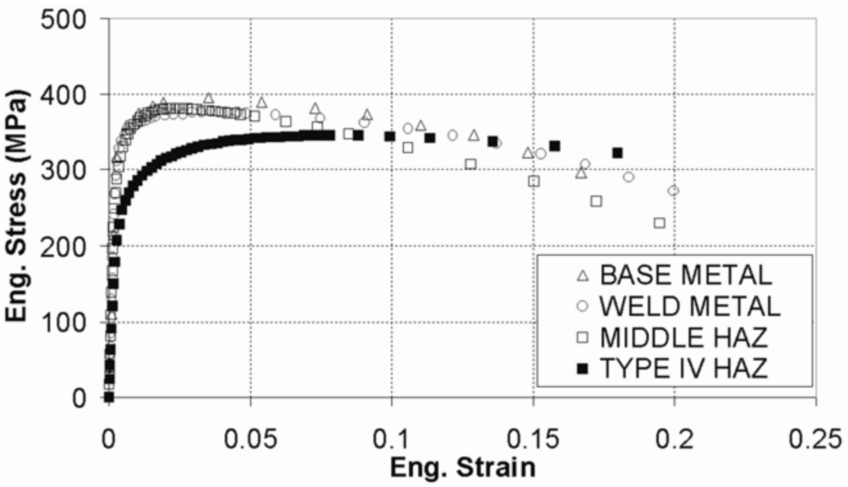

Figure 3.1. Stress vs. strain curves of P22 BM, WM and HAZ standard tensile (ST) specimens at 550 C°.

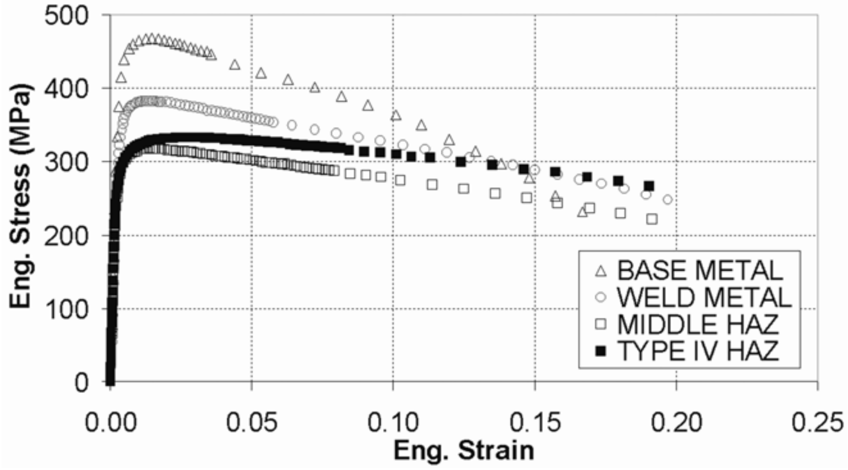

Figure 3.2. Stress vs. strain curves of P91 BM, WM and HAZ standard tensile (ST) specimens at 600 C°.

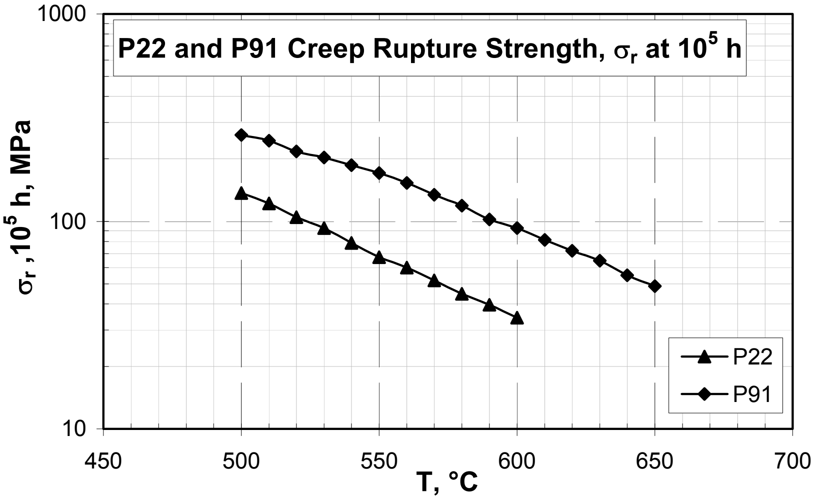

Figure 3.3. Creep rupture strength of P22 and P91 steels at 10^5 hours at 550 °C and 600 °C, respectively [90].

Figure 3.4 shows the variation of creep rupture strength vs. rupture time, t_r, for both P22 and P91 steels. The available data cover a very large range of time from 30 hours to $3x10^5$ hours.

It is observed that although the magnitudes of creep rupture strengths of P91 are higher than those of P22, the creep strength of P91 decreases at a higher rate than that of P22 and becomes almost equal to it after 30,000 hours. This situation sheds some light on the materials behaviour as it is exposed to high temperature for longer times of over 10,000 hours.

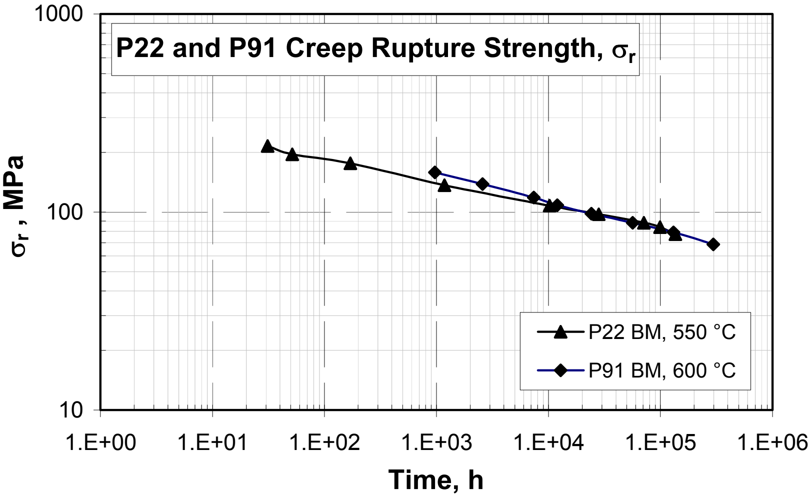

Figure 3.4. Variation of creep rupture strength of P22 and P91 steels with time at 550 °C and 600 °C, respectively [91].

3.2. 2.25Cr1Mo STEEL (P22)

2.25Cr1Mo (P22) steel is a low alloy steel which has been used worldwide since over 50 years. These type of steels are widely used in pressure part applications in boilers fired by fossil fuels and also in Heat Recovery Steam Generators (HRSG's) [92]. Typically, these are tubing alloys used in the temperature range where mild steel becomes too weak under creep conditions. Alloys of this type are also used in thick section components such as headers and steam pipes.

The key property requirements are

- Good tensile strength at temperatures up to 450 °C,
- Creep strength at temperatures up to 550 °C (T/P22, T/P23),
- Excellent weldability with no requirement for post-weld heat treatment,
- Resistance to steam oxidation,
- Resistance to low NO_x corrosion usually by weld overlay or spray coatings.

The alloy widely known as Grade 22 based on the ASME alloy designation has been used successfully in power plant applications requiring reasonable high temperature strength derived primarily from a dispersion of fine molybdenum carbide precipitates and resistance to oxidation derived from the chromium present. Example specification numbers from the USA, UK, Germany and Japan are given in Table 3.3. The material is available in forms of tubes, pipes, forgings, castings, bars, rods, plate and sheet. The most common applications are in superheater and reheater tubing as well as high temperature heading and piping where operation up to about 600 °C. In fact different codes and manufacturers recommend different peak temperatures for 2.25Cr1Mo low alloy steel as depicted in Table 3.4.

Table 3.3 Example material specifications for 2.25Cr1Mo low alloy steels [93]

ASME	British	German	Japanese
SA-213 T22	3059 S1 622-490	1715 10CrMo9-10	G3462 STBA24
SA-335 P22	3604 CFS622	1715 10CrMo910	G3458 STPA24

Table 3.4 Peak operating temperature recommendations [93]

ASME Specification	ASME, °C	B&M, °C	Alstom, °C	Riley, °C
SA-335 P22	650	600	580	580

Experience suggests that for reliable long term performance, the sustained metal temperature should be below about 593 °C. However it is apparent that the specific information regarding pressure, temperature and environment should be considered in selecting material and component geometry.

The microstructure of P22 depends on the composition and heat treatment history. Typically slower cooling rates, which are nearer to equilibrium result in the formation of the ferrite, with bainite, whereas martensite formed under more rapid cooling conditions. The particular microstructure formed can be identified using Time – Temperature Transformation diagrams (TTT's). Figure 3.5 shows the typical ferritic microstructure of the P22 test material.

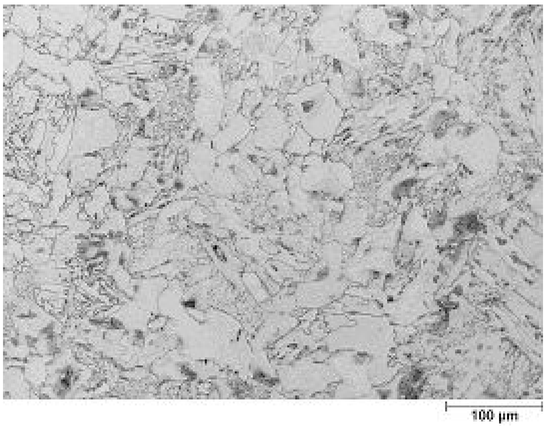

Figure 3.5. Typical microstructure of P22 BM showing predominantly ferritic microstructure.

In practical applications, fast cooling rates will typically be seen associated with welding so that the WM and HAZ will typically exhibit bainitic microstructure. Slow cooling will occur following heat treatment of large thick section components so in this components mostly ferritic microstructures are seen. This heterogeneity in microstructure in weldments caused by different cooling rates of different weldment zones will typically result in variation in materials properties (Figure 3.1). PWHT will reduce welding residual stresses and temper the microstructure.

3.3. Mod - 9Cr1Mo STEEL (P91)

The Mod – 9Cr1Mo steel is one of the recently developed 9-12% Cr steels which are used in both boilers and in steam turbines for many components including pipes, headers, rotors, casings and chests with a (current) maximum operating temperature of ~620°C. These alloys have lower coefficients of thermal expansion and higher thermal conductivities than austenitic steels and should therefore be more resistant to thermal cycling. In boilers, these steels are used for tubing in superheaters and reheaters, operating with metal temperatures up to about

620°C. Thick-section parts such as headers and steam pipes are also fabricated from these materials. The key requirements are

- · Creep strength and long-term structural stability at the operating temperature,
- · Ac_1 temperature consistent with relatively high tempering temperature,
- · Good weldability with low susceptibility to type IV cracking,
- · Resistance to steam oxidation,
- · Low-cost relative to austenitic materials,
- · Good performance under cyclic and variable load conditions.

The P91 alloy composition was modified with addition of small amount of V, Nb and N. This led to the considerably improved creep and tensile strength and excellent ductility and toughness. This grade has been called " Mod-9Cr1Mo or 9Cr1MoV and was incorporated into the ASME specifications as SA-213-T91 for tubing, SA-387-Grade 91 for plates, SA-335-P91 and SA-369-FP91 for pipe and SA-182-F91 and SA-336-F91 for forgings. Figure 3.6 shows the typical martensitic microstructure of P91 test material.

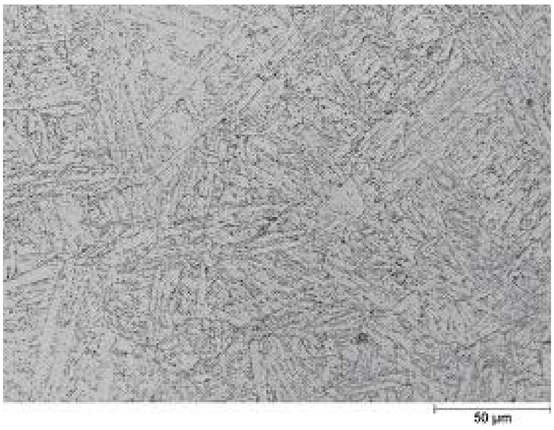

Figure 3.6. Typical microstructure of P91 BM showing predominantly martensitic microstructure.

In the typical service temperature range of these materials in existing fossil powered systems from 538 °C to 621 °C, this material offers twice better advantage in design allowable stresses over 2.25Cr1Mo steels (Figure 3.3). Unlike the 2.25Cr1Mo steel, the most remarkable feature of the Mod-9Cr1Mo is material is that it does not suffer significant creep at ASME Boiler and Pressure Vessel Code (BPVC) [55] design stresses at temperatures up to 593 °C [94]. However, recent reports indicate same weaknesses that will also be reported in this thesis.

Comparison of required wall thickness of a 200 mm thick pressurised pipe (320 bar) at 593.3 °C for various steels is illustrated for various high temperature steels in Figure 3.7. It is calculated that P91 requires 58% less material than P22 for the same amount of piping needed.

Although with the proper welding procedures and control Mod-9Cr1Mo is highly weldable, the higher alloy content makes it more hardenable in the weld region and more susceptible to weld cracking if conditions about preheat, cleanliness and moisture control of consumable given in ASME Boiler Code Section IX [55] are not properly followed. The code obligates the PWHT at 704 °C minimum after welding and allows no exemptions to PWHT.

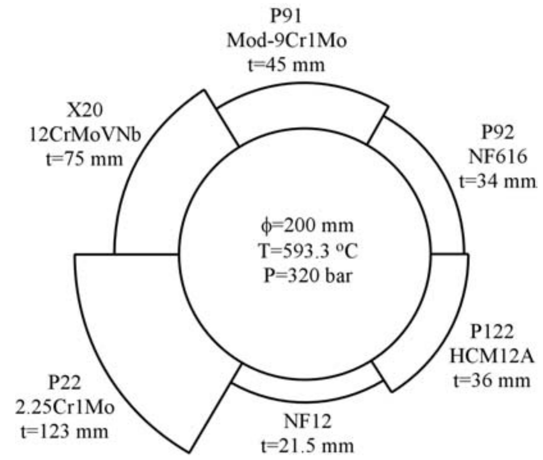

Figure 3.7. Comparison of required wall thickness for various steels for the same design conditions [95].

Studies have also shown that Mod-9Cr1Mo possesses resistance to hydrogen attack and stress relief cracking equal to or better than 2.25Cr1Mo [96]. This, combined with its through hardening capability and superior toughness makes it an attractive alloy for thick walled pressure vessels for coal liquefaction and petrochemical applications, although its major application area is in the fossil power plant piping.

4. EXPERIMENTAL PROCEDURE

4.1. WELDING AND HEAT TREATMENT OF TEST MATERIALS

The experimental material is acquired from similar butt-welded pipes of P22 and P91 steels which were produced in the EC Project SOTA [87] by the Shielded Metal Arc Welding (SMAW) process. The dimensions of the welded pipes were 220 mm outer diameter and 48 mm wall thickness for P22, and 295 mm outer diameter and 58 mm wall thickness for P91.

Single V-type bevels were machined at the edges of the pipes to ensure good welding quality. One-side-inclined (30°) and two-side-inclined (30°) bevels for P22 pipes and one-side-inclined (30°) bevel for P91 pipes were introduced. Sketches of the welded pipes of P22 and P91 are given in Appendices B.3 and B.4, respectively.

The pipes were pre-heated prior to welding in order to ensure good welding quality by reducing the risk of hydrogen cracking and enabling controlled cooling. Controlled cooling during welding is essential in order to reduce the level of residual stresses in weld and hardness of HAZ. Pre-heat temperatures for P22 and P91 are given in Tables 4.1 and 4.2, respectively.

Table 4.1. Details of the welding procedure for P22 steel pipes

Weld Pass	**Process**	**Welding Position**	**Electrode**	**Elec. Dia., mm**	**Gas**	**Current, A**			**Pre-heat Temp., °C**
							Min.	**Max.**	
1	GTAW	1G	OK Tigrod 13.22	2.4	Argon	DC(-)	70	130	250
2-3	SMAW	1G	OK 76.28	3.2	-	DC(+)	90	135	250
4-17	SMAW	2G	OK 76.28	4.0	-	DC(+)	130	200	250

Table 4.2. Details of the welding procedure for P91 steel pipes

Weld Pass	**Process**	**Welding Position**	**Electrode**	**Elec. Dia., mm**	**Gas**	**Current, A**			**Pre-heat Temp., °C**
							Min.	**Max.**	
1	GTAW	1G	OK Tigrod 13.38	2.4	Argon	DC(-)	70	130	260
2-3	SMAW	1G	OK 76.98	3.2	-	DC(+)	90	135	200
4-17	SMAW	1G	OK 76.98	4.0	-	DC(+)	130	200	200

17 weld passes were used to weld the whole thickness in both steels by using electrodes of different diameters. The first weld passes (root pass) were made by using Gas Tungsten Arc Welding (GTAW) process in argon with non-consumable electrodes of 2.4 mm diameter, OK Tigrod 13.22 and OK Tigrod 13.38 for P22 and P91 steel pipes, respectively. Following the root pass the pipes were welded by SMAW process using electrodes of OK 76.28 and OK 76.98 for P22 and P91 steel pipes, respectively. Both type of electrodes are basic covered.

The P22 steel pipes were welded using both flat (1G) and horizontal (2G) welding positions during different passes (Table 4.1), whereas P91 pipes were welded using only flat (1G) welding position (Table 4.2). The chemical compositions of the electrodes are given in Table 4.3.

Table 4.3. Chemical compositions of electrodes

Material	**Process**	**Composition** **Electrode**	**C**	**Si**	**Mn**	**Cr**	**Ni**	**Mo**	**N**	**V**	**Nb**
P22	GTAW	OK Tigrod 13.22	0.08	0.7	1.0	2.6	-	1.0	-	-	-
	SMAW	OK 76.28	0.07	0.3	0.6	2.2	-	1.0	-	-	-
P91	GTAW	OK Tigrod 13.38	0.1	0.2	0.8	8.7	0.6	1.0	-	-	-
	SMAW	OK 76.98	0.1	0.4	0.7	9.0	0.7	1.0	0.05	0.2	0.06

The welded P22 and P91 pipes were post-weld heat treated (PWHTed) at 710 °C and 760 °C, respectively, in order to obtain the desired mechanical properties of weldments. The details of the PWHT procedures for both P22 and P91 steel pipes are given in Table 4.4.

Table 4.4. Details of the PWHT of P22 and P91 steel pipes

PWHT	**P22**	**P91**
Start Temp., °C	400	400
Heating Rate, °C/h	<135	<135
Soaking Temp., °C	710±30	760±10
Soaking Time, h	2	2
Cooling Rate, °C/h	<175	Still Air

Note the stringent soaking temperature range for the PWHT of P91 compared with P22 steel. The reported data were supplied by the industrial partners of the SOTA project.

4.2. MICROTENSILE TESTS

Local material behaviour of weldment zones at high temperatures is an important issue for investigation due to the variation of material properties of functionally graded structure of weldments. Local material behaviour plays an important role in structural behaviour and the data required for determining the component behaviour. Allen [39] and Dogan [97] have reported on CrMoV, P22 and P91 steel welds that high temperature, particularly creep failure in uniaxial cross-weld tests involves complex interactions between zones in tensile loading, emphasising the importance of local material behaviour.

Microtensile (MT) testing, although not standardised yet, is a good method for characterising local properties of different weldments zones. Although the published data are limited to low temperatures [98, 99], recent publications [100,101] have extended the method into the high temperature field.

In this thesis, MT specimens machined out of similar welds of P22 and P91 steels are tested at 550 °C and 600 °C, respectively. MT specimens of similar welds with microstructural constituents sampling of weldment zones of base metal (BM), heat affected zone (HAZ) and weld metal (WM), were machined out of the butt-welded pipe segments by EDM technique, as shown in Figure 4.1. The microtensile specimens are 2 mm wide and the gage length is 9 mm (Figure 4.2). Thickness of microtensile specimens were recorded prior to testing, varying between 0.5 and 0.65 mm.

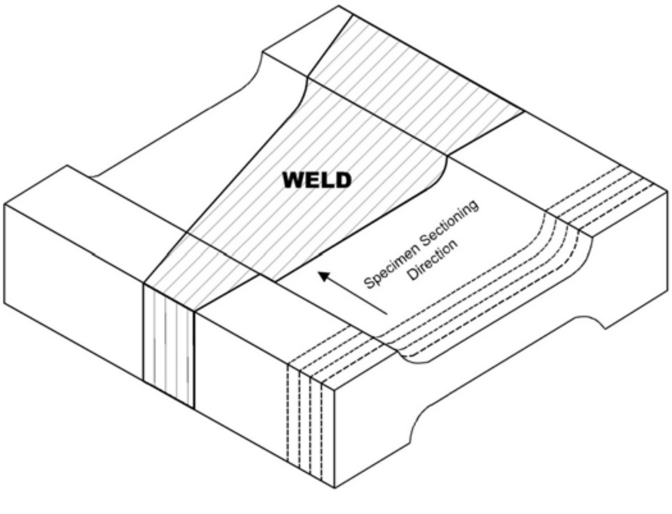

Figure 4.1 Extraction of MT specimens from vicinity of weldment of a pipe.

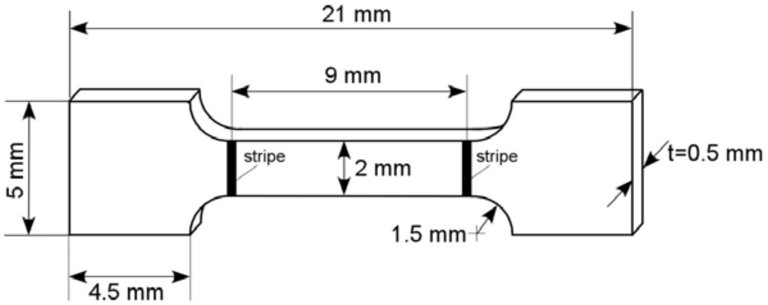

Figure 4.2 Details of a microtensile (MT) specimen

Specimens with different surface conditions are tested in order to study the effect of surface condition on deformation and tensile properties. These included two different surface conditions for P22 steel (Electric Discharge Machined (EDM), and polished (down to 1 μm by diamond paste)), whereas three different surface conditions are used for P91 steel (Electric Discharge Machined (EDM), polished (down to 1 μm by diamond paste), and electropolished)). Tensile tests are conducted by using Zwick Roell Z005 type electromechanical testing machine with load cell (±2.5 kN) at room temperature and high temperatures of 550 °C and 600 °C (Figure 4.3). The machine has the minimum loading rate capacity of 0.1 mm/h.

Mechanical data obtained on MT specimens are compared with standard tensile (ST) specimens carried out in EC Project SOTA [87], using WM and BM as well as material with simulated HAZ. The simulated HAZ materials were produced for mechanical and creep property determination by thermal cycling in a Gleeble weld simulator machine. Deformation and fracture behaviour are studied on sectioned side surfaces of tested specimens using SEM and OM. Mechanical data are correlated with microstructural constituents in specific zones of weldments.

Specimens are heated using an inductive coil heating system. Displacement is measured by using a Fiedler Optoelektronik GmbH type laser extensometer where two stripes with a gauge length of 9 mm are marked (Figure 4.4). Specimens are loaded at two different loading rates, 0.2 mm/min and 0.5 mm/min, in order to study the loading rate effect on high temperature tensile properties, $R_{p0.2}$ and R_m and corresponding strain values.

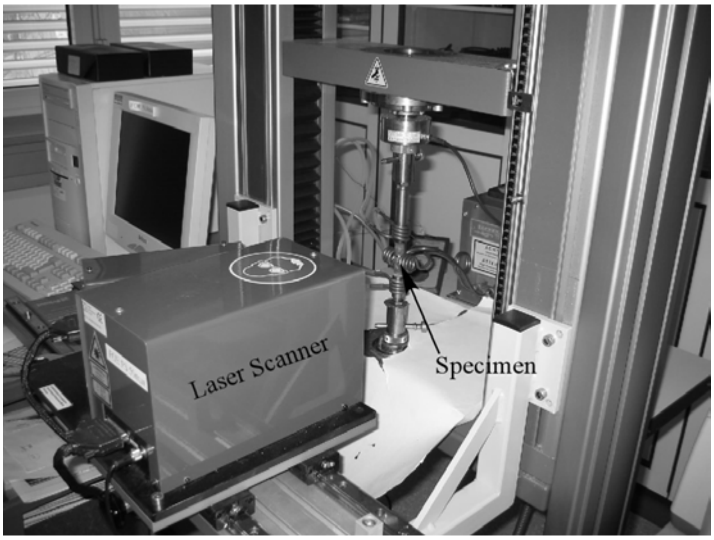

Figure 4.3. Overview of the MT test set-up

Laser extensometer is employed for contact free measurement of extension, from which, strain in a tensile specimen in a very narrow gauge is determined. The fundamentals of the operation of a laser extensometer are based on the principle where a set of contrasting fringes (stripes) applied to the flat surface of the sample is repetitively scanned by a laser beam. The backscattered light is collected by the receiving optics onto a photodiode and formed in an electrical pulse train [102]. Recorded load and displacement are converted into engineering stress and engineering strain data by dividing the measured values with initial cross-section area and initial gauge length, respectively. The displacement measurement and the output force are presented in stress-strain data form as presented in Section 5.1.

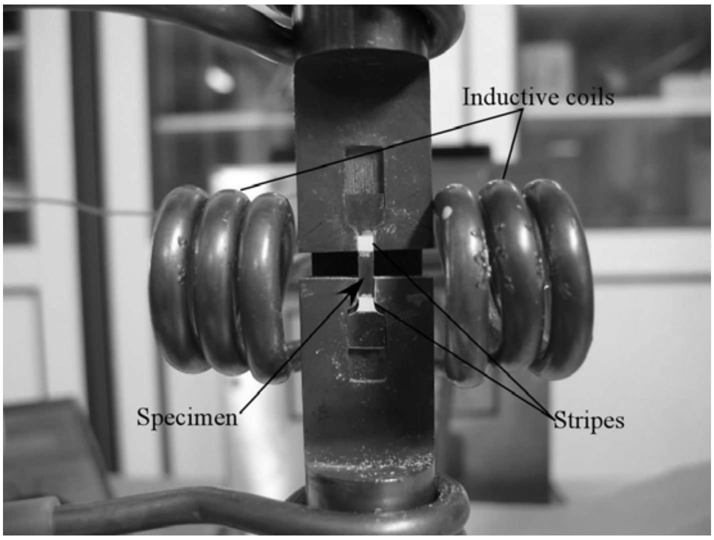

Figure 4.4. MT specimen with loading grip and inductive heating coil.

Selected specimens are analysed in a scanning electron microscope (SEM) for deformation and damage studies with respect to the loading rate and weldment zone. Metallographic results are presented in Section 5.1.2.

4.3. HIGH TEMPERATURE FRACTURE MECHANICS TESTS

4.3.1 Test Specimens

Four different specimen geometries, namely compact tension, C(T), C-Shape Tension, CS(T), Round Notch Bar Tension, RNB(T), and Single Edge Notched Bend, SEN(B), are used for obtaining CCI and CCG data. Specimen dimensions and starter crack type (fatigue pre-crack or EDM slit) are varied in order to study the effect of these variables on HT behaviour. The specimens are side-grooved by 20% in thickness, B, in order to increase the constraint to establish plane strain condition [3,6] in testing. Specimen details of test matrices of P22 and P91 steels' weldments are tabulated in Appendices B.1 and B.2, respectively.

Specimens are sampled from different weldment zones, in order to study the CCI and CCG behaviour of different microstructural constituents of weldments which play role in the lifetime of a welded structure operating at high temperatures. Figure 4.5 shows an example of specimen extraction from a butt-weld pipe blank containing different weldment zones. Sectioning of blanks for specimen machining is shown for P22 and P91 in Appendices B.3 and B.4, respectively. All specimens are aligned in blanks according to L-R configuration. Suggested specimen alignment details are given in Appendix B.5.

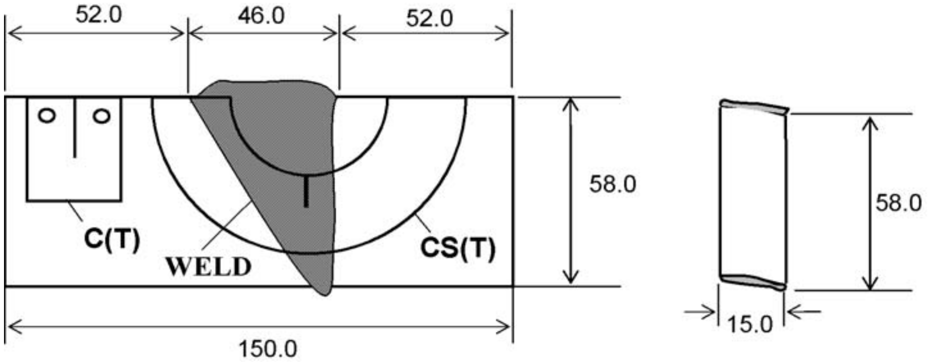

Figure 4.5. Extraction of a C(T) specimen with the starter notch in BM and a CS(T) specimen with the starter notch in WM from a blank.

Specimens manufacturing details including the technical drawings are given in Appendix B.6. EDM type of starter notches was introduced by using a cutting wire of 0.1 mm diameter. Some of the specimens were fatigue pre-cracked for sharp starter crack. The maximum allowable fatigue load is calculated using the formula [6]

$$P_f = \frac{0.4\, B_n \left(W - a_0\right)^2 \sigma_y}{\left(2W + a_0\right)} \tag{4.1}$$

The ratio of the minimum fatigue load to maximum allowable fatigue load was 0.1. It should be noted that the factor of 0.4 in Equation. 4.1 can be decreased or increased according to the ductility of the material at temperature of fatigue pre-cracking. High ductility allows use of a higher factor, hence a higher maximum load for fatigue pre-cracking. However, it is suggested [103] that this factor must not exceed 0.6 or the force corresponding to a maximum stress intensity factor to modulus of elasticity (K_{max}/E) is equal to or less than $1.5\text{x}10^{-4}$ $m^{0.5}$. For the 3-point SEN(B), Equation 4.1 takes the form

$$P_f = \frac{1.6\, B_n \left(W - a_0\right)^2 \sigma_y}{6\, L} \tag{4.2}$$

where L is the half distance between two supports. RNB(T) specimens are never fatigue pre-cracked and have a sharp EDM round notch with a tip radius of 0.2 mm (See Appendix B.6.).

4.3.2 Testing Equipment

The high temperature experimental set-up designed for high temperature crack growth studies is shown in Figure 4.6. The system facilitates testing under constant load, displacement rate and cross-head speed down to 1μm/h by use of a signal controlled electric motor. The test set-up comprises a laser system, a furnace with four windows for laser beam scan and visual inspection.

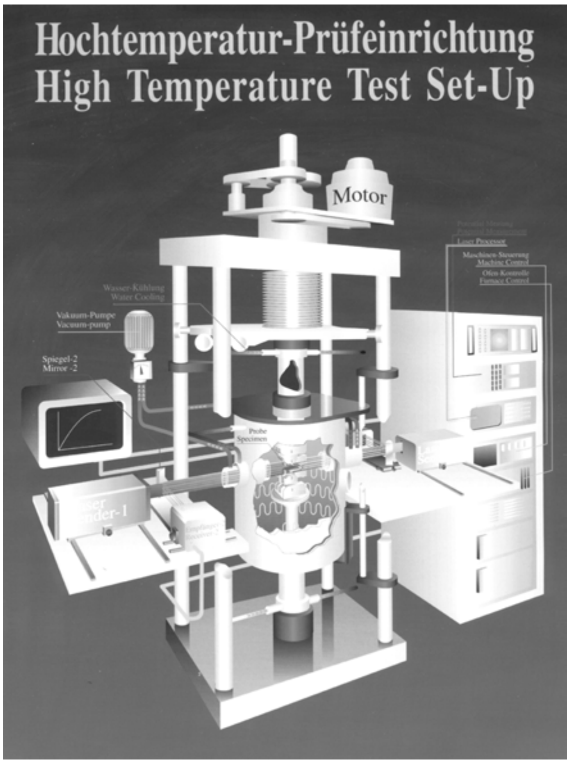

Figure 4.6. High temperature fracture mechanics test set-up.

The furnace is of a split type where the back and front halves can be moved horizontally for specimen installation. Electric resistant elements are used to heat up specimens. It operates with a water cooling system, which assists to keep the temperature stable during the test. The furnace can be operated at temperatures up to 1100 C°. Testing environment is laboratory air. Two glass tubes, which facilitate transmission of laser beam, have quartz glasses of 60 mm in diameter and 10 mm in thickness. The glasses have surface roughness of max. 0.003 mm, and wedge error of max. 6 min. The glass tubes are vacuumed in order to stabilise the laser beam transmitted through and received by laser receiver. This ensures a precise displacement measurement.

The laser scanner is of a ZYGO Model 1102 type laser dimension sensor. It uses a scanning laser beam to provide non-contact measurements of dimensions or part positions. It functions in high speed with a ±1.2μm repeatability, and has a 50.8 mm measurement range [104]. A high speed (150 scan of the measurement region per sec.), collimated scanning laser beam of 0.75 μm spot size is projected from a He-Ne gas laser (<1mW output) via a rotating mirror and collimating lense. The light band is in the form of parallel moving beam, which casts shadow of the objects placed in it, at temperatures up to 1900 C°. In the present application, the scanning beam casts shadows of the four pins on either side of the specimen. The receiver detects the edges of the cast pin shadows and transmits them to the processor (a multiple 32 bit microprocessor). The processor calculates the dimension that is the position of edges, from which the displacement is determined. The calculation is based on the precise timing of the edge positions and scanning speed of the laser beam.

4.3.3 Specimen Preparation

Four circular cross-section pins are laser welded onto a specimen for displacement measurements as shown for a C(T) specimen in Figure 4.7. Pins are welded on side surfaces at positions for LLD and local CTOD (δ_5) measurements at starter crack tip. In case it is not possible to laser weld the pins onto the specimen, heat resistant extensions are used to ensure deflection measurement by the laser scanner. Figure 4.8 shows a CS(T) specimen with pins at local CTOD (δ_5) location and extensions for LLD measurement, since the specimen geometry does not allow for welding pins onto the specimen. Such specimen designs facilitate measurement of displacement on load-line, and at initial crack-tip.

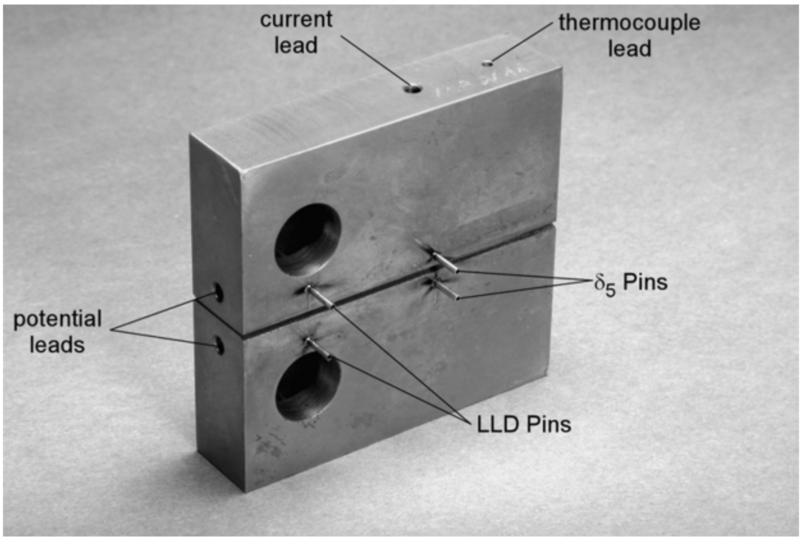

Figure 4.7 Compact tension, C(T), specimen with welded pins and potential, current and thermocouple leads for measurement of displacement and PD.

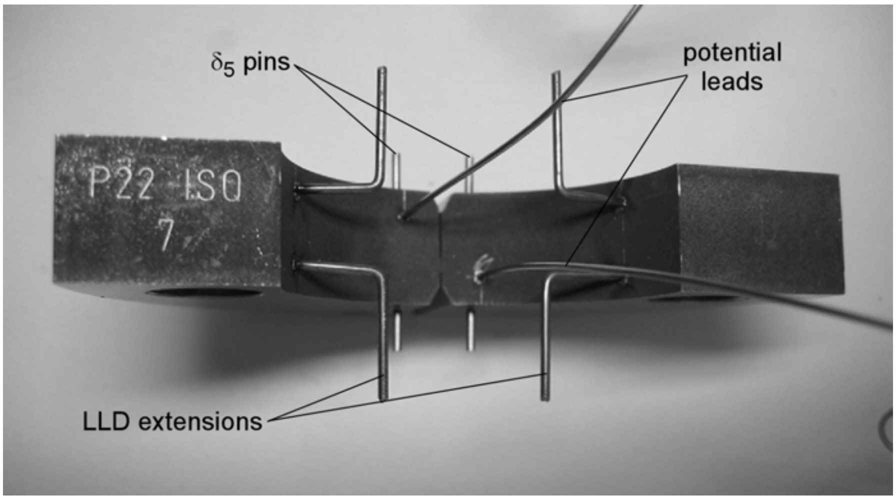

Figure 4.8 C-Shape tension, CS(T), specimen with welded pins, extension for LLD measurement and wires for PD measurement.

It is important to laser weld the pins to ensure stability in position at the test temperature, and to confine the HAZ, so that the microstructure in the vicinity of the crack tip would not be affected. The HAZ size of pin welds is typically < 0.5 mm wide and < 0.15mm deep [105], are shown in Figure 4.9.

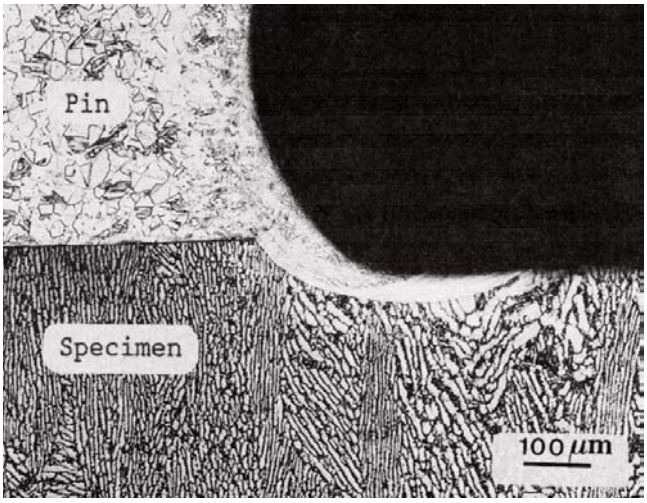

Figure 4.9 Through section of a laser welded pin on the specimen [105]

4.3.4 Crack Length Monitoring

A direct current (DC) potential drop (PD) system (DCPD) of TET Electronic Model M5P 8-50 Al is used to monitor the crack extension throughout the experiment. The system has 0-50 A current and a 0-8 V potential range capacity. DCPD technique is widely used in fracture testing and offers several advantages. The reasons for choice of DCPD method for the current study are (i) it can be used for any geometry, (ii) continuous monitoring of the crack length can be achieved, (iii) simple instrumentation (thus low cost) is needed, (iv) it is stable, (v) very small increments of crack extension can be detected and (vi) non-uniform crack growth can be monitored. The DCPD system is illustrated schematically in Figure 4.10.

The initial and final PD values (V_o and V_f) need to be determined to estimate crack length. Once the initial and final crack size (a_o and a_f) and PD voltage (V_o and V_f) are available, a correction to all data between a_o and a_f is done by linear interpolation using

$$a = \left[\left(a_f - a_o \right) + \frac{V - V_o}{V_f - V_o} \right] + a_o \tag{4.3}$$

where V is the instantaneous potential difference corresponding to the crack size, a.

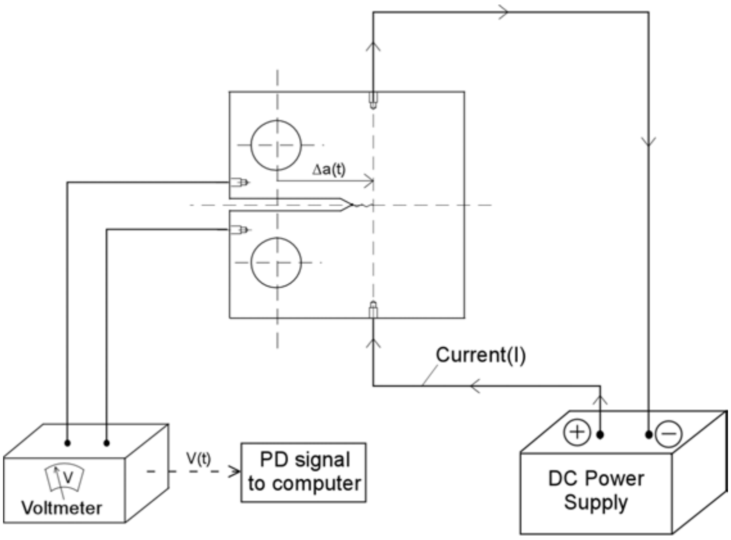

Figure 4.10 Schematic view of the DCPD crack monitoring system

Correct use of PD data is particularly important when determining CCI as several possible types of PD-time behavior may be observed as shown schematically in Figure 4.11.

The scatter in crack size using PD method increases due to crack channelling with unbroken ligaments as observed on fracture surfaces of tested specimens. An accurate measurement of the initial (a_o) and final (a_f) crack size were made when the specimen were broken open outside the furnace after testing. The final measured crack length may be used to calibrate the crack lengths obtained from potential data using Johnson's formula. Alternatively, linear interpolation between measured initial and final crack sizes determined on the broken open specimen fracture surface (FS) may be used for crack length calculations.

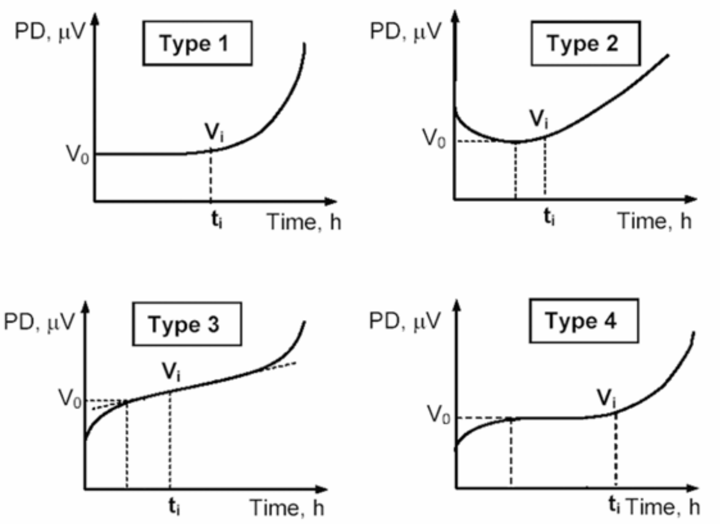

Figure 4.11 Types of potential drop (PD) vs. time records in creep crack growth tests

In some cases, PD readings decrease after initial loading (which indicates an apparent decrease in the crack length), reach a minimum value and then start to increase (Type 2 in Figure 4.11). For such cases, the value of V for all points of decreasing PD output should be taken to be the minimum value at the point of increase of the PD output. The initial increase as seen in Type 3 & 4 in Figure 4.11, recorded prior to crack tip opening is probably due to contacting pre-cracked faces, contacting debris or deformation. Therefore, it should not be considered as crack extension. Any jumps that occur in the PD reading without an obvious reason should be corrected by subtracting the magnitude of the jump in the PD reading from the subsequent data points.

4.3.5 Test Procedure

The Code of Practice (CoP) [6] is used for conducting high temperature (HT) fracture mechanics tests on weldments in this study. The HT fracture mechanics tests were carried out on the weldments of P22 and P91 steels including the weldment zones of BM, WM and HAZ at 550 °C and 600 °C, respectively. Different types of specimen geometries were tested in order to study the specimen geometry effect on CCI and CCG data. Although the tests were mainly conducted under constant load (F_{const}), constant displacement rate (CDR) tests were also carried out at displacement rates down to 0.003 mm/h in order to study the displacement rate effect on high temperature fracture mechanics properties of the steel weldments. Details of the conducted tests are given in Appendices C.1 and C.2 for steel weldments of P22 and P91, respectively.

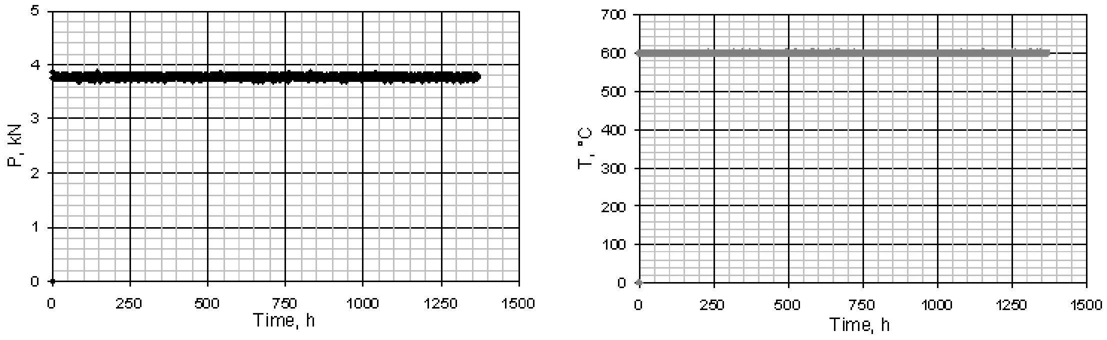

(a) Load vs. Time

(b) Temperature vs. Time

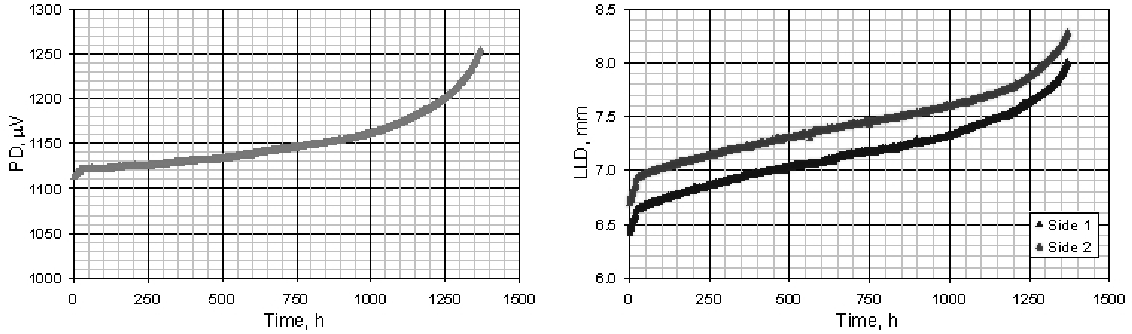

(c) Potential Drop vs. Time

(d) Load Line Displacement vs. Time

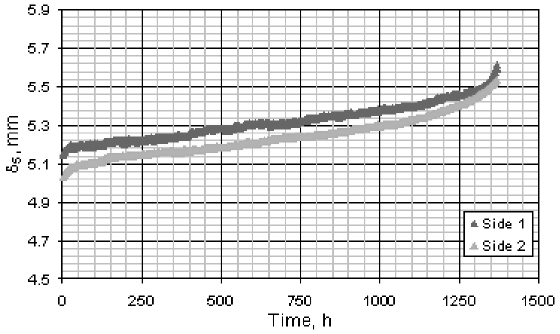

(e) Crack Tip Opening Displacement (δ_5) vs. Time

Figure 4.12 Experimental data records of a P91 BM (I91B7A25) C(T) specimen, tested for 1370 hours at 600 °C: (a) load, (b) temperature, (c) PD, (d) LLD and (e) δ_{ts} vs. time.

The load, potential drop (PD), load line displacement (LLD) and local CTOD (δ_{ts}) data are logged all the way to full load starting from pre-load for the subsequent analysis of the data for crack size and crack tip parameters C^* and K determination. The LLD and δ_{ts} data are recorded from pins on both sides of the specimens, in order to observe the variation of LLD and δ_{ts}. The data acquired from a C(T) specimen of P91 BM tested for 1370 hours at 600 °C is shown in Figure 4.12. It should be noted that although the LLD and δ_{ts} measurements on either side of the specimens show difference, their tendencies (slopes) are quite similar, which is expected for specimens of BM, with uniform crack growth through the specimen thickness. The average of displacement measurements made on both side surfaces of a specimen is taken for assessment.

Particular attention is paid in the early stage of testing, where the acquired data are very essential for CCI studies. Short crack length attained in the early part requires reliable data acquisition.

The tests are terminated as soon as both the potential drop and the displacement measurements show acceleration in crack growth rates and displacement rates, indicating that final failure of the specimen is imminent. On-line crack length calculations using Johnson's formula [3] or unloading compliance measurements may also give guidance in deciding when to terminate the test.

The acquired data are recorded on a IBM-PC of 32 bit processor by use of the data acquisition computer programme, DATERF-HT TP-Version 3.2, which was developed in the Institute of Materials Research of GKSS Research Centre, by using Test Point™ from Capital Equipment Corp. The programme acquires data from 13 channels, including load, temperature, PD, LLD and δ_5.

In long-term high temperature fracture mechanics tests, the amount of the acquired data points might be enormous. Therefore, the computer programme, DATERF-HT TP-Version 3.2 is designed with an algorithm which reduces the number of data points by omitting selected data points [106]. In principle, the computer programme starts with a data acquisition modus with high frequency which would cause an extreme number of data points at the end of the test. However, after the number of data points reaches a predefined value by the operator (e.g. total of 2000 data points), the computer reduces the frequency of data acquisition by half (i.e. the time interval between consecutive data points is doubled) and every second data point in the data matrix is erased. Using this algorithm, the number of data points at the end of a long high temperature fracture mechanics test is kept in a desirable manageable level for data assessment. Even if the test duration is unexpectedly short, the data acquired is still sufficient for analyses due to the initially high data acquisition rate. Figure 4.13 shows schematically the data acquisition concept of the algorithm.

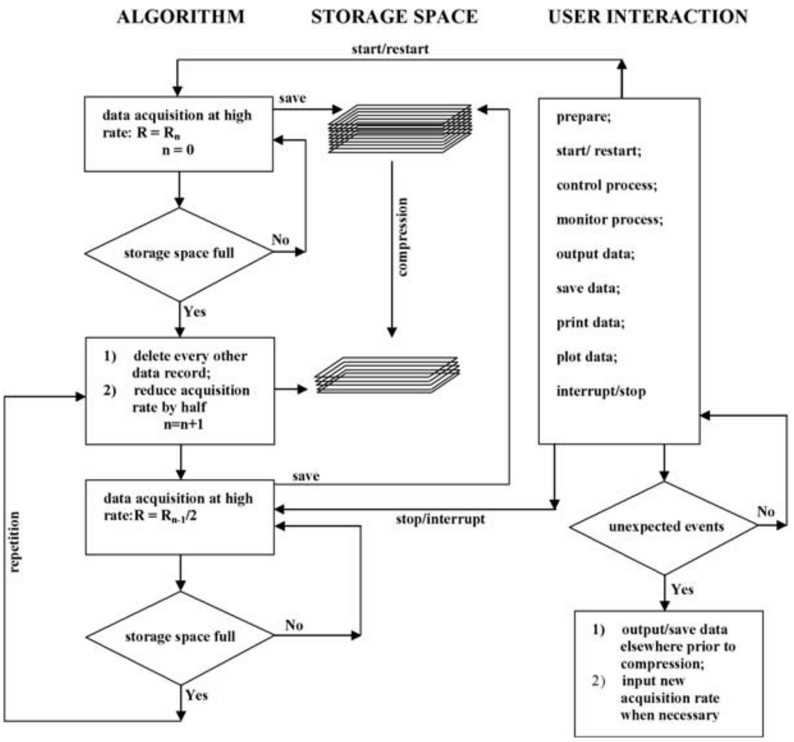

Figure 4.13 Schematic showing the concept of the algorithm used in long term high temperature crack growth data acquisition in the GKSS Research Centre, Germany [106].

The number of recorded data points is reduced to manageable size, e.g. 50-100 data points/specimen and then, if needed, data are fitted by regression method. The obtained data set is assessed by using data sheets for the calculation of related fracture mechanics parameters. As an example, data sheet of a SEN(B) specimen of P22 WM tested for 1613.3 hours at 550 °C is given in Appendix C.3. The assessment of raw data is presented in Section. 5.2.2.

4.3.6. Post Test Measurements and Metallographic Examination

The tests are stopped after some crack growth to avoid separation into two pieces in order to obtain initial and final crack sizes measured on the crack opened fracture surfaces of the tested specimens. The initial and final measured crack lengths are used to compute the incremental crack length from PD measurements obtained during the tests. A sectioned specimen half is used for metallographic examination at the crack tip (Figure 4.14). Determination of crack size by area method on the fracture surface of a P22 WM specimen tested at 550 °C for 3002 hours is shown in Figure 4.15. Final crack area A_f, half of the specimen thickness, B/2, and half of the net specimen thickness $B_n/2$, are measured by use of a special software. Alternatively, the crack size can be measured incrementally on one half of a specimen at minimum of 8 equally spaced points, where the crack size is the average of these measurements.

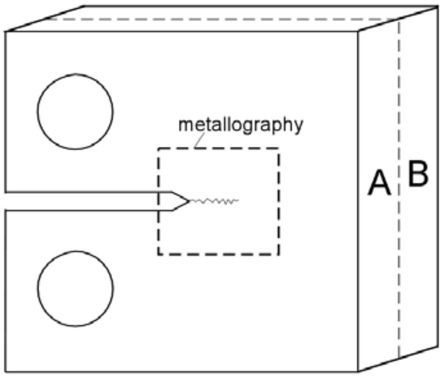

Figure 4.14. Sectioning of specimens for metallographic examination (Section A) and measurement of crack size on crack opened specimen half (Section B).

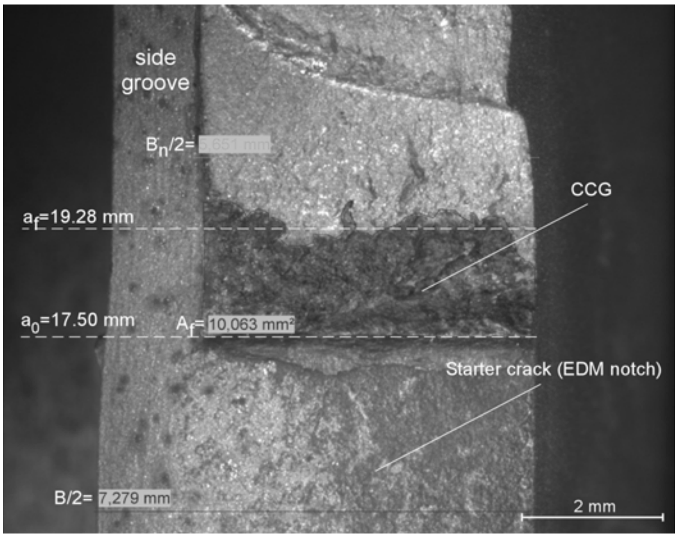

Figure 4.15. Determination of crack length on fracture surface of a sectioned specimen half of a C(T) specimen.

4.3.7. Determination of Creep Crack Growth Correlation Parameters

Two parameters; the stress intensity factor, K and C^* are widely used, both for crack growth rate correlation and in life assessment codes for structural components at elevated temperatures. The correlations of steady state crack growth rate with K and C^* are represented by straight lines of different slopes on log/log plots and expressed by power laws of the form

$$\dot{a} = A'K^{m'} \tag{4.4}$$

$$\dot{a} = D_o C^{*\phi} \tag{4.5}$$

where A', D_o, m', and ϕ are material constants. A steady state relationship between crack growth rate and the parameters in Equation 4.4 and Equation 4.5 imply a progressively accelerating creep crack growth rate. Steady-state is said to have been achieved when a fully developed creep stress distribution has been produced around the crack tip.

The recorded data consisting of time,t, load, F, temperature, T, potential drop, PD, load line displacement, Δ^{LLD}, displacement at the initial crack tip,Δ^{CTOD} (δ_5)[23] are analysed to determine fracture mechanics parameters and crack growth rate.

4.3.7.1. Stress Intensity Factor, K

Creep crack growth rate da/dt expressed as a function of K may characterise the resistance of a material to crack growth under conditions of creep deformation when extensive creep condition does not occur at the crack tip. In order to correlate creep crack growth, da/dt with K, elastic displacements must be dominant during the creep crack growth test, i.e. $\dot{\Delta}_c / \dot{\Delta} < 0.25$ [6]. Correlation of da/dt with K does not require any information, like material properties, about the material, rather than the creep crack growth test data.

For any specimen geometry, stress intensity factor, K, can be determined from

$$K = \sigma\sqrt{a}\;\; Y(a/W) \tag{4.6}$$

where $Y(a/W)$ is a function of geometry and crack length a. Y(a/W) functions are given for each specimen geometry in Appendix A. For specimens loaded under a tensile load F the membrane stress is given by

$$\sigma_m = F/(BW) \tag{4.7}$$

and for specimens subjected to a constant bending moment M the nominal bending stress at the surface is given by

$$\sigma_b = 6M/(BW^2) \tag{4.8}$$

For a side-grooved specimen, with a thickness B_n, the stress intensity factor, K, will be higher than a plain specimen. Stress intensity factor for a side-grooved specimen, K_n, is calculated as follows:

$$K_n = K\left(\frac{B}{B_n}\right)^{0.5} \tag{4.9}$$

4.3.7.2 C^* Integral

The CCG parameter, C^*-Integral is defined as path-independent line or surface integral that encloses the crack front from one crack surface to the other, as presented in Sec.2.1.4.2. The C^* is used to characterise the local stress-strain rate fields at any instant around the crack front in a body subjected to extensive creep conditions. C^* is calculated experimentally from the load-line displacement rate, $\dot{\Delta}^{\mathrm{LLD}}$, or crack mouth opening displacement rate, $\dot{\Delta}^{\mathrm{CMOD}}$, using the following equations

$$C^* = \frac{F\dot{\Delta}^{\mathrm{LLD}}}{B(W-a)} H^{\mathrm{LLD}} \eta^{\mathrm{LLD}} \tag{4.10}$$

or

$$C^* = \frac{F\dot{\Delta}^{\mathrm{CMOD}}}{B(W-a)} H^{\mathrm{CMOD}} \eta^{\mathrm{CMOD}} \tag{4.11}$$

Solutions for the functions H^{LLD}, H^{CMOD}, η^{LLD} and η^{CMOD} follow the specimen type. Solutions are given for plain sided specimens of thickness, B. For side-grooved specimens B in Equations 4.10 and 4.11 should be replaced by B_n.

The η^{LLD} and η^{CMOD} factors are geometrical factors provided as a function of relative crack depth, a/W. For some crack geometries, the value of η^{LLD} and η^{CMOD} is sensitive to the creep exponent, n, and relative specimen height, L/W. This variability has been taken into account in some recent studies [6, 107] through the use of a mean value for a range of n and L/W values and an uncertainty which quantifies the potential variability in η^{LLD} and η^{CMOD} as a function of geometry and material. The geometrical factors H^{LLD}, H^{CMOD}, η^{LLD} and η^{CMOD} are given for each specimen geometry in Appendix A.

Creep Displacement Rate

If the test adheres to condition of $\dot{\Delta}_c / \dot{\Delta} \geq 0.5$, then dΔ/dt being the total displacement rate data can be processed further for estimating C^*. If a check is needed to estimate the extent of $\dot{\Delta}_c / \dot{\Delta}$ then where plasticity can be discounted $d\Delta_c/dt$ is calculated as follows

$$\dot{\Delta}_c = \dot{\Delta} - \dot{\Delta}_e - \dot{\Delta}_p \approx \dot{\Delta} - \frac{\dot{a}B_n}{P}\left[\frac{2K^2}{E'}\right] \tag{4.12}$$

The elastic portion $\dot{\Delta}_e$ can be estimated from available compliance formulae of the geometry. When working with highly ductile materials such as austenitic stainless steels, it may be necessary to include additional term to account for plasticity [6].

Transition Time

Transition time, t_T is the time required for extensive creep conditions to develop in a cracked body. For test specimens, this is typically the time required for the zone of creep deformation to spread through a substantial portion of the uncracked ligament, or in the region which is under the influence of a crack in the case of a finite crack in a semi-infinite medium.

The condition to allow the application of C^* is that it must be established that test times $t \gg t_T$ beyond which point $C_t = C^*$. To determine the transition time t_T the following estimation is employed

$$t_T = \frac{K^2(1-\nu^2)}{E(n+1)C^*(t_T)} \tag{4.13}$$

The calculation of t_T varies with the current value of C^*. For each test time increment starting from zero the instantaneous transition time t'_T is calculated and plotted versus $C^*(t_T)$. The transition time t_T is then the first peak value of t'_T in the data set. Data, for which time exceeds the transition time, t_T, are correlated by C^*. The data for which time is $t \leq t_T$ are correlated only by C_t or K. It should be also noted that if there is found to be any extent of plasticity upon loading of the specimen it can be assumed that t_T estimated from the above equation will be conservative as plasticity in itself will assist to rapid relaxation at the crack tip.

Validity Criteria

A check for validity of the C^* parameter consists of three conditions being fulfilled [6]. These are as follows:

a) The specimen does not undergo extensive plasticity (i.e. $\dot{\Delta}_p$ is small),

b) The ratio of creep displacement rate/total displacement rate $\dot{\Delta}_c / \dot{\Delta} \geq 0.5$,

c) Experimental test times $t >> t_T$ for C^* to be valid.

Once these conditions are established the C^* estimation, given in Eqn. 4.10 (or 4.11), can be determined using the total measured displacement rate $\dot{\Delta}$.

5. RESULTS

5.1. DAMAGE AND FRACTURE IN MICROTENSILE TESTS

5.1.1. Microtensile Test Results

5.1.1.1. P22 Similar Weldments

Microtensile test specimens machined out of BM, HAZ and WM zones of P22 similar weldments were tested at room temperature (RT) and 550 °C. The specimens were prepared with two surface conditions of machined (EDM), and machined and polished surfaces. The test speeds varied from 0.2 mm/min to 0.5 mm/min in order to study the effect of loading rate on deformation and mechanical properties. The tensile stress-strain data are presented in Figures 5.1-5.4.

The stress-strain data determined at RT on as EDM machined and polished specimens are depicted in Figures 5.1 and 5.2, respectively. Effect of surface finish on tensile data is not observed. However, the tensile properties at 550 °C shows dependence on both surface finish and loading rate as seen in Figures 5.3 and 5.4, where specimens with EDM machined, and polished surface conditions are given, respectively.

The specimen surface condition is of particular importance in studying deformation and fracture behaviour of weld metal and HAZ due to grain size and microstructural variation that increase susceptibility to surface crack initiation. Furthermore, due to small specimen thickness and large grain size and/or dendritic structure fracture from surface cracks will be facilitated. The specimens with machined (EDM) surface condition show high scatter in stress-strain data obtained at 550 °C. The difference in tensile behaviour of different weldment zones of P22 steel are compared with the data from standard tensile (ST) tests (Figure 3.1) emphasises the thickness effect on the data. The surface condition of specimens is enhanced by polishing down to 6 µm, where the possible surface cracks and other irregularities introduced by EDM machining are removed. The tensile behaviour of polished specimens sampled out of different weldment zones can be determined by MT tests. The stress-strain data follow the same sequence as the ST test behaviour. However, lower strength measured in HAZ seen in Figure 3.1 is emphasised in MT specimens (Figure 5.4.) compared to BM and WM.

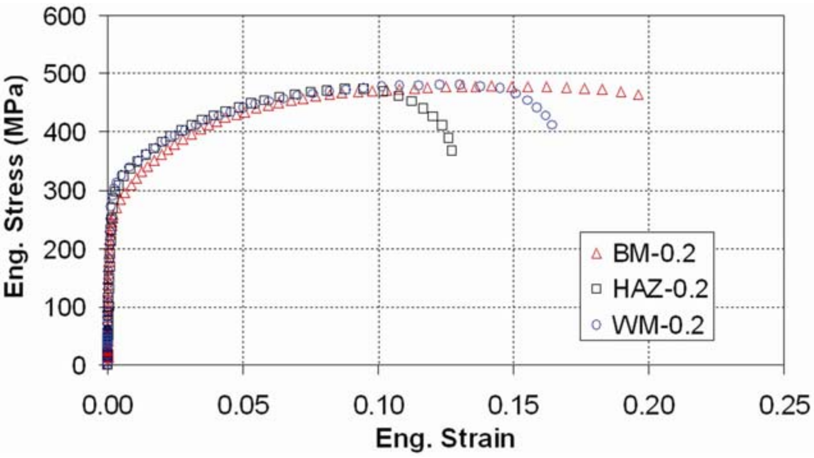

Figure 5.1. Stress vs. strain behaviour of BM, WM and HAZ of P22 specimens determined with EDM machined surface specimens at RT.

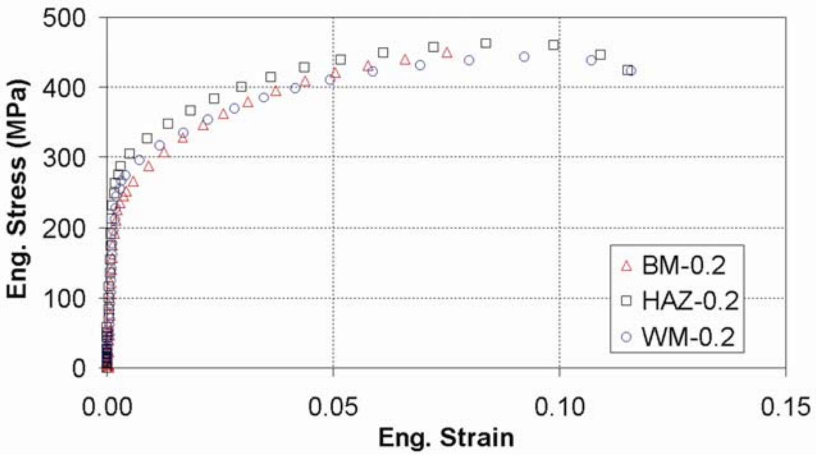

Figure 5.2. Stress vs. strain behaviour of BM, WM and HAZ of P22 specimens determined with polished surface specimens at RT.

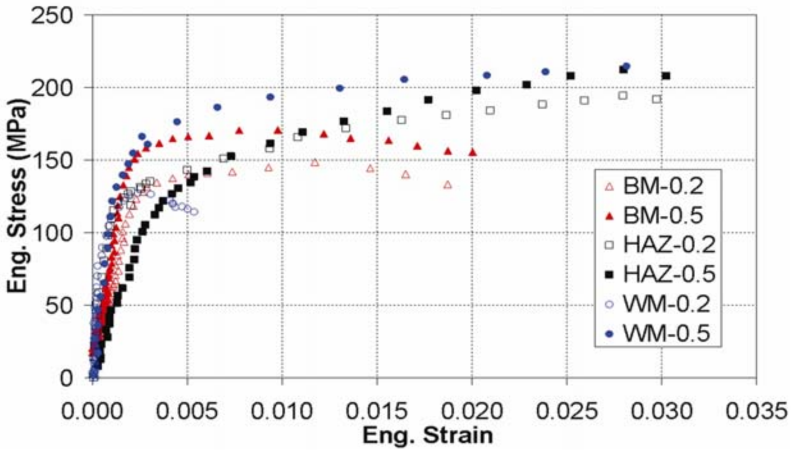

Figure 5.3. Stress vs. strain behaviour determined on as EDM machined specimens from P22 weldment zones at 550 °C.

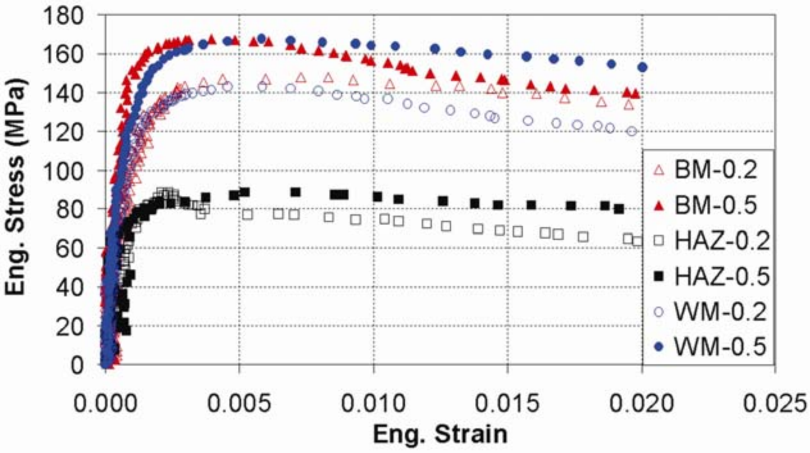

Figure 5.4. Stress vs. strain behaviour determined on specimens with polished surface from P22 weldment zones at 550 °C.

Yield strength, $R_{p0.2}$, and ultimate tensile strength, R_m, determined across the P22 weldment at varying temperature and loading rate are determined on specimens with as machined EDM and polished surfaces given in Tables 5.1 and 5.2, respectively. The tensile strength values decrease substantially with temperature for both surface conditions. However, while the yield strain value, $\varepsilon_{p0.2}$ is not affected by temperature, tensile strain, ε_m, at ultimate tensile strength,

R_m, decreases at an order up to 20.This is a typical thin specimen behaviour related to inhomogeneous deformation of thin plates.

More representative material properties data similar to those obtained on ST specimens are determined on specimens with polished surface conditions. However, tensile strain values, ε_m, at ultimate tensile strength, R_m, decreases with increasing loading rate, except that the value remains almost the same for the HAZ zone. Furthermore, the strain $\varepsilon_{p0.2}$ at yield strength, $R_{p0.2}$, is unaffected by the loading rate.

Although the sequence of strength of different weldment zones (BM, WM and HAZ) coincides with the ST test results, materials strength values from MT tests with polished surface are lower than the properties obtained on ST tests. Therefore, in order to determine materials properties in MT tests, correction factors are needed. These are determined experimentally for P22 BM and P22 WM in this study as $\approx$2.9 and $\approx$2.5 for loading rates 0.2 mm/min and 0.5 mm/min, respectively. A correction factor of $\approx$3.4 is suggested for P22 HAZ for both loading rates.

Table 5.1. Tensile data of P22 weldments (BM, HAZ, WM) determined at RT and 550 °C. Specimens with EDM machined surface tested at loading rates 0.2 mm/min and 0.5 mm/min.

M. Zone	T (°C)	Loading rate (mm/min)	$R_{p0.2}$ (MPa)	R_m (MPa)	$\varepsilon_{p0.2}$	ε_m
BM	RT	0,2	266,2	484,1	0,0032	0,1540
BM	550	0,2	137,1	149,3	0,0042	0,0117
BM	550	0,5	165,4	171,3	0,0042	0,0098
HAZ	RT	0,2	301,7	473,7	0,0330	0,0919
HAZ	550	0,2	135,1	204,7	0,0031	0,0401
HAZ	550	0,5	139,2	214,1	0,0053	0,0300
WM	RT	0,2	318,7	480,7	0,0037	0,1290
WM	550	0,2	127,3	127,4	0,0024	0,0026
WM	550	0,5	171,0	218.2	0,0034	0,0334

Table 5.2. Tensile data of P22 weldments (BM, HAZ, WM) determined at RT and 550 °C. Specimens with polished surface tested at loading rates 0.2 mm/min and 0.5 mm/min.

M. Zone	T (°C)	Loading rate (mm/min)	$R_{p0.2}$ (MPa)	R_m (MPa)	$\varepsilon_{p0.2}$	ε_m
BM	RT	0,2	256,0	*	0,0047	*
BM	550	0,2	146,3	149,3	0,0024	0,0333
BM	550	0,5	146,9	167,7	0,0026	0,0038
HAZ	RT	0,2	291,0	463,3	0,0035	0,0901
HAZ	550	0,2	71,4	72,0	0,0030	0,0057
HAZ	550	0,5	79,1	88,8	0,0021	0,0059
WM	RT	0,2	293,6	443,1	0,0041	0,0970
WM	550	0,2	107,8	111,4	0,0036	0,0072
WM	550	0,5	141,3	153,9	0,0029	0,0052

(*) Test stopped to study deformation on the side surface

5.1.1.2. P91 Similar Weldments

Microtensile test specimens machined out of P91 similar welds are tested at RT and 600 °C at loading rates of 0.2 mm/min and 0.5 mm/min. Three groups of specimens tested in as EDM machined, polished and electropolished surface conditions. The tensile properties are presented in Figures. 5.5-5.10. Tensile data from standard tensile specimen tests for each material zone of P91 including simulated HAZ are presented in Figure 3.2. Similar to P22, the RT data show little variation with surface finish. Similar variation is observed in HT data. However, the higher loading rate (0.5 mm/min) yield higher tensile strength values than that of the lower loading rate (0.2 mm/min).

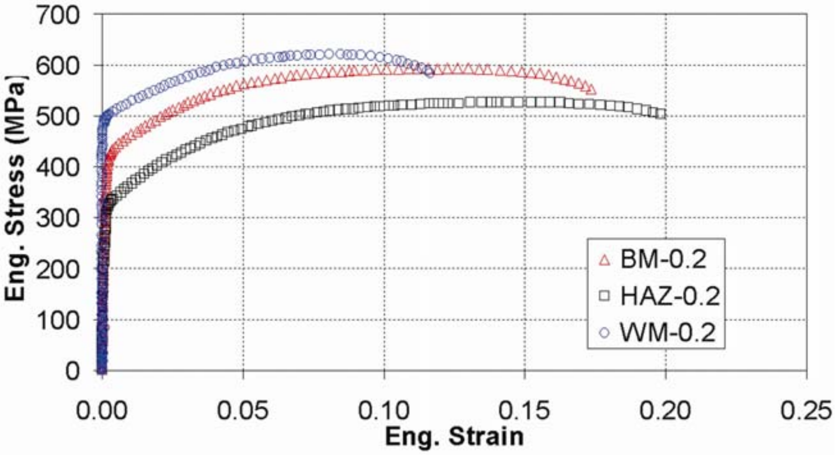

Figure 5.5. Stress vs. strain behaviour of BM, WM and HAZ of P91 specimens determined with EDM machined surface specimens at RT.

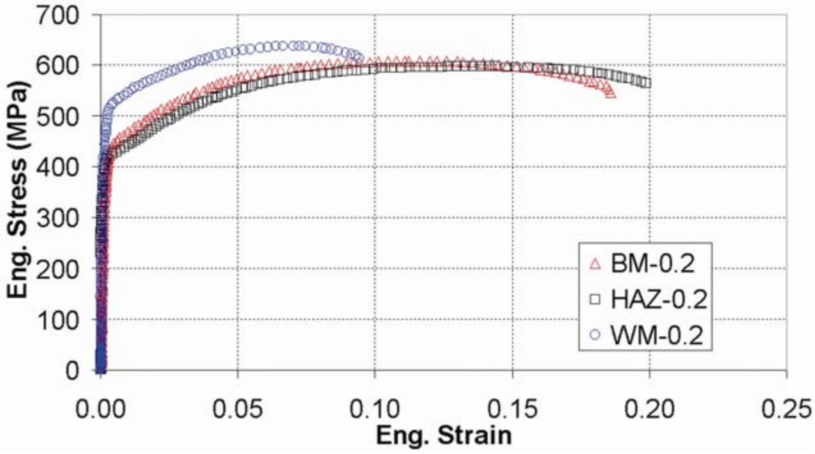

Figure 5.6. Stress vs. strain behaviour of BM, WM and HAZ of P91 specimens determined with polished surface specimens at RT.

A good agreement is observed between ST specimens (Figure 3.2) and the MT specimens with polished surface, especially at the standard test loading rate of 0.2 mm/min (Figure 5.9). However, MT specimens with machined surface (Figure 5.8) show high scatter and therefore, cannot represent the standard material behaviour. The scatter is probably due to the rough surface condition with residual stresses caused by EDM machining, which may initiate microcracks up to 200 µm on the surface of the specimen with extensive oxidation. Despite lower scatter in data obtained by using electropolished surface specimens compared to as EDM machined surface specimens, the highest tensile strength values are determined on HAZ specimens. However, the ST tests yield the highest tensile strength value in BM, followed by WM and HAZ (Figure 3.2).

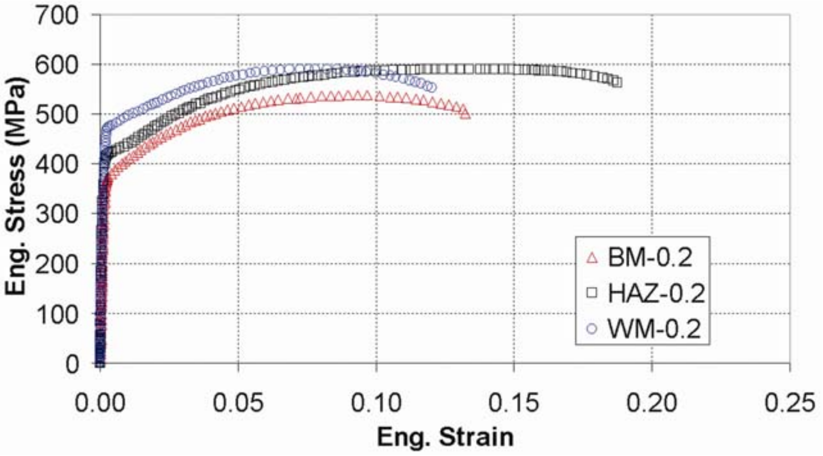

Figure 5.7. Stress vs. strain behaviour of BM, WM and HAZ of P91 specimens determined with electropolished specimens at RT.

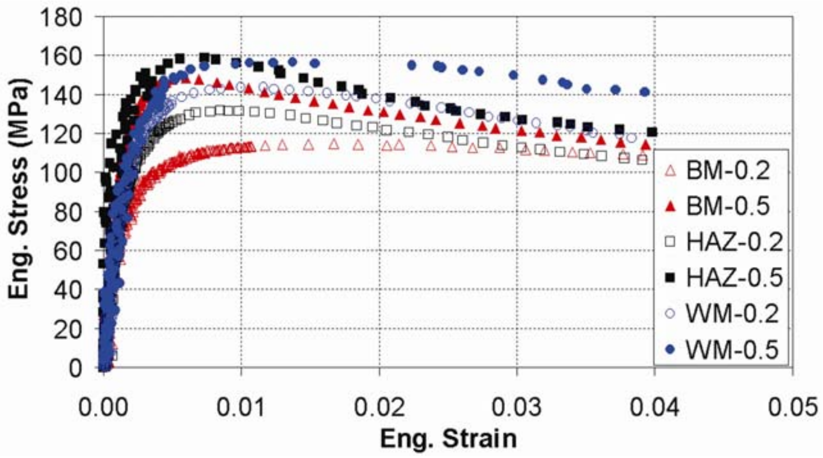

Figure 5.8. Stress vs. strain behaviour determined on as EDM machined specimens from P91 weldment zones at 600 °C.

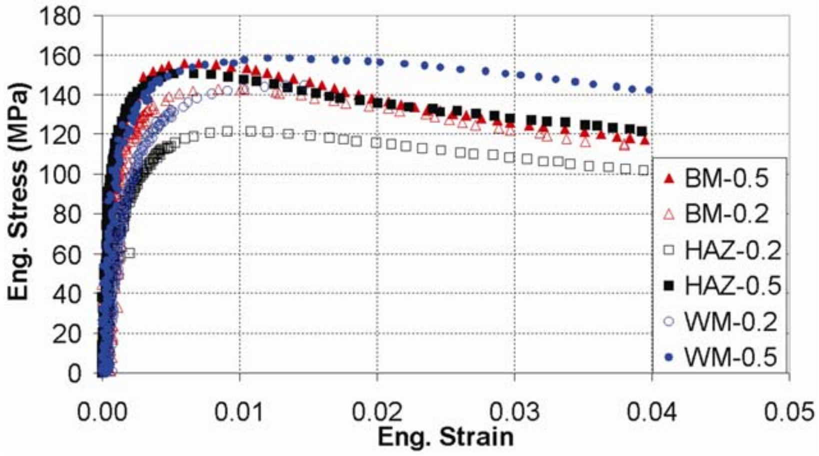

Figure 5.9. Stress vs. strain behaviour determined on polished surface specimens from P91 weldment zones at 600 °C.

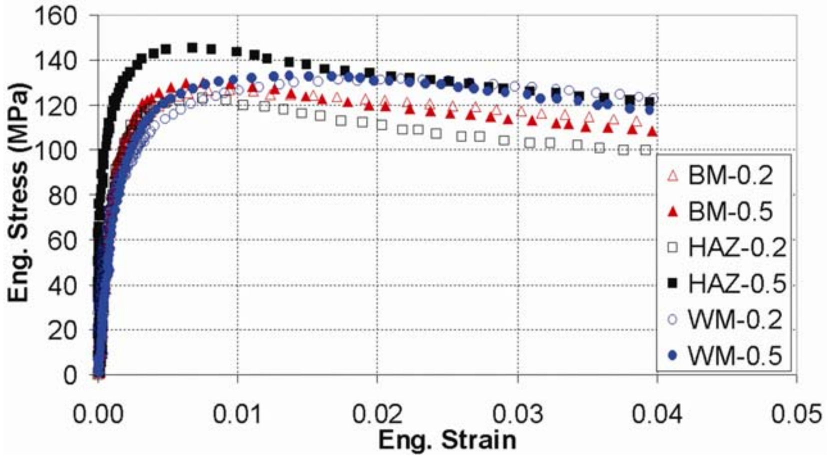

Figure 5.10. Stress vs. strain behaviour determined on electropolished surface specimens from P91 weldment zones at 600 °C.

The tensile properties across the P91 weldment zones at test temperatures and loading rates are presented for as machined (EDM), polished, and electropolished surfaces in Tables 5.3, 5.4 and 5.5, respectively. A large discrepancy in tensile property data is seen in the tables. Increase in tensile strength and decrease in tensile strain are observed with increasing loading rate conforming the standard behaviour with work hardening. However, effect of specimen surface condition varies in different weldment zones.

The specimens with polished surface conditions, which produced data similar to the ST specimens showed loading rate dependence of tensile strains $\varepsilon_{p0.2}$ and ε_m. The strains decrease with increasing loading rate, except in the WM zone. Substantial decrease of tensile strain values ε_m is seen with increasing temperature. The yield strain, $\varepsilon_{p0.2}$, is unaffected in all weldment zones. As in P22 steel, correction factors are needed for MT data to be considered as material property data. These are determined as 3.5 for the loading rate of 0.2 mm/min and 2.7 for the loading rate of 0.5 mm/min.

Table 5.3. Tensile data of P91 weldments (BM, HAZ, WM) determined at RT and 600 °C. Specimens with EDM machined surface tested at loading rates 0.2 mm/min and 0.5 mm/min.

M. Zone	**T (°C)**	**Loading rate (mm/min)**	**$R_{p0.2}$ (MPa)**	**R_m (MPa)**	**$\varepsilon_{p0.2}$**	**ε_m**
BM	RT	0,2	430,5	593,7	0,0028	0,1210
BM	600	0,2	88,5	105,8	0,0032	0,0175
BM	600	0,5	127,5	134,0	0,0036	0,0073
HAZ	RT	0,2	334,1	527,3	0,0034	0,1410
HAZ	600	0,2	119,6	132,1	0,0034	0,0081
HAZ	600	0,5	138,9	159,2	0,0026	0,0069
WM	RT	0,2	492,7	621,2	0,0025	0,0805
WM	600	0,2	136,0	143,1	0,0062	0,0097
WM	600	0,5	129,0	159,4	0,0041	0,0106

Table 5.4. Tensile data of P91 weldments (BM, HAZ, WM) determined at RT and 600 °C. Specimens with polished surface tested at loading rates 0.2 mm/min and 0.5 mm/min.

M. Zone	T (°C)	Loading rate (mm/min)	$R_{p0.2}$ (MPa)	R_m (MPa)	$\varepsilon_{p0.2}$	ε_m
BM	RT	0,2	432,1	608,0	0,0032	0,1090
BM	600	0,2	137,1	143,1	0,0046	0,0086
BM	600	0,5	143,1	157,7	0,0026	0,0078
HAZ	RT	0,2	421,4	597,7	0,0027	0,1260
HAZ	600	0,2	97,0	121,5	0,0025	0,0106
HAZ	600	0,5	139,8	150,8	0,0020	0,0061
WM	RT	0,2	509,8	638,5	0,0029	0,0679
WM	600	0,2	116,7	142,1	0,0032	0,0134
WM	600	0,5	136,2	157,9	0,0036	0,0145

Table 5.5. Tensile data of P91 weldments (BM, HAZ, WM) determined at RT and 600 °C. Specimens with electropolished surface tested at loading rates 0.2 mm/min and 0.5 mm/min.

M. Zone	T (°C)	Loading rate (mm/min)	$R_{p0.2}$ (MPa)	R_m (MPa)	$\varepsilon_{p0.2}$	ε_m
BM	RT	0,2	407,2	537,5	0,0032	0,0880
BM	600	0,2	98,4	126,6	0,0032	0,0084
BM	600	0,5	107,6	117,9	0,0032	0,0750
HAZ	RT	0,2	419,9	590,9	0,0029	0,1250
HAZ	600	0,2	116,5	122,6	0,0035	0,0072
HAZ	600	0,5	130,2	145,3	0,0017	0,0062
WM	RT	0,2	496,7	591,0	0,0027	0,0794
WM	600	0,2	103,1	116,4	0,0033	0,0181
WM	600	0,5	107,0	127,9	0,0031	0,0103

5.1.2. Metallography

Side surfaces of selected tested specimens are examined by using Scanning Electron Microscope (SEM) for deformation and crack initiation studies. Specimens extracted from different weldment zones (BM, HAZ and WM), which were tested at different loading rates, are studied in order to correlate damage with microstructural constituents. Damage is studied in different areas of each specimen, 1) necking area which undergoes the most severe damage in a specimen beneath the fracture surface, 2) head of the specimen which was not damaged during testing and 3) a region between the head and the necking in which an intermediate level of damage are observed. The metallographic studies are undertaken to establish a micromechanics basis for fracture mechanical characterisation of studied materials. Furthermore, service behaviour of components made of these materials will be assessed based on micromechanical information.

5.1.2.1. P22 Similar Weldments

The comparison of results obtained from P22 similar weld MT specimens machined from the same weldment zones and tested at different loading rates, showed the loading rate dependence of strength data conforming the metallographic evidences. Recovery observed in specimens tested with lower loading rate that yield lower strength data compared to higher loading rates. Grain size varied between 3-10 μm. For any zone of weldment, deformed grains along the main loading axis is also observed for specimens tested at low loading rate. Comparison is made with specimens tested at high loading rate (Figures 5.11-5.12).

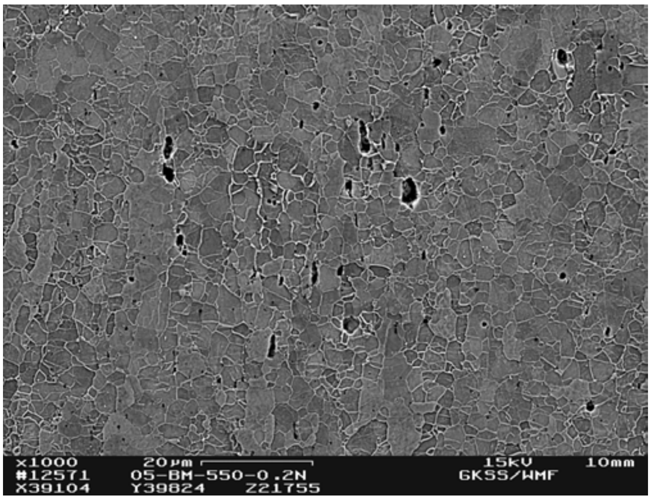

Figure 5.11. SEM picture from necking area of P22 BM tested at 0.2 mm/min ($\varepsilon_{\text{final}}$=14%).

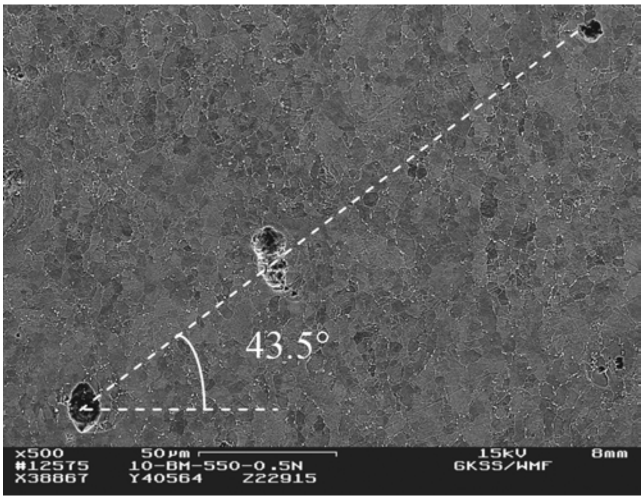

Figure 5.12. SEM picture from necking area of P22 BM tested at 0.5 mm/min with pore formation at 43.5° to horizontal plane ($\varepsilon_{\text{final}}$=8%).

This behaviour is attributed to the longer time at low rates leading to deformation softening mechanisms by recovery. Figure 5.12 (BM, 0.5 mm/min) and. Figure 5.13 (WM, 0.2 mm/min), show the damage process by pore formation along shear deformation plane (Figure 5.14) aligned at 43.5° for the BM specimen and 49.5° for the WM specimen to the main loading plane. Material deformation on shear plane is seen in Figure 5.14. Pore opening is observed in the vicinity where high stresses act on hard particles/phases that lead to pore opening by debonding local deformation mechanism as described above for Figure 5.12.

Fracture process is delineated by grain boundary damage and microcracking in highly strained area beneath the fracture surface as seen for WM specimen tested at 0.5 mm/min loading rate in Figure 5.15. The enlarged area showing the grain boundary damage and cracking is seen in Figure 5.16. Loading rate effect is not observed in specimens tested at high loading rates compared with the specimen tested with 0.2 mm/min loading rates.

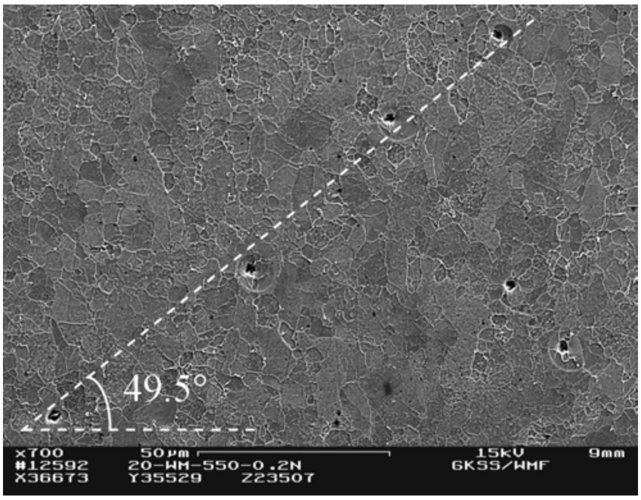

Figure 5.13. SEM picture from necking area of P22 WM tested at 0.2 mm/min with pore formation at 49.5° to horizontal plane (ε_{final}=8%).

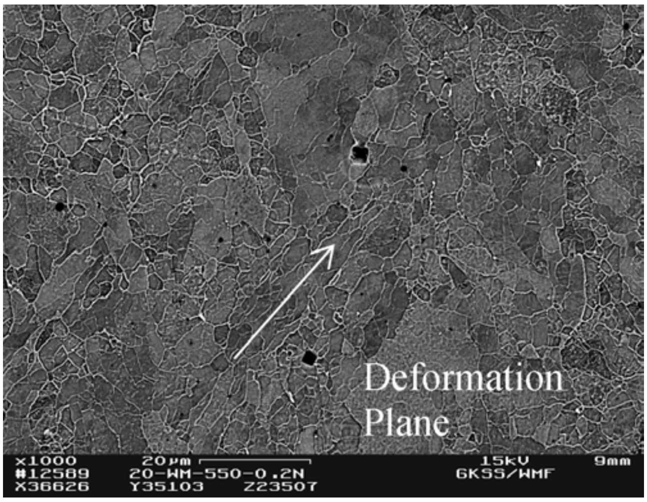

Figure 5.14. SEM picture from necking area of P22 WM tested at 0.2 mm/min showing deformation band with elongated grains and opened pores (ε_{final}=8%).

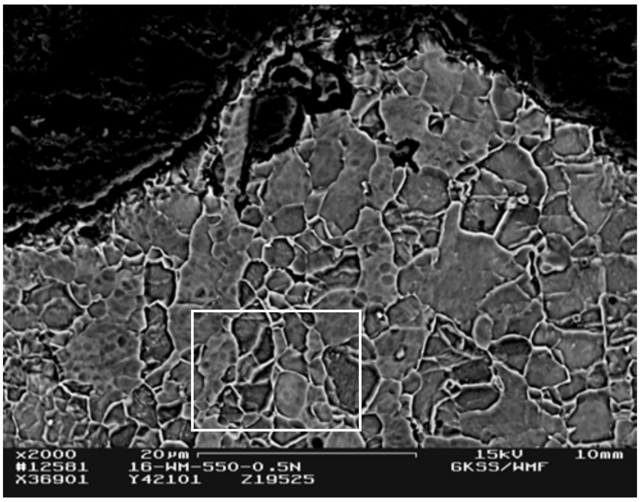

Figure 5.15. SEM showing damage in necking zone beneath fracture surface of P22 WM tested at 0.5 mm/min (ε_{final}=15%)

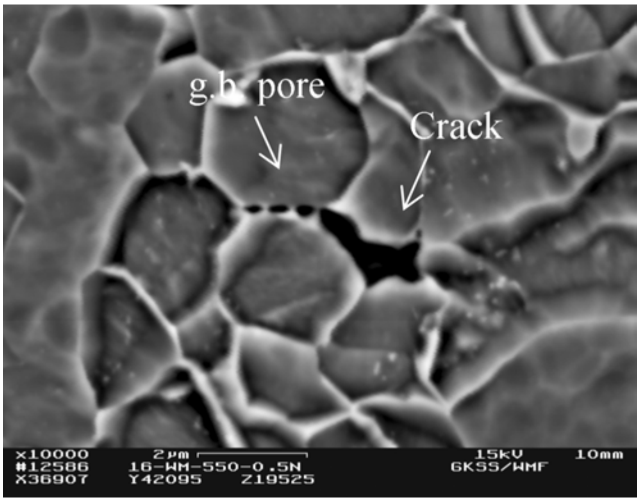

Figure 5.16. SEM picture of P22 WM tested at 0.5 mm/min, grain boundary failure by pore formation and microcracking (ε_{final}=15%)

5.1.2.2. P91 Similar Weldments

The microstructures of P91 BM and WM in the deformed sections of specimens are shown in Figures 5.17(a) and 5.17(b), respectively. Martensitic-transformed bainitic microstructure with prior austenite grain boundaries is delineated. Slight deformation observed in elongated ferritic lamellae along main loading axis is more pronounced in BM. Transformed austenitic martensitic structure with carbide precipitation is seen in WM (Figure 5.17(b)).

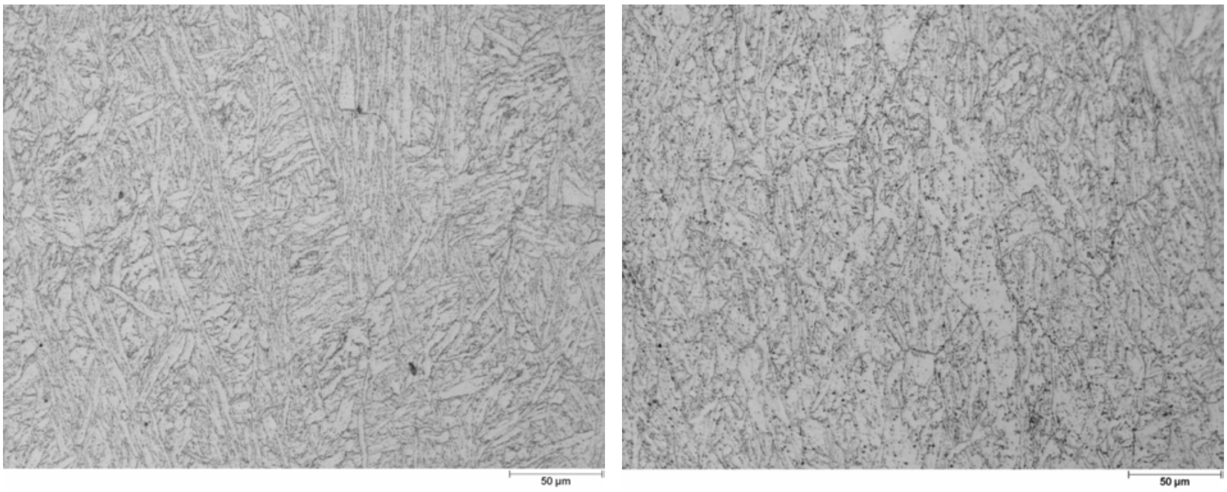

(a) (b)

Figure 5.17. OM pictures of (a) P91 BM with bainitic microstructure containing elongated ferrites along loading axis tested at 0.2 mm/min (ε_{final}=28%). (b) P91 WM tested at 0.5 mm/min (ε_{final}=17%), where prior austenite grain boundaries are delineated.

Higher magnification SEM micrograph depicts the deformation in BM and WM zones in Figures 5.18 and 5.19, respectively. The fracture site deformation zone is confined that extends into material well over 50 μm where pore formation and growth are observed (Figure 5.18). A uniform damage at grain boundaries is seen in WM (Figure 5.19).

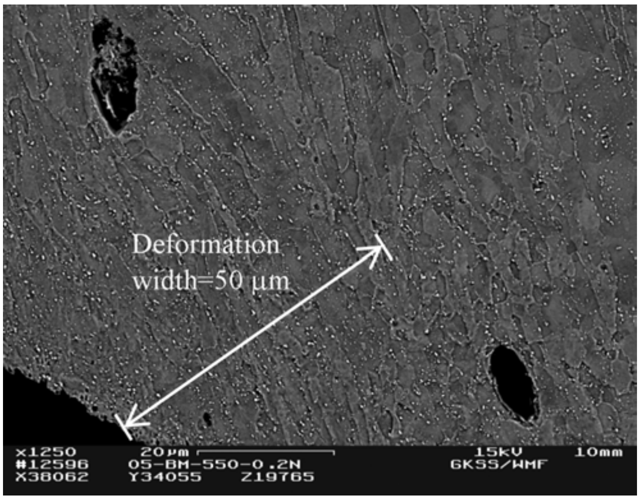

Figure 5.18. SEM picture from necking area of P91 BM tested at 0.2 mm/min with elongation of grains ($\varepsilon_{\text{final}}$=28%).

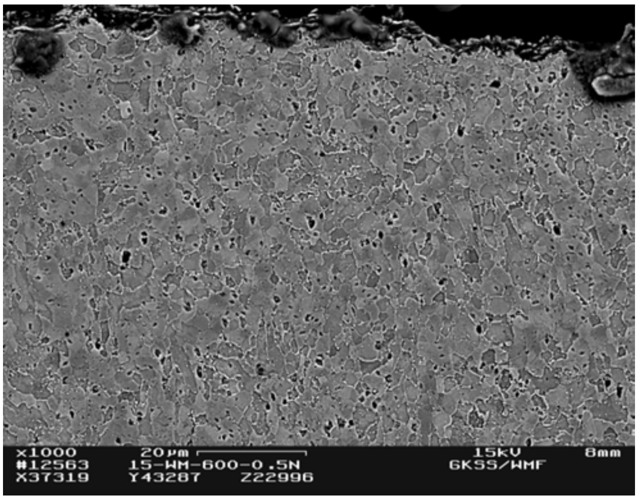

Figure 5.19. SEM picture of fracture zone of P91 WM tested at 0.5 mm/min ($\varepsilon_{\text{final}}$=17%)

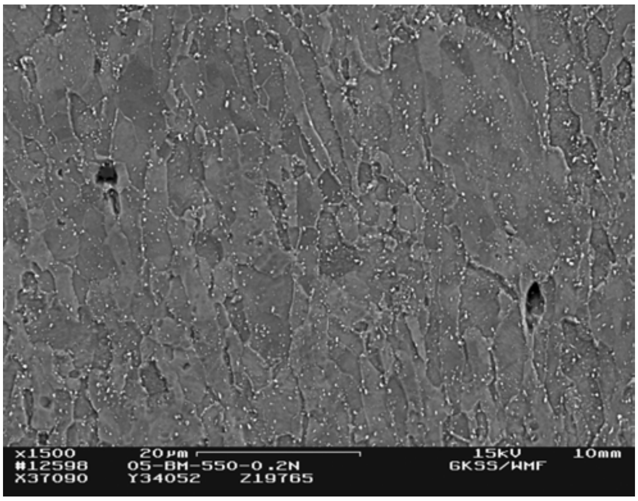

Figure 5.20. SEM picture from heavily deformed necking area of P91 BM tested at 0.2 mm/min ($\varepsilon_{\text{final}}$=28%).

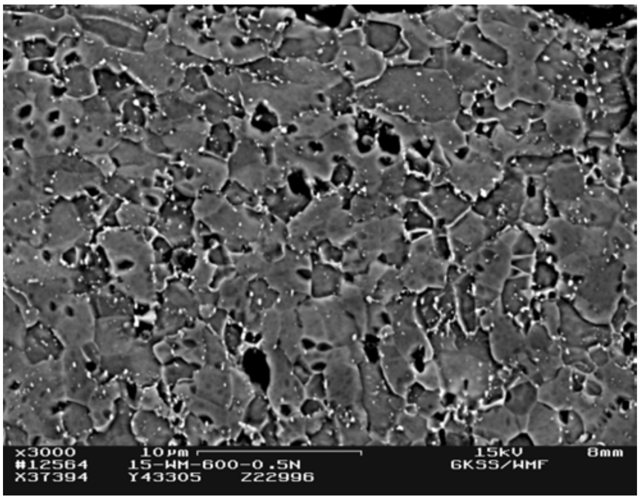

Figure 5.21. SEM picture from fracture zone of P91 WM tested at 0.5 mm/min showing grain boundary failure with enlarged pores (ε_{final}=17%).

Failure sites are observed at grain boundaries and martensitic grains as seen in Figures 5.20 and 5.21 in near to fracture zones of specimens of BM and WM, respectively. The observed deformation and fracture modes are comparable to the crack tip material behaviour in creep crack growth tested specimens [89]. Therefore, present results serve for a quick and reliable assessment of deformation and fracture behaviour of materials in service. They will provide basis for assessment of component behaviour in high temperature service as explained in details in Sections 5.2 and 5.3.

5.1.3. Post-Test Micro-hardness Testing

Micro-hardness measurements were conducted on selected tested MT specimens for each weldment zone and each loading rate. The measurement locations were a) the necking part, which was highly deformed and thermally exposed, b) specimen head which was not deformed but thermally exposed. Table 5.6 and 5.7 show the measured Vickers (HV 0.1) micro-hardness values from head and necking parts of P22 and P91, respectively. Effect of high temperature deformation is seen in necked zone measurements with reduced hardness except that of the P22 BM.

A slight increase in microhardness values are seen for both in BM and WM of P91 in measurement zones of head necking with increasing loading rates. A significant softening effect on thermally exposed and crept high temperature steels compared to only thermally exposed steels has also been mentioned by Cerjak et.al.[108]. This is similar to the effect of softening in MT specimens as in the present study of thermally exposed and plastically deformed zones.

Table 5.6. Micro-hardness values (HV 0.1) of P22 BM and WM at head (undamaged) and necking (damaged) parts

P22 BM			**P22 WM**		
Loading Rate (mm/min)	**Head**	**Necking**	**Loading Rate (mm/min)**	**Head**	**Necking**
0.2 mm/h	152.9	164.1	**0.2 mm/h**	158.3	149.2
0.5 mm/h	152.2	176.5	**0.5 mm/h**	159.9	160.7

Table 5.7. Micro-hardness values (HV 0.1) of P91 BM and WM at head (undamaged) and necking (damaged) parts

P91 BM			**P91 WM**		
Loading Rate (mm/min)	**Head**	**Necking**	**Loading Rate (mm/min)**	**Head**	**Necking**
0.2 mm/h	190.4	181.3	**0.2 mm/h**	218.4	179.3
0.5 mm/h	192.5	184.3	**0.5 mm/h**	227.7	185.3

5.2. HIGH TEMPERATURE FRACTURE MECHANICS TEST RESULTS

5.2.1 Introduction

High temperature fracture mechanics tests were conducted using specimen geometries given in Appendix B.6. Specimens were machined out of P22 and P91 butt-welded pipes, and tested in lab air at 550 °C and 600 °C, respectively. The specimens were heated to test temperature in a resistance furnace and kept constant within the limits permitted by standards [3, 6]. The specimen loading was completed within 30 minutes by step loading in a electro-mechanical testing machine.

The recorded data consisting of time (t), load (F), temperature (T), potential drop (PD), load line displacement (Δ^{LLD}), displacement at the initial crack tip ((Δ^{CTOD} (δ_5)) are analysed to determine fracture mechanics parameters and crack growth rate (See Section 4). The number of recorded data points is reduced to manageable size, e.g. 50-100 data points/specimen and then, if needed, data are fitted by regression method. The obtained data set is assessed by using data sheets for the calculation of related fracture mechanics parameters. As an example, data sheet of a SEN(B) specimen of P22 WM tested for 1613.3 hours at 550 °C is given in Appendix C.3. The assessment of recorded test data is presented in the following Section 5.2.2. The below example is given to illustrate the data analysis procedure and steps involved in analyses of each data set from each data set.

5.2.2 Assessment of High Temperature Crack Growth Data – An Example

High temperature crack growth test data of SEN(B) specimen made of P22 WM tested at 550 °C for 642.6 hours were analysed following the procedure given in Chapter 4. Figure 5.22 - 5.25 show the records of typical raw test data of PD, Δ^{LLD}, Δ^{CMOD} as a function of time. PD vs. t plot of the test is of Type 2 (see for reference Figure 4.11) indicates that the initial value of PD (V_0) is taken at minimum value recorded at t=87.6 hours in Figure 5.23. PD vs. t diagram is re-plotted with this correction as shown in Figure 5.26.

The dataset is then fitted by using regression methods in order to eliminate the non-material related experimental scatter in the data. Figure 5.27 shows a dataset for PD which is fitted by a 5th order polynomial using least squares fit regression method. R^2 value indicates the data fit quality with a value close to one. Δ^{LLD} and Δ^{CMOD} vs. time datasets are also fitted by 5th order polynomial functions using least squares fit regression method.

Initial and final crack lengths are determined on the fracture surface pictures of the crack-opened specimen after testing (Figure 5.28). Crack extension, Δa, is calculated from PD vs. time data using Equation 4.3. The dataset is reduced to a manageable number by taking the data points with intervals of certain crack extension, such as 25 μm. The fitted and reduced datasets of Δa, Δ^{LLD} and Δ^{CMOD} are depicted in Figure 5.29 as a function of test time.

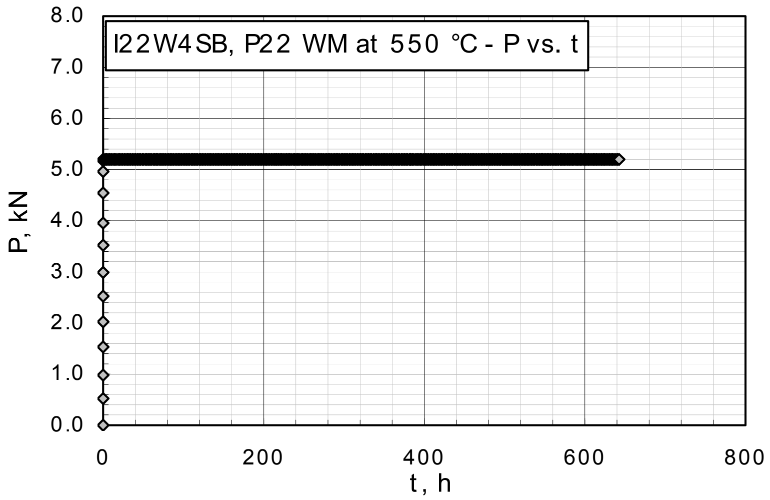

Figure 5.22. Load (P) vs. time (t) plot of the SEN(B) specimen ,I22W4SB, of P22 WM tested at 550 °C for 643 hours.

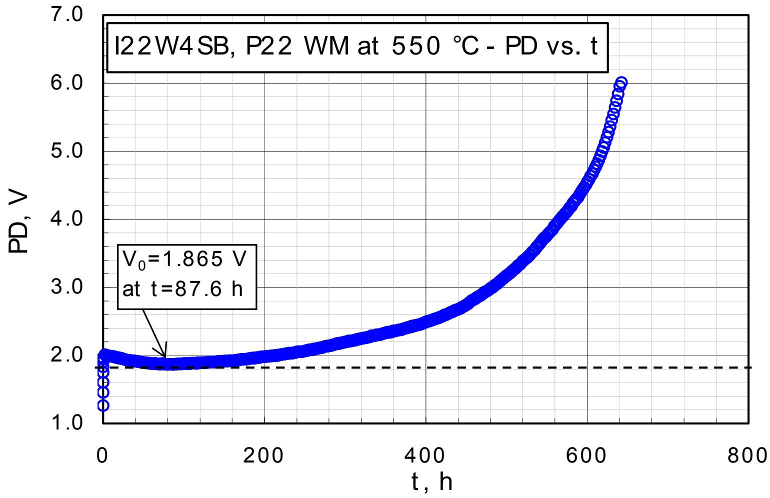

Figure 5.23. Potential drop (PD) vs. time (t) plot of the SEN(B) specimen, I22W4SB, of P22 WM tested at 550 °C for 643 hours.

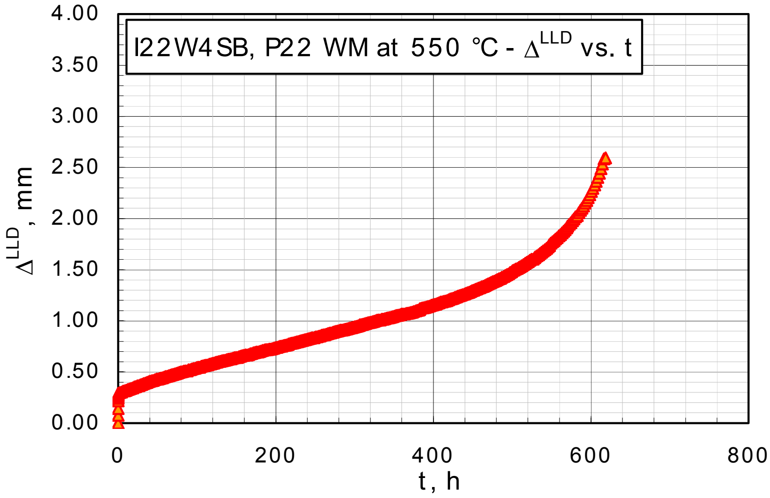

Figure 5.24. Load line displacement (Δ^{LLD}) vs. time (t) plot of the SEN(B) specimen, I22W4SB, of P22 WM tested at 550 °C for 643 hours.

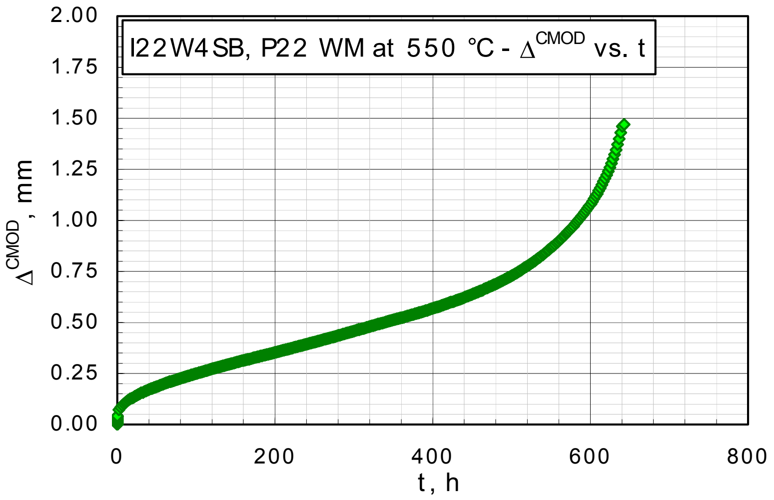

Figure 5.25. Crack mouth opening displacement (Δ^{CMOD}) vs. time (t) plot of the SEN(B) specimen ,I22W4SB, of P22 WM tested at 550 °C for 643 hours.

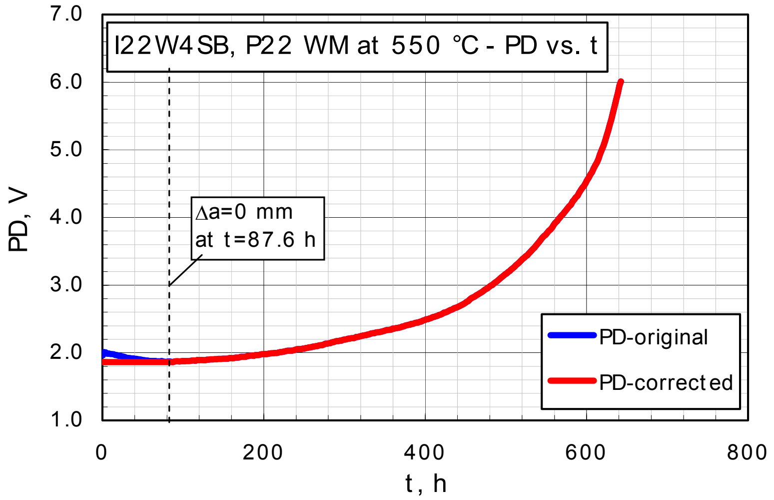

Figure 5.26. Potential drop (PD) vs. time (t) plot of the SEN(B) specimen, I22W4SB, of P22 WM tested for 643 hours at 550 °C.

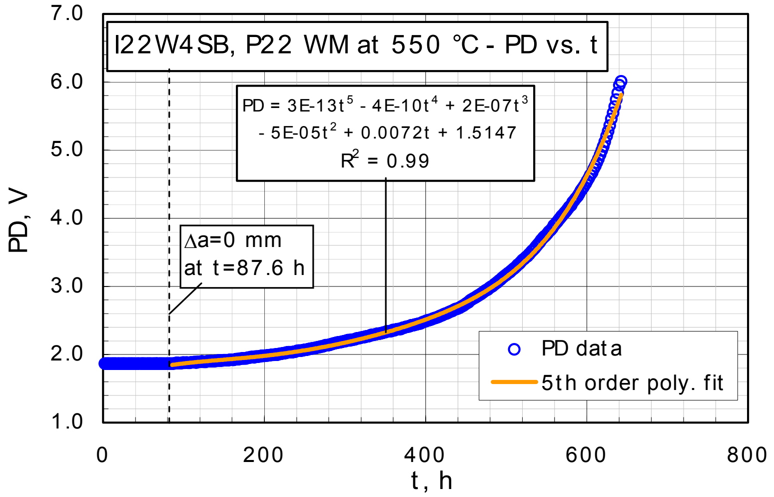

Figure 5.27. Fitting of potential drop (PD) vs. time (t) of the SEN(B) specimen, I22W4SB, by a 5th order polynomial function using least squares fit regression method.

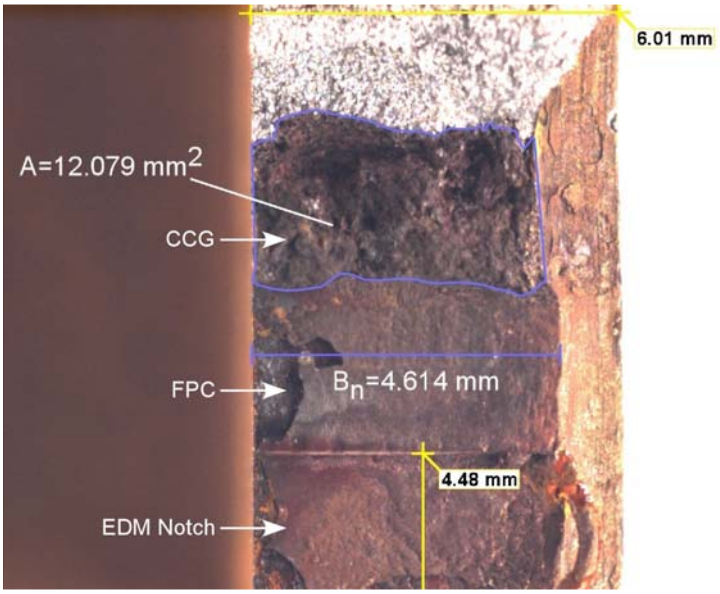

Figure 5.28. Fracture surface of the SEN(B) specimen, I22W4SB, crack opened by cyclic loading after testing.

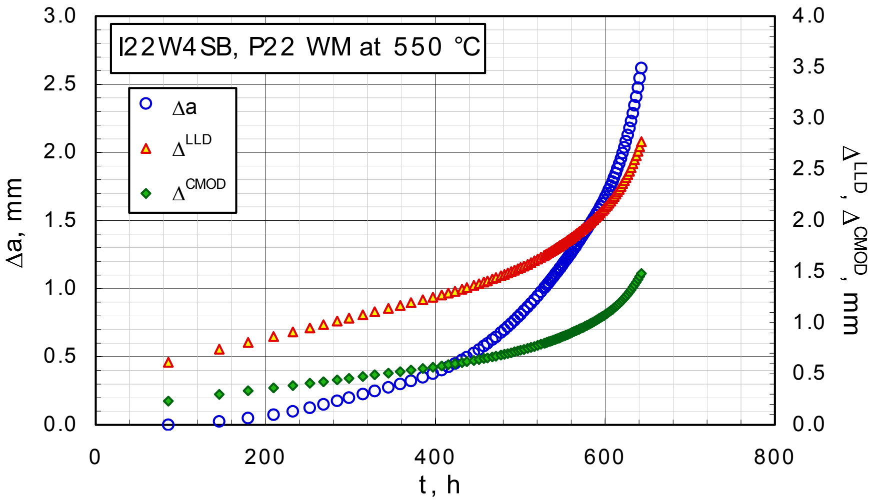

Figure 5.29. Reduced experimental dataset of SEN(B) specimen, I22W4SB, of P22 WM tested at 550 °C for 643 hours. Data are reduced by sampling crack extension steps of 25 μm. The load line displacement (Δ^{LLD}) and crack mouth opening displacement (Δ^{CMOD}) are also included.

The test data are further processed to determine crack growth rate and deflection rates of $\dot{\Delta}^{LLD}$ and $\dot{\Delta}^{CMOD}$ to calculate crack tip parameter, C^* (Equation 4.10-11), which is correlated with crack growth rate. The crack growth and deflection rates are calculated using either the secant method or 7-point method following ASTM E1457-00 [3] and the CoP [6] for testing of weldments. The above presented dataset of I22W4SB specimen is assessed using secant method to determine the crack growth rate, $\dot{a}$, and deflection rates ($\dot{\Delta}^{LLD}$ and $\dot{\Delta}^{CMOD}$) as shown in Figure 5.30. Creep component of the load line displacement rate, $\dot{\Delta}_c^{LLD}$, required for determination of C^* is deduced from measured data using the Equation 4.12. Note that high test loads may lead to plastic deformation at the crack tip that elastic-plastic stress and strains dominate the crack tip field ($\dot{\Delta}_c^{LLD} / \dot{\Delta}^{LLD} << 1$). Creep dominance of the crack tip stresses and strains are checked as in Figure 5.31 where creep component of the displacement rate

($\dot{\Delta}_c^{LLD}/\dot{\Delta}^{LLD}$) is depicted. The creep deformation dominates the crack tip (i.e. $\dot{\Delta}_c^{LLD}/\dot{\Delta}^{LLD} \geq 0.5$ as it is given in Section 4.2.7.2), which is also confirmed by the validity criterion t_T>>t for all data points. Hence, the crack tip correlation parameter C^* is valid for all of the data points determined in the assessed test.

Creep crack growth correlation parameters are determined from the reduced test data using the procedures explained in Section 4.2.7. Microsoft® Excel data sheets (Figure 5.32) are used to calculate the creep crack growth correlation parameters (C^* and K), creep crack growth rate ($\dot{a}$), creep component of load line displacement rate ($\dot{\Delta}_c^{LLD}$) and other related parameters which are required during calculations.

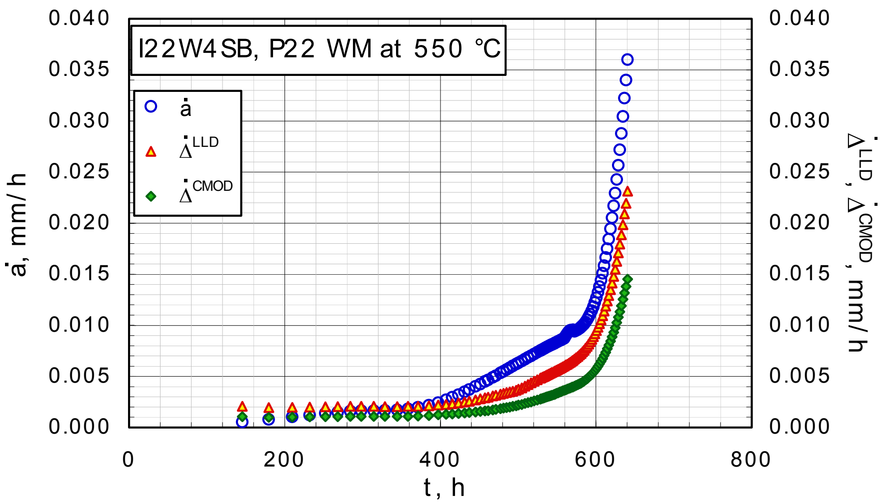

Figure 5.30. Crack growth rate ($\dot{a}$), load line displacement rate ($\dot{\Delta}^{LLD}$) and crack mouth opening displacement rate ($\dot{\Delta}^{CMOD}$) vs. time (t) plots of the SEN(B) specimen, I22W4SB, tested at 550 °C for 643 hours.

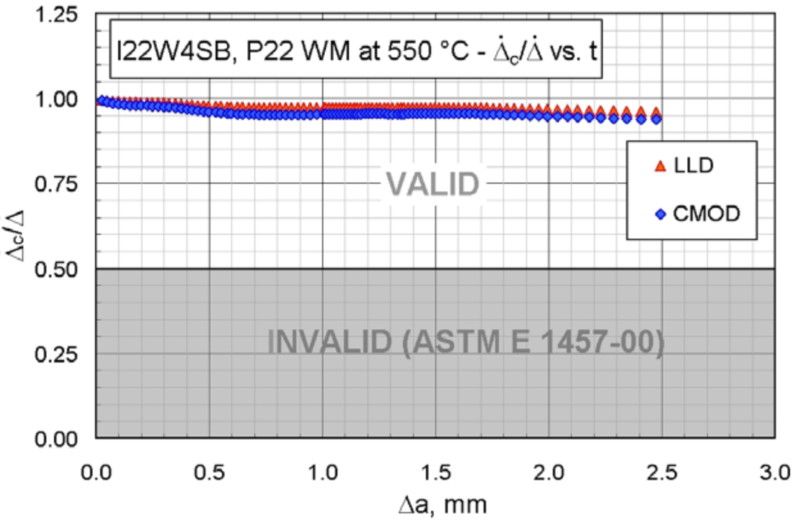

Figure 5.31. Creep component of displacement $\Delta_c^{LLD}/\Delta^{LLD}$ is determined for the SEN(B) specimen, I22W4SB, tested at 550 °C for 643 hours confirming the creep dominance at t growing crack tip for valid CCG correlations.

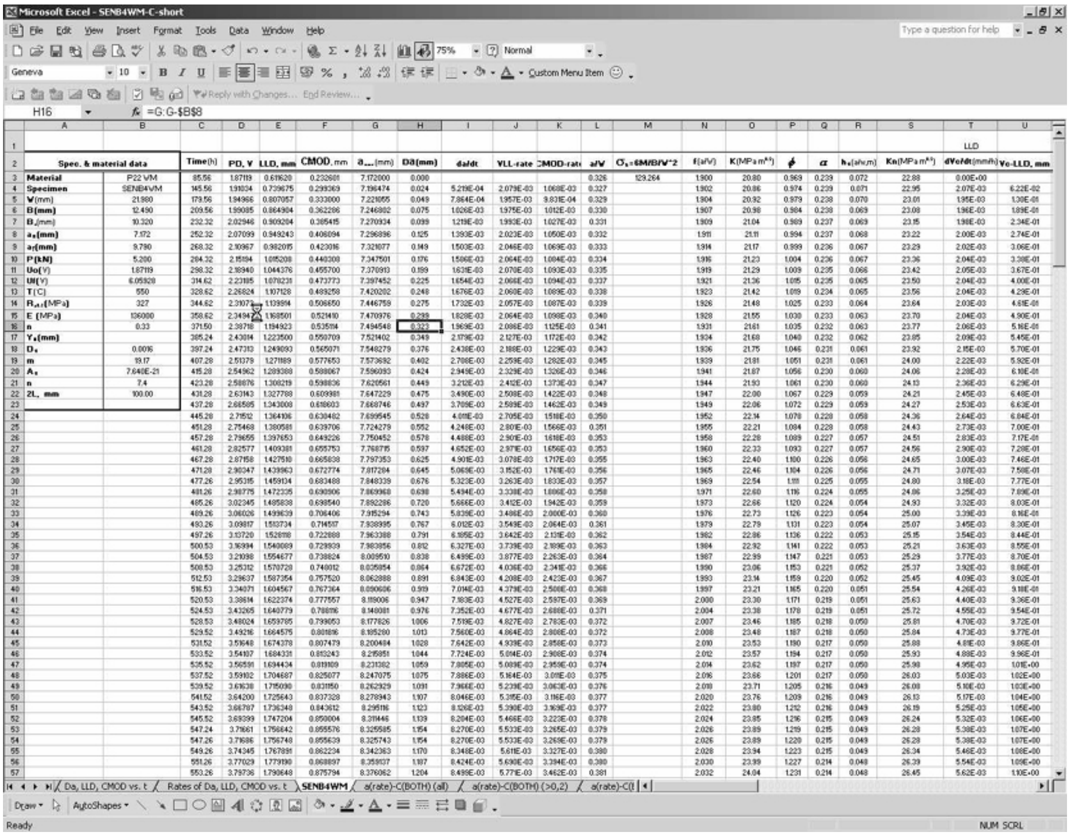

H16 =G:G-B8

	A	B	C	D	E	F	G	H	I	J	K	L	M	N	O	P	Q	R	S	T	U
1																				LLD	
2	Spec. & material data		Time(h)	PD, V	LLD, mm	CMOD, mm	a...(mm)	Δa(mm)	da/dt	VLL-rate	CMOD-rat	a/W	σ_n=6M/BW^2	f(a/W)	K(MPa m^0.5)	ϕ	α	h_1(a/w,m)	Kn(MPa m^0.5)	dVe/dt(mm/h)	Ve-LLD, mm
3	**Material**	P22 WM	85.56	1.87119	0.611620	0.232681	7.172000	0.000				0.326	129.264	1.900	20.80	0.969	0.239	0.072	22.88	0.00E+00	
4	**Specimen**	SENB4WM	145.56	1.91034	0.739675	0.299369	7.196474	0.024	5.219E-04	2.079E-03	1.068E-03	0.327		1.902	20.86	0.974	0.239	0.071	22.95	2.07E-03	6.22E-02
5	**W**(mm)	21.980	179.56	1.94966	0.807057	0.333000	7.221055	0.049	7.864E-04	1.957E-03	9.831E-04	0.329		1.904	20.92	0.979	0.238	0.070	23.01	1.95E-03	1.30E-01
6	**B(mm)**	12.490	209.56	1.99085	0.864904	0.362286	7.246802	0.075	1.026E-03	1.975E-03	1.012E-03	0.330		1.907	20.98	0.984	0.238	0.069	23.08	1.96E-03	1.89E-01
7	**B_n**(mm)	10.320	232.32	2.02946	0.909204	0.385415	7.270934	0.099	1.219E-03	1.993E-03	1.027E-03	0.331		1.909	21.04	0.989	0.237	0.069	23.15	1.98E-03	2.34E-01
8	**a_0(mm)**	7.172	252.32	2.07099	0.949243	0.406094	7.296896	0.125	1.393E-03	2.023E-03	1.050E-03	0.332		1.911	21.11	0.994	0.237	0.068	23.22	2.00E-03	2.74E-01
9	**a_f(mm)**	9.790	268.32	2.10967	0.982015	0.423016	7.321077	0.149	1.503E-03	2.046E-03	1.069E-03	0.333		1.914	21.17	0.999	0.236	0.067	23.29	2.02E-03	3.06E-01
10	**P(kN)**	5.200	284.32	2.15194	1.015208	0.440308	7.347501	0.176	1.586E-03	2.064E-03	1.084E-03	0.334		1.916	21.23	1.004	0.236	0.067	23.36	2.04E-03	3.38E-01
11	**Uo**(V)	1.87119	298.32	2.18940	1.044376	0.455700	7.370913	0.199	1.631E-03	2.070E-03	1.093E-03	0.335		1.919	21.29	1.009	0.235	0.066	23.42	2.05E-03	3.67E-01
12	**Uf**(V)	6.05928	314.62	2.23185	1.070231	0.473773	7.397452	0.225	1.654E-03	2.066E-03	1.094E-03	0.337		1.921	21.36	1.015	0.235	0.065	23.50	2.04E-03	4.00E-01
13	**T**(°C)	550	328.62	2.26824	1.107128	0.489258	7.420202	0.248	1.676E-03	2.060E-03	1.089E-03	0.338		1.923	21.42	1.019	0.234	0.065	23.56	2.04E-03	4.29E-01
14	**$R_{p0.2}$**(MPa)	327	344.62	2.31072	1.139994	0.506650	7.446759	0.275	1.732E-03	2.057E-03	1.087E-03	0.339		1.926	21.48	1.025	0.233	0.064	23.64	2.03E-03	4.61E-01
15	**E (MPa)**	136000	358.62	2.34947	1.168501	0.521410	7.470976	0.299	1.828E-03	2.064E-03	1.098E-03	0.340		1.928	21.55	1.030	0.233	0.063	23.70	2.04E-03	4.90E-01
16	**n**	0.33	371.50	2.38718	1.194923	0.535114	7.494548	0.323	1.969E-03	2.086E-03	1.125E-03	0.341		1.931	21.61	1.035	0.232	0.063	23.77	2.06E-03	5.16E-01
17	**Y_0(mm)**		385.24	2.43014	1.223500	0.550709	7.521402	0.349	2.179E-03	2.127E-03	1.172E-03	0.342		1.934	21.68	1.040	0.232	0.062	23.85	2.09E-03	5.45E-01
18	**D_0**	0.0016	397.24	2.47313	1.249093	0.565071	7.548279	0.376	2.438E-03	2.188E-03	1.229E-03	0.343		1.936	21.75	1.046	0.231	0.061	23.92	2.15E-03	5.70E-01
19	**m**	19.17	407.28	2.51379	1.271189	0.577653	7.573692	0.402	2.708E-03	2.259E-03	1.282E-03	0.345		1.939	21.81	1.051	0.231	0.061	24.00	2.22E-03	5.92E-01
20	**A_0**	7.640E-21	415.28	2.54962	1.289388	0.588067	7.596093	0.424	2.949E-03	2.329E-03	1.326E-03	0.346		1.941	21.87	1.056	0.230	0.060	24.06	2.28E-03	6.10E-01
21	**n**	7.4	423.28	2.58876	1.308219	0.598836	7.620561	0.449	3.212E-03	2.412E-03	1.373E-03	0.347		1.944	21.93	1.061	0.230	0.060	24.13	2.36E-03	6.29E-01
22	**2L, mm**	100.00	431.28	2.63143	1.327788	0.609981	7.647229	0.475	3.490E-03	2.508E-03	1.422E-03	0.348		1.947	22.00	1.067	0.229	0.059	24.21	2.45E-03	6.48E-01
23			437.28	2.66585	1.343008	0.618603	7.668746	0.497	3.709E-03	2.589E-03	1.462E-03	0.349		1.949	22.06	1.072	0.229	0.059	24.27	2.53E-03	6.63E-01
24			445.28	2.71512	1.364106	0.630482	7.699545	0.528	4.011E-03	2.705E-03	1.518E-03	0.350		1.952	22.14	1.078	0.228	0.058	24.36	2.64E-03	6.84E-01
25			451.28	2.75468	1.380581	0.639706	7.724279	0.552	4.248E-03	2.801E-03	1.566E-03	0.351		1.955	22.21	1.084	0.228	0.058	24.43	2.73E-03	7.00E-01
26			457.28	2.79655	1.397653	0.649226	7.750452	0.578	4.488E-03	2.901E-03	1.618E-03	0.353		1.958	22.28	1.089	0.227	0.057	24.51	2.83E-03	7.17E-01
27			461.28	2.82577	1.409381	0.655753	7.768715	0.597	4.652E-03	2.971E-03	1.656E-03	0.353		1.960	22.33	1.093	0.227	0.057	24.56	2.90E-03	7.28E-01
28			467.28	2.87158	1.427510	0.665838	7.797353	0.625	4.901E-03	3.078E-03	1.717E-03	0.355		1.963	22.40	1.100	0.226	0.056	24.65	3.00E-03	7.46E-01
29			471.28	2.90047	1.439963	0.672774	7.817284	0.645	5.069E-03	3.152E-03	1.761E-03	0.356		1.965	22.46	1.104	0.226	0.056	24.71	3.07E-03	7.58E-01
30			477.26	2.95315	1.459134	0.683488	7.848339	0.676	5.323E-03	3.263E-03	1.833E-03	0.357		1.969	22.54	1.111	0.225	0.055	24.80	3.18E-03	7.77E-01
31			481.26	2.98775	1.472335	0.690906	7.869968	0.698	5.494E-03	3.338E-03	1.886E-03	0.358		1.971	22.60	1.116	0.224	0.055	24.86	3.25E-03	7.89E-01
32			485.26	3.02345	1.485838	0.698540	7.892286	0.720	5.666E-03	3.412E-03	1.942E-03	0.359		1.973	22.66	1.120	0.224	0.054	24.93	3.32E-03	8.03E-01
33			489.26	3.06026	1.499639	0.706406	7.915294	0.743	5.839E-03	3.486E-03	2.000E-03	0.360		1.976	22.73	1.126	0.223	0.054	25.00	3.39E-03	8.16E-01
34			493.26	3.09817	1.513734	0.714517	7.938995	0.767	6.012E-03	3.549E-03	2.064E-03	0.361		1.979	22.79	1.131	0.223	0.054	25.07	3.45E-03	8.30E-01
35			497.26	3.13720	1.528118	0.722888	7.963388	0.791	6.185E-03	3.642E-03	2.131E-03	0.362		1.982	22.86	1.136	0.222	0.053	25.15	3.54E-03	8.44E-01
36			500.53	3.16994	1.540089	0.729939	7.983856	0.812	6.327E-03	3.739E-03	2.189E-03	0.363		1.984	22.92	1.141	0.222	0.053	25.21	3.63E-03	8.55E-01
37			504.53	3.21098	1.554677	0.738824	8.009510	0.838	6.499E-03	3.877E-03	2.263E-03	0.364		1.987	22.99	1.147	0.221	0.053	25.29	3.77E-03	8.70E-01
38			508.53	3.25312	1.570728	0.748012	8.035854	0.864	6.672E-03	4.036E-03	2.341E-03	0.366		1.990	23.06	1.153	0.221	0.052	25.37	3.92E-03	8.86E-01
39			512.53	3.29637	1.587354	0.757520	8.062888	0.891	6.843E-03	4.208E-03	2.423E-03	0.367		1.993	23.14	1.159	0.220	0.052	25.45	4.09E-03	9.02E-01
40			516.53	3.34071	1.604567	0.767364	8.090606	0.919	7.014E-03	4.379E-03	2.508E-03	0.368		1.997	23.21	1.165	0.220	0.051	25.54	4.26E-03	9.18E-01
41			520.53	3.38614	1.622374	0.777557	8.119006	0.947	7.183E-03	4.527E-03	2.597E-03	0.369		2.000	23.30	1.171	0.219	0.051	25.63	4.40E-03	9.36E-01
42			524.53	3.43265	1.640779	0.788116	8.148081	0.976	7.352E-03	4.677E-03	2.688E-03	0.371		2.004	23.38	1.178	0.219	0.051	25.72	4.55E-03	9.54E-01
43			528.53	3.48024	1.659785	0.799053	8.177826	1.006	7.519E-03	4.827E-03	2.783E-03	0.372		2.007	23.46	1.185	0.218	0.050	25.81	4.70E-03	9.72E-01
44			529.52	3.49216	1.664575	0.801816	8.185280	1.013	7.560E-03	4.864E-03	2.808E-03	0.372		2.008	23.48	1.187	0.218	0.050	25.84	4.73E-03	9.77E-01
45			531.52	3.51648	1.674378	0.807479	8.200484	1.028	7.642E-03	4.939E-03	2.858E-03	0.373		2.010	23.53	1.190	0.217	0.050	25.88	4.81E-03	9.86E-01
46			533.52	3.54107	1.684331	0.813243	8.215851	1.044	7.724E-03	5.014E-03	2.908E-03	0.374		2.012	23.57	1.194	0.217	0.050	25.93	4.88E-03	9.96E-01
47			535.52	3.56591	1.694434	0.819109	8.231382	1.059	7.805E-03	5.089E-03	2.959E-03	0.374		2.014	23.62	1.197	0.217	0.050	25.98	4.95E-03	1.01E+00
48			537.52	3.59102	1.704687	0.825077	8.247075	1.075	7.886E-03	5.164E-03	3.011E-03	0.375		2.016	23.66	1.201	0.217	0.050	26.03	5.03E-03	1.02E+00
49			539.52	3.61638	1.715090	0.831150	8.262929	1.091	7.966E-03	5.239E-03	3.063E-03	0.376		2.018	23.71	1.205	0.216	0.049	26.08	5.10E-03	1.03E+00
50			541.52	3.64200	1.725643	0.837328	8.278943	1.107	8.046E-03	5.315E-03	3.116E-03	0.377		2.020	23.76	1.209	0.216	0.049	26.13	5.17E-03	1.04E+00
51			543.52	3.66787	1.736348	0.843612	8.295116	1.123	8.126E-03	5.390E-03	3.169E-03	0.377		2.022	23.80	1.212	0.216	0.049	26.19	5.25E-03	1.05E+00
52			545.52	3.69399	1.747204	0.850004	8.311446	1.139	8.204E-03	5.466E-03	3.223E-03	0.378		2.024	23.85	1.216	0.215	0.049	26.24	5.32E-03	1.06E+00
53			547.24	3.71661	1.756642	0.855576	8.325585	1.154	8.270E-03	5.533E-03	3.265E-03	0.379		2.026	23.89	1.219	0.215	0.049	26.28	5.38E-03	1.07E+00
54			547.26	3.71686	1.756748	0.855639	8.325743	1.154	8.270E-03	5.533E-03	3.269E-03	0.379		2.026	23.89	1.220	0.215	0.049	26.28	5.38E-03	1.07E+00
55			549.26	3.74345	1.767891	0.862234	8.342363	1.170	8.348E-03	5.611E-03	3.327E-03	0.380		2.028	23.94	1.223	0.215	0.049	26.34	5.46E-03	1.08E+00
56			551.26	3.77029	1.779190	0.868897	8.359137	1.187	8.424E-03	5.690E-03	3.394E-03	0.380		2.030	23.99	1.227	0.214	0.048	26.39	5.54E-03	1.09E+00
57			553.26	3.79736	1.790648	0.875794	8.376062	1.204	8.499E-03	5.771E-03	3.462E-03	0.381		2.032	24.04	1.231	0.214	0.048	26.45	5.62E-03	1.10E+00

Figure 5.32. Sample Microsoft® Excel data sheet including test data used for calculating C^*, K, $\dot{a}$, $\dot{\Delta}^{LLD}$ for crack tip deformation and crack growth correlation.

Crack tip deformation and crack initiation and extension behaviour are assessed. The crack growth rate, da/dt, is correlated with crack tip loading parameters, K, C^* and K^c_{mat}. The values of C^*, K and K^c_{mat} corresponding to engineering definition of creep crack initiation at crack extension Δa=0.2 or 0.5 mm, are determined for creep crack initiation assessment as given below in Section 5.2.4. The assessed data of creep crack initiation and extension are substantiated by metallographic and fractographic evidence for a better understanding of creep crack initiation and growth behaviour of the material for eventual assessment of engineering components.

The creep crack growth rate, da/dt of the SEN(B) specimen, I22W4SB of P22 WM is correlated with C^* and K in Figures 5.33 and 5.34, respectively. The C^* correlation is in a good agreement with the NSW creep crack growth model, which is introduced in Section 2.1.4.4. The exponent of the correlating parameter (Equation 2.37), ϕ=0.84, is very close to the value of 0.88 taken creep exponent n=7.4.

Detailed analysis of a typical crack growth rate correlation is presented below. The creep crack growth rate, da/dt, correlation with C^* has two different stages, namely Stage I and Stage II (Figure 5.35). A lower crack growth rate following the crack growth initiation extends to 1.3 mm, crack growth in Stage I. Higher crack growth rate is observed in the Stage II where the CCG rate is plotted as a function of crack extension. Post-test metallographic investigation revealed that the shift from Stage I to Stage II corresponds to a sharp change of direction of the crack growth path, following a zig-zag route (Figure 5.36) in WM. Note the crack deviation from the main crack growth path at an angle of 60 °C in Stage I, in the dendritic WM structure. As the crack extends to $\Delta a \cong 1.39$ mm, along easy crack mode, it changes its direction by $\approx 90°$ and continues to propagate at a higher rate assisted by microcrack coalescence in damaged material. Damage accumulation in Stage II is similar to

Stage I, preferentially aligned along dendrites. However, the crack propagates perpendicular to dendrite cooling structure at weld pass boundary by coalescence of microcracks leading to zig-zag crack propagation that conforms to the slip line field theory [109].

This example emphasises the ambiguity of high temperature crack growth testing of weldments [39,110,111], because of their heterogeneous microstructure with varying creep strength. The crack path proceeds through creep-weak and creep-strong zones within weldment. It also sheds some light on the evaluation and interpretation of high temperature creep crack growth data of weldments, where the scatter of the data which is inherited from testing and/or the heterogeneous microstructure of the material needs special care and should be treated accordingly [112]. It is worth mentioning here that the knee in crack growth rate correlation plot may also be seen if the fitting of raw data is not done properly (See Figure 6.3).

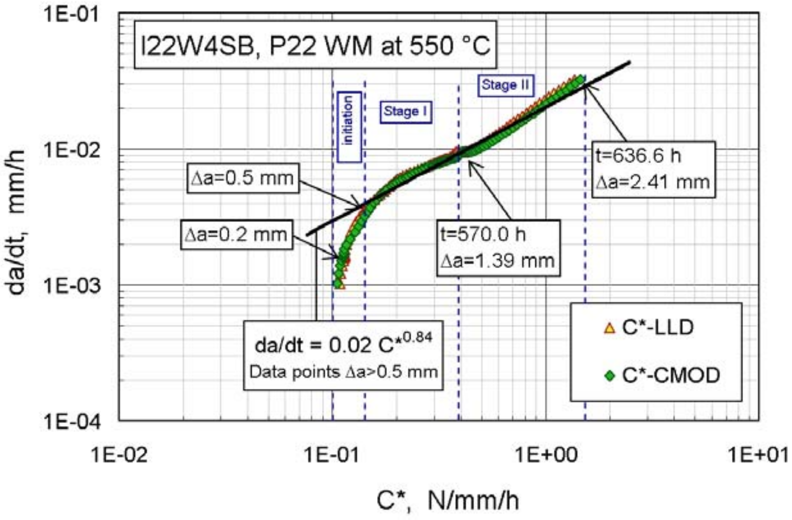

Figure 5.33. Correlation of creep crack growth rate, da/dt, of the SEN(B) specimen, I22W4SB, tested for 643 hours at 550 °C, with crack tip parameter C^*. The power function curve is fitted by least squares fit regression method for data with Δa>0.5 mm.

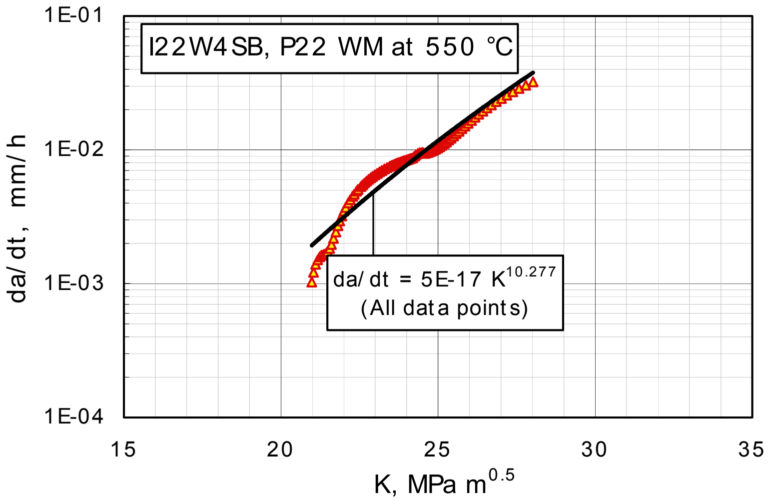

Figure 5.34. Correlation of creep crack growth rate of P22 WM SEN(B) specimen, I22W4SB, tested at 550 °C for 643 hours, with K. Complete dataset (without reduction) is fitted by least squares regression method.

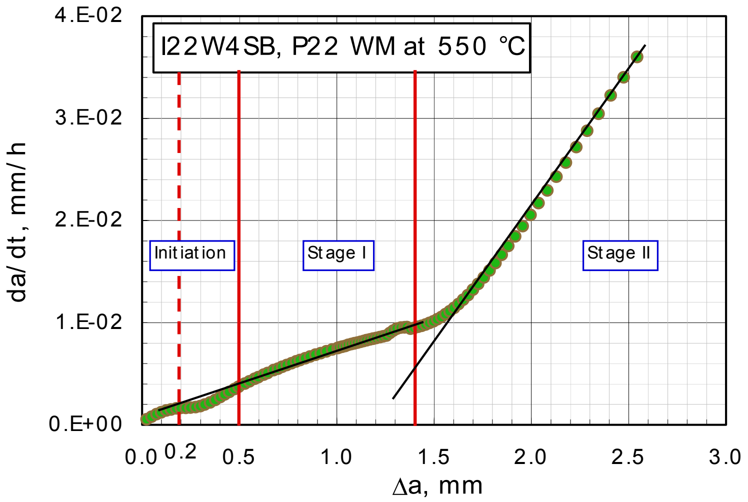

Figure 5.35. Crack growth rate, da/dt, as a function of crack extension Δa of the SEN(B) specimen, I22W4SB, tested at 550 °C for 643 hours showing two stages of crack growth.

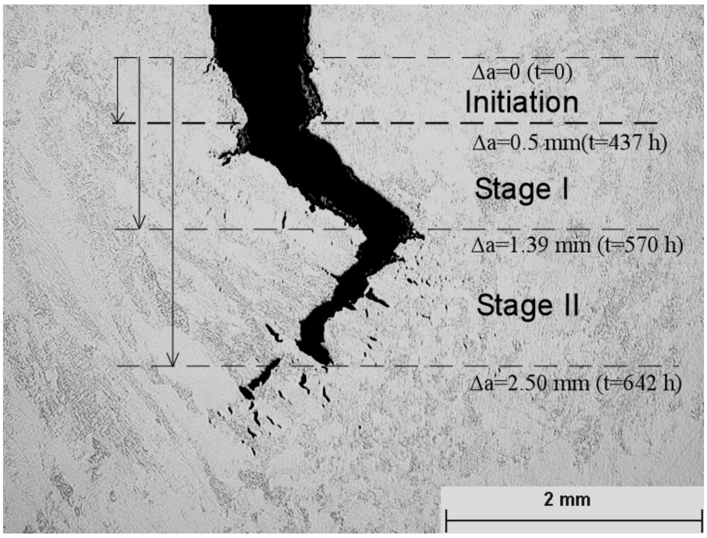

Figure 5.36. Deviation of the crack growth path in dendritic weld microstructure. Change of crack growth path is seen at weld bead boundary. The SEN(B) specimen, I22W4SB, tested at 550 °C for 643 hours, showing two stages of crack growth.

5.2.3 Test Results

The high temperature fracture mechanics tests were conducted following the procedure in the CoP [6] for high temperature crack initiation and growth testing of weldments. The recorded data is further processed by data fitting, followed by data reduction for the calculation of crack growth rates and fracture mechanics parameters. Thus obtained data are correlated to assess the CCI and CCG behaviour of P22 and P91 weld materials. Figures 5.37 to 5.38 show the crack growth, Δa, and the load line displacement, Δ^{LLD}, histories of tested specimens from different weldment zones of P22 steel. The presented data is determined on different specimen geometries (C(T), CS(T), SEN(B), RNB(T)) and loading modes (F_{const} and CDR).

These data are further assessed for the correlation of the CCI and CCG behaviour of the material. The legend given on graphs consists of specimen code, geometry, width (W), gross thickness (B), net thickness (B_n) and loading mode (“Fconst” for constant load test, “CDR” for constant displacement rate test), consecutively.

Test durations of the plotted specimens vary between 158 to 2262 hours. A longer crack growth, Δa, with shorter load line displacement, Δ^{LLD}, observed in CS(T) specimens is a peculiarity of the specimen geometry. A comparison between C(T) specimens E22B1A25 (P22 BM) and E22F1025 (P22 HAZ) reveals that a longer Δa can be obtained for a shorter Δ^{LLD} in creep-weaker weldment zone tests. A short crack length of 0.1 mm is noted for RNB(T) specimen (E22W1ARB) tested for 2074 hours, giving only CCI data, which is very valuable for component assessment data.

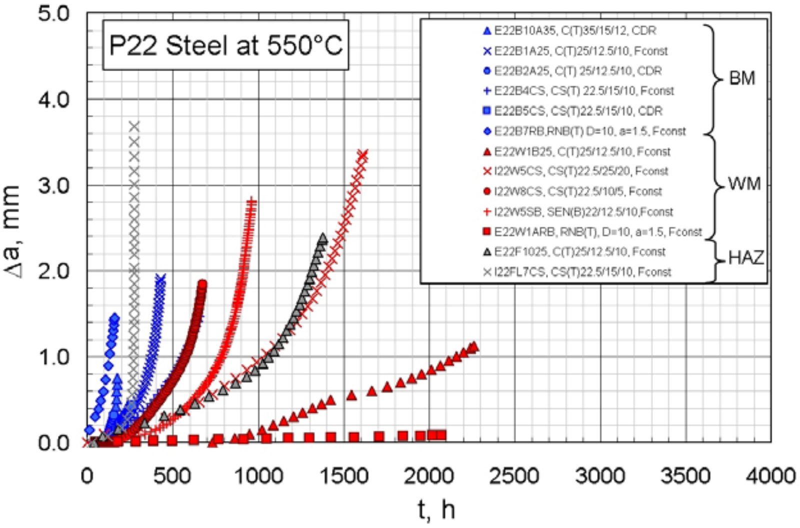

Figure 5.37. Crack extension, Δa, as a function of time, t, for specimens of P22 steel weldments (BM, WM, HAZ) tested at 550 °C. Specimen geometry, size and loading mode is given in the legend.

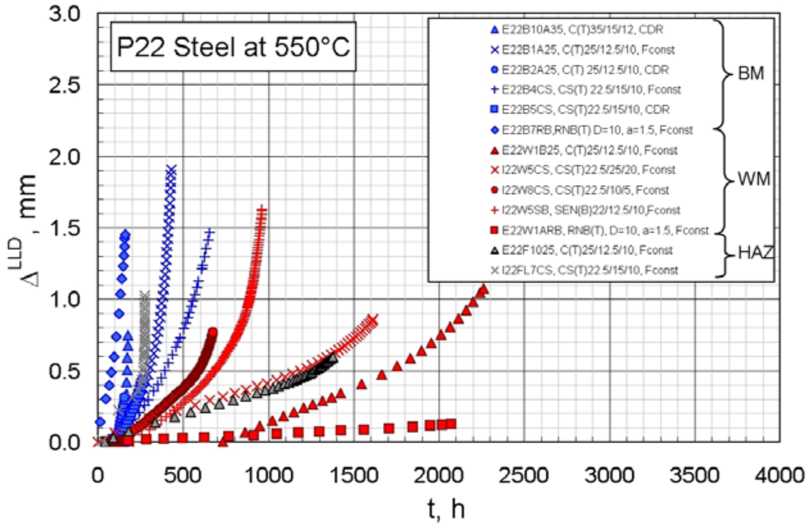

Figure 5.38. Load line displacement, Δ^{LLD}, as a function of time, t, for various fracture mechanics test specimens of P22 steel weldments (BM, WM, HAZ) tested at 550 °C. Specimen geometry, size and loading mode is given in the legend.

Similarly, the crack growth, Δa, and the load line displacement, Δ^{LLD}, histories of various specimens from different weldment zones of P91 steel is given in Figures 5.39 and 5.40. Test durations vary between 59 to 4853 hours. The testing of RNB(T) specimen, I91W5ARB, which lasted only 59 hours showed a quick response to loading, it was ended before fracture of the specimen. Note that the C(T) specimen PPB1 of P91 BM was tested in CDR mode with changing loading rates of 0.001 mm/h and 0.005 mm/h. The incubation period of the C(T) specimen PTIV2 of P91 HAZ lasted about 3700 hours.

For both of P22 and P91 steels (Figures. 5.38 and 5.40), the Δ^{LLD} decreases as the test duration of the specimen increased. This decay corresponds to exhaustion of the creep properties of the material with exposure to stress and high temperature, as it is observed in creep strain vs. time curves of material obtained by testing standard tensile (ST) specimens at different stress levels.

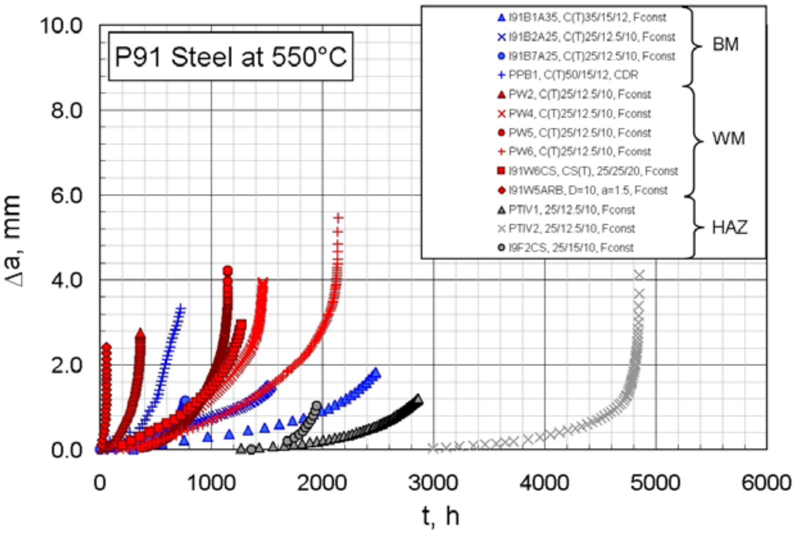

Figure 5.39. Crack extension, Δa, as a function of time, t, for various fracture mechanics test specimens of P91 steel weldments (BM, WM, HAZ) tested at 600 °C. Specimen geometry, size and loading mode is given in the legend.

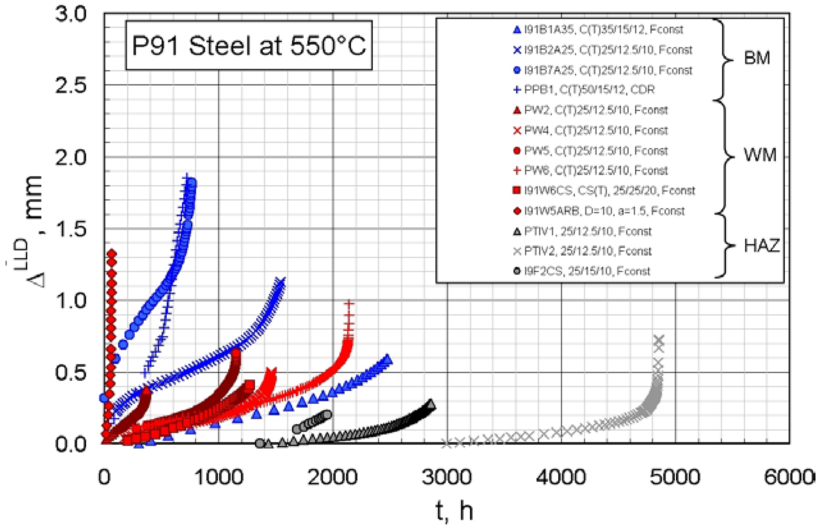

Figure 5.40. Load line displacement, Δ^{LLD}, as a function of time, t, for various fracture mechanics test specimens of P91 steel weldments (BM, WM, HAZ) tested at 600 °C. Specimen geometry, size and loading mode is given in the legend.

5.2.4 Creep Crack Initiation Results

The data for creep crack initiation (CCI) are taken at crack extensions of Δa=0.2 mm or Δa=0.5 mm based on engineering definitions of CCI. The CCI times are correlated with the crack tip parameters, stress intensity factor, K, and C^* in order to determine the crack initiation resistance of P22 and P91 steel weldments. Furthermore, the data is correlated with K^c_{mat}, creep crack initiation toughness, which are later used for the construction of the Time Dependent Failure Assessment Diagram (TDFAD) for component assessment. The application and construction procedure of the TDFAD method are presented in Section 2.3.3.1.

An overview of CCI resistance of different weldment zones of P22 and P91 steels are presented in Figures 5.41 to 5.44. The CCI data are correlated with the loading parameters K and C^*, at crack extensions Δa=0.2 and 0.5 mm. The datasets and further details are presented in Sections 5.2.4.1 and 5.2.4.2.

Comparison of correlations of CCI resistance of identical weldment zones of P22 and P91 steels in terms of K or C^* reveals that the corresponding weldment zone of P91 steel at 600 °C has a higher CCI resistance than P22 steel at 550 °C. However, the correlation of CCI resistance with C^* shows that the CCI resistance of P91 BM declines much quicker than the P22 BM's, although it is higher than P22 BM's at early crack initiation times.

The reason for higher CCI resistance obtained at Δa=0.5 mm than at Δa=0.2 mm is that the load is increased to grow crack in crack resistant material. Hence, the crack tip parameter has higher values at larger crack extension of 0.5 mm. Therefore, the choice of engineering definition of CCI changes the amount of resistance as well and the determined CCI resistance should not be treated as absolute but an engineering relevant value.

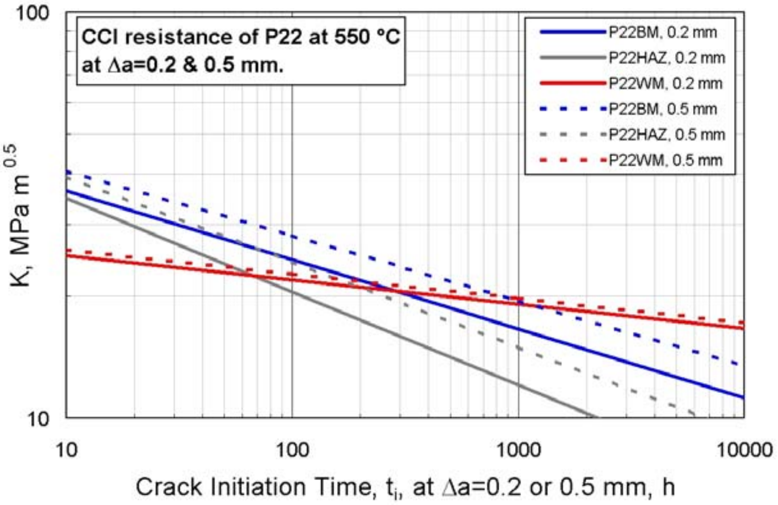

Figure 5.41. Comparison of CCI resistance trendlines in terms of K for P22 steel weldment zones at 550 °C. The initiation time data at 0.2 mm crack extension (solid lines) and at 0.5 mm crack extension (dashed lines) are shown.

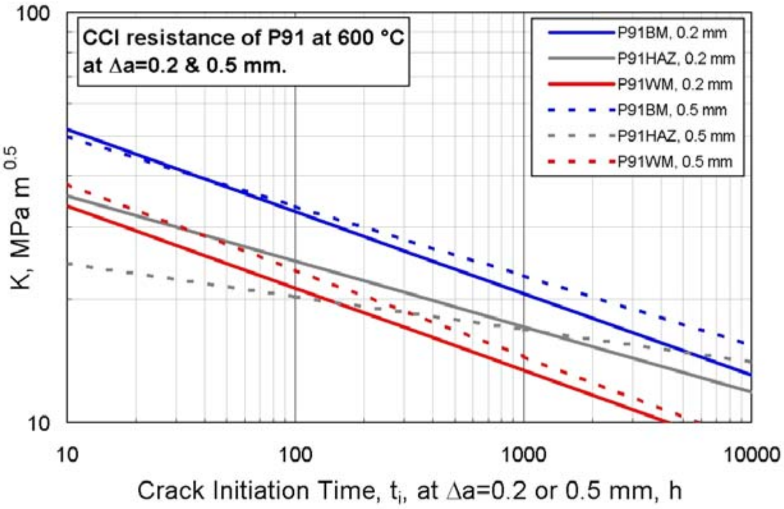

Figure 5.42. Comparison of CCI resistance trendlines in terms of K for P91 steel weldment zones at 600 °C.

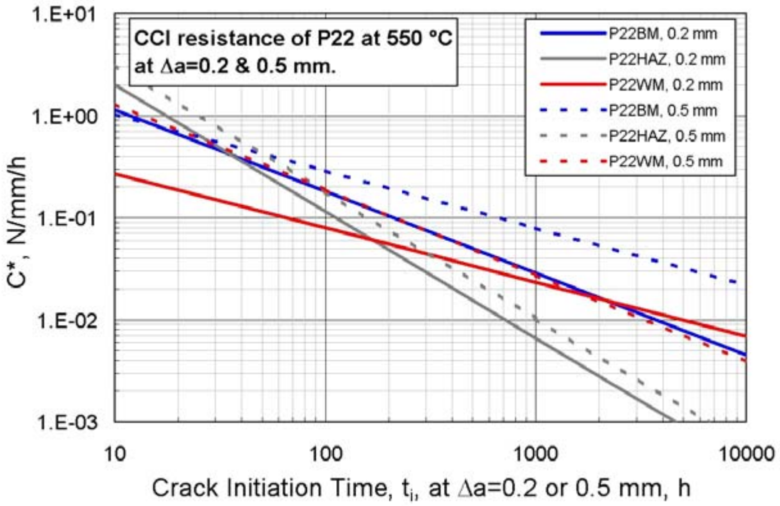

Figure 5.43. Comparison of CCI resistance trendlines in terms of C^* for P22 steel weldment zones at 550 °C.

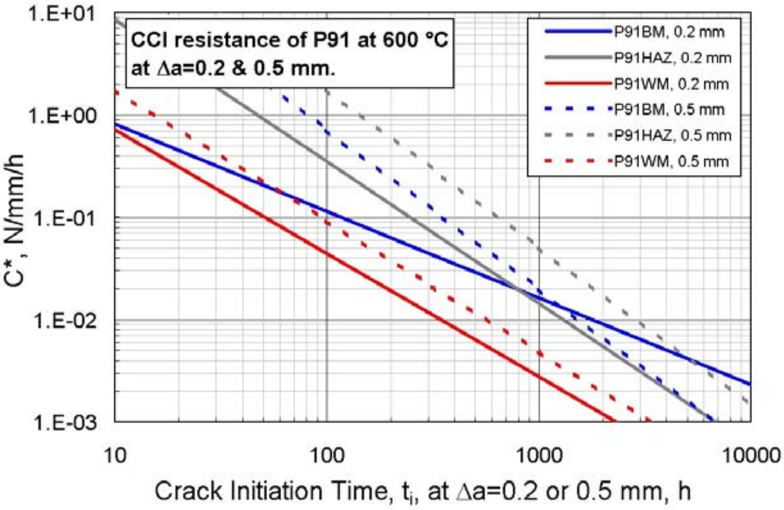

Figure 5.44. Comparison of CCI resistance trendlines in terms of C^* for P91 steel weldment zones at 600 °C.

Although P22 WM does not have the highest early CCI resistance, it has the lowest slope of CCI resistance with initiation time, seen in K correlation. A similar tendency is observed, however, being the second lowest slope of CCI resistance with time in C^* correlation. The lower slope points out the higher resistance to damage and crack growth rate of P22 BM is also remarkable. This particular type of CCI resistance behaviour of a material is important for the engineering performance of components made of these materials. Particularly, the service loading and assessment of components is the ultimate goal of the present studies. Note that the difference in CCI resistance obtained by using different fracture mechanics parameters directs attention to the validity of those fracture mechanics parameters at early (crack initiation) and later (crack growth) stages of crack extension. This issue is addressed in studies of ESIS TC11 WG on testing of weldments which produced a CoP [6] and in ECCC as in the relevant documents [113].

5.2.4.1. Creep Crack Initiation Behaviour of P22 Steel Weldment

The CCI initiation times defined at crack extensions, Δa=0.2 and 0.5 mm for different weldment zones of P22 steel loading parameters correlated with K, C^* and K^c_{mat} are presented in Figures. 5.45 to 5.50. The CCI data from high temperature fracture mechanics tests on three different specimen geometries, C(T), CS(T) and SEN(B) are presented. It is noted that there is no significant specimen geometry effect on the CCI times of the P22 weldments. A power function curve is fitted to each dataset correlation by use of the least squares fit regression method. The power function curves are extended for comparison of different weldment zones. Upper and lower bounds for correlation of CCI initiation times with C^* are determined by use of NSW model equation (Equation 2.45) for determination of CCI time [34], as given in Section 2.1.4.5. The bounds are plotted using the material properties given in Table 3.2. Peculiarity is observed in P22 WM with higher resistance at longer times. It is not conforming to the NSW model either. Such behaviour is not observed in P91 WM (see Figure 5.53). This may be due to weld material properties that lead to such crack behaviour. It emphasises the need for extensive study including metallographic evidence for building a complete picture of material assessment using continuum mechanics approach.

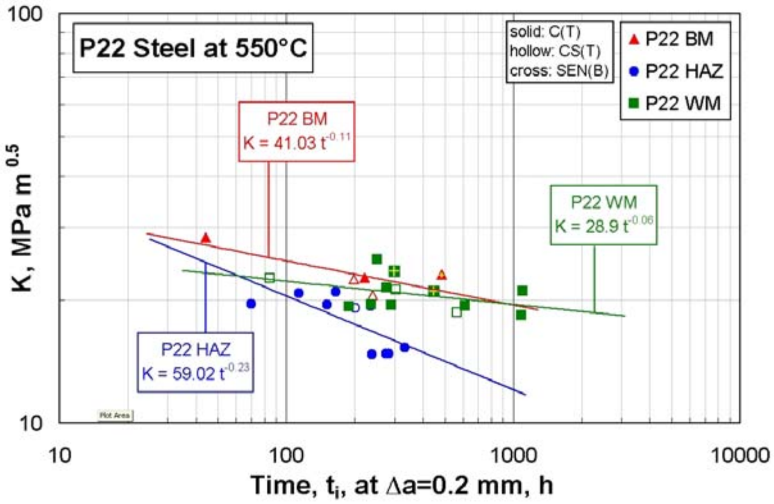

Figure 5.45. Crack initiation resistance in terms of K for P22 weldment zones at 550 °C correlated with the initiation time at crack extension, $\Delta a = 0.2$ mm.

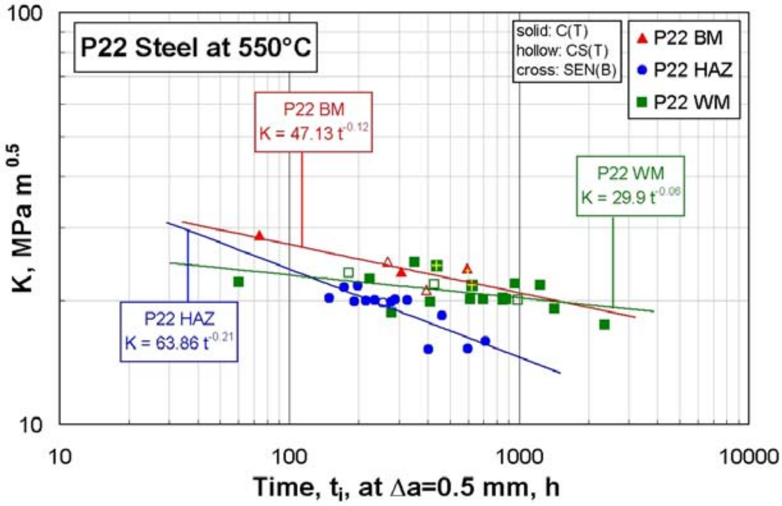

Figure 5.46. Crack initiation resistance in terms of K for P22 weldment zones at 550 °C correlated with the initiation time at crack extension, $\Delta a = 0.5$ mm.

Crack initiation times of different weldment zones at Δa=0.2 and 0.5 mm correlated with K (Figures 5.45-46) yield that P22 HAZ has the weakest crack initiation resistance compared to the other weldment zones. Low decrease rate in crack initiation resistance of P22 WM with increasing crack initiation time, t_i, is remarkable. While the similar low decrease rate in crack initiation resistance of P22 WM is noted by the correlation of crack initiation time with C^* at $\Delta a=0.2$ mm (Figure 5.47), the lowest value of crack initiation resistance is observed at $\Delta a=0.5$ mm in P22 BM (Figure 5.48)**.**

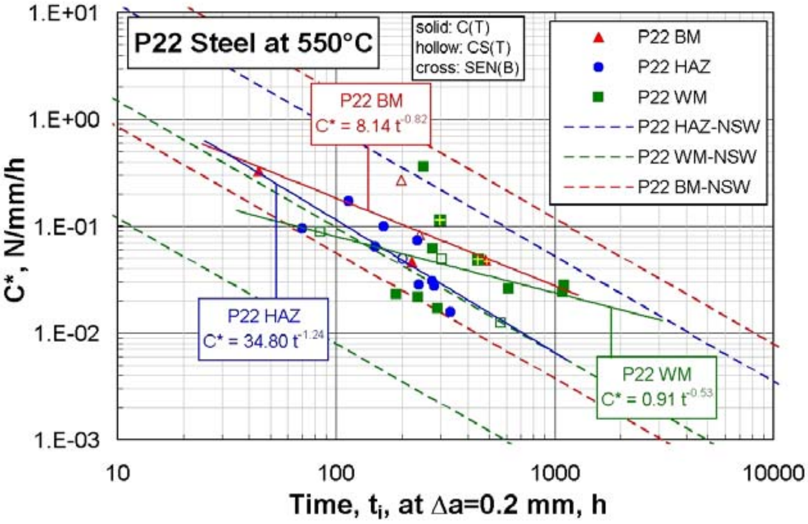

Figure 5.47. Creep crack initiation resistance in terms of C^* for P22 weldment zones at 550 °C. The solid lines indicate the power function curve fitted by least squares fit method to data. The dashed lines are upper and lower bounds calculated based on NSW model.

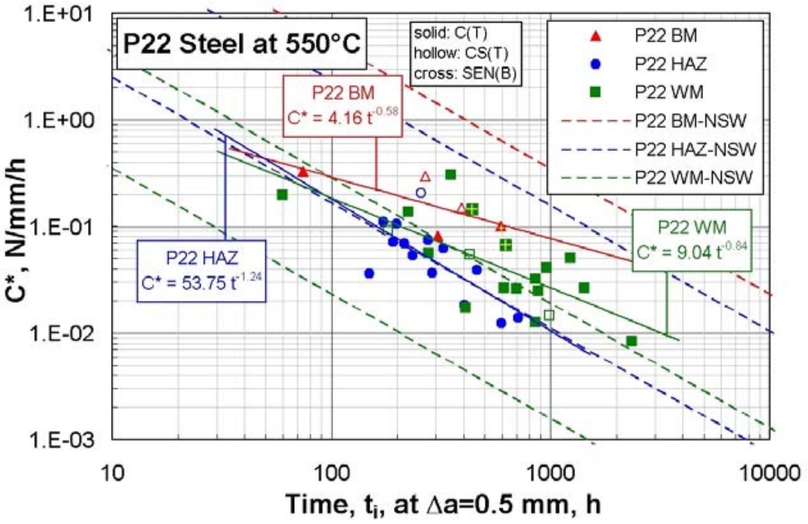

Figure 5.48. Creep crack initiation resistance in terms of C^* for P22 weldment zones at 550 °C. The solid lines indicate the power function curve fitted by least squares fit method to data. The dashed lines are upper and lower bounds calculated based on NSW model.

The upper and lower bound plots for P22 BM were determined by use of Equation 2.45 from the NSW model. The whole experimental data are covered including both for $\Delta a=0.2$ mm (Figure 5.47) and $\Delta a=0.5$ mm (Figure 5.48). P22 HAZ data points lie in the immediate vicinity of the lower bound. Note that the power curve fitted to the correlation of crack initiation time of P22 HAZ with C^* at $\Delta a=0.5$ coincides with the lower bound determined by Equation 2.45 (Figure 5.48).

The data points of crack initiation times of P22 WM at $\Delta a=0.2$ and 0. 5 mm in Figures 5.47 and 5.48, respectively, however, lie at or above the upper bound. It is also to be noted that the power curves fitted to P22 WM data points at Δa=0.2 and 0. 5 mm decrease at much lower rate with increasing initiation time, t_i. This is mainly the scatter in P22 WM data, due to variation of properties which are not reflected properly in NSW model. This observation is of particular importance for long time extrapolation of data for structural assessment in service components.

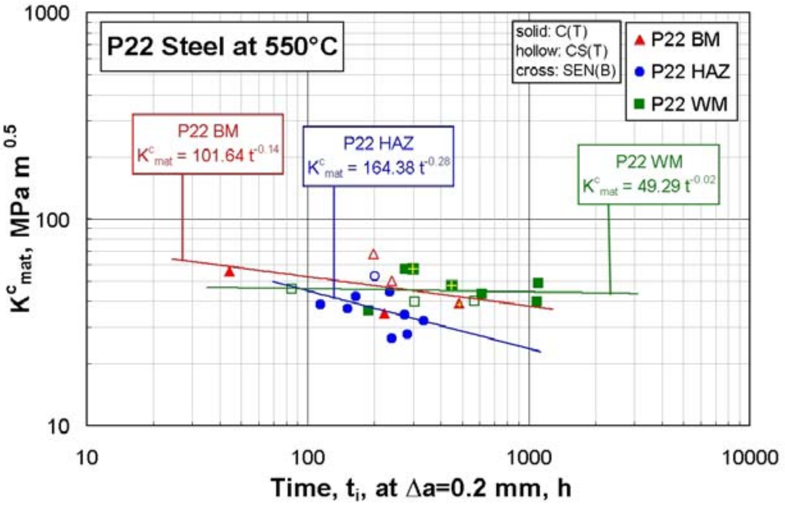

Figure 5.49. Creep crack initiation toughness in terms of K^c_{mat} for P22 weldment zones at 550 °C correlated with the time to crack initiation at Δa = 0.2 mm.

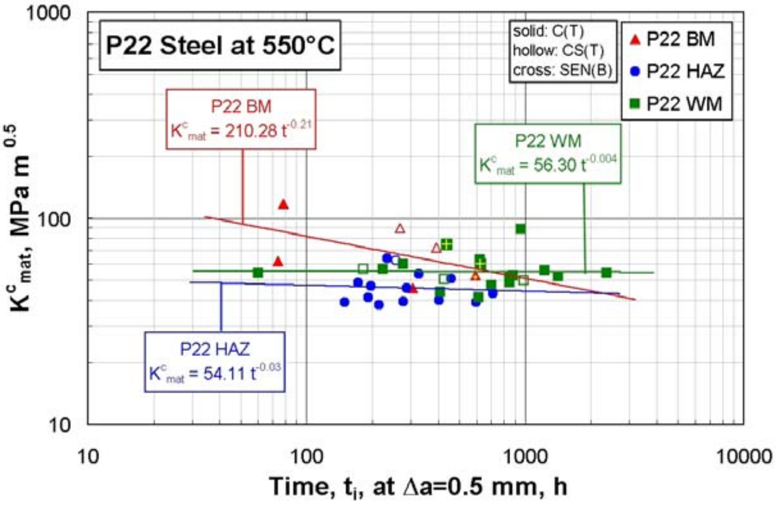

Figure 5.50. Creep crack initiation toughness in terms of K^c_{mat} for P22 weldment zones at 550 °C correlated with the time to crack initiation, Δa = 0.2 mm.

5.2.4.2. Creep Crack Initiation Behaviour of P91 Steel Weldment

The CCI initiation times defined at crack extension of Δa=0.2 and 0.5 mm in tests from specimens machined out of weldment zones of P91 steel are correlated with loading parameters K, C^* and K^c_{mat}, as shown in Figures. 5.51 to 5.56. The crack initiation data were obtained from specimens of three different specimen geometries, namely C(T), CS(T) and RNB(T). The same data analysis procedure is applied as in P22 weldment tests. A power function curve is fitted for each weldment zone by use of least squares fit regression method and these are extended to longer service times. The upper and lower bounds are determined for crack initiation data based on the NSW model (Equation 2.45) using the material properties given in Table 3.2.

Crack initiation times at crack extension of Δa=0.2 and 0.5 mm determined for different weldment zones are correlated with stress intensity factor, K in Figures 5.51 and 5.52, respectively. The P91 WM has the lowest, and P91 BM the highest crack initiation resistance for crack initiation times defined at Δa=0.2 mm and 0.5 mm. The rate of reduction in crack initiation resistance is the lowest in P91 HAZ with crack initiation time, t_i at Δa=0.5 mm. This is similar to the CCI behaviour of P22 WM (Figures 5.45 and 5.46). The type IV fracture mode in P91 HAZ leads to lower fracture resistance and shorter CCI times.

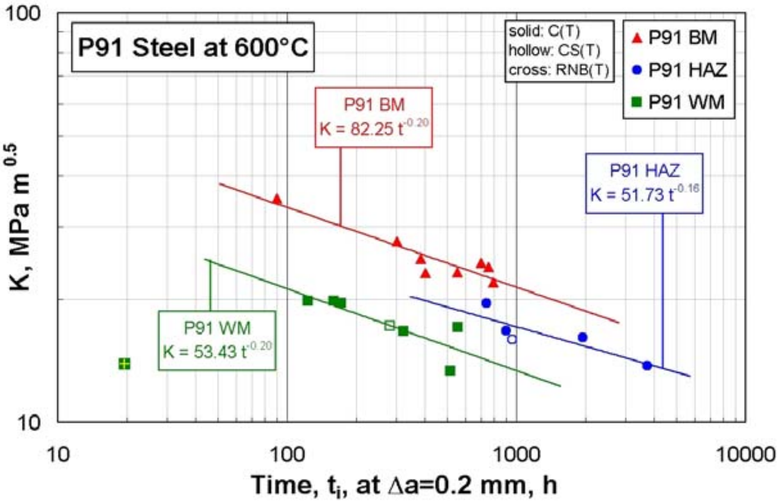

Figure 5.51. Crack initiation resistance of P91 weldment zones at 600 °C in terms of K correlated with the time to crack initiation at Δa = 0.2 mm.

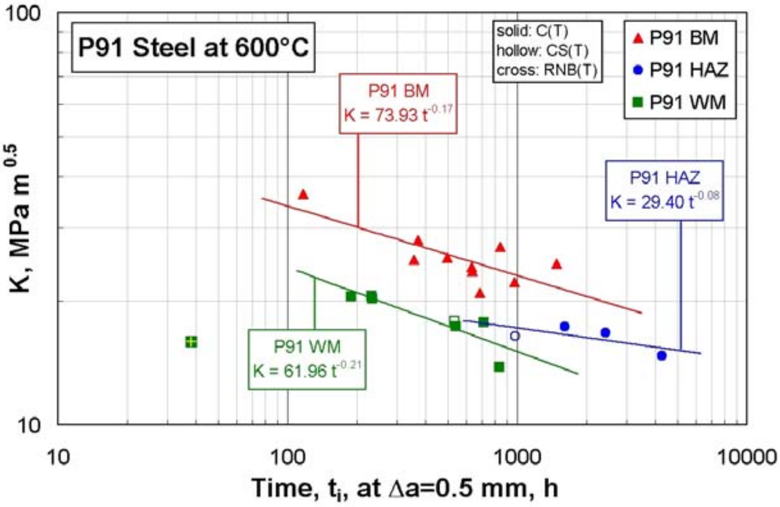

Figure 5.52. Crack initiation resistance of P91 weldment zones at 600 °C in terms of K correlated with the time to crack initiation at Δa = 0.5 mm.

The C^* correlation with crack initiation times for Δa=0.2 and Δa=0.5 mm crack extension are depicted in Figures. 5.53 and 5.54, respectively. Similar to K correlations, P91 WM has the lowest crack initiation resistance. However, on the contrary to microstructural fracture resistance correlations with K, the P91 HAZ has the highest crack initiation resistance with longer initiation time. For the crack initiation defined at Δa=0.2 mm (Figure 5.53), the decrease of crack initiation resistance with increasing crack initiation time, t_i, is the lowest for P91 BM. Note that the crack initiation data at Δa=0.2 mm crack extension has higher scatter than that at Δa=0.5 mm crack extension (Figure 5.54).

The upper and lower bound NSW model prediction lines determined using Equation 2.45 are plotted for different weldment zones of P91. The experimental P91 WM data lie closer to the upper bound prediction lines for both crack initiation at Δa=0.2 mm and Δa=0.5 mm crack extension (Figures 5.53-54). Therefore, similar to P22 WM, the NSW model predicts conservative crack initiation time for P91 WM. The experimental data which lie above the upper bound NSW prediction line is directing attention to the need for revision of the NSW prediction method.

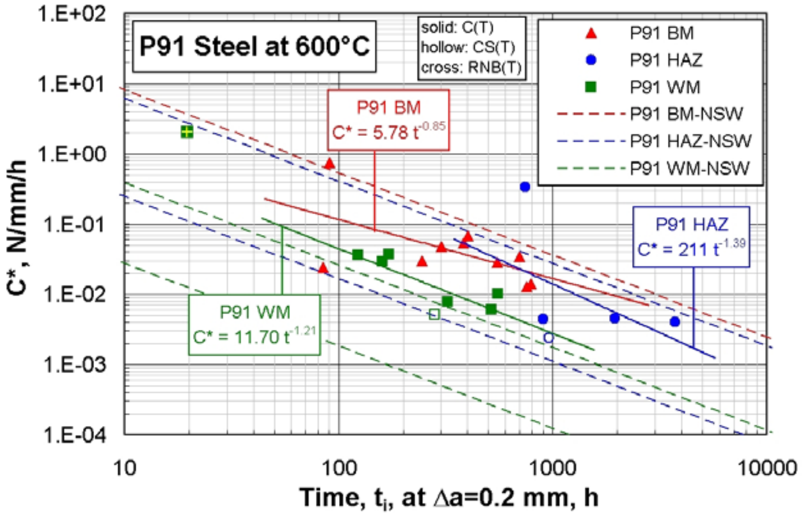

Figure 5.53. Creep crack initiation resistance of P91 weldment zones at 600 °C in terms of C^* correlated with the time to crack initiation at Δa = 0.2 mm. The upper and lower bound NSW prediction bounds are given in dashed lines for the weldment zones of BM, HAZ and WM.

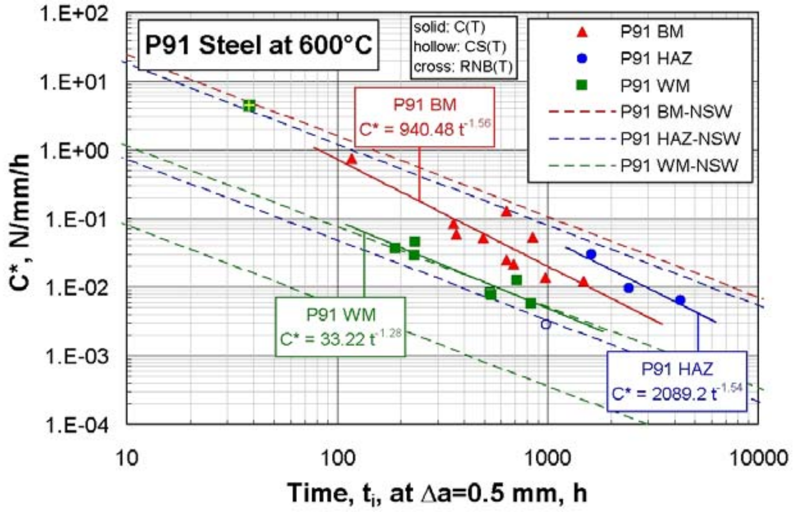

Figure 5.54. Creep crack initiation resistance of P91 weldment zones at 600 °C in terms of C^* correlated with the time to crack initiation at Δa = 0.5 mm. The upper and lower bound NSW prediction bounds are given in dashed lines.

There is no significant effect of specimen geometries (C(T) and CS(T)) on the CCI behaviour of P91 steel weldment at 600 °C. However, crack initiation time obtained on RNB(T) specimen with high constraint lie away from the data from C(T) and CS(T) specimen geometries. Therefore, RNB(T) data is not included in fitting of power function curves to the data which define the trend of crack initiation resistance of material needed for structural assessment of components. RNB(T) data may be used for specific component assessment with similar loading conditions. The CCI behaviour of P91 weldments are correlated with

K^c_{mat}, presented in Figures 5.55-5.56. The data ranking for the weldment zones is similar to those of K correlation. In terms of CCI studies K^c_{mat} does not seem to offer any advantage over the K. However, K^c_{mat} is required for component assessment using TDFAD approach.

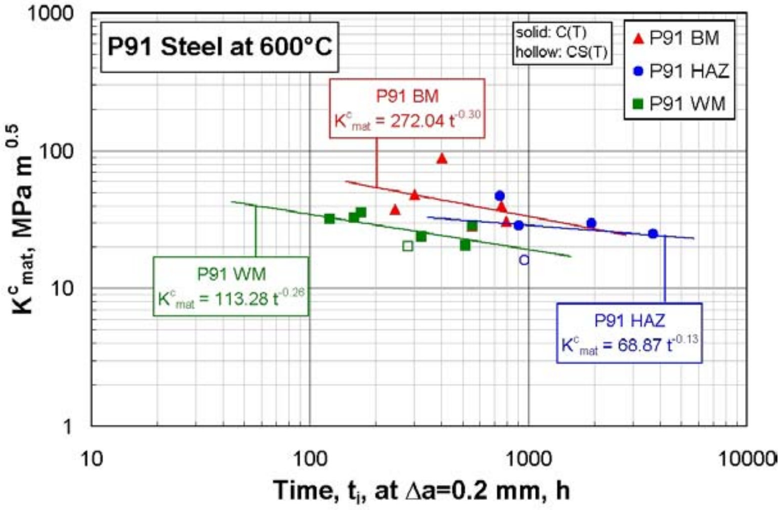

Figure 5.55. Crack initiation resistance of P91 weldment zones at 600 °C in terms of K^c_{mat} correlated with the time to crack initiation at $\Delta a = 0.2$ mm.

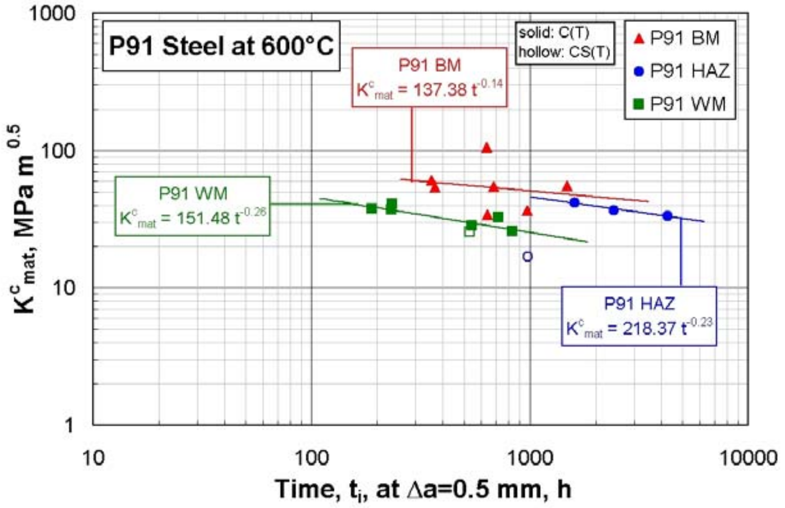

Figure 5.56. Crack initiation resistance of P91 weldment zones at 600 °C in terms of K^c_{mat} correlated with the time to crack initiation at $\Delta a = 0.5$ mm.

5.2.5 Creep Crack Initiation and Growth Tests Data Analyses

The testing and evaluation of data for creep crack growth studies is well established in the field of time dependent high temperature fracture mechanics [3,6]. The experimental creep crack initiation and growth data were obtained from the fracture mechanics tests of specimen with different geometries. The details of tested specimen geometries are given in Appendix B.6. The test data are analysed and evaluated in order to determine the crack tip parameters K and C^* following the procedure described in Section 4.2.7. Crack growth rate, da/dt, is correlated with the crack tip parameters for the different weldment zones of P22 steel at 550 °C, and P91 steel at 600 °C as presented in Sections. 5.2.5.1 and 5.2.5.2. The plots showing each single specimen with details are also provided. Specimen test details are given in the legends including specimen code, geometry, width (W), gross thickness (B), net thickness (B_n) and loading mode (“Fconst” for constant load test, “CDR” for constant displacement rate test), consecutively.

The detailed analyses of test data include CCG rate correlated with the crack tip parameter C^*, (i) using the complete dataset and (ii) the data after the CCI (Δa>0.2 mm and 0.5 mm). The data from early crack extension up to crack growth initiation (Δa>0.5 mm) (i.e. tails) are correlated with K for transition creep crack growth assessment. The NSW model plane stress and plane strain predictions from Equation 2.36 are superimposed on the CCG correlation diagrammes. The material properties given in Table 3.2 are used for the NSW prediction upper and lower bounds.

A relationship between CCG rate and the crack tip parameters, K and C^* are represented by power laws on log/log plots [19,114].

$$\dot{a} = A'K^{m'} \tag{5.1}$$

$$\dot{a} = D_o C^{*\phi} \tag{5.2}$$

where A', D_o, m', and ϕ are material constants. Steady-state creep is achieved when a fully developed creep stress distribution is produced at the farfield of a crack tip. Therefore, a power function curve is fitted to each correlation by use of the least squares fit regression method in order to determine the above material constants. The fitted data are extrapolated for long time material behaviour in different weldment zones.

The CCG rate correlates well with C^* in the steady state extensive creep range (e.g. where stress redistribution is completed) beyond the crack initiation defined at crack extension at Δa>0.2 mm. From the correlations of CCG rate with K and C^*, the material constants, A', D_o, m', and ϕ are determined as given in Table 5.8.

Table 5.8. Material constants A', D_o, m', and ϕ, which are obtained from HT CCG test results of weldment zones of P22 steel at 550 °C and P91 steel at 600 °C.

Material	A'	m'	D_o	ϕ
P22 BM	9.0E-12	6.33	0.024	0.80
P91 BM	3.0E-12	6.49	0.030	0.75
P22 HAZ	2.0E-12	7.34	0.068	0.91
P91 HAZ	7.0E-15	9.30	0.098	1.02
P22 WM	3.0E-13	7.35	0.027	0.85
P91 WM	8.0E-12	6.78	0.170	0.97

5.2.5.1. Creep Crack Growth Behaviour of P22 Steel Weldment

High temperature crack growth data determined on P22 steel weldments at 550 °C are evaluated and the CCG rate is correlated with crack tip parameters K and C^*. The C^* correlation of crack growth rate include complete datasets along with reduced datasets excluding so called "tails" or early crack extension (Δa>0.2 mm). Early crack extension data covers the crack incubation and transition creep prior to steady state CCG where stress redistribution is not completed. CCG rate correlations for P22 BM, P22 HAZ and P22 WM are given in Figures 5.57 to 5.60, 5.61 to 5.64 and 5.65 to 5.71, respectively. Reduced data correlates well with C^*. The RNB(T) data is singled out, not fitting the rest of the data, that requires in-depth study and modelling of fracture behaviour.

The predicted plane stress and plane strain bounds using the NSW model are included in the correlation diagrams. The NSW predictions are not consistent for all weldment zones. Particularly, the predictions of P22 WM CCG behaviour direct attention to the need for revision of the model. This issue is being addressed by NSW authors that led to a modified NSW formula [115].

Comparing the CCG behaviour of different weldment zones of P22 steel at 550 °C, it is observed that P22 BM and P22 WM have very similar CCG resistance (See Table 5.8). However, P22 HAZ has a lower CCG resistance compared to the other weldment zones and its resistance decreases sharply, as also seen in the values of the exponent, ϕ.

Although the correlations with stress intensity factor, K, are consistent for earlier crack growth rates for all weldment zones of P22 steel at 550 °C, they lose their consistency at later stages of crack growth rates, hence, should not be used for correlation of CCG rate in extensive (steady state) creep range. Therefore, only the early crack extension data are correlated with K as seen in Figures 5.60, 5.64 and 5.71 for P22 BM, P22 HAZ and P22 WM, respectively. As in the C^* correlation, the RNB(T) specimens fall out of the general trend that requires in depth study of material behaviour and stress-state in loading.

Behaviour of P22 BM

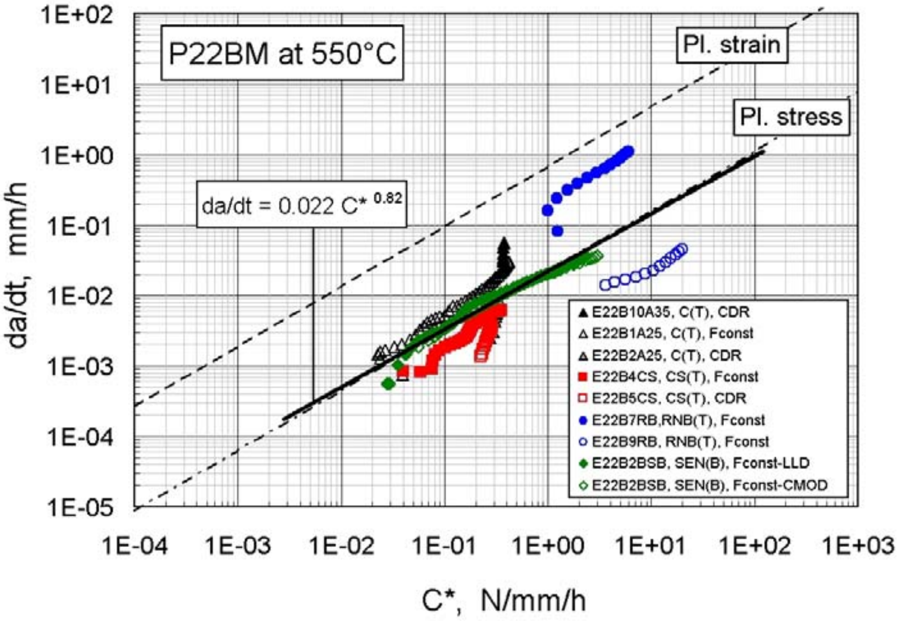

Figure 5.57. Correlation of CCG rate with C^* for P22 BM tested on different geometries (C(T), CS(T) and RNB(T)) specimens and loading conditions (F_{const} and CDR) at 550 °C. Complete test data points are included. The superimposed plane stress – plane strain prediction lines are determined from NSW model.

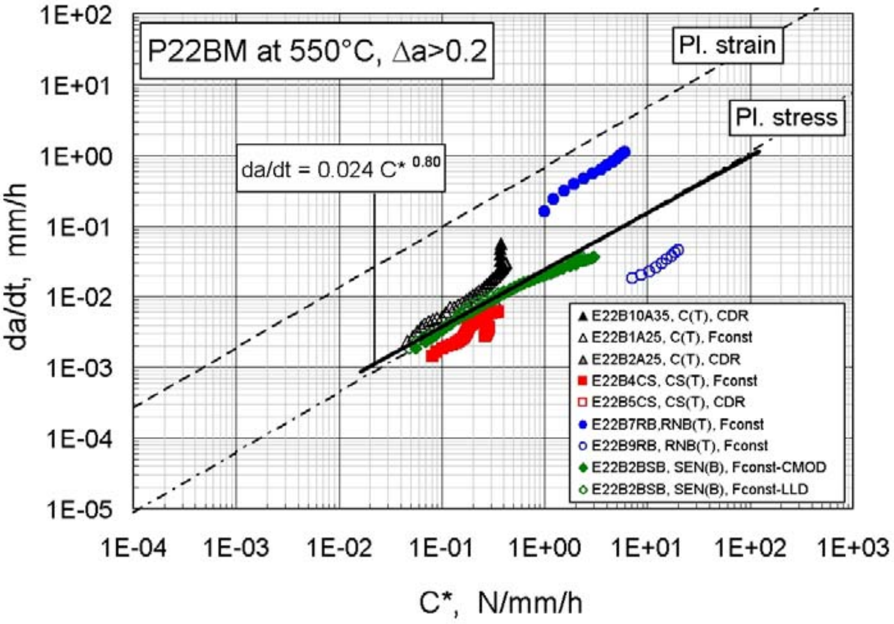

Figure 5.58. Correlation of CCG rate with C^* of P22 BM at 550 °C. Different specimens are shown with different symbols. Reduced data beyond CCI at Δa>0.2 mm, are included. The superimposed plane stress and plane strain prediction lines are determined from the NSW model.

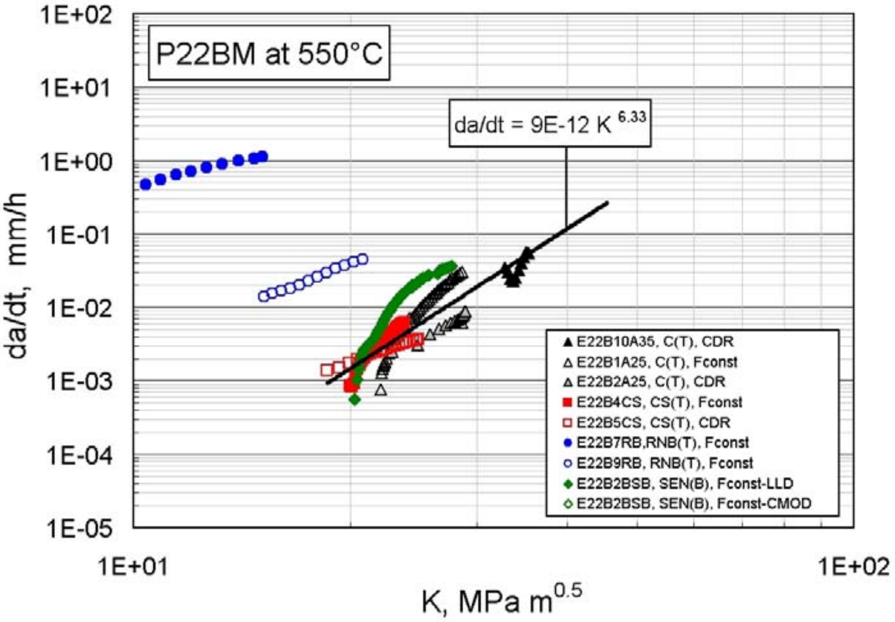

Figure 5.59. Correlation of CCG rate with K for different specimens of P22 BM tested at 550 °C. Specimens with different geometry and loading mode are shown with different symbols. Complete test data points are included.

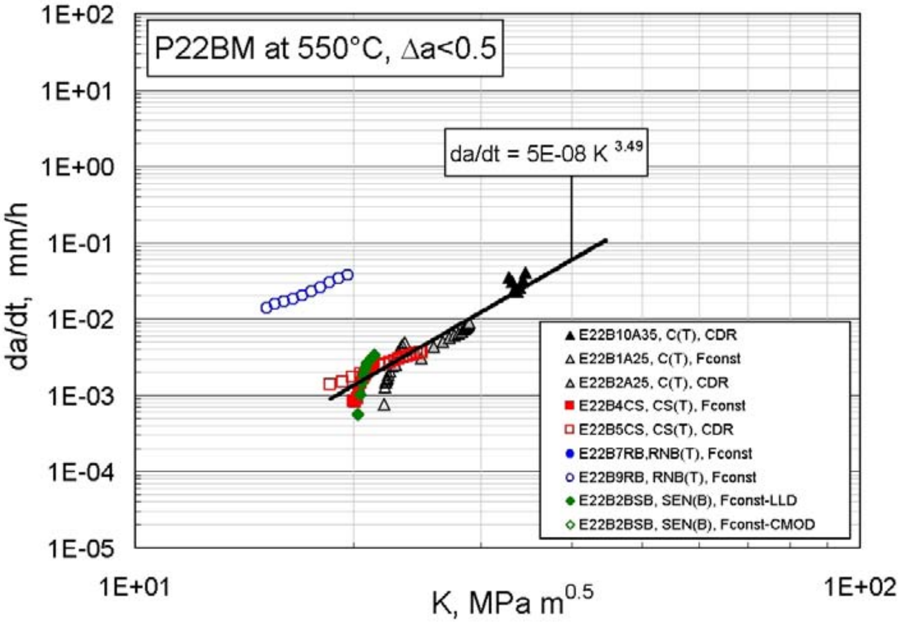

Figure 5.60. Correlation of crack growth rate with K for different specimens of P22 BM tested at 550 °C. Different specimens are shown with different symbols. Reduced data points prior to crack initiation at Δa=0.5 mm are included.

Behaviour of P22 HAZ

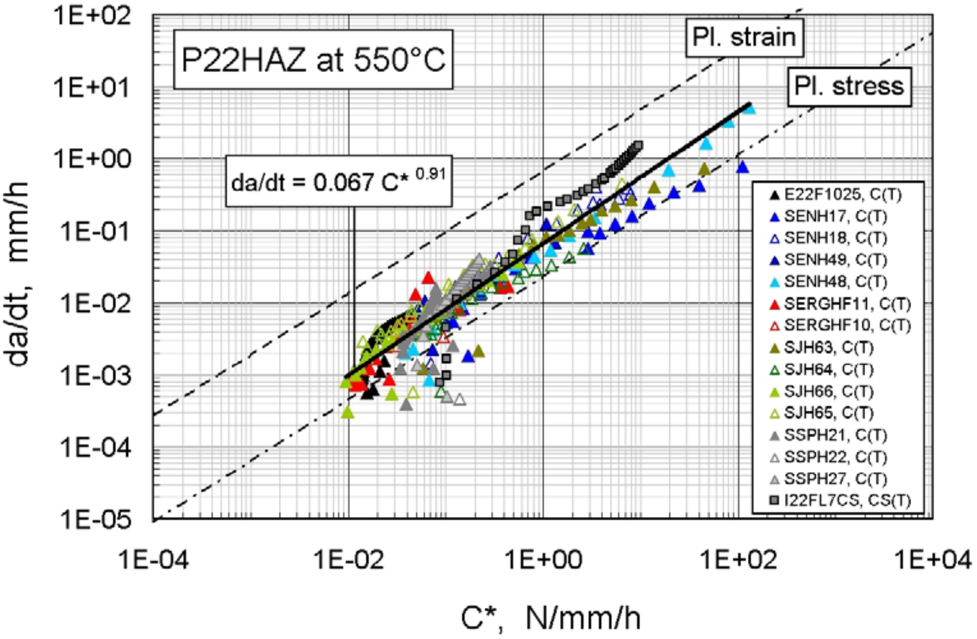

Figure 5.61. Correlation of CCG rate with C^* for P22 HAZ at 550 °C. Complete test data points are included. C(T) and CS(T) specimens are tested under constant load. The plane stress – plane strain prediction lines are determined from NSW model.

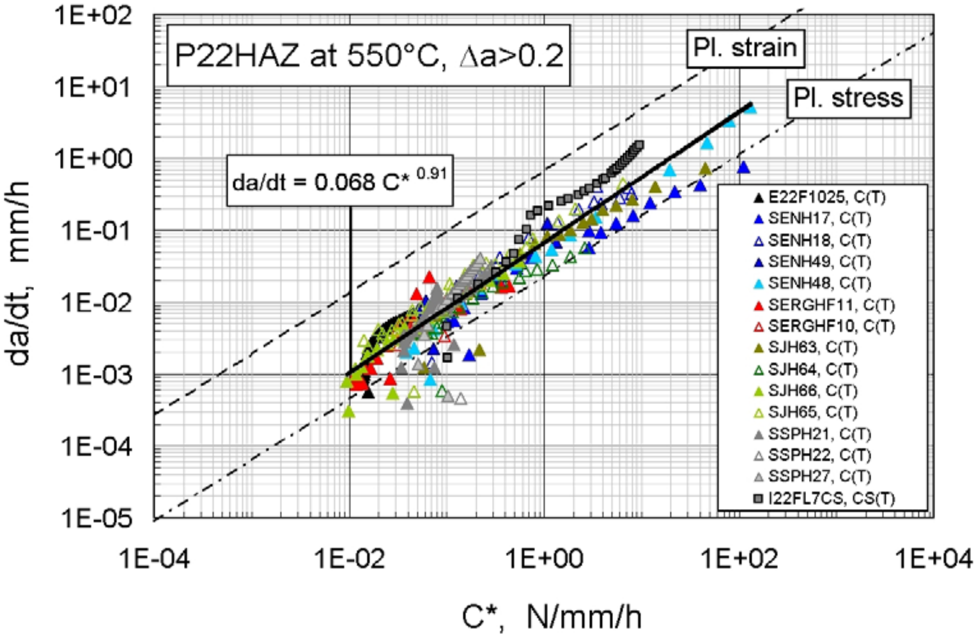

Figure 5.62. Correlation of CCG rate with C^* for P22 HAZ at 550 °C. Reduced data points beyond CCI (Δa>0.2 mm) are included. C(T) and CS(T) specimens are tested under constant load. The plane stress – plane strain prediction lines are determined from NSW model.

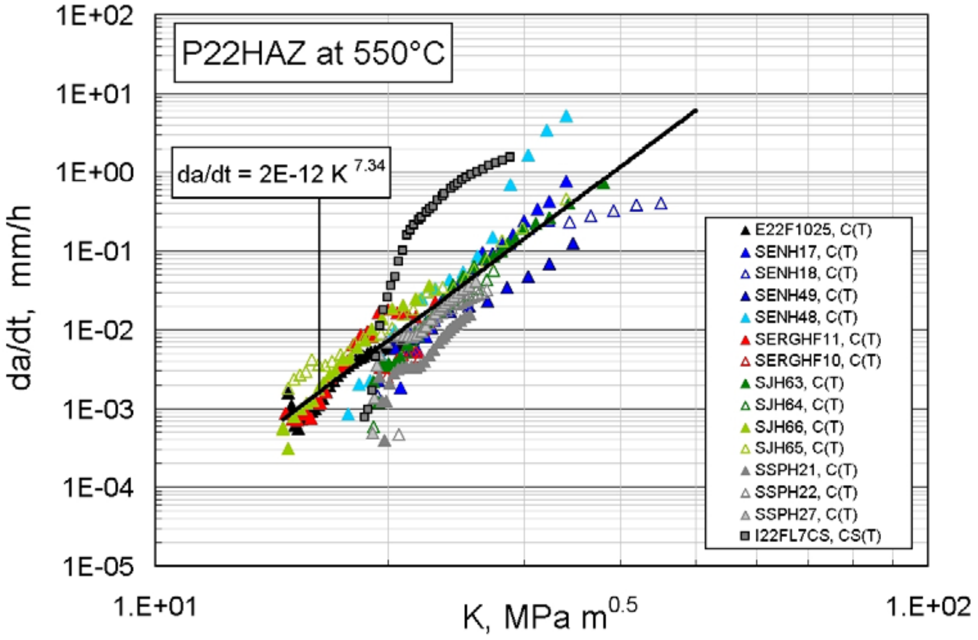

Figure 5.63. Correlation of CCG rate with K for different specimens of P22 HAZ tested under constant load at 550 °C. Complete test data points are included.

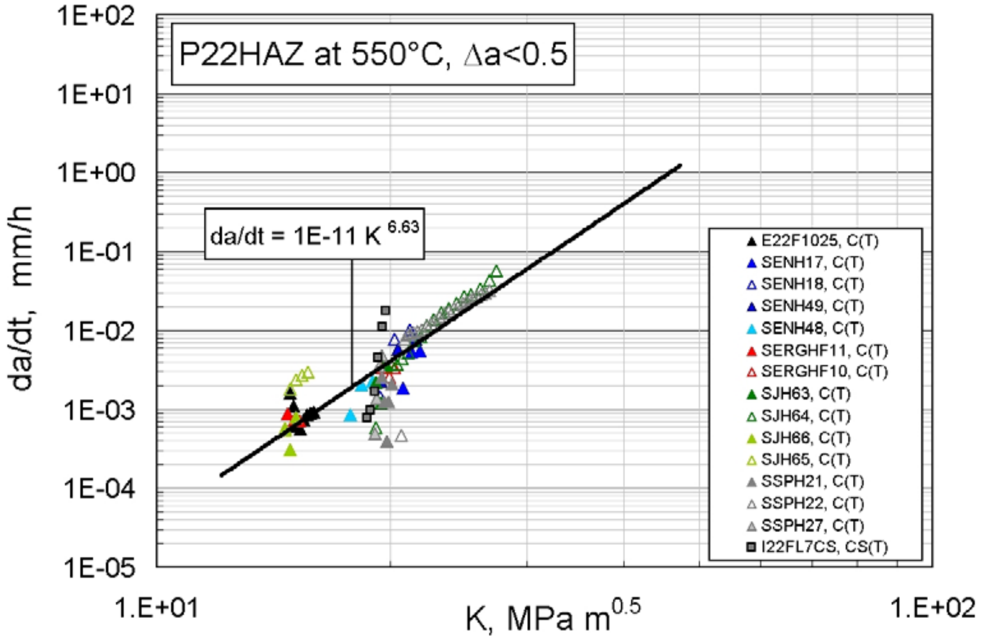

Figure 5.64. Correlation of crack growth rate with K for specimens of P22 HAZ tested under constant load at 550 °C. Reduced data points prior to crack initiation at Δa=0.5 mm are included.

Behaviour of P22 WM

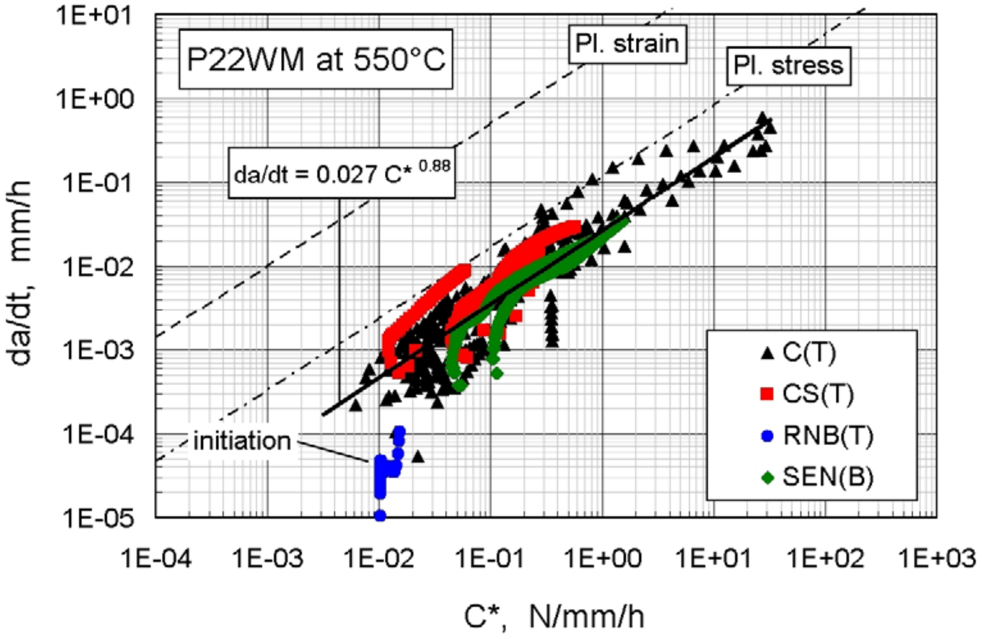

Figure 5.65. Correlation of CCG rate with C^* for P22 WM tested at 550 °C. Complete data points from various specimen geometries are included. The plane stress – plane strain prediction lines are determined from NSW model.

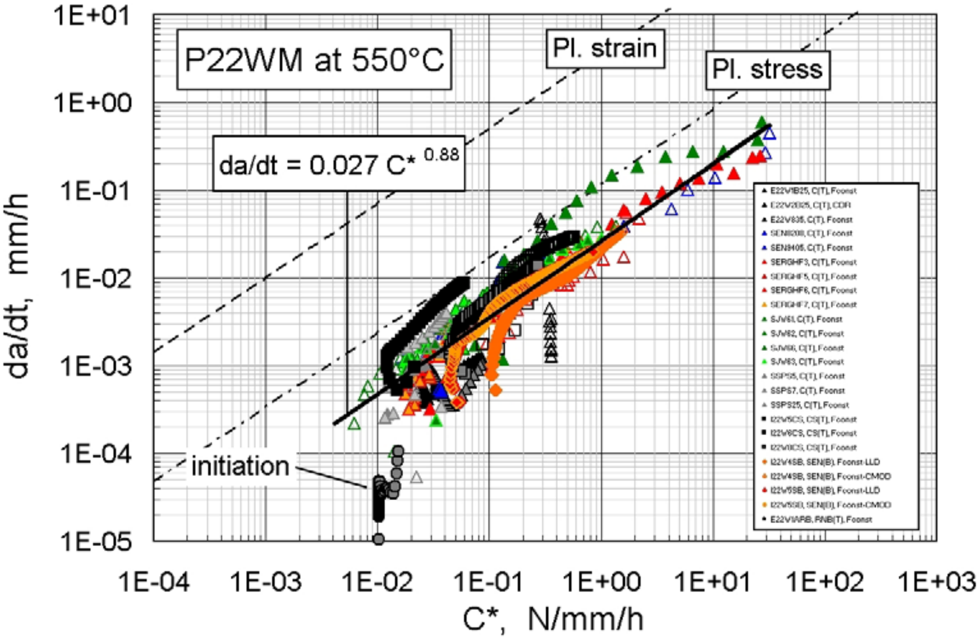

Figure 5.66. Correlation of CCG rate with C^* for P22 WM. Different specimen geometries (C(T), CS(T), RNB(T) and SEN(B)) are tested under different loading conditions of F_{const} and CDR at 550 °C. Complete test data points are included. The plane stress – plane strain prediction lines are determined from NSW model.

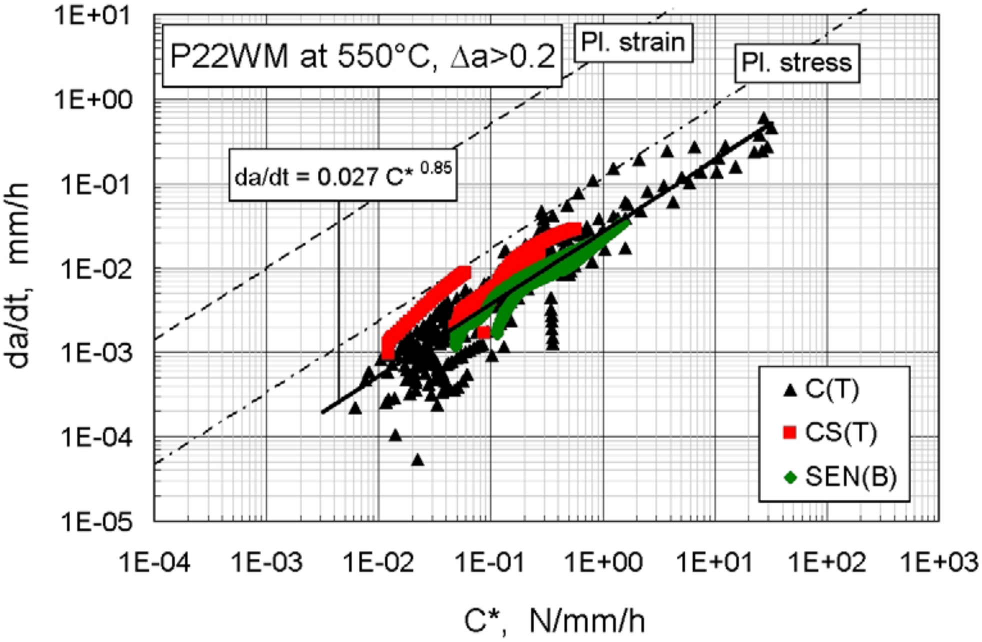

Figure 5.67. Correlation of CCG rate with C^* for P22 WM tested at 550 °C. Reduced data points from various specimen geometries (C(T), CS(T) and SEN(B)) after CCI (Δa>0.2 mm) are included.

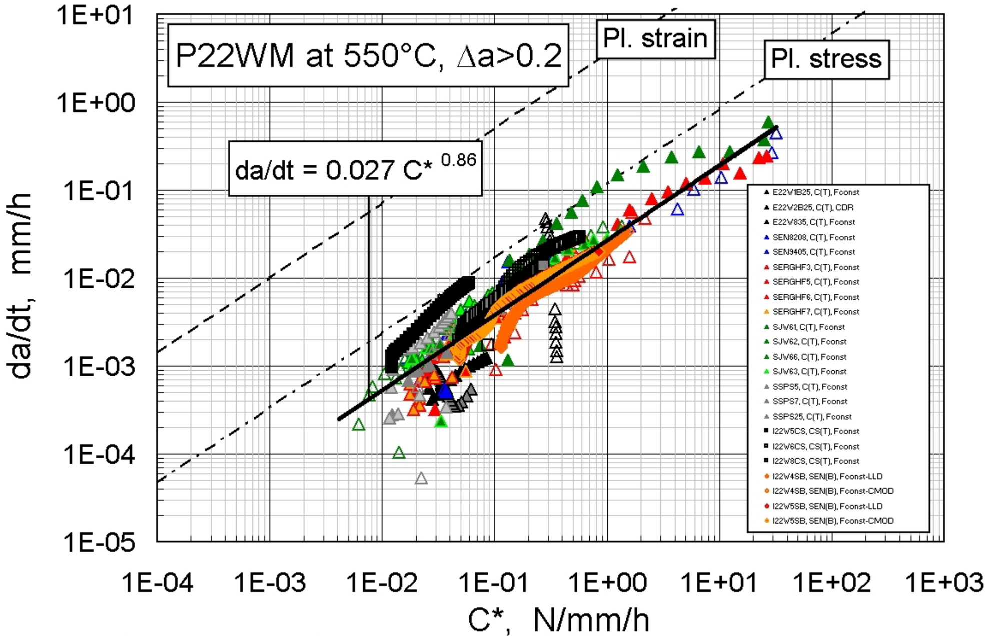

Figure 5.68. Correlation of CCG rate with C^* for C(T), CS(T) and SEN(B) specimens of P22 WM tested under different conditions of F_{const} and CDR at 550 °C. Reduced data points after CCI ($\Delta a > 0.2$ mm) are included. The plane stress – plane strain prediction lines are determined from NSW model.

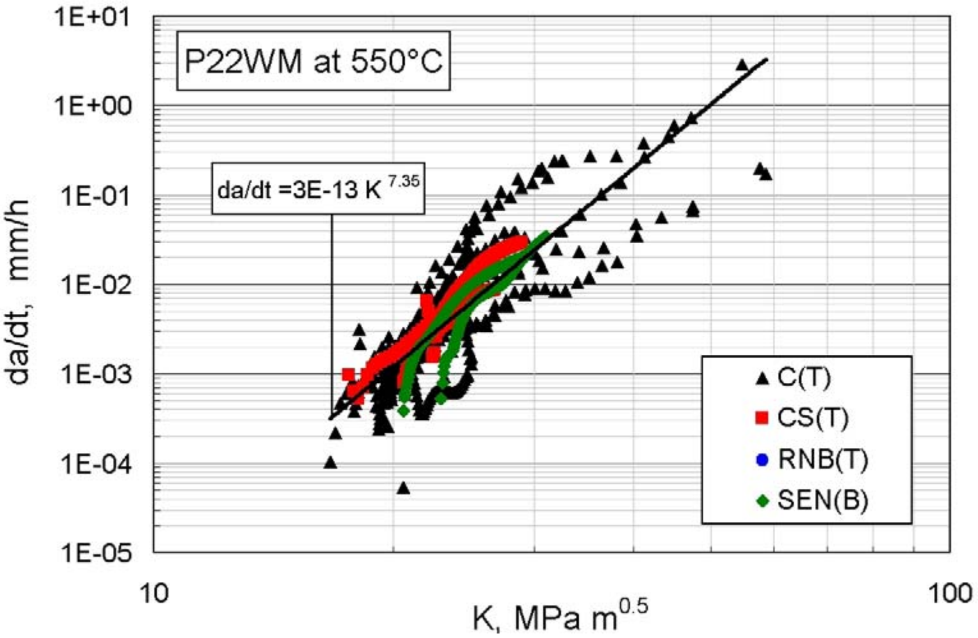

Figure 5.69. Correlation of CCG rate with K for P22 WM tested at 550 °C. Complete test data points from various specimen geometries are included.

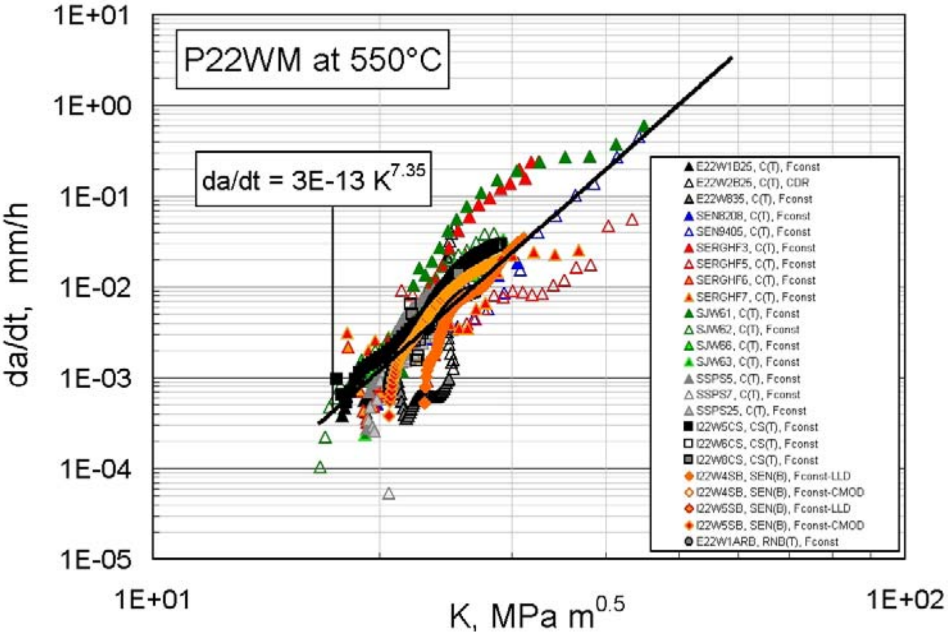

Figure 5.70. Correlation of CCG rate with K for P22 WM. Specimens with different loading geometries under different loading conditions are tested at 550 °C. Complete test data points are included.

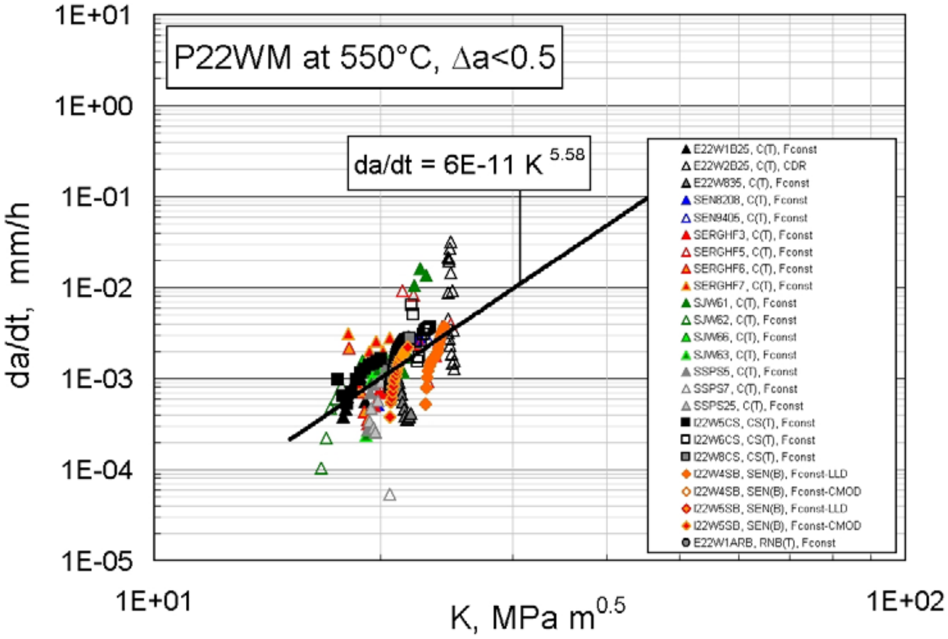

Figure 5.71. Correlation of crack growth rate with K for P22 WM tested at 550 °C. Different specimen geometries and loading conditions are shown. Reduced data points prior to crack initiation at Δa=0.5 mm are included.

5.2.5.2. Creep Crack Growth Behaviour of P91 Steel Weldment

High temperature crack growth data are determined on specimens from P91 steel weldments at 600 °C. The data are evaluated and CCG rate is correlated with crack tip parameters K and C^*. Crack growth rate correlations with C^* for complete dataset and also for the reduced dataset by excluding the crack incubation data points up to crack extension, $\Delta a > 0.2$ mm, are plotted. The reduced datasets exclude the data points from transition, so-called "tails", prior to steady state creep of deformation. The crack growth correlations for P91 BM, P91 HAZ and P91 WM are given in Figures.5.72 to 5.75, 5.76 to 5.79 and 5.80 to 5.86, respectively.

The plane stress and plane strain crack growth correlation boundaries are predicted using the Equation 2.36 based on the NSW creep crack growth model as explained in Section 2.1.4.4. The material properties given in Table 3.2 are used in these prediction calculations. The plane stress predictions are closer to the experimental data for P91 BM and P91 HAZ which lie very close to the plane stress bound, whereas the data for P91 WM lies below the plane stress prediction. This observation on P91 WM points out the need for modification of the NSW model [115]. Further observations include the rather good correlation of crack growth rate data with C^* whereas higher scatter is seen in K correlations. The sources of data scatter can be examined by metallographic study of test specimens for the location of crack initiation with associated microstructural component and crack growth path deviation as seen in Figures 5.76 and 5.82. The test data which is lower than the plane stress prediction values are obtained from a test where crack deviated after crack initiation. Note also that the CCG behaviour of the RNB(T) specimen, I91W5ARB, of P91 WM deviates from the rest of the data with similar crack growth rate slope in C^* correlations in Figure 5.81. This is due to the applied load level that is higher than the other specimen geometries. If the load level is corrected, the data collates with the rest of the data as expected from the slope of the correlation. Therefore, the RNB(T) data are not included in the determination of the CCG rate trendline shown in Figures 5.80 to 5.86. Similarly, the C(T) specimen of P91 HAZ, PHAZ2 in Figure 5.76 deviates from the rest of the data due to crack path deviation, hence invalid data according to the test standard [3]. Therefore, it is not included in the determination of the prediction lines for the CCG rate correlation with C^*.

Comparison of the CCG behaviour of different weldment zones of P91 steel shows that P91 BM is the most CCG resistant with lower creep exponent whereas the P91 WM is the least CCG resistant. Furthermore, the CCG resistance of P91 HAZ decreases at a higher rate than any other weldment zone as the values of CCG rate exponent, ϕ, given in Table 5.8, indicate.

Similar to the results obtained on P22 steel weldments, in correlations of CCG rate with stress intensity factor, K, high scatter is seen in all weldment zones. The correlation of data from early crack growth also shows considerable scatter. The present data direct attention to statistical treatment of such data to derive a sound conclusion of material behaviour, for reliable data to be used for component assessment.

Behaviour of P91 BM

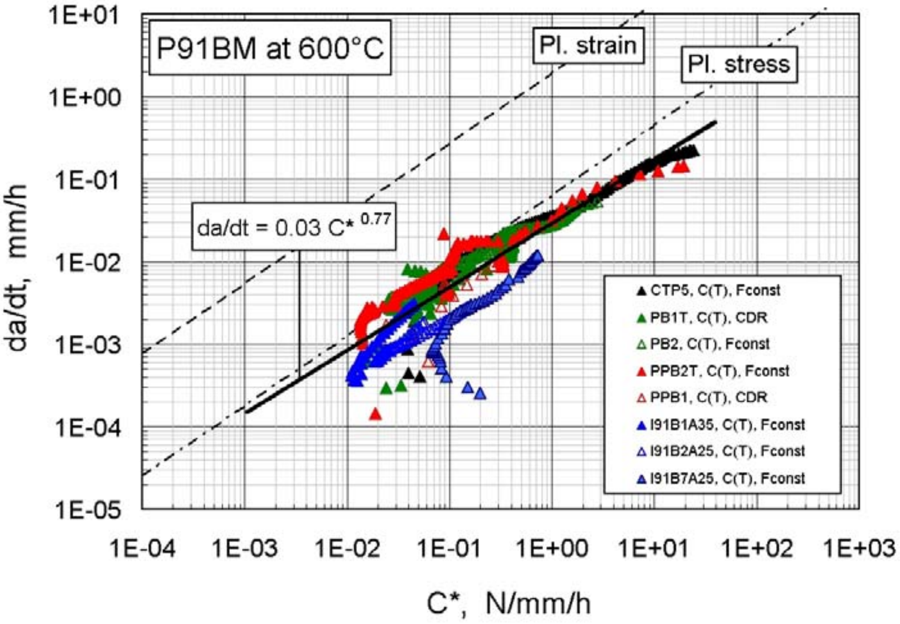

Figure 5.72. Correlation of CCG rate with C^* for C(T) specimens of P91 BM tested under different conditions of F_{const} and CDR at 600 °C. Complete test data points are included. The plane stress – plane strain prediction lines are determined from NSW model.

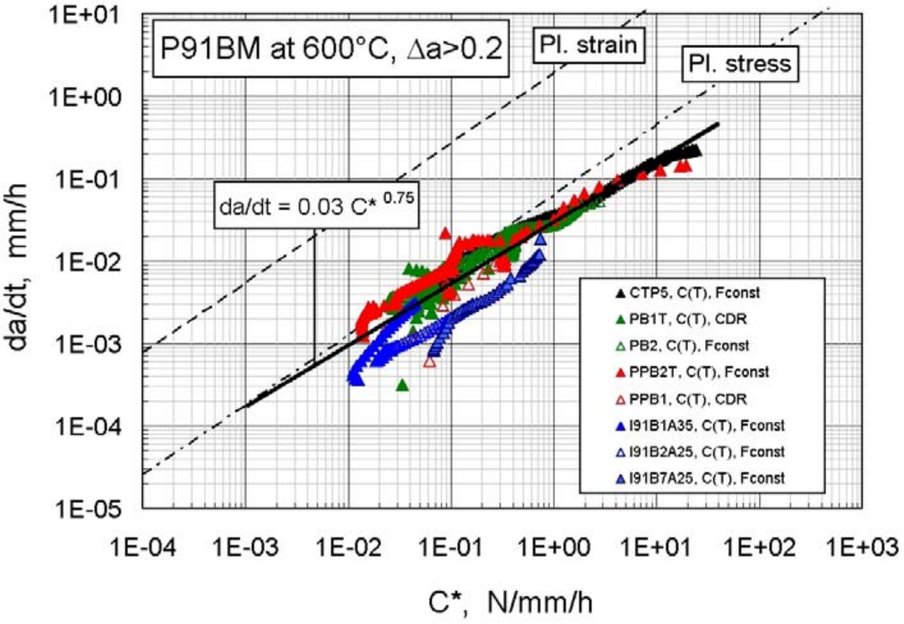

Figure 5.73. Correlation of CCG rate with C^* for P91 BM tested under different loading conditions at 600 °C. Reduced data beyond CCI at $\Delta a > 0.2$ mm are included. The plane stress – plane strain prediction lines determined from NSW model are included.

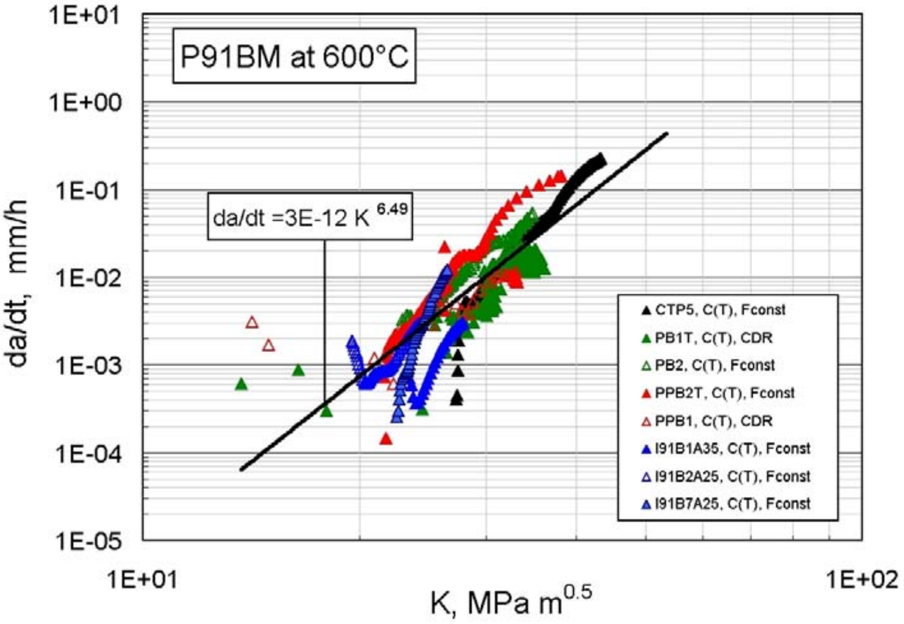

Figure 5.74. Correlation of CCG rate with K for P91 BM tested under different loading conditions at 600 °C. Complete test data points are included.

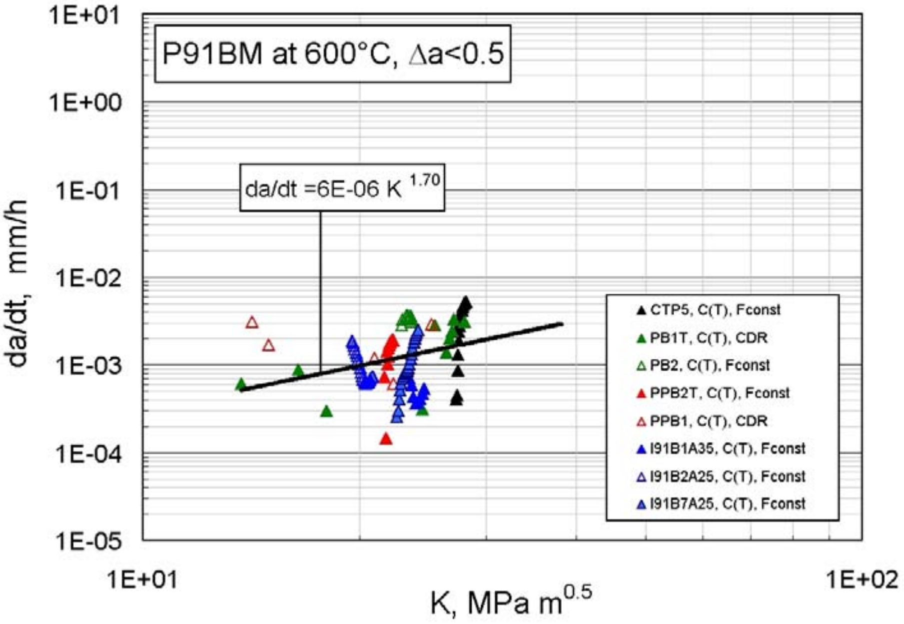

Figure 5.75. Correlation of crack growth rate with K for P91 BM tested under different loading at 550 °C. Reduced data points prior to crack initiation at Δa=0.5 mm are included.

Behaviour of P91 HAZ

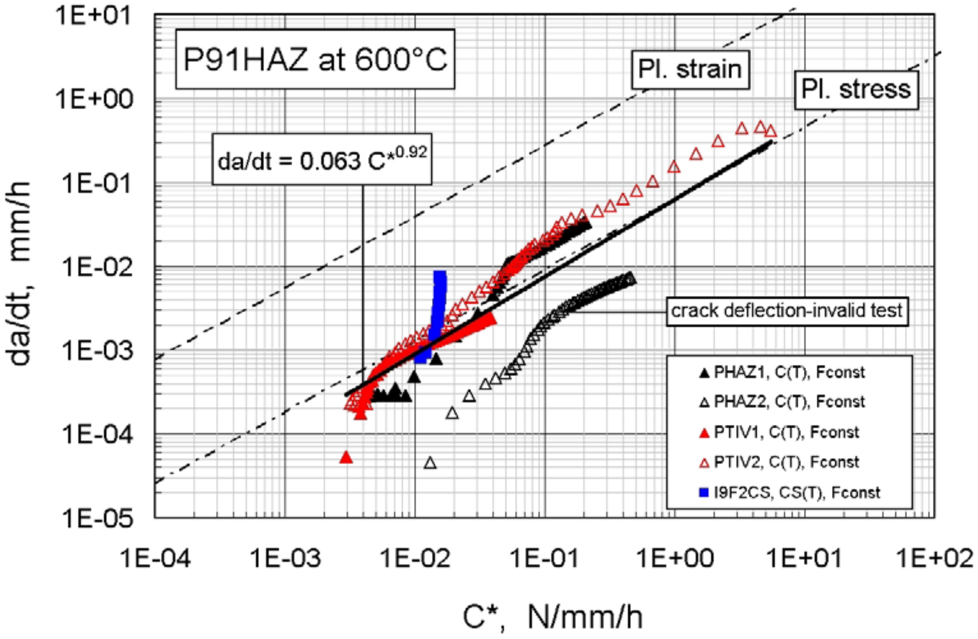

Figure 5.76. Correlation of CCG rate with C^* for P91 HAZ tested under constant load at 600 °C. Complete test data from coarse grain HAZ and Type IV (TIV) are included. The plane stress – plane strain prediction lines are determined from NSW model.

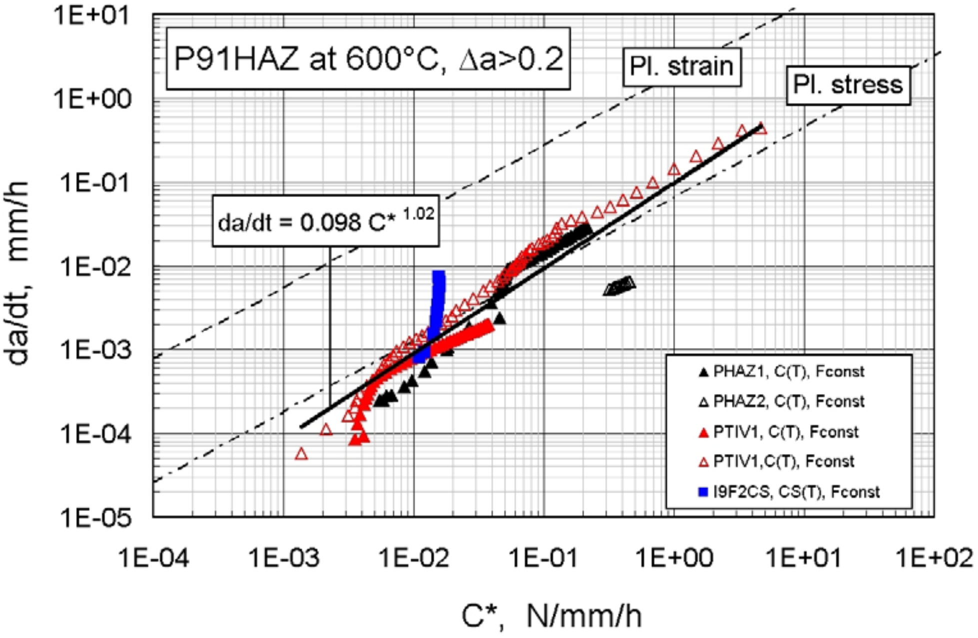

Figure 5.77. Correlation of CCG rate with C^* for P91 HAZ tested under constant load at 600 °C. Reduced data obtained after CCI, Δa>0.2 mm, from coarse grain HAZ and Type IV (TIV) are included. The plane stress – plane strain prediction lines are determined from NSW model.

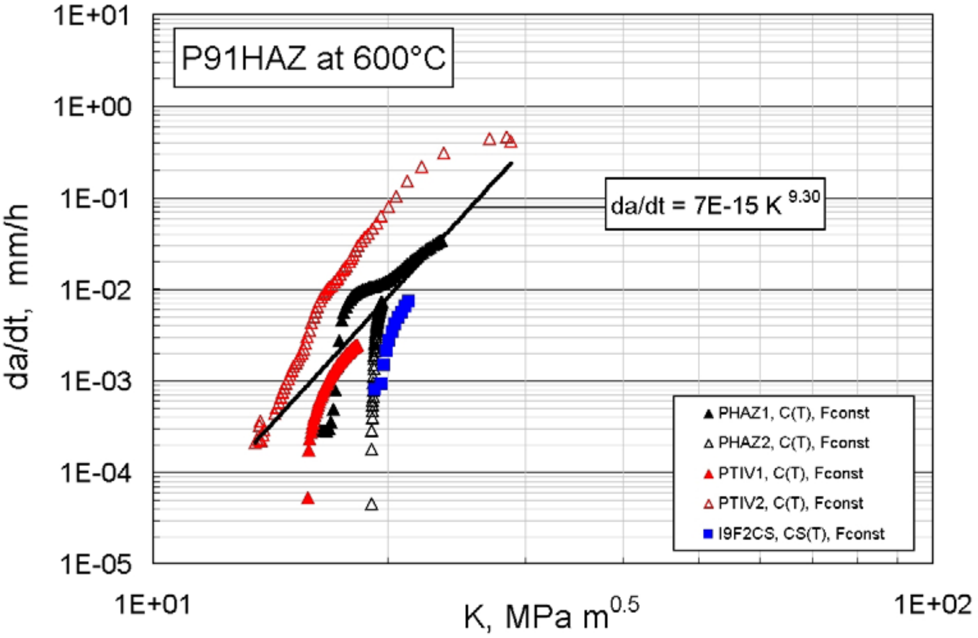

Figure 5.78. Correlation of CCG rate with K for P91 HAZ tested under constant load at 600 °C. Complete test data from coarse grain HAZ and Type IV (TIV) are included.

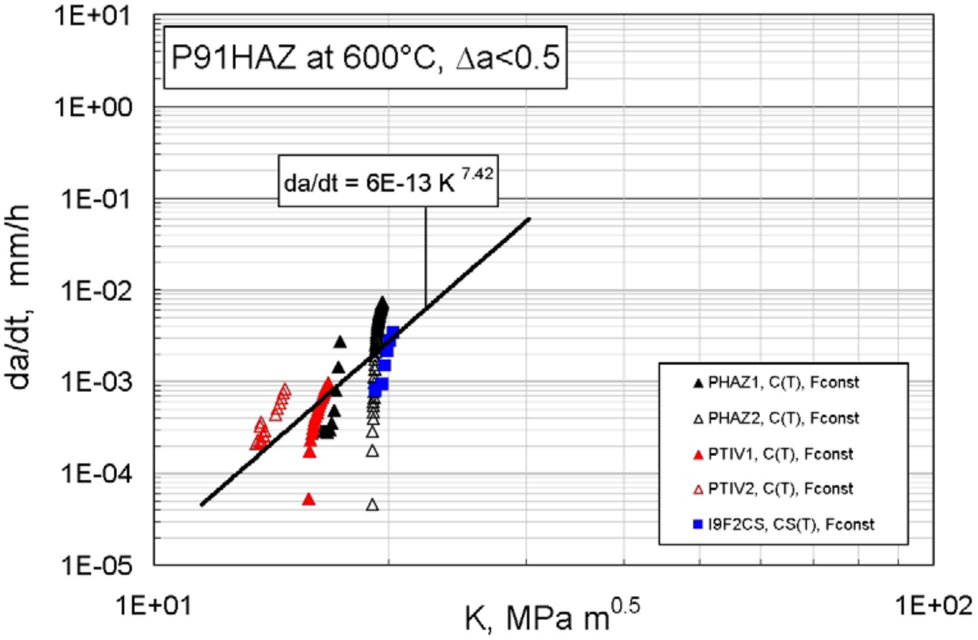

Figure 5.79. Correlation of crack growth rate with K for P91 HAZ tested at 550 °C. Reduced data points prior to crack initiation at Δa=0.5 mm are included.

Behaviour of P91 WM

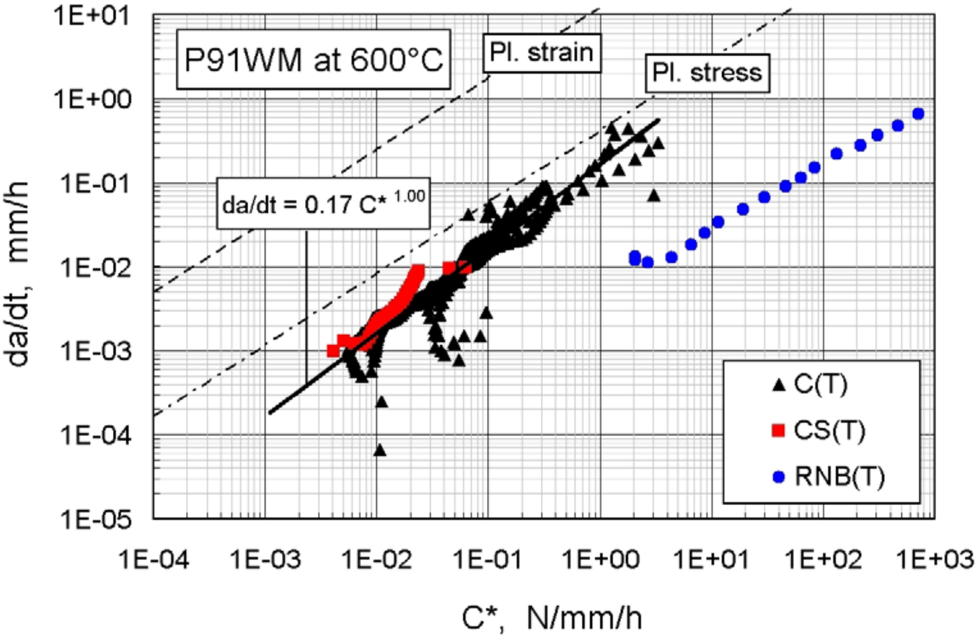

Figure 5.80. Correlation of CCG rate with C^* for P91 WM at 600 °C. Complete test data from different specimen geometries are plotted.

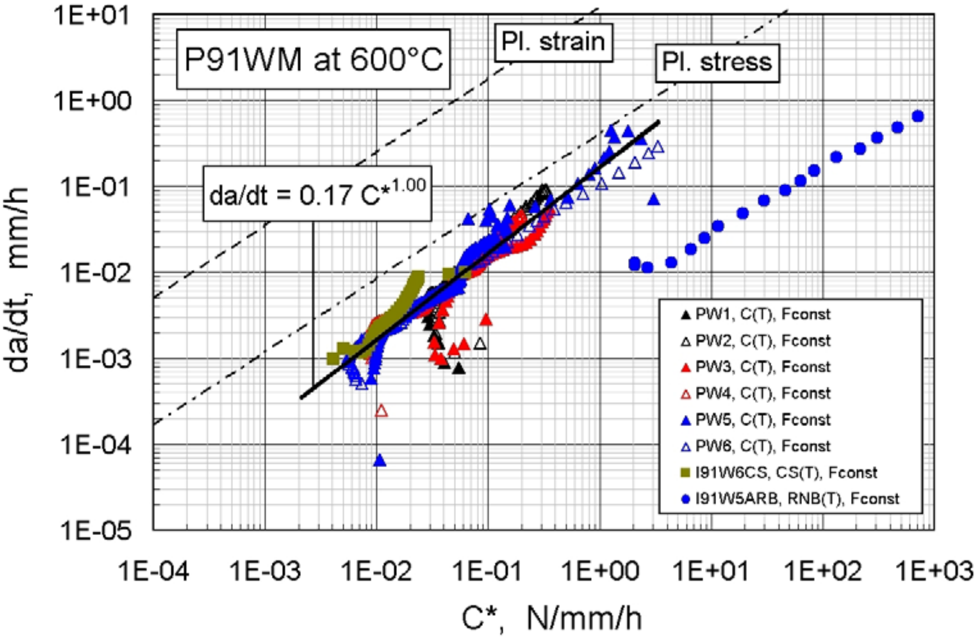

Figure 5.81. Correlation of CCG rate with C^* for P91 WM determined from tests under constant load on C(T), CS(T) and RNB(T) specimens at 600 °C. The plane stress – plane strain prediction lines are determined from NSW model. Note the similar slope of CCG correlation in RNB(T) specimen.

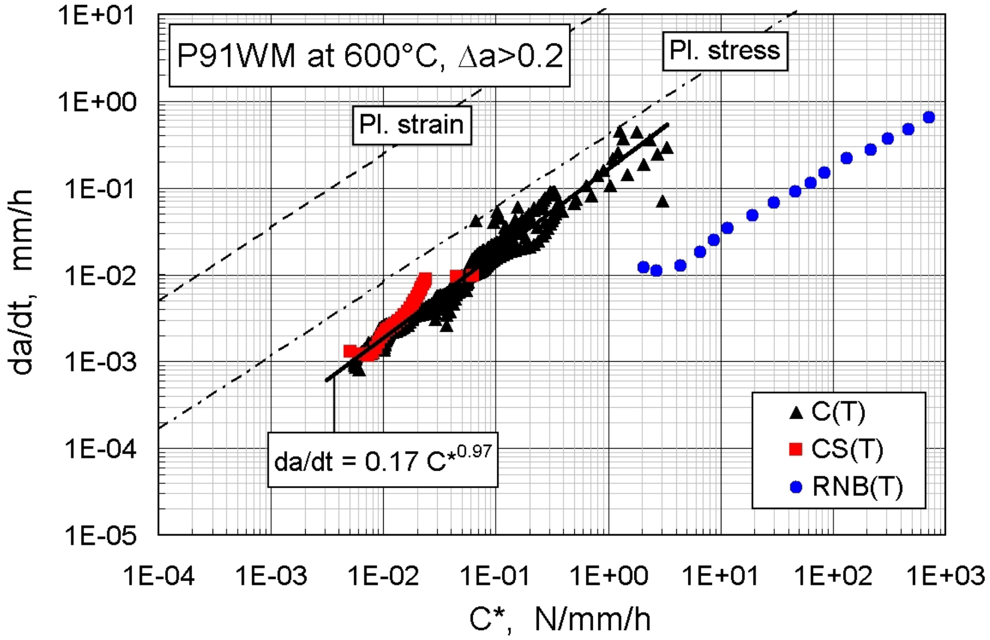

Figure 5.82. Correlation of CCG rate with C^* for P91 WM at 600 °C. Reduced data beyond CCI at Δa>0.2 mm are included.

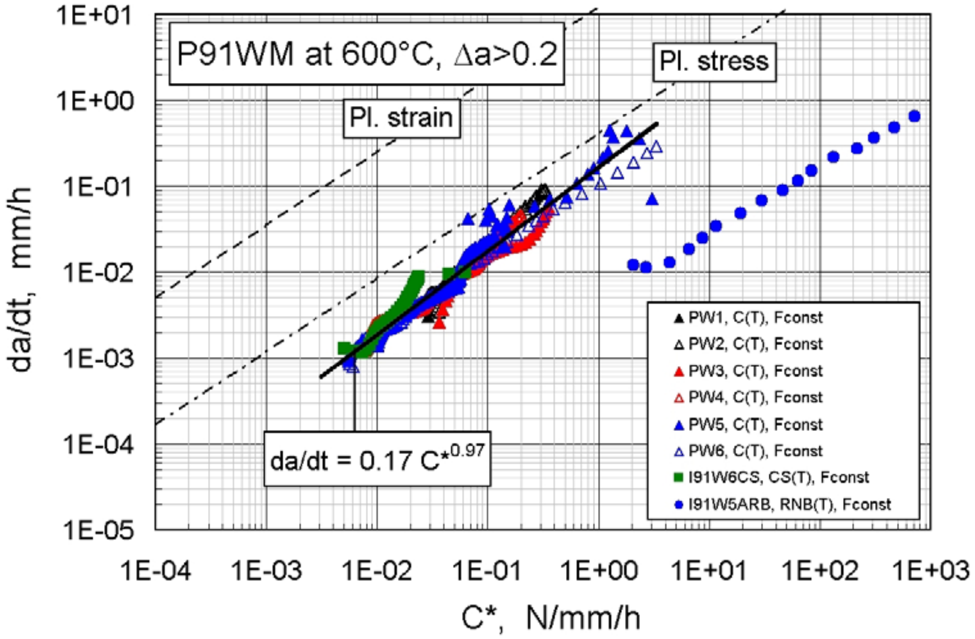

Figure 5.83. Correlation of CCG rate with C^* for P91 WM determined from tests under constant load on C(T), CS(T) and RNB(T) specimens at 600 °C. Reduced data beyond CCI at Δa>0.2 mm are included. The plane stress – plane strain prediction lines are determined from NSW model.

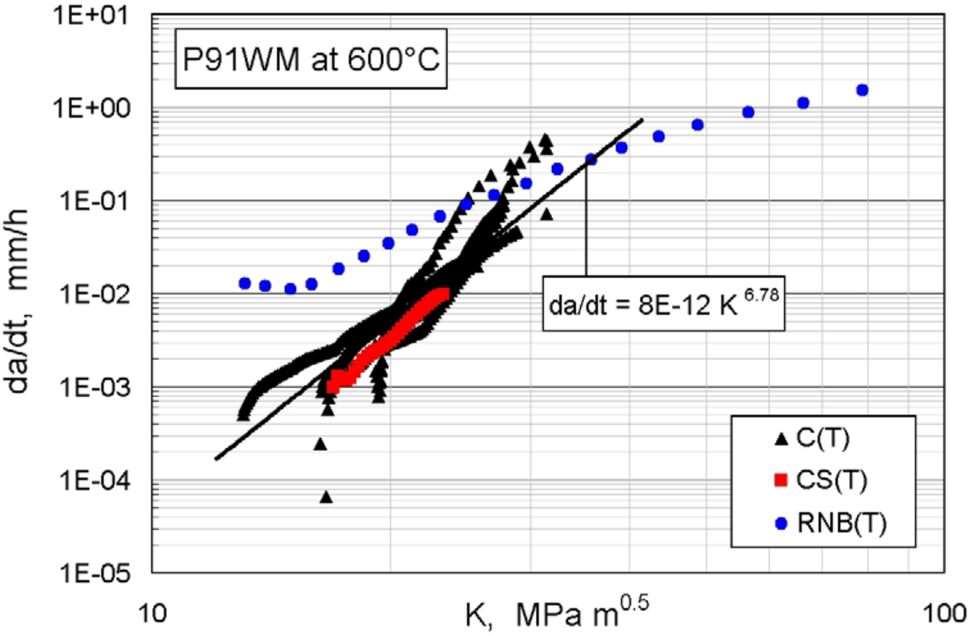

Figure 5.84. Correlation of CCG rate with K for P91 WM at 600 °C. Complete test data from C(T), CS(T) and RNB(T) specimens.

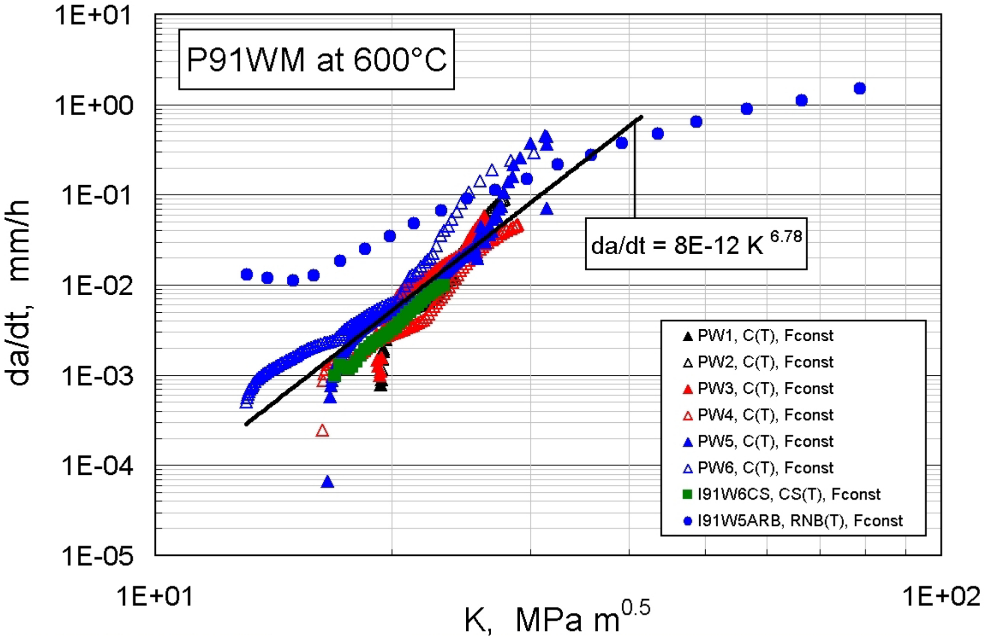

Figure 5.85. Correlation of CCG rate with K for P91 WM tested at 600 °C. Complete test data from different specimens tested under constant load.

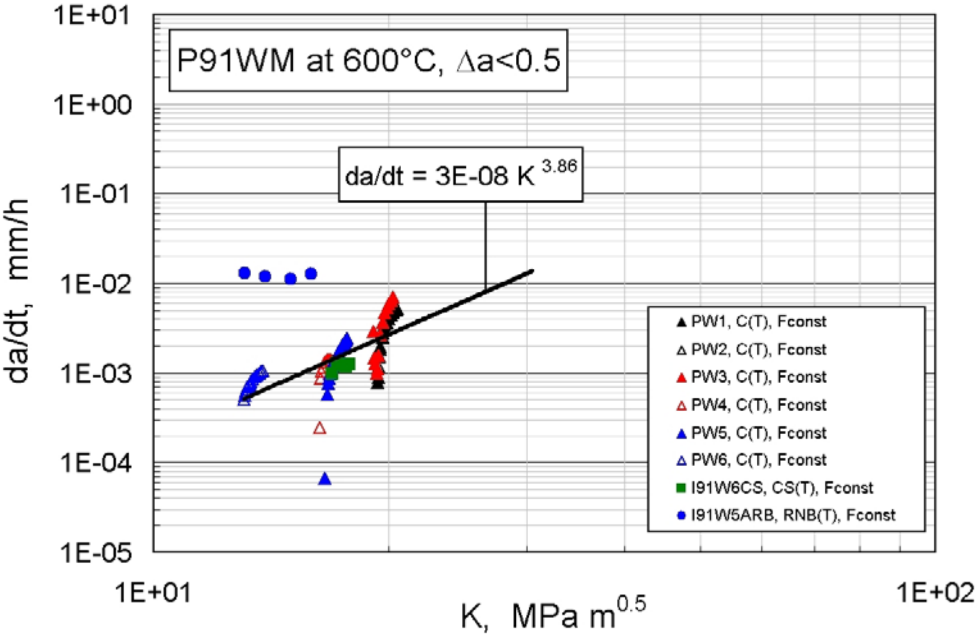

Figure 5.86. Correlation of crack growth rate with K for P91 WM tested under constant load on different specimen geometries at 550 °C. Reduced data points prior to crack initiation at Δa=0.5 mm are included.

5.2.6 Creep Master Curve Concept Applied to CCG Data of P22 and P91 Weldments

Master curve method was proposed for low temperature data analysis [116]. A similar approach is taken in the present study using the high temperature crack growth dataset obtained from tests on P22 and P91 weldments. A power function curve is fitted to the correlation of crack growth rate with crack tip parameter, C^*, by using least squares fit regression method to the dataset including reduced data where crack extension, Δa>0.2 mm. Figure 5.87 shows the creep master curve fitted to the above mentioned dataset.

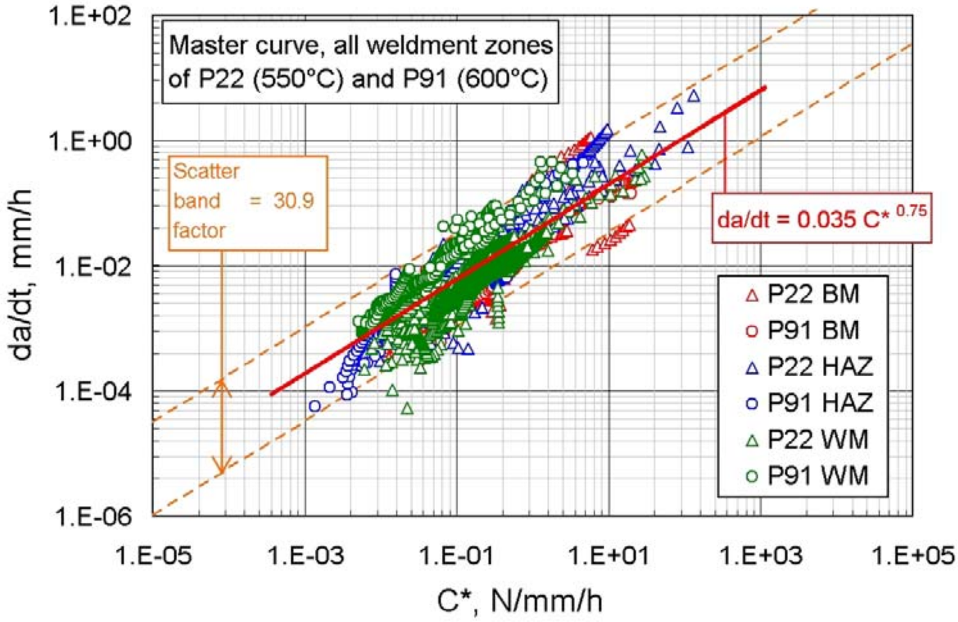

Figure 5.87. Master curve fitted to the dataset including the data from all weldment zones of P22 and P91 at 550 °C and 600 °C, respectively. Different weldment zones, BM (red), HAZ (blue) and WM (green) of P22 (triangle) and P91 (circle) are indicated separately.

The fitted power curve yields the following equation (Equation 5.3) to the correlation between crack growth rate and crack tip parameter, C^*,

$$\dot{a} = 0.035\, C^{*\,0.75} \tag{5.3}$$

which is in the form of Equation 5.2. The scatter band factor is determined as 30.9, which is smaller than the factor in plane stress – plane strain predictions. Note also the value of ϕ=0.75 which is slightly lower than that of the reported value for BM of 0.85.

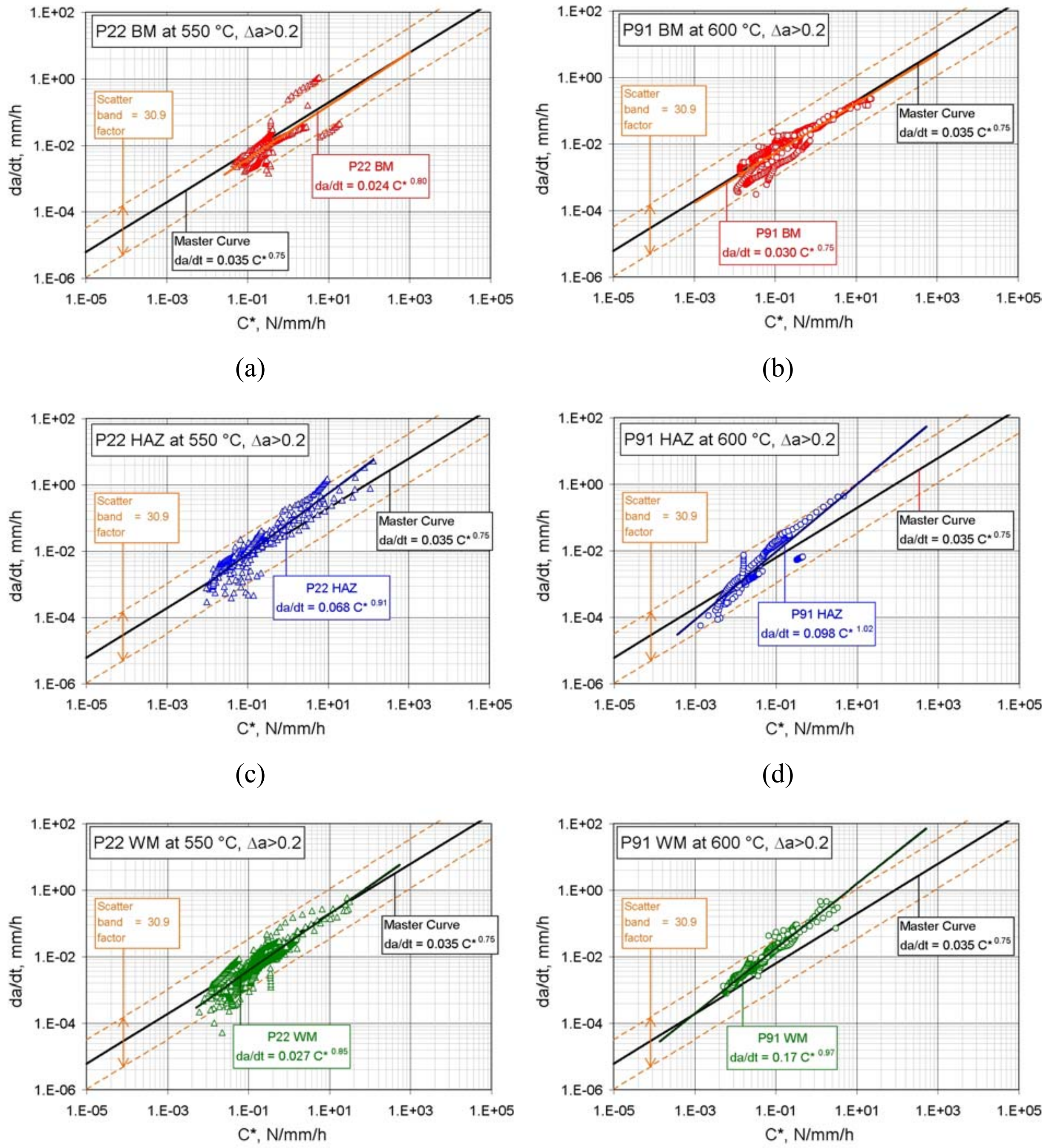

(a) (b)

(c) (d)

(e) (f)

Figure 5.88. Comparison of the master curve with the C^* correlations of the experimentally determined crack growth rates of (a) P22 BM, (b) P91 BM, (c) P22 HAZ, (d) P91 HAZ, (e) P22 WM and (f) P91 WM.

The obtained master curve is compared in Figure 5.88 with the individual C^* correlations of crack growth rate of each weldment zone of P22 and P91 at 550 °C and 600 °C, respectively. It is observed that as the master curve agrees very well with the C^* correlations of P22 BM, P22 WM and P91 BM. The CCG rate values are lower than that of the P22 HAZ, P91 HAZ and P91 WM at higher crack growth rates. Particularly, the C^* correlation of P91 BM complies excellently with the master curve. This is expected as the master curve concept is developed mainly for BM. For estimations for both P22 HAZ at 550 °C and P91 HAZ at 600 °C, which are known to be CCG critical weldment zones, master curve gives lower crack growth rate. However, the difference is small, therefore, considering the range of microstructures and specimen geometries, the approach is successful for future developments and applications.

Note that the master curve involved both P22 and P91 weldments estimates the crack growth rate satisfactorily at earlier crack growth rates, e.g. in the range of $10^{-4} - 10^{-2}$ mm/h. This range of crack growth rate has particular importance for engineering applications, such as component design and life estimation. An overview of applicability of master curve concept for CCG rate predictions for various weldment zones of P22 and P91 is shown in Figure 5.88. Deviation of master curve fit from individual test dataset is seen in P91 HAZ and P91 WM which needs further study to classify the high CCG rates determined with ϕ=1.02 and 0.97, respectively.

5.2.7 Failure Assessment Using TDFAD Method

The structural behaviour is studied using time dependent failure assessment (TDFAD) method to the high temperature crack growth data. The TDFAD curves are constructed following the procedure given in Section 2.3.3.1 with related creep and crack growth data. The curves are constructed for different service times of interest varying from t=0 h (R6-Option 2 [57]) to 10^5 h. For each specimen, the TDFAD parameters L_r (ligament damage) and K_r (crack tip damage) are calculated using the Equations. 2.70-2.71. The crack initiation is defined at engineering values of flaw size where crack extension of Δa=0.2 and 0.5 mm are considered. The creep crack initiation toughness, K^c_{mat}, curves of different weldments zones of P22 at 550 °C and P91 at 600 °C were presented in Sections 5.2.4.1 and 5.2.4.2. The TDFADs are constructed using these values. Prediction of failure at CCI using TDFAD approach is determined for service time up to 10^5 h. The predictions are compared with experimental data determined at crack extension of 0.2 and 0.5 mm.

Different shapes of the TDFADs constructed for different weldment zones direct attention to the ability of the methodology in describing the different CCI behaviour of weldments. Higher scatter is seen in experimental data of P91 weldment zones at failure initiation as seen on the TDFADs. This is in line with master curve results where P91 WM and HAZ deviates from the rest. It is also observed that the TDFAD method is relatively more conservative in estimating the CCI of P91 weldments zones compared to P22 weldment zones.

5.2.7.1. Application of the TDFAD to P22 Steel Weldment

The TDFAD curves are constructed and plotted for different weldment zones of P22 steel using the related creep and crack growth properties, as shown in Figures 5.89 to 5.91. The TDFAD parameters, L_r and K_r, are plotted for each specimen on the TDFADs for engineering definitions of CCI, at crack extensions of Δa=0.2 and 0.5 mm. Specimen geometry effects are observed particularly with respect to constraint and deformation behaviour as seen in C(T), CS(T), SEN(B) and RNB(T) specimens. Notch effect with increased local constraint is seen in C(T) and CS(T) specimens.

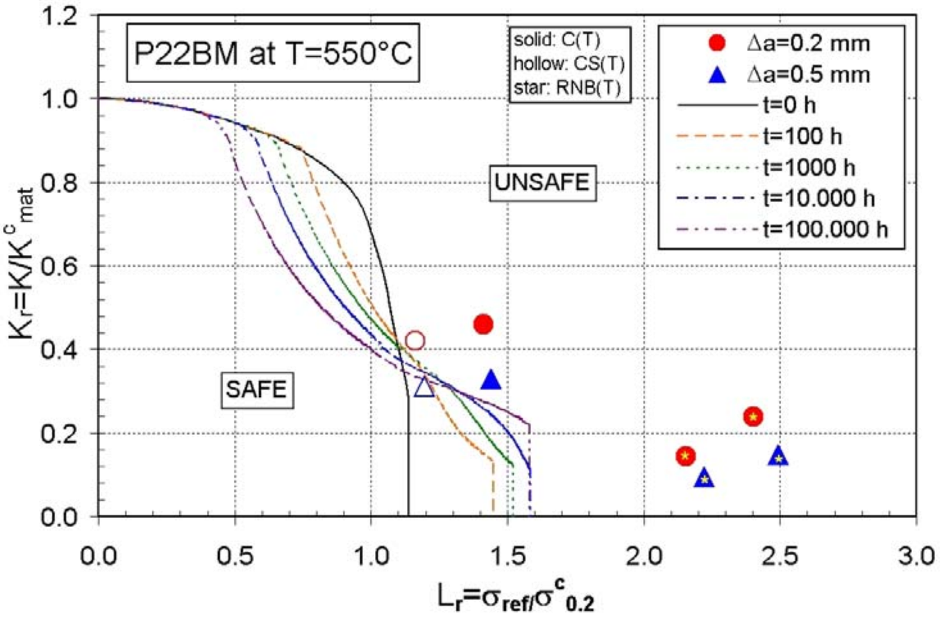

Figure 5.89. TDFAD of P22 BM at 550 °C. Experimental data determined at crack extension of Δa=0.2 mm (circular symbols) and 0.5 mm (triangular symbols). Effect of specimen geometries C(T),CS(T) and RNB(T) are seen.

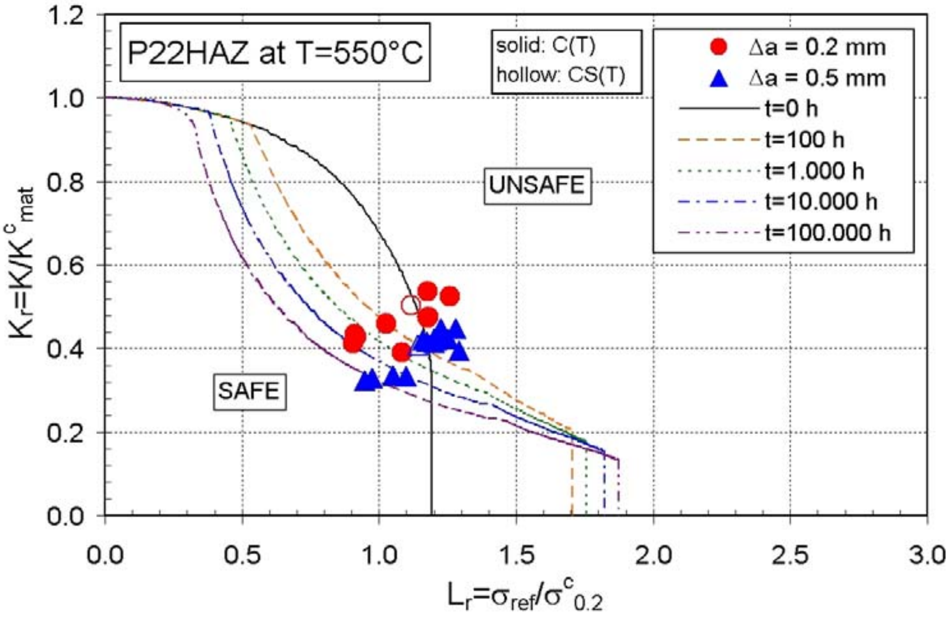

Figure 5.90. TDFAD of P22 HAZ at 550 °C. Experimental data determined at crack extension of Δa=0.2 mm (circular symbols) and 0.5 mm (triangular symbols).

The TDFAD predictions show that CCI is controlled by a mixture of crack tip damage (K_r) and ligament damage (L_r) (Figures 5.89-5.91). Time effect is seen in reduced K_r due to increased K^c_{mat}. Similar effect is seen with increased crack extension. However, in RNB(T) specimens of P22 BM (Figure 5.89) and P22 WM (Figure 5.91), crack tip fracture (K_r) value is low with high ligament damage (L_r). Therefore, metallographic evidence is sought to clarify this behaviour. Figure 5.92 shows the micrograph of the damage accumulation in the RNB(T) specimen presented in insert of Figure 5.91. The specimen was tested for 2074 hours at 550 °C. It is observed that particularly farfield damage by pore formation at ferritic grain boundaries and pore coalescence is seen. The damage is concentrated in the vicinity of the notch at a critical distance of about 0.13 mm with maximum stress intensity that agrees with numerical predictions. The phenomenon of concentration of maximum damage zone away from the notch root in time during creep is consistent with the recent work of Lin and Brocks [117] which extends a Chaboche-type infinitesimal viscoplastic theory to finite-strain cases. This observation indicates that the TDFAD method successfully captures the damage type which dominantly contributes to the onset of CCI and sheds light on the applicability of the TDFAD method at different loading conditions. The SEN(B) specimens shown in Figure 5.91, lie in the “safe” region closer to the failure boundary whereas specimens of other geometries are consistent with the boundaries separating safe and unsafe zones.

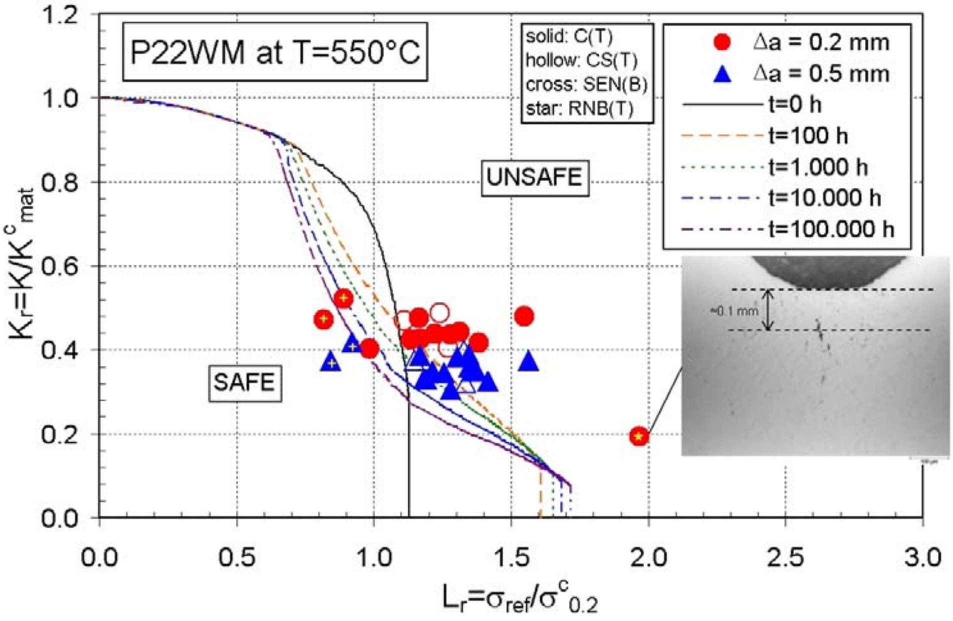

Figure 5.91. TDFAD of P22 WM at 550 °C. Experimental data determined at crack extension of Δa=0.2 mm (circular symbols) and 0.5 mm (triangular symbols). Notch effect is observed in C(T) and CS(T) specimens compared with SEN(B) and RNB(T) specimens. A typical stress concentration at 0.1 mm distance from the crack tip is seen in the RNB(T) notch root micrograph.

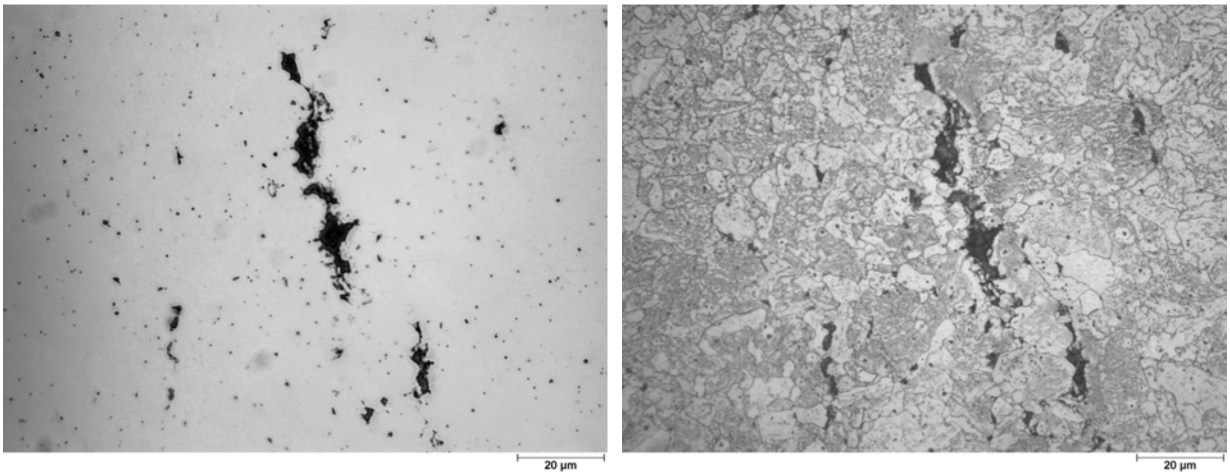

(a)

(b)

Figure 5.92. Damage accumulated near to the notch of the RNB(T) specimen in Figure 5.91 of P22 WM tested for 2074 hours at 550 °C. Pore formation at grain boundaries leading to microcracks is seen. Non-etched (a) and etched (b) micrographs are given.

5.2.7.2. Application of the TDFAD to P91 Steel Weldment

The TDFAD curves are constructed and plotted for different weldment zones of P91 steel using the related creep and crack growth properties, as shown in Figures 5.93 to 5.95. The failure predictions for specimen are shown on the TDFADs for engineering definitions of CCI at crack extensions of Δa=0.2 and 0.5 mm.

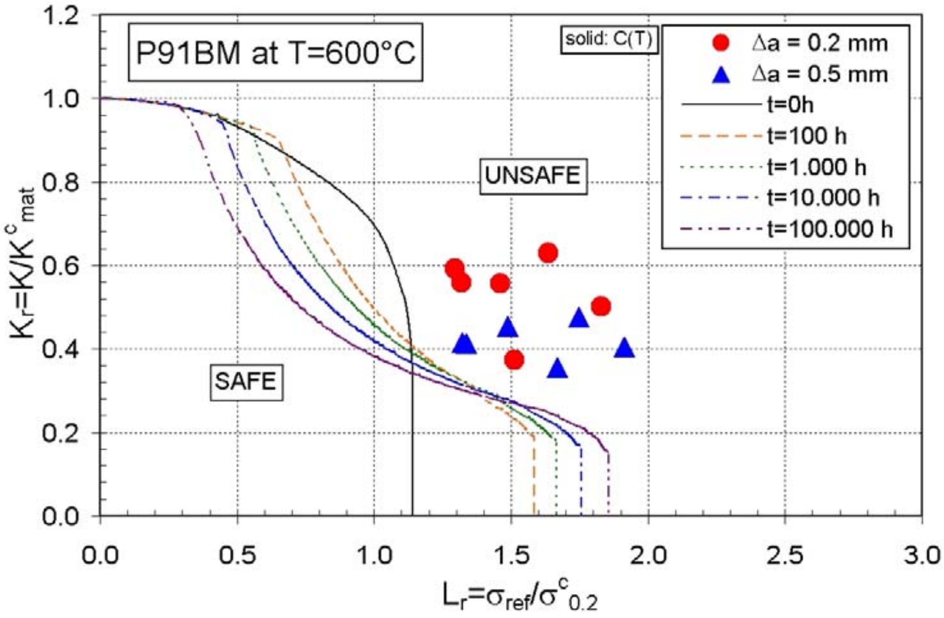

Figure 5.93. TDFAD of P91 BM at 600 °C. Experimental data determined at crack extension of Δa=0.2 mm (circular symbols) and 0.5 mm (triangular symbols). Scatter in experimental data lie in the unsafe zone indicating a conservative prediction of TDFAD for this material.

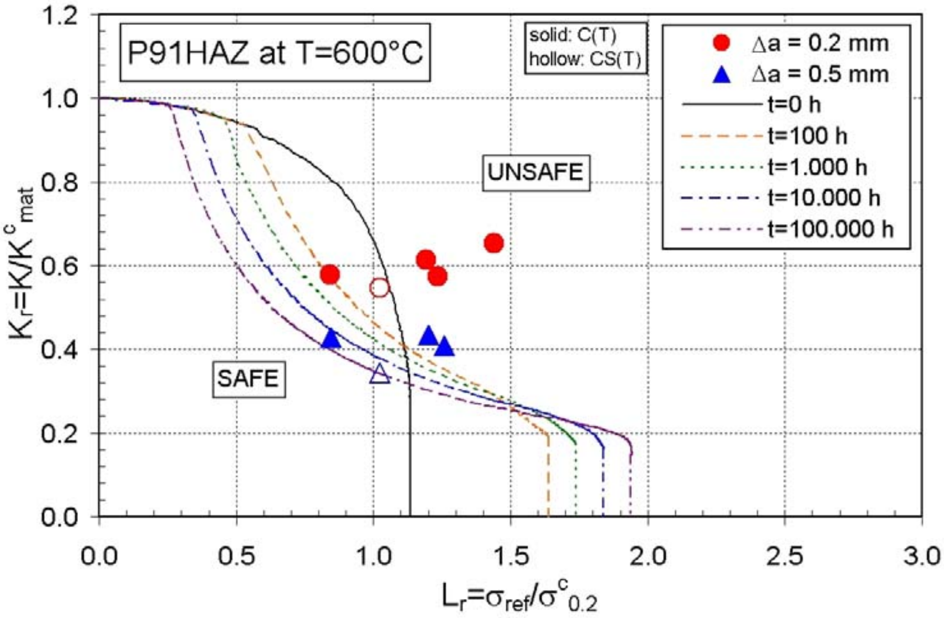

Figure 5.94. TDFAD of P91 HAZ at 600 °C. Experimental data determined at crack extension of Δa=0.2 mm (circular symbols) and 0.5 mm (triangular symbols).

It is observed that all experimental data from C(T) and CS(T) specimen geometries lie in the unsafe failure region of the TDFAD for different weldment zones. However, the only RNB(T) specimen of P91 WM lies in the safe region of the TDFAD. The crack initiation determined in this specimen may have not reached the critical value of crack extension. Similar to specimens of P22 weldment, all of the specimens lie on a region where CCI is controlled by a mixture of crack tip fracture (K_r) and ligament damage (L_r). Higher scatter is observed in P22 HAZ where some of the data points lie on the prediction line (Figure 5.94) indicating the possible failure with time. Different shapes of the predicted TDFADs for various weldment zones, indicate the different deformation and CCI behaviour of weldment zone materials under loading conditions.

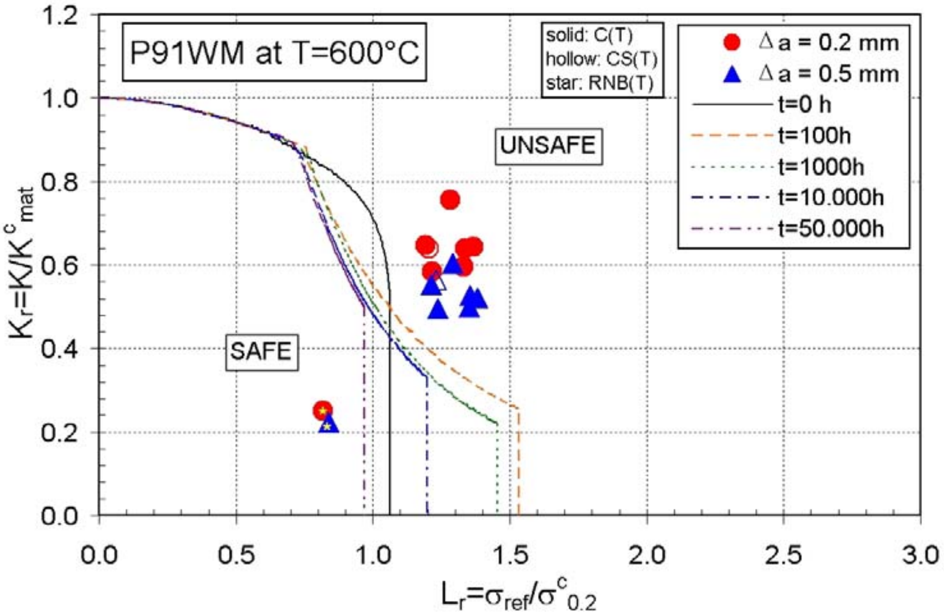

Figure 5.95. TDFAD of P91 WM at 600 °C. Experimental data determined at crack extension of Δa=0.2 mm (circular symbols) and 0.5 mm (triangular symbols). The time for failure covering the range of 100 to 50,000 h vary little with early cut-off lines.

5.2.8 Failure Assessment Using Two-Criteria-Diagram (2CD) Method

The two-criteria-diagram (2CD) method developed by Siemens in Germany, as presented in Section 2.3.3.2, is applied to the high temperature crack extension data. The crack initiation prediction lines, given in [47], are used to define the failure boundary between "crack-no crack" zones. Different mechanisms contributing to CCI are indicated on 2CDs. The 2CD parameters, R_K (crack tip damage) and R_σ (ligament damage) are calculated using the Equation 2.72, for engineering definitions of CCI, at crack extension Δa=0.2 and 0.5 mm (Figures 5.96-5.101). Damage and CCI behaviours of weldments are studied on different specimen geometries. It is observed that the 2CD is capable of determining CCI of different weldment zones capturing the damage mechanisms leading to CCI for different specimen geometries.

However, the present 2CD which was proposed in 1984 is only valid for materials which are not subject to the notch weakening effect. If the creep rupture elongation (A_u) of the material is lower than a certain value, then the shape of the 2CD has to be changed. Therefore, Ewald [118] proposed some modifications to 2CD which will enable the use of the 2CD for brittle materials as well. He suggested to modify 2CD depending on the creep ductility level of material [119]. This modification is also considered for brittle zones of weldments in the light of experimental evidence as in the present study.

5.2.8.1. Application of the 2CD to P22 Steel Weldment

The two-criteria-diagrams are constructed with data from specimens of P22 weldments tested at 550 °C. The results are shown in Figures 5.96-5.98. The failure by CCI defined at crack extension of $\Delta a=0.2$ and 0.5 mm are indicated in the figures. It is seen that the 2CD method is able to predict the CCI of weldments for all materials and specimen geometries.

The experimental data determined on C(T) and CS(T) specimens lie in the “mixed mode damage” zone, whereas RNB(T) specimens with bulk damage lie in the “ligament damage” zone as seen in Figure 5.98. The constraint due to round notch leads to cracks at a critical distance ahead of the notch tip although overall deformation is ligament damage. The data from C(T) and CS(T) specimens of P22 HAZ lie in the region of “mixed mode damage”. Similar behaviour is observed in P22 WM specimen in C(T) and CS(T) specimens as well (Figure 5.98). The data from RNB(T) specimen of WM lies in the region of “ligament damage”. The micrograph of the damage site in the RNB(T) specimen, which was tested for 2074 hours at 550 °C was shown in Figure 5.92. It is observed that particularly farfield damage by pore formation at ferritic grain boundaries is seen. The damage is concentrated in the vicinity of the notch at a critical distance in a location of maximum stress intensity. However, the high constraint SEN(B) specimens of P22 WM lie on the $R_\sigma/R_K=0.5$ boundary, indicating the severity of stress controlled “crack tip damage”. Therefore, the damage mechanism leading to CCI for the specimen geometry of SEN(B) is more prone to crack tip damage mechanism. This case directs attention to the selection of specimen geometry for obtaining data required for assessment of components in service. The failure prediction using 2CD resembles the predictions using TDFAD method. The described constraint effect in various specimen geometries and load levels as in RNB(T) specimens is captured in failure assessment. Note that the correlation axes are exchanged in 2CD to that of TDFAD.

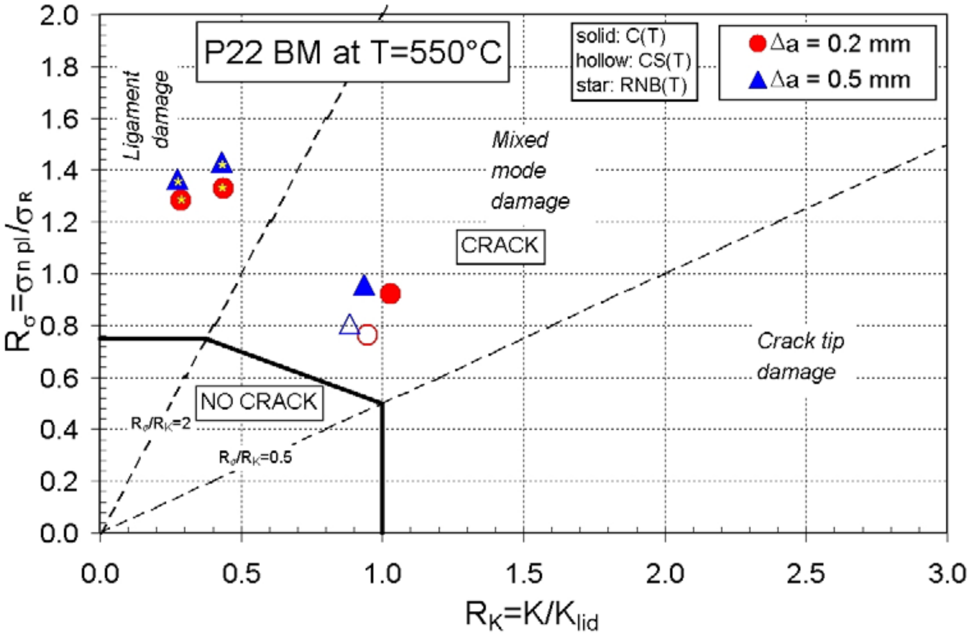

Figure 5.96. 2CD of P22 BM tested at 550 °C. Crack initiation data determined at $\Delta a=0.2$ mm (circular symbols) and 0.5 mm (triangular symbols) for C(T), CS(T) and RNB(T) specimens. Dominant ligament damage in RNB(T) specimens place them in ligament damage zone whereas mixed mode damage failure is determined in in C(T) and CS(T) specimens.

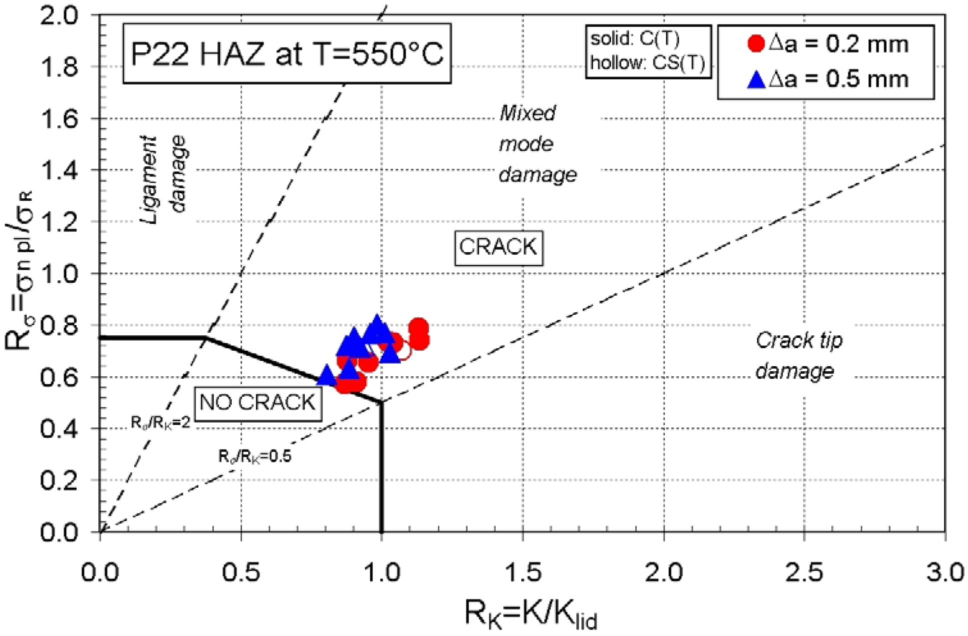

Figure 5.97. 2CD of P22 HAZ tested at 550 °C. Crack initiation data determined at Δa=0.2 mm (circular symbols) and 0.5 mm (triangular symbols) for C(T) and CS(T) specimens.

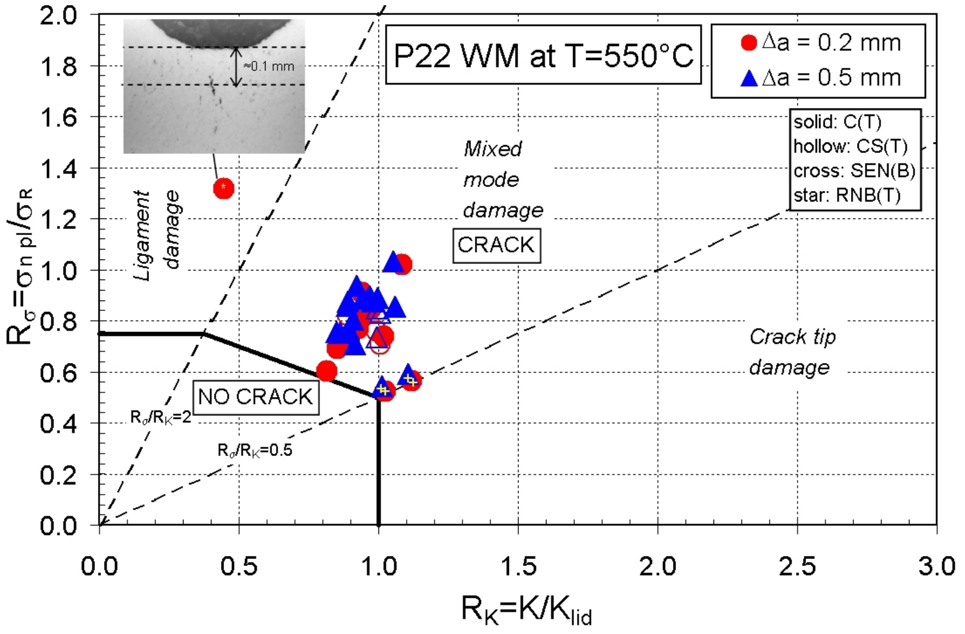

Figure 5.98. 2CD of P22 WM tested at 550 °C. Crack initiation data determined at Δa=0.2 mm (circular symbols) and 0.5 mm (triangular symbols). Effect of constraint is illustrated in C(T) and CS(T) specimens with mixed damage, RNB(T) specimen with ligament damage and SEN(B) specimens with high constraint leading to crack tip damage.

5.2.8.2. Application of the 2CD to P91 Steel Weldment

The 2CD method is applied to the data from tested specimens of different weldment zones of P91 steel at 600 °C. The results are shown in Figures 5.99 to 5.101. Engineering definitions of failure by CCI at crack extensions of Δa=0.2 and 0.5 mm are used for failure assessment. It is observed that the 2CD method is able to predict the failure for all specimens, regardless different weldment materials and specimen geometries.

Similar to P22 steel, the data points of different weldment zones obtained from the specimen geometries, C(T) and CS(T) lie in the region of “mixed mode damage”. However, it is remarkable that the failure of the RNB(T) specimen of P91 WM can not be determined by the 2CD method, as the data point lies in the "no crack" region (Figure 5.101). This issue needs to be further studied in connection with the applicability of the methodology to materials with different creep damage mechanisms and properties used in construction of the failure boundaries. The 2CD is already being modified for creep brittle materials. Therefore, present study contributes to further modification based on the loading conditions in various specimen geometries and weldment zones. This resembles the real component behaviour in high temperature service.

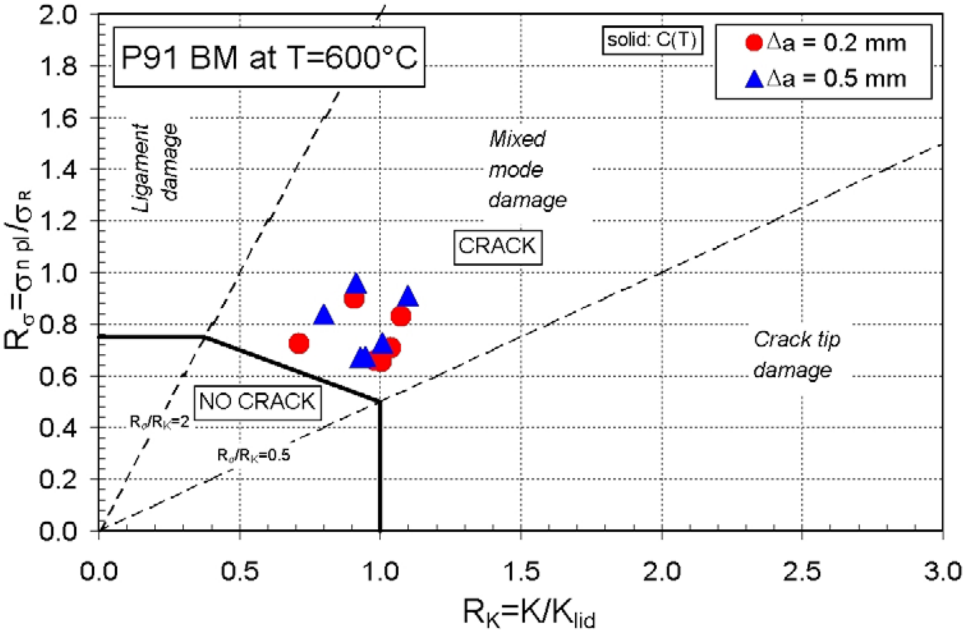

Figure 5.99. 2CD of P91 BM tested at 600 °C. Crack initiation data determined at Δa=0.2 mm (circular symbols) and 0.5 mm (triangular symbols) for C(T) specimen.

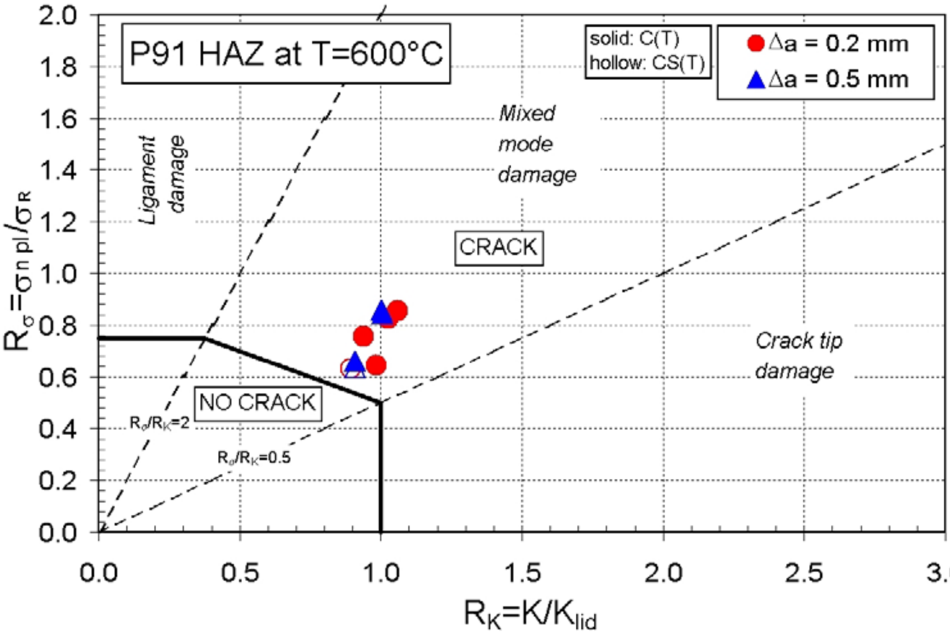

Figure 5.100. 2CD of P91 HAZ tested at 600 °C. Crack initiation determined at Δa=0.2 mm (circular symbols) and 0.5 mm (triangular symbols) for C(T) and CS(T) specimens.

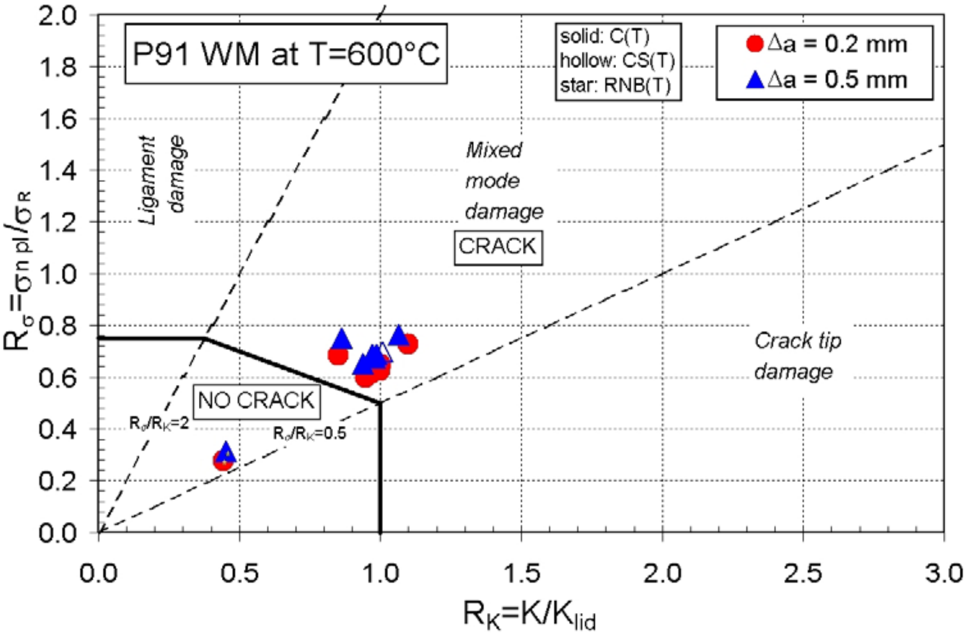

Figure 5.101. 2CD of P91 WM tested at 600 °C. Crack initation data determined at Δa=0.2 mm (circular symbols) and 0.5 mm (triangular symbols) for C(T), CS(T) and RNB(T) specimens. No crack behaviour is predicted for the RNB(T) specimen.

5.3 SENSITIVITY ANALYSIS OF CRACK GROWTH DATA

5.3.1 Introduction

The sensitivity of the high temperature crack growth data of P22 and P91 steel weldments to variations of input testing parameters is studied. The testing parameters include geometrical factors (dimensions of specimens, crack length), material properties and loading.

Two different approaches, namely deterministic and probabilistic sensitivity analyses are performed, which are explained in detail in Sections 2.4.4 and 2.4.5, respectively. Deterministic sensitivity analysis is performed for one input parameter by changing it stepwise in the related fictitious variation range and calculating output parameters. The variation given to testing parameters are assumed in realistic ranges, which might have referred to a measurement error or miscalculation. The sensitivity of each output parameter to the unit variation of each single input parameter is illustrated by tornado diagrams. The tornado diagram reveals the impact of variation of each single input parameter on output parameter as well as the relativity of the effects of all parameter with respect to each other.

The probabilistic approach involves use of the Monte Carlo simulation, which is a stochastic technique using random numbers and probability statistics to obtain an answer for its probability. Probability statistics is applied to input parameters in order to determine their statistical distributions. In case of scarcity of data, a normal statistical distribution is assumed within a reasonable range. The use of Monte Carlo simulation facilitates the calculation of probability of thousands of different combinations of input parameters by computer, which enables the user to discard the cases with very low probability and obtain more reliable and less conservative results. These results can facilitate the user to build an opinion in determining more reliable margins to be used in deterministic sensitivity analysis, which is more practical and less costly.

5.3.2 Deterministic Sensitivity Analysis

5.3.2.1 Deterministic Sensitivity Analysis of Effect of Material Properties on Crack Growth Rate Correlations

The variation of the correlation of crack growth rate, da/dt with C^* of a C(T) specimen of P22 BM tested at 550 °C by a stepwise change in creep exponent, n, is illustrated in Figure 5.102. The value of the parameter is changed from n=1 to n=20. The determined experimental value of n is 17.80. It is pointed out that the change in C^* becomes insignificant as creep exponent, n, increases beyond 3, particularly 5. The explanation to this behaviour relies on that n is represented by the ratio n/(n+1) in the calculation of C^* from experimental data, where the ratio tends to 1 as n goes to infinity. Note also that the creep crack growth behaviour notably change as creep exponent, n, changes from 1 to 3. This change refers to the change of creep deformation mechanism from Harper-Dorn creep to power-law creep, as reported in Reference [109].

However, the level of impact of the other mechanical properties on correlation of crack growth rate with C^* may not be as significant as the impact of the creep exponent, n. The effect of variation of modulus of elasticity, E, from 10^5 MPa to $2.5 \cdot 10^5$ MPa is depicted in Figure 5.103. The determined experimental value of E is $2.5 \cdot 10^5$ MPa. Its impact on correlation of crack growth rate with C^* is insignificant, therefore, it needs not to be included in future deterministic and probabilistic sensitivity analyses of creep crack growth data.

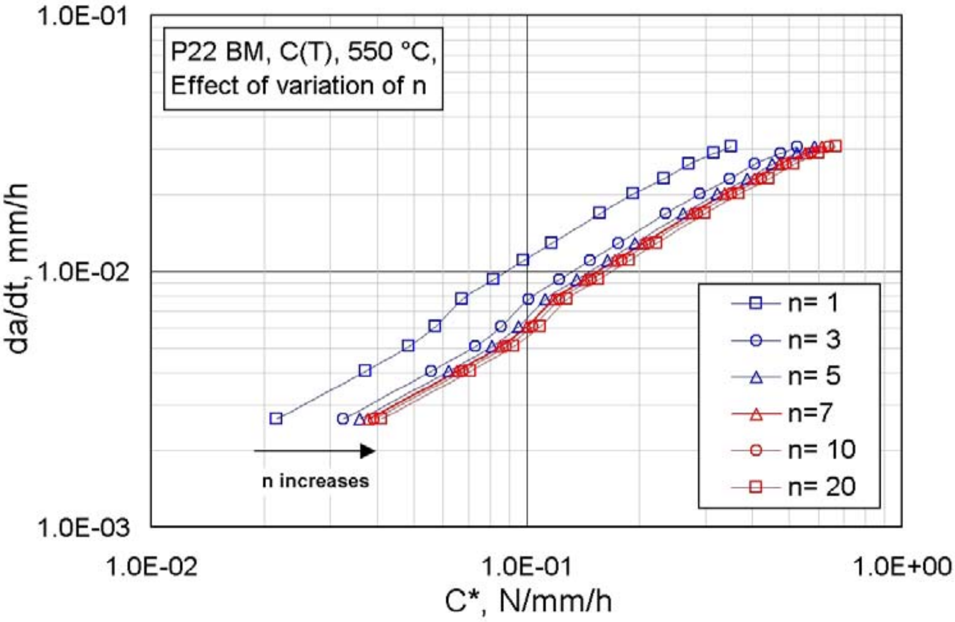

Figure 5.102. Effect of variation of creep exponent, n, on crack tip parameter C^* of P22 BM C(T) specimen tested at 550 °C.

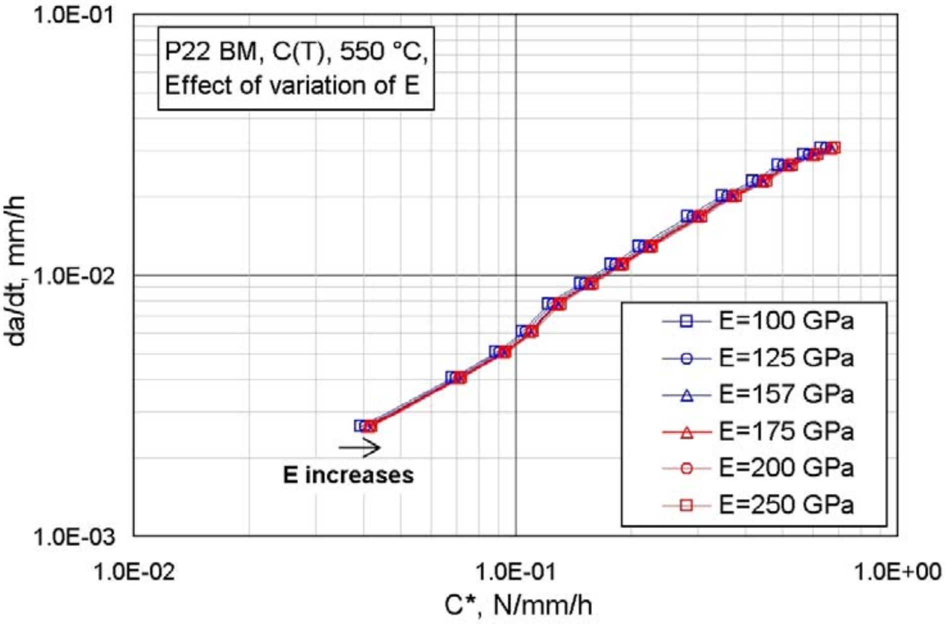

Figure 5.103. Effect of variation of modulus of elasticity, E, on crack tip parameter C^* of P22 BM C(T) specimen tested at 550 °C.

5.3.2.2 Deterministic Sensitivity Analysis of Effect of Geometrical Factors on Crack Growth Rate Correlations

The effect of variation of final crack length, a_f, and specimen size, W, on the correlation of crack growth rate with C^* of a CS(T) specimen of P22 BM tested at 550 °C is given in Figures 5.104 and 5.105, respectively. The possible variation of final crack length comes from the fact that the initial and final crack length of high temperature fracture mechanics specimens are measured optically on the crack opened fracture surface of specimens. The variation of a_f has two fold impact on calculations both on C^* and crack growth rate, da/dt.

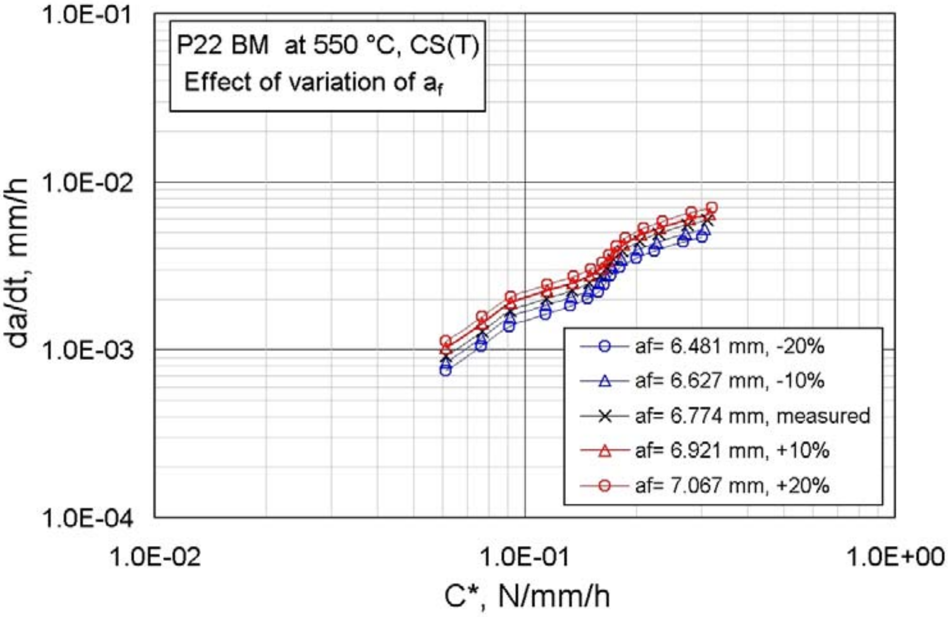

Figure 5.104. Effect of final crack length, a_f on da/dt vs. C^* plot of P22 BM CS(T) specimen tested at 550 °C

Similarly, the impact of the specimen size, W, is examined for the same CS(T) specimen of P22 BM at 550 °C. W is varied between ±10% of the measured value. It is observed that the change of the specimen size, W, from -10% to +10% leads to a variation of the C^* at 1.5 times. Note that such a variation of the experimentally determined crack tip parameter, C^*, may lead to significant calculation errors in component design and life assessment at high temperatures.

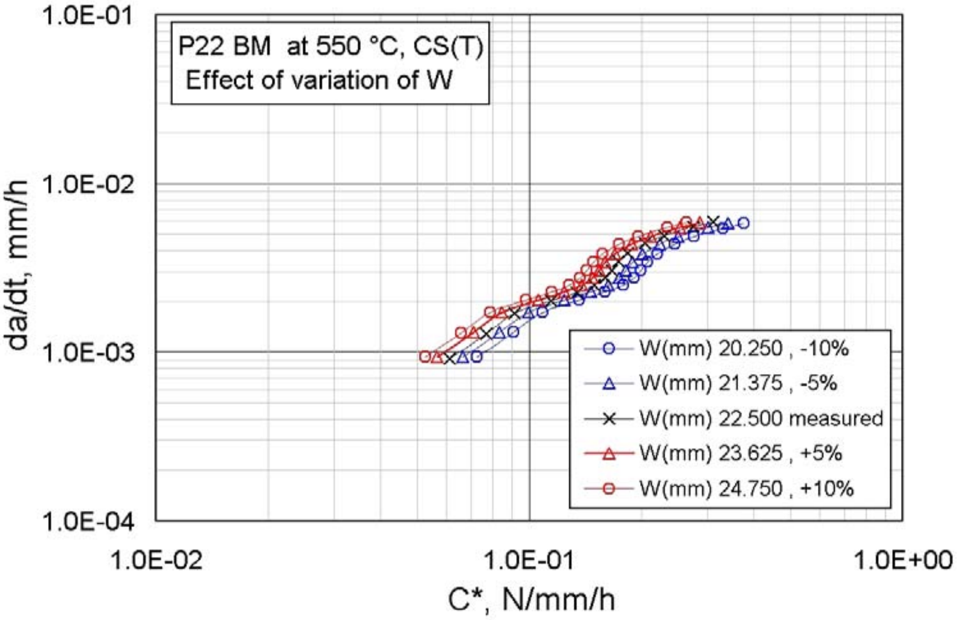

Figure 5.105. Effect specimen size, W, on da/dt vs. C^* plot of P22 BM CS(T) specimen tested at 550 °C

5.3.3 Probabilistic Sensitivity Analysis

5.3.3.1 Probabilistic Sensitivity Analysis of Crack Growth Rate Correlations

Probabilistic sensitivity analysis is performed on correlation of experimentally obtained crack growth rate with crack tip parameter, C^* of test data on C(T) specimens of P91 steel. In the first example, sensitivity of the correlation of crack growth rate to the change of ratio of initial crack length to specimen size, a_0/W, is shown. In the second example, the sensitivity of the correlation of crack growth rate to variation of initial crack length, a_o, is presented. For both examples, Monte Carlo simulations are performed.

1st Example

The distribution of the ratio of initial crack length to specimen size, a_o/W, is obtained from tested specimens. Statistical parameters mean value, μ, and standard deviation, σ, are determined using statistical methods. The determined statistical parameters are used to generate a normal distribution of the ratio, a_o/W, with the same statistical parameters, but with a higher number of samples. The distribution obtained, consisting of 10,000 data points with $\mu=0.4896$ and $\sigma=0.0205$ is shown in Figure 5.106.

The distribution of a_o/W obtained by random number generation, is used in Monte Carlo simulation that yields the sensitivity of the C^* correlation of P91 WM data. The simulation is repeated for 1000 times. For the presentation of the results from the Monte Carlo simulation, 20 results out of 1000 are sampled. Power functions are fitted to each of those 20 results, which give the steady state relationship (Equation 5.2) of crack growth rate with crack tip parameter, C^*. The results are shown in Figure 5.107. It is observed that as the value of D_o given in Equation 5.2 varies between 0.121 and 0.175, the value of exponent, ϕ, varies from

0.93 to 1.01. Note that the intersection of the fitted lines at $5{\cdot}10^{-3}$ of C^* reveals that variation of the exponent, ϕ, is more significant than the variation of D_o, since ϕ gives the slope of the fitted line in log-log scale.

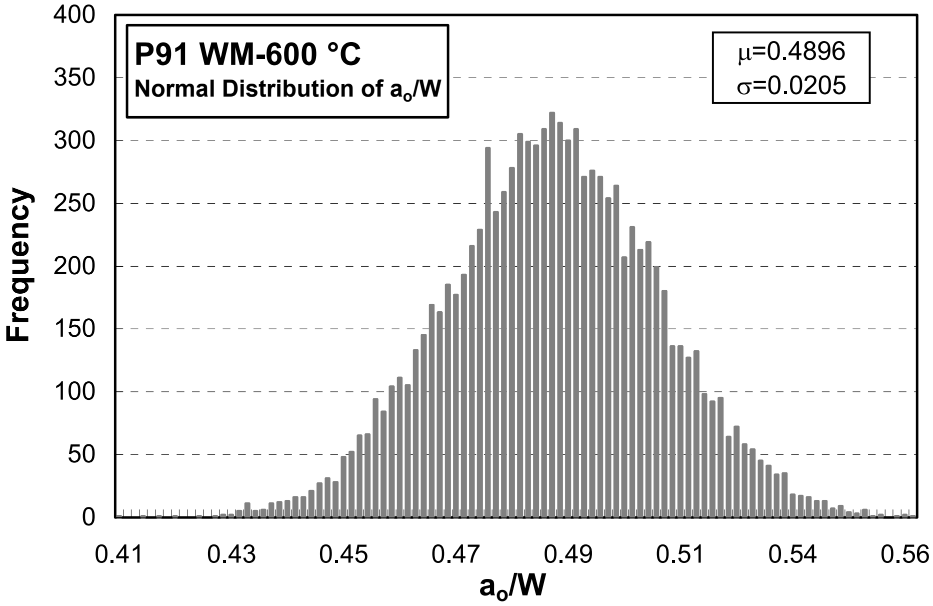

Figure 5.106. Normal distribution of the ratio of initial crack length to specimen size, a_o/W, generated by use of the statistical values obtained from tested specimens.

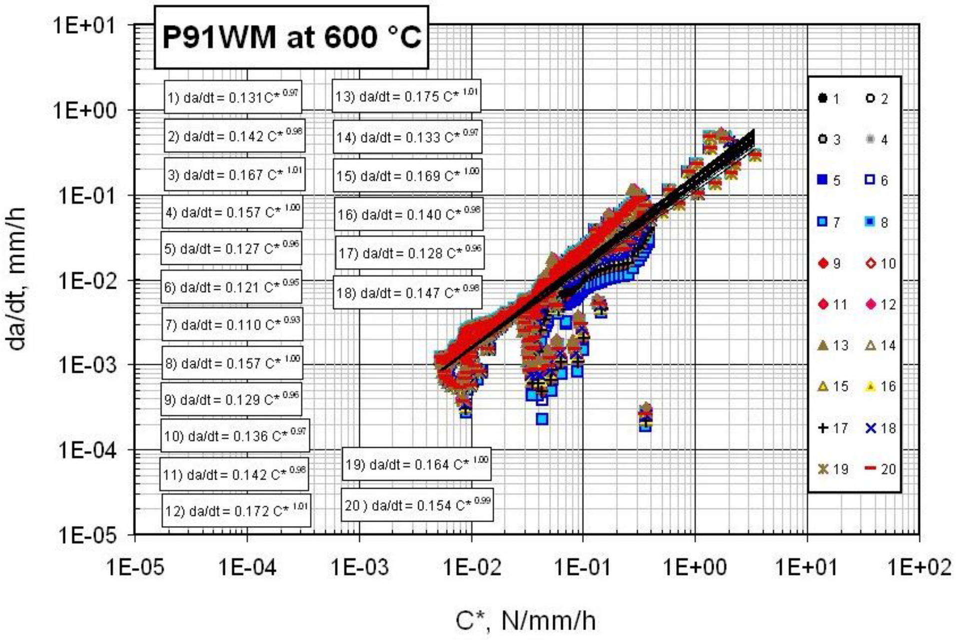

Figure 5.107. Monte Carlo simulation performed on correlation of the crack growth data of P91 WM at 600 °C with C^*. 20 results are sampled out of 1000.

2nd Example

Monte Carlo simulation is performed for the probabilistic sensitivity analysis of the C^* correlation of crack growth rate of a P91 BM C(T) specimen tested at 600 °C, to variation of initial crack length, a_o. The specimen size, W, is taken equal to 35 mm. The specimen has an EDM starter notch equal to 17.5 mm. A Monte Carlo simulation is performed in order to determine the sensitivity of the C^* correlation of the crack growth rate of the specimen. A dataset of 10,000 points for initial crack length, a_o, with normal distribution is generated by a random number generator. It is taken that the mean value, μ, of the distribution is 17.5 and standard deviation, σ, is 0.1. The distribution of the a_o is shown in Figure 5.108.

The Monte Carlo simulation is performed for 1000 times in order to obtain a set of results which shows the impact of the distribution of initial crack length, a_o. The results are shown in Figure 5.109. Note that the effect of the variation of a_o on the crack growth rate, da/dt, is more significant than the effect on the crack tip parameter, C^*. This directs attention to the factors of safety used in high temperature defect assessment procedures, such as in R5 [29], 2CD [47], which rely on correlation of experimental crack growth data correlated with crack tip parameters, K or C^*.

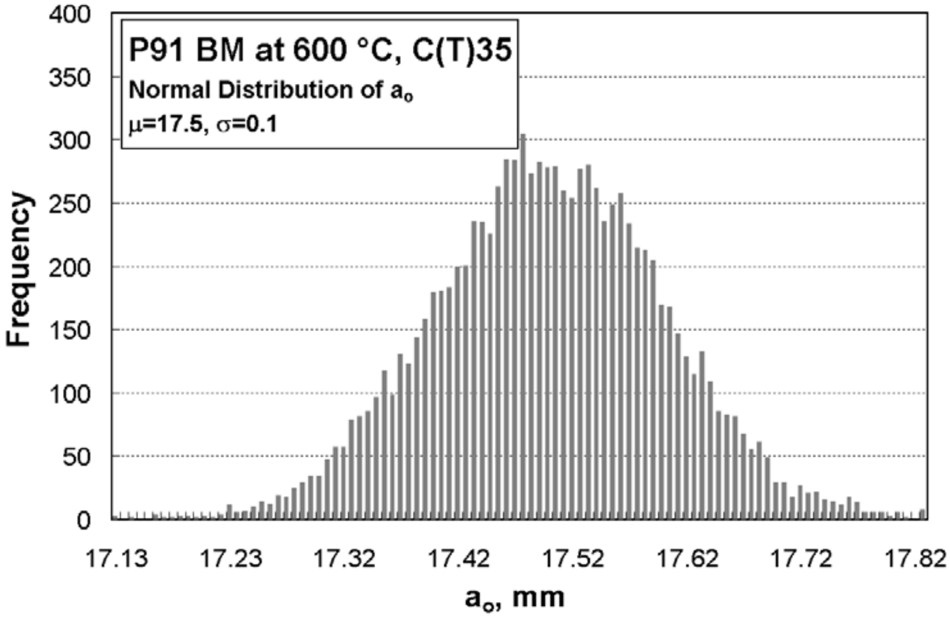

Figure 5.108. Normal distribution of the initial crack length, a_o, generated by a random number generator, using the values, μ=17.5 and σ=0.1.

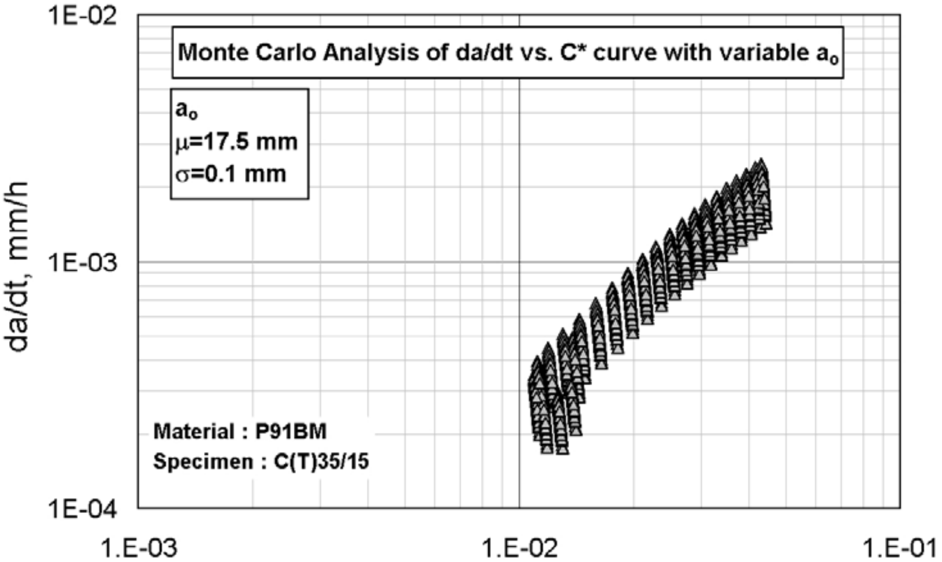

Figure 5.109. Monte Carlo simulation performed on the C^* correlation of the crack growth data of the C(T) specimen of P91 BM tested at 600 °C.

5.3.3.2 Probabilistic Sensitivity Analysis of Estimation of Crack Initiation Time with Time Dependent Failure Assessment Diagram

The combined impact of variation of various geometrical parameters and test load, F, on estimation of CCI time is simulated by using Monte Carlo method. The data from P22 BM CS(T) specimen which was tested at 550 °C is used for CCI in TDFAD approach. The Monte Carlo simulation is performed for 1000 times for both engineering definitions of CCI at crack extensions of Δa=0.2 mm and Δa=0.5 mm. The selected input parameters are initial crack length, a_o, and final crack length, a_f, test load, F, specimen width, W, specimen thickness, B, and specimen net thickness, B_n. All parameters have normal distribution.

The impact on TDFAD is shown in Figure 5.110. The impact on both TDFAD parameters, K_r and L_r, accumulate as time is increased from 10 hours to 1000 hours. The K_r values are significantly different for crack extensions 0.2 and 0.5 mm at long times. The magnitude of standard deviation, σ, of L_r and K_r at 1000 hours given in Figure 5.110 reflects the extent of scatter in these parameters. It is observed that the combined effect of input parameters leads obviously to higher scatter in L_r than in K_r.

The tornado diagrams for the defect assessment parameters, L_r and K_r at 1000 hours for the crack extension, Δa=0.2 mm are given in Figure 5.111. The direction of the effect of each input parameter is in the same direction for both L_r and K_r. Note that the regression correlation coefficients of L_r determined for each input parameter is higher than that of K_r, which is indicating higher impact of each individual input parameters on L_r than on K_r. It is seen that the most influential input parameter is the test load, F, which is followed by the initial crack length a_o. Final crack length, a_f, is not included among the input parameters in the tornado diagram, since a_f has no contribution to calculation of TDFAD parameters.

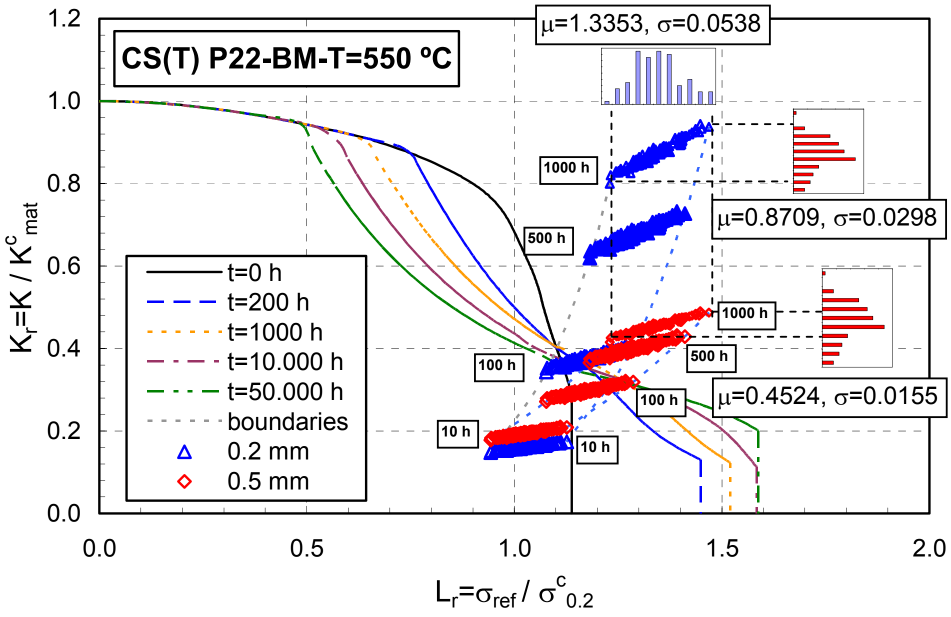

Figure 5.110. Cumulative effect of variation at W, B, B_n, a_o, a_f and F on TDFAD diagram of a P22 BM CS(T) specimen at 550 °C.

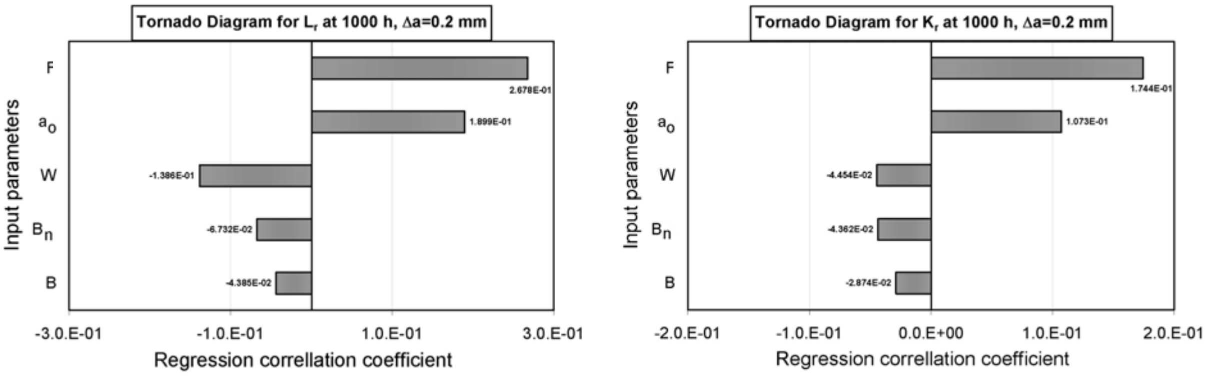

(a) (b)

Figure 5.111. Tornado diagrams for TDFAD parameters (a) L_r and (b) K_r at 100 hours for Δa=0.2 mm of a P22 BM CS(T) specimen tested at 550 °C.

5.4. METALLOGRAPHIC STUDIES

5.4.1. Deformation and Micromechanics of Cracks in P22 and P91 Steels

Metallographic studies of deformation and cracking of P22 and P91 steel weldments are done on specimens tested at 550 °C and 600 °C, respectively. The specimens are sectioned through their mid-planes by EDM technique. One of the specimen half is polished and etched with picric acid for metallographic examination using optical microscopy (OM) and scanning electron microscopy (SEM). Samples taken from different weldment zones of BM, HAZ and WM are examined in order to correlate the damage in the vicinity of the crack tip leading to crack growth with microstructural constituents. The observations provided evidence for operating damage mechanism in microstructural zones. Hence, damage mechanistic basis was established for the correlations of crack growth rate with loading parameters.

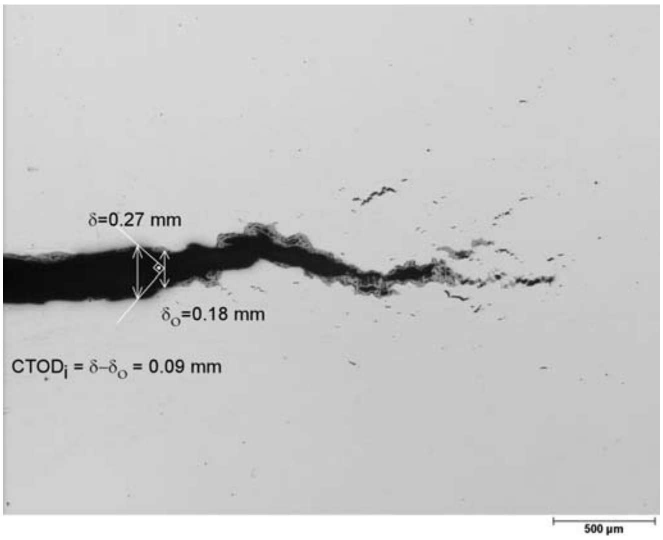

Figure 5.112. Micrograph of the crack tip of the C(T) specimen of P22 BM tested for 428 h at 550 °C on the polished side surface. Wide-spread microcracks are seen.

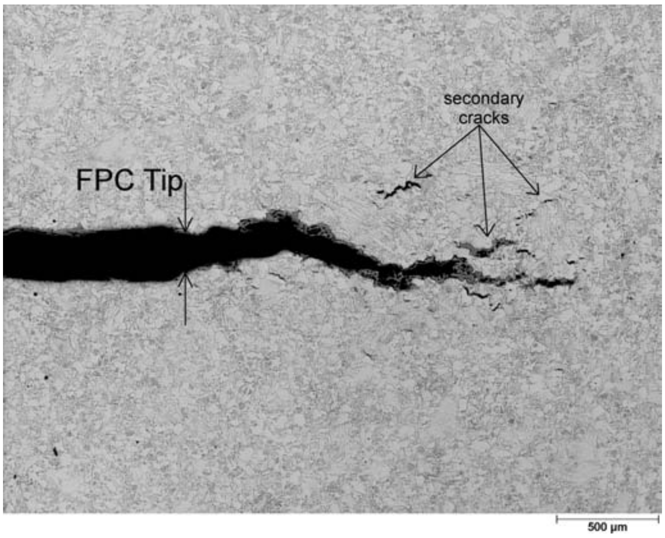

Figure 5.113. Micrograph of the crack tip of the C(T) specimen of P22 BM with coarse-grained ferritic microstructure tested for 428 h at 550 °C, showing the damage leading to crack growth. Secondary crack are indicated.

Crack tip damage is observed in the micrographs of polished and etched side surfaces of the C(T) specimens of P22 BM (Figures 5.112-5.113) and of P91 BM (Figures 5.114-5.115). Note that the P22 BM specimen was tested at 550 °C for 428 h and P91 BM specimen was tested at 600 °C for 1543 h. Such damage seen in Figure 5.113 for P22 BM, indicates creep deformation at grain boundaries. Several secondary cracks observed around the crack tip of the C(T) specimen of P22 BM shows that the coalescence of microvoids at grain boundaries leading to microcracks is more likely to occur in this material. The overview of the crack tip of the SEN(B) specimen of P22 BM tested for 768 h at 550 °C is seen in Figure 5.116. A typical example of widespread excessive damage accumulated around the main crack. The crack growth process follows the coalescence of microvoids at grain boundaries.

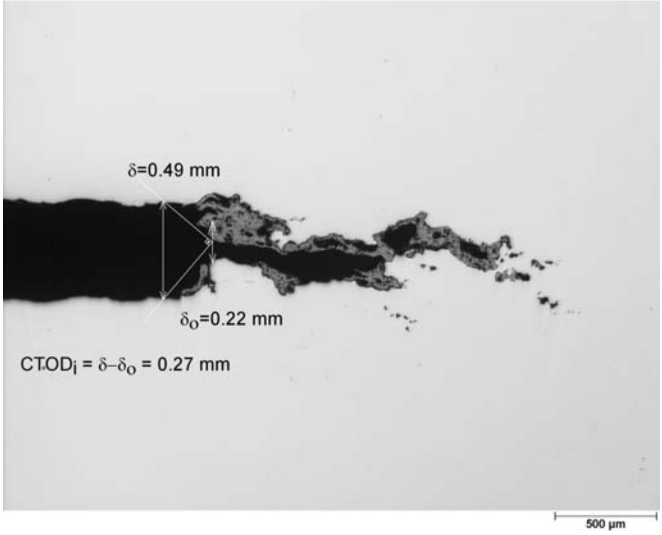

Figure 5.114. Micrograph of the crack tip of the C(T) specimen of P91 BM tested for 1543 h at 600 °C on the non-etched side surface. Small number of microcracks is observed.

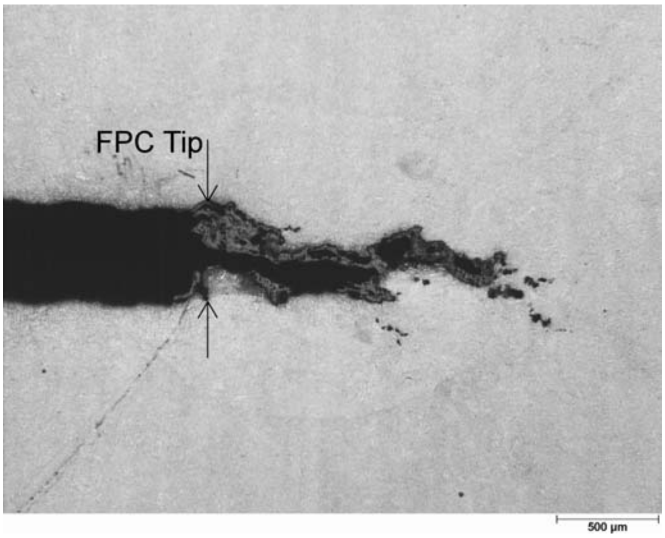

Figure 5.115. Micrograph of the crack tip of the C(T) specimen of P91 BM with fine-grained martensitic microstructure tested for 1543 h at 600 °C, showing the damage leading to crack growth.

The observed higher creep resistance of P91 BM that shows significantly less microcracks and secondary cracks on the crack plane (Figure 5.115) is related to lower susceptibility to pore formation at grain boundaries. Localised but less damage, compared to P22, is related to the fine microstructure and homogeneous deformation of P91 steel. Damage accumulates along crack growth planes, as shown in Figure 5.119. This observation has the implication on the CCI correlations of P22 and P91 steels described in Section 5.2.4. Early CCI resistances of P91 weldment zones are higher than that of the P22 weldment zones. Furthermore, local CTOD measured on P22 BM and P91 BM specimens are given in Figures 5.112 and 5.114, respectively. The initiation value of the CTOD ($CTOD_i$=0.27 mm) for P91 BM specimen is three times bigger than that of the P22 BM's ($CTOD_i$=0.09 mm). This indicates that P91 BM accommodates more damage (higher creep strain) than that of P22 BM at the crack tip prior to CCI. The described creep resistance leads to higher values of crack tip parameters, K and C^*, at crack initiation as described in Section 5.2.4. Thus the correlation between microstructural constituents in steel weldments and measured fracture resistance shown in CCI and CCG plots is described based on micromechanical approach.

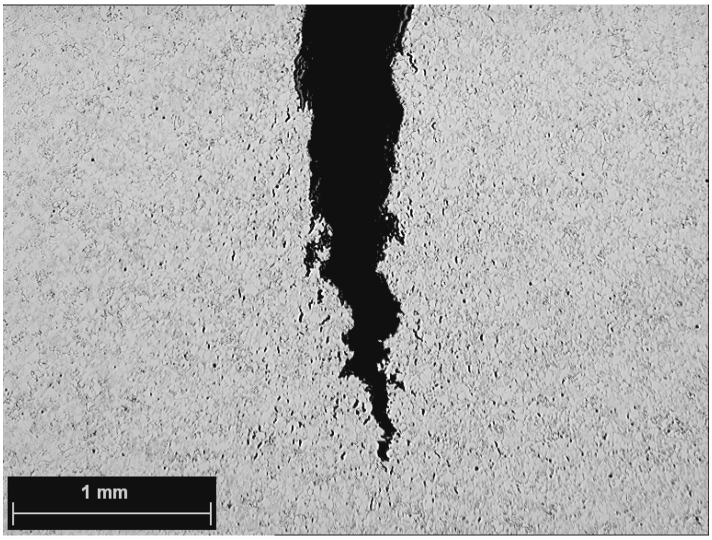

Figure 5.116. Micrograph of the crack tip of the SEN(B) specimen of P22 BM tested for 768 h at 550 °C. Wide-spread microvoid formation at grain boundaries leading to microcracks is seen along the crack growth path.

Figure 5.117 shows the damage accumulated at the crack tip of a P22 BM C(T) specimen tested for 428 h at 550 °C. Non-uniform carbide distribution is seen in the micrograph. Formation of microvoids is seen either at grain boundaries or in the carbide-rich sub-grains. Coalescence of microvoids leads to microcracks and secondary cracks ahead of main crack tip. Sub-grain formation occurred possibly during heat treatment leads to increased number of grain boundaries susceptible to creep damage. Hence, the possibility of pore formation leading to fracture increases. Figure 5.118 shows the chain-like oriented pore formation at grain boundaries. Note that the orientation of these pores is perpendicular to the direction of the main stress. According to the classification scale proposed by Neubauer [120], this case corresponds to the 3rd grade of evolution of creep damage in ferritic steels, which will lead to grain boundary separation by microcrack growth.

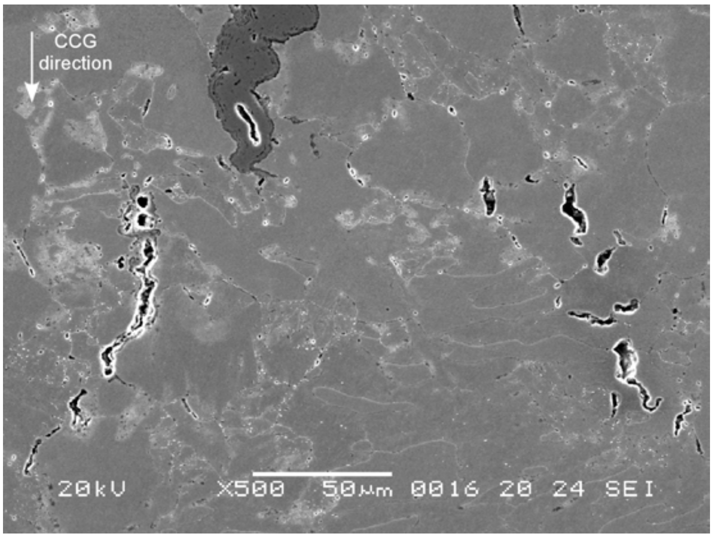

Figure 5.117. Micrograph of the vicinity of the crack tip of the C(T) specimen of P22 BM tested for 428 h at 550 °C . Deformation by microvoid formation along the main deformation path leading to separation at grain boundaries prior to crack growth. Crack grows by microcrack coalescence along nearby deformation plane. The second cracked zone remains as a secondary crack.

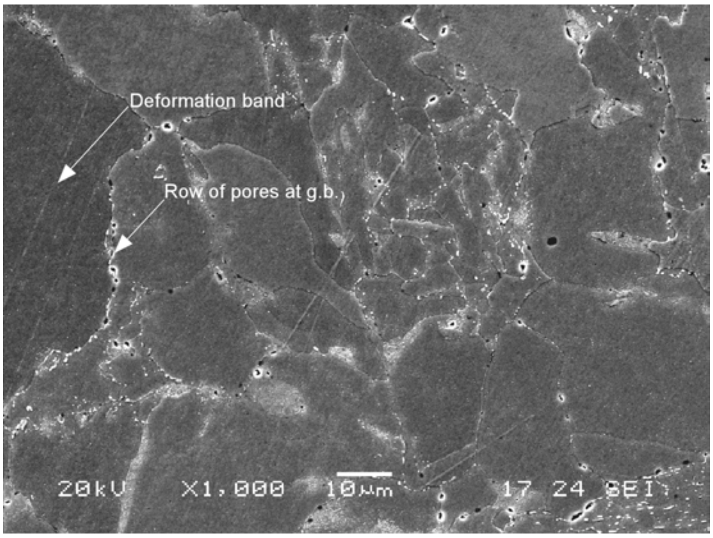

Figure 5.118. Rows of chain-like pores and deformation bands within the grains are observed in the damaged zone of the crack tip of the P22 BM C(T) specimen. Non-uniform carbide distribution followed by microvoid formation is seen. Sub-grain formation is delineated.

The lamellar bainitic-martensitic structure at the crack tip of the P91 BM C(T) specimen tested for 1543 h at 600 °C is shown in Figure 5.119. Deformation concentrated in shear bands which comply with the slip-line field theory [109] are shown. Carbide depletion in the vicinity of the damage zone is delineated. Figures 5.120 and 5.121 show the enlarged damage zones in the right and left slip line field halves of the Figure 5.119, respectively. The formation of large pore damage is shown in Figure 5.120 where the sequence of 1) grain boundary damage, 2) opening (debonding) of damage particle, 3) Falling of the debonded particle, is followed. This is a micromechanical process of high temperature damage where creep resistant large grains resist deformation. The easy creep deformation of small grains is exemplified here. However, this directs attention to long-time strength problem of P91.

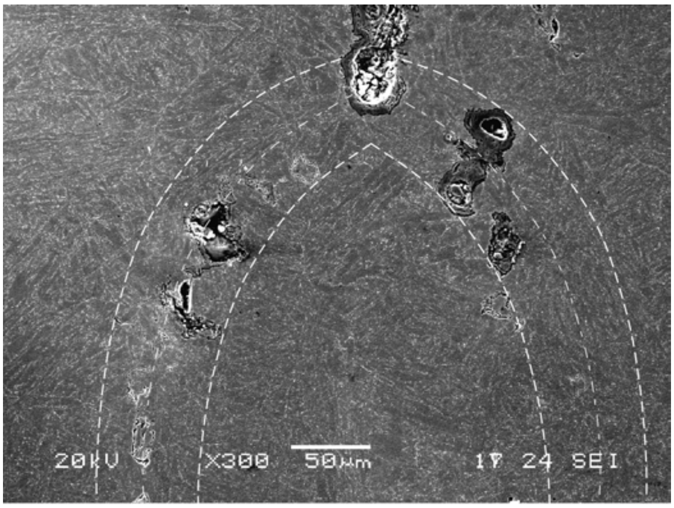

Figure 5.119. Micrograph of the crack tip of the C(T) specimen of P91 BM tested for 1543 h at 600 °C. Highly strained slip line fields in which damage occurred. Fine uniform carbide distribution is seen.

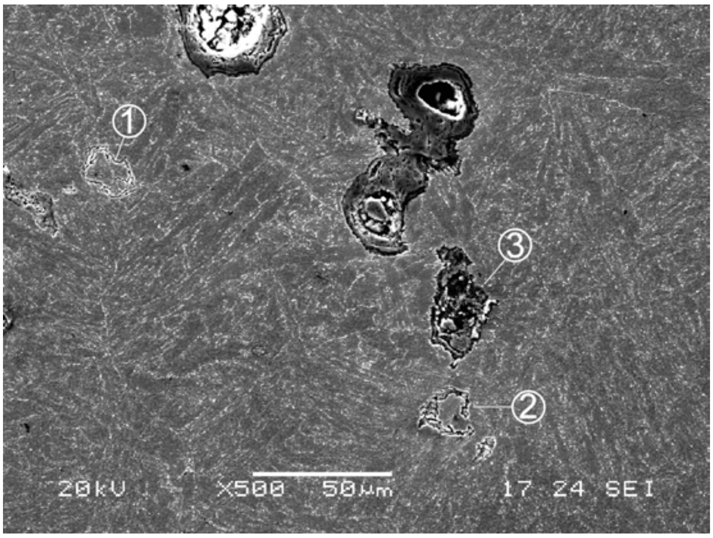

Figure 5.120. Damage observed in the right slip line field of the specimen in Figure 5.119. Transformed bainitic microstructure with prior austenite grain boundaries is seen.

Compared to P22 BM, large transformed bainitic structure with prior austenite grain boundaries are observed in P91 BM. This leads to much less grain boundary pore formation compared to P22 (Figure 5.117). Instead of microvoids leading to microcracks at grain boundaries as seen in P22 BM, microcracks at small sub-grains are observed (Figure 5.121).

The creep damage along prior austenite grain boundaries that is delineated with carbide precipitates debonding and grain boundary failure at hard phases are seen in Figure 5.122. This process leads to continuous microcracks causing disintegration of whole sub-grain (Figure 5.123) leading to large pore formation along deformation bands. Eventually, fracture advances by coalescence of deformed and disintegrated grains. The high creep resistance of P91 is attributed to the uniform large transformed bainitic microstructure with uniform carbide distribution at grain boundaries and in the grains.

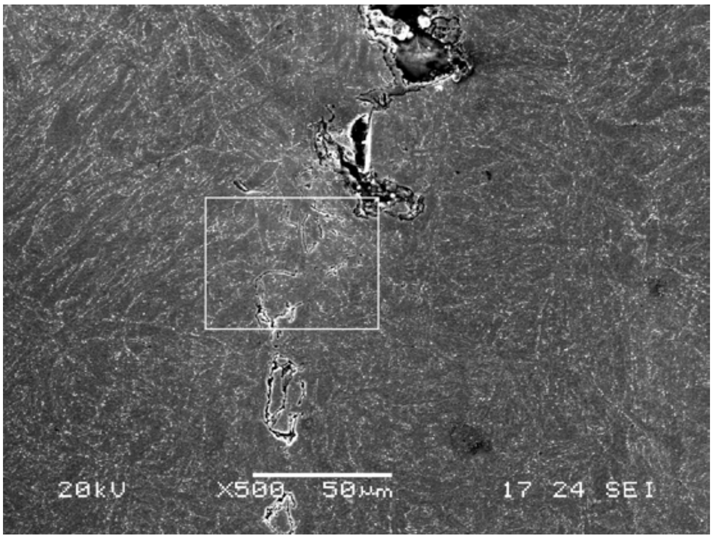

Figure 5.121. Damage observed in the left slip line field of the specimen in Figure 5.119. A chain of microcracks that lead to pore formation at grain boundaries are seen.

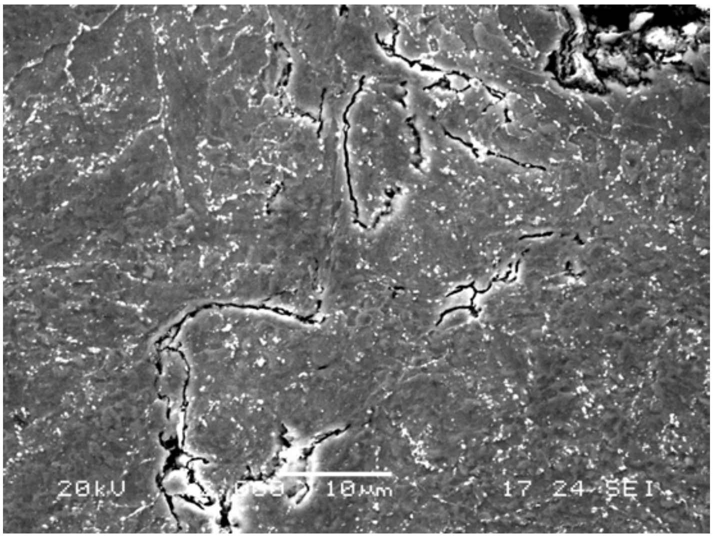

Figure 5.122. Enlarged area in Figure 5.121 showing microcracks at the grain boundaries at the crack tip of the specimen. This damage type is comparable to damage observed at grain boundaries of P22 BM (Figure 5.118).

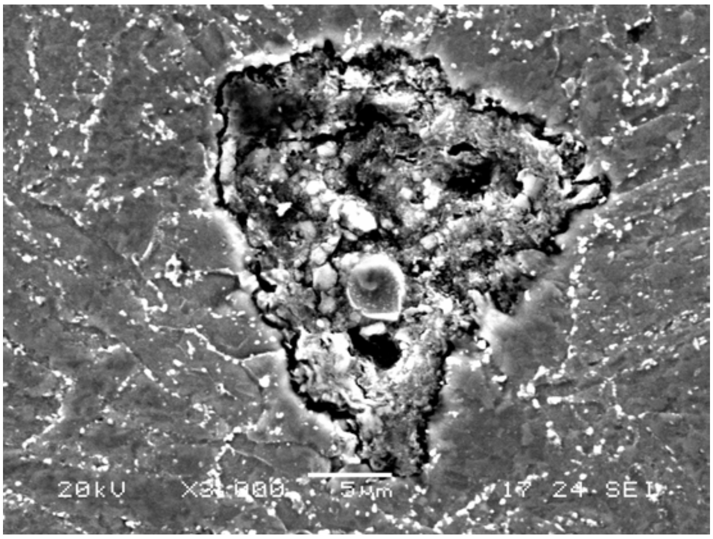

Figure 5.123. Disintegration of a small strained grain in the C(T) specimen of P91 BM leading to large pores. Carbide segregation at grain boundaries and inside the grains in bainitic microstructure.

5.4.2. Metallography of Crack Initiation and Crack Growth

In crack initiation and crack growth testing of weldments by using industrial type specimens, starter crack position with respect to microstructural phases has utmost importance. It determines the crack tip behaviour by growing on the crack plane if positioned properly, or leads to crack deviation by forming unbroken ligaments. The starter crack, therefore, is located by pre-fatigue or EDM method [6] in the selected weldment zone (BM, WM or HAZ), for which CCI and CCG properties will be determined. It can also be introduced into the interface between two different weldment zones, in order to trace the growing crack in creep-weak zone or deviations at creep-strong microstructural zones. Therefore, experimental CCI and CCG data should be substantiated by metallographic evidence. This includes correlation of the data with microstructural constituents as well as the description of the orientation of the crack during growth. This is particularly important in interpretation of CCG behaviour when increase or decrease in crack growth rate may be described by local phenomena. Furthermore such information is needed in material microstructural design and defect assessment in service components. Note that this industrially vital issue is not considered in the only available high temperature crack growth testing standard, ASTM E1457-00 [3], where only testing of base metal is considered.

Evidence for the above discussion is provided in Figure 5.124 where the crack growth of a C(T) specimen of P22 weldment tested for 1378 h at 550 °C is depicted. Starter crack is positioned in the fusion line (FL) between WM and HAZ. During the crack propagation, crack deviates into the HAZ. This behaviour conforms to the experimental results of fracture mechanics tests, where fine-grain P22 HAZ is the creep-weakest among weldment zones (See Table 5.8). Jump of the crack is observed at the later stage of the crack growth, which is caused by the excessive creep damage accumulated in the creep-weak HAZ. Note that such a jump cannot be detected by PD crack monitoring method. Therefore, post-test metallographic examination is imminent. This draws attention in high temperature testing of weldments to the essence of interpretation of CCG rate correlations by using metallographic examination in order to provide reliable data for structural integrity assessment of these materials in service.

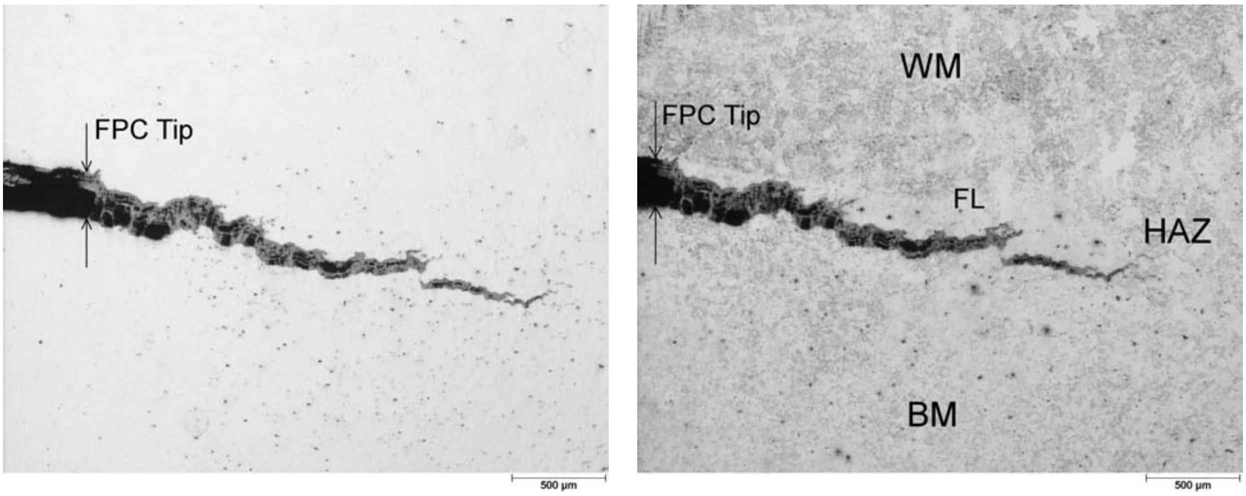

(a) (b)

Figure 5.124. Crack growth in C(T) specimen with starter crack located in FL of P22 weldment tested for 1378 h at 550 °C. Crack orientation into creep-weak HAZ is shown in polished (a) and etched (b) micrographs.

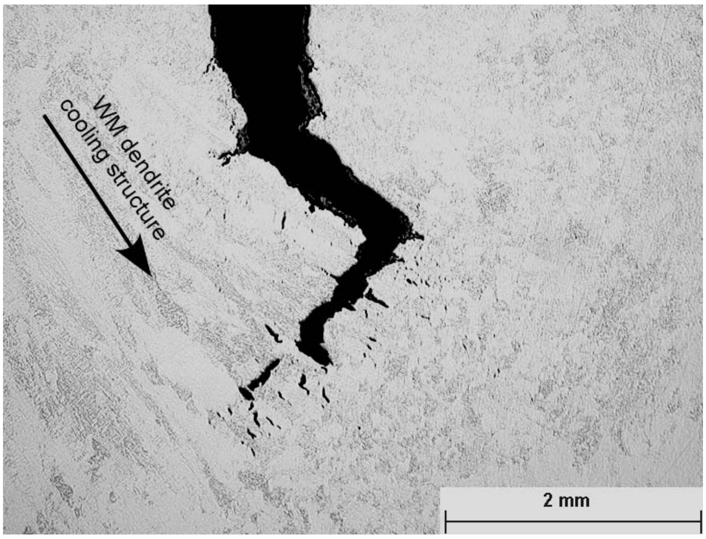

Figure 5.125. Deviation of the crack from the main crack plane due to heterogeneous WM microstructure in a SEN(B) specimen of P22 WM tested for 643 h at 550 °C. Crack growth along welding pass boundary with WM dendritic cooling structure is observed.

Further evidence is provided in Figures 5.125 and 5.126 where the effect of heterogeneous microstructure on crack growth behaviour is seen in two different SEN(B) specimens of P22 WM which were tested at 550 °C for 643 h and 962 h, respectively. Deformed dendritic WM microstructure is seen in both specimens along the crack growth path. The propagation of the crack in zigzag manner complies with the slip line field theory [109]. Microcracks oriented along the dendritic cooling structure that lead to deviation of the crack in early stage of the crack growth from the main crack plane. This is the main source of the scatter in early crack growth rate data as presented as a function of loading parameter K or C^*. The crack propagates further by coalescence of microcracks oriented in the direction of dendrite cooling structure, as shown in Figure 5.127. This case reveals that the material is creep-weak in the perpendicular direction to the dendritic weld cooling structure. Therefore, the use of tensile and creep properties obtained from tensile specimens in assessment of crack growth data must be revised for weldments with heterogeneous microstructure in order to determine reliable base data for fracture mechanical assessment of components in service.

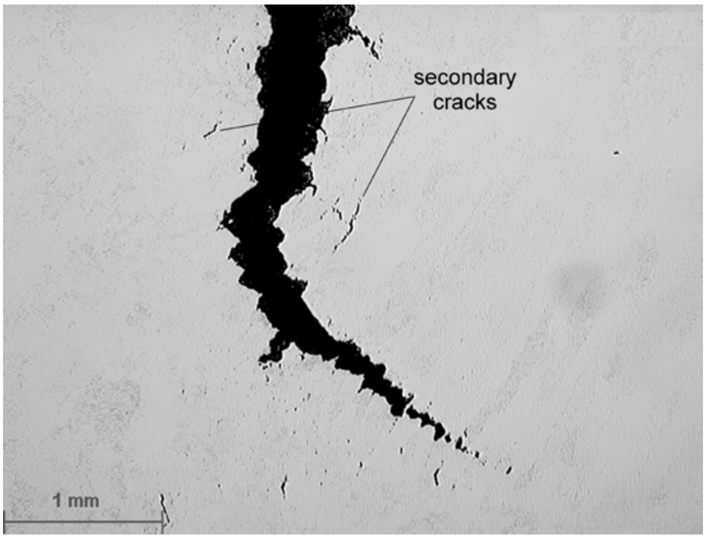

Figure 5.126. Deviation of the crack of a SEN(B) specimen of P22 WM tested for 962 h at 550 °C from the main crack plane due to heterogeneous WM microstructure. Secondary cracks in the dendrite WM cooling structure is observed.

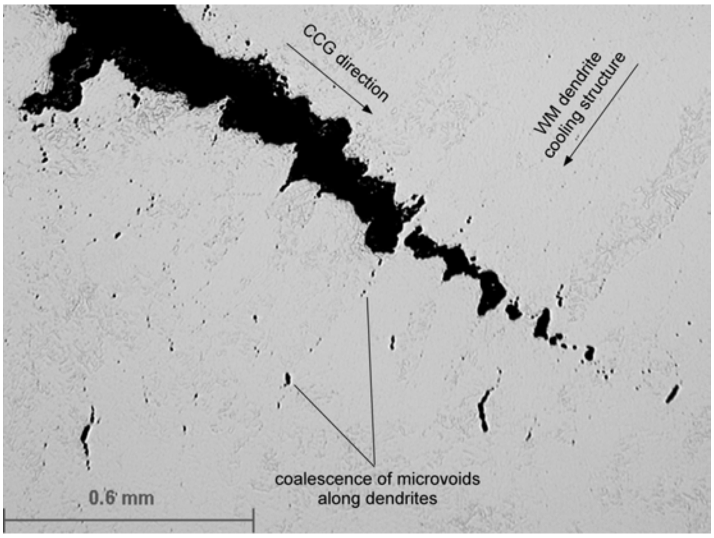

Figure 5.127. Enlarged crack tip area of Figure 5.126 showing coalescence of microvoids oriented along the dendritic WM structure leading to the crack propagation perpendicular to the direction of the cooling structure.

6. DISCUSSION

6.1. DAMAGE AND FRACTURE ANALYSIS BY MICROTENSILE TESTS

Functionally graded microstructures of weldments have different mechanical and creep properties in weldment zones of BM, HAZ, and WM which in turn directly influence the stress redistribution and damage accumulation within these zones. This directs attention to the effect of interaction between different weldment zones, which are primarily the cause of failure in weldments. Failure primarily occurs due to loading parallel to the welding direction, for instance due to hoop stresses in a circumferential butt weld in a pressurised pipe. For loading essentially transverse to the weld as may be the case due to weight of pipe system for example, such redistribution is essentially limited to amount of material local to the interfaces between the different microstructures.

Time dependent high temperature deformation in uniaxial cross-weld tests involves complex interactions between weldment zones. Adjacent strong material can constrain deformation and retard failure in a weak zone which is thinner compared to the specimen diameter. This structural constraint behaviour of weld materials causes many of the observed test failures in cross-weld uniaxial specimens which are highly artificial [39]. For example, the P22 WM / P22 HAZ conjoint failure mechanism by ductile strain interaction and necking is clearly a peculiarity of the plain bar specimen geometry and does not represent the actual interaction between different weldment zones in a component. Therefore, the results require careful analysis. These considerations direct attention to the material behaviour and test methods that facilitate determination of local material properties in constitutive zones of weldments. The MT testing is proposed for determination of local material properties that involves conducting tests across weldment by using little amount of material. The MT test is also useful for in-service material characterisation that may possibly be compared with other miniature test methods such as small punch testing [121]. Because of the data and material behaviour information required for plant assessments at service temperatures, the MT testing for determination of local material properties along with deformation and fracture behaviour of weldments of P22 and P91 steels are emphasised in the presently reported work.

The MT results presented in Section 5.1, highlight the advantages of MT testing and characterisation as well as deficiency of the method that needs further study and development. MT tests on P22 and P91 materials produced similar strength and deformation properties where stress and strain are considerably lower than those of ST test values. However, the obtained data follows a similar ranking of properties for the tested weldment zones. Therefore, correction factors are proposed to overcome deficit in MT for determining material property data. However, these corrections factors are suggested using only the test data of P22 and P91 steel weldments at 550 °C and 600 °C, respectively. Therefore, they must be substantiated by further test data.

The microstructural inhomogeneity in thinner specimens as used in MT tests may suffer a backdraw where the specimen cross-section contains only a few grains. The specimen surface finish is an important factor affecting the test data. The scatter is probably due to the irregular surface condition caused by EDM machining, where the machining surface defects and irregularities may act as failure initiation sites and may initiate microcracks on the surface of the specimen with extensive oxidation that are more effective than in standard tensile specimens. It is already shown in test results of both P22 and P91 steel weldments that the removal of surface roughness by mechanical polishing down to 6 μm, reduces the scatter in tensile data.

An effect of loading rate is observed in the polished surface specimen data of the P22 weldment where the sequence of mechanical properties in test zones follows the order of standard tensile test properties. Lower P22 HAZ data (Figure 5.4) may be related to specimen thickness and possible decarburisation effects. Similarly, loading rate effect is seen in stress-strain behaviour of P91 steel weldment zones. On the other hand, the lower scatter in MT tensile data of P91 than those of P22 is remarkable. The reported differences in MT data may be related to deformation and fracture behaviour studied on the side surfaces of tested specimens. A homogeneous deformation with localised shear bands and defects are observed in ferritic material of P22. Failure mode by grain boundary pore formation and cracking is delineated (Figure 5.16). Material deformation on the shear plane is seen where the pore opening is observed in the vicinity due to stresses acting on hard particles. It is seen that recovery occurred at specimens tested at lower loading rate. Elongation of grains along the main loading axis is observed in specimens tested at low loading rate compared to the specimens tested at high loading rate where strain hardening occurs (Figures. 5.11-5.12). The longer test time at low loading rates, deformation is accompanied by softening mechanisms of recovery. This deformation behaviour is observed in specimens with elongation bands as seen in the vicinity of the crack tip of the C(T) specimen of P22 BM tested for 428 h at 550 °C (Figure 5.113).

Deformation in P91 BM is uniform with confined deformation in shear zones as large as 50 μm (Figure 5.18). Slight deformation observed in elongated ferritic lamellae along main loading axis is more pronounced in BM (Figure 5.17(a)). Transformed austenitic martensitic structure with carbide precipitation is seen in WM (Figure 5.17(b)). Similar to P22, elongation of grains in the loading direction is observed for the specimens tested at lower loading rates. The observed deformation and fracture modes are comparable to the crack tip material behaviour in creep crack growth tested specimens of various geometries. This provides evidence for using MT testing for a quick, cheap and reliable assessment of deformation and fracture behaviour of materials in service. The method may provide basis for assessment of component behaviour in high temperature service.

Effect of high temperature is observed in necked specimen zone with reduced hardness. It is also observed the higher loading rate during the test leads to increase in hardness values. A significant softening effect on thermally exposed and crept high temperature steels compared to only thermally exposed steels is reported [108]. This is attributed to the above mentioned softening effect in thermally exposed and plastically deformed necking parts of MT specimens. This case also encourages the use of MT testing for determining reliable data and information on the damage and fracture behaviour of steel weldments in high temperature service.

6.2. HIGH TEMPERATURE FRACTURE BEHAVIOUR

6.2.1 High Temperature Fracture Mechanics Testing

Testing and assessment of weldments for creep crack initiation and crack growth behaviour at high temperatures is of industrial importance. Particularly, aging plant structures in utilities emphasise the industrial need for testing and assessment of weldments. Heterogeneous microstructure of weldments which leads to complex interactions between different weldment zones requires special care in testing, data assessment and interpretation of results. Therefore, industrial interest coincides with the academic interest for reliable testing and assessment methods. Joining of expertise in the field will lead to a widely accepted method for crack growth testing at high temperatures. A European CoP [6] on high temperature crack growth testing of weldments has been produced recently European group of industrialists and academicians active in ESIS [4]. The CoP provides guidelines for specimen selection, testing and data analysis for weldments that include novel aspects such as testing of industrial specimen geometries for creep crack initiation and growth testing. The guidelines of the CoP are followed in this thesis for testing of specimens of different geometries from different weldment zones of P22 and P91 steel weldments at 550 °C and 600 °C, respectively.

The choice of specimens for testing to determine creep crack initiation and growth rate data requires criteria of machine capacity, material availability and the volume and dimensions of usable material to be satisfied. The shape of the component from which test specimens will be machined out can also influence the choice of specimen. For instance, the CS(T) specimen is particularly suited to testing material from tubular components and the SEN(T) would be appropriate for blade type components. The location and orientation of the crack in the specimen also need to be consistent with the defect orientation in the component being assessed. The specimen thickness should normally be chosen to be equal to, or exceed, the section thickness of the component being assessed. However this does not exclude the testing of other thicknesses as long as the tests are checked for validity.

Where loading capacity is limited, the highly constrained C(T), CS(T) and SEN(B) specimens will require lower test loads for given ligament dimensions than the RNB(T) geometry. The stress state at the crack tip of a specimen and the mode of loading of the component in service could also influence the choice of specimen. Longer crack lengths, Δa, with shorter load line displacement, Δ^{LLD}, which are observed in CS(T) specimens (Figures 5.37-5.40) is a good example of correct choice.

6.2.2 Determination of Displacement Rates and CCG Rate

The crack length, load-line (and crack tip opening) deflection and time data need to be processed for determining the load-line (and crack tip opening) displacement rate, $d\Delta^{LLD}/dt$ or $d\Delta^{CMOD}/dt$, and the creep crack growth rate, da/dt. The data points are chosen consisting of crack length and the corresponding load-line displacement and time such that crack extension between successive data points is of the order of 0.005W. If the crack growth is small, smaller Δa values should be chosen such that a minimum of ten data points will be determined for the total crack growth range.

The present study confirmed that both the secant method and the incremental polynomial method (7-point method) can be used in determining the load-line (crack tip opening) displacement rate, $d\Delta^{LLD}/dt$ ($d\Delta^{CMOD}/dt$), and the creep crack growth rate, da/dt. The incremental polynomial method smoothes the data, hence, reduces the scatter in determined rates. However, for the tests with small crack growth as in small size specimens of weldments which have usually small number of data points, the secant method is recommended for determining rates. The rationale is provided below for the recommendations.

Secant Method

Although the secant method technique proposed in ASTM E 1457 [3] for computing crack growth rate and deflection rate simply involves the point itself (i) and the consecutive point (i+1) to determine the creep crack growth rate or load-line (crack tip opening) displacement rate at the point (i), the technique proposed herewith which is proposed in the CoP [6] involves calculating the slope of a straight line connecting two neighbouring points (i-1 and i+1) on the a versus t and the Δ versus t curve. (Figure 6.1) It is formulated in formulae as below,

$$\dot{a}_i = \left(\frac{da}{dt}\right)_i = \left(a_{i+1} - a_{i-1}\right)/\left(t_{i+1} - t_{i-1}\right) \tag{6.1}$$

$$\dot{\Delta}_i = \left(\frac{d\Delta}{dt}\right)_i = \left(\Delta_{i+1} - \Delta_{i-1}\right)/\left(t_{i+1} - t_{i-1}\right) \tag{6.2}$$

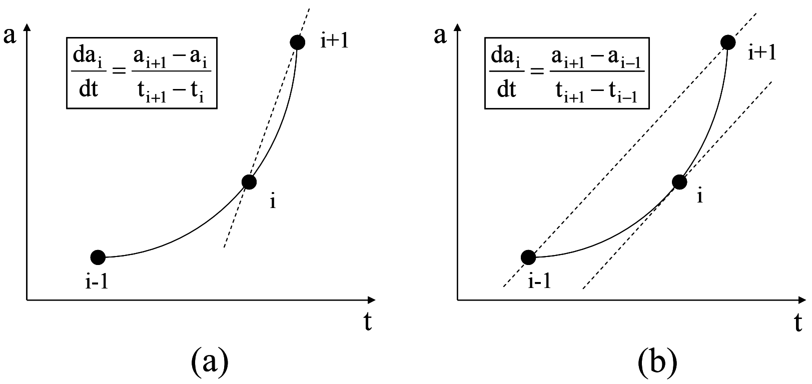

Figure 6.1. Secant method proposed in a) ASTM E1457 and b) present CoP.

Incremental Polynomial Method (7-point method)

As depicted in Figure 6.2, this method for computing da/dt and dΔ/dt involves fitting a second order polynomial parabola to sets of 7 successive data points.

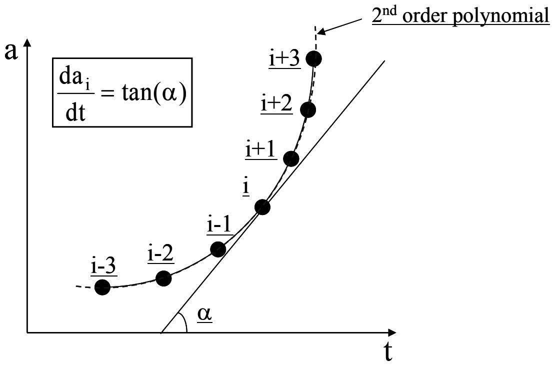

Figure 6.2. Determination of crack propagation rate, da/dt, by ASTM 7-Points (7P) method

For each data point, 3 previous and 3 successive points are taken for 2nd order polynomial fit,

$$a\,(\text{or}\,\Delta) = A\,t^2 + B\,t + C \tag{6.3}$$

Taking the 1st derivative of Equation 6.3, crack growth (or displacement) rate can be determined from

$$\dot{a}\,(\text{or}\,\dot{\Delta}) = 2A\,t + B \tag{6.4}$$

where A, B and C are fitting constants. The fitting procedure given above may be done by using available commercial software.

It is also possible to fit alternative mathematical functions relating the load-line displacement and crack growth to time. These functions can then be differentiated to determine load-line displacement and creep crack growth rates. However, combining different fitting functions may yield difference in crack growth rate data. Junction points of several functions used to fit PD vs. t data lead to artificial kinks at da/dt vs. C^* plot at positions corresponding to these junction points as seen in Figure 6.3.

Prevention of kinks at da/dt vs. C^* plots requires special care during the processing of data. Experience in data processing will help smoothening the data and preventing artificial disorders which do not represent the materials behaviour.

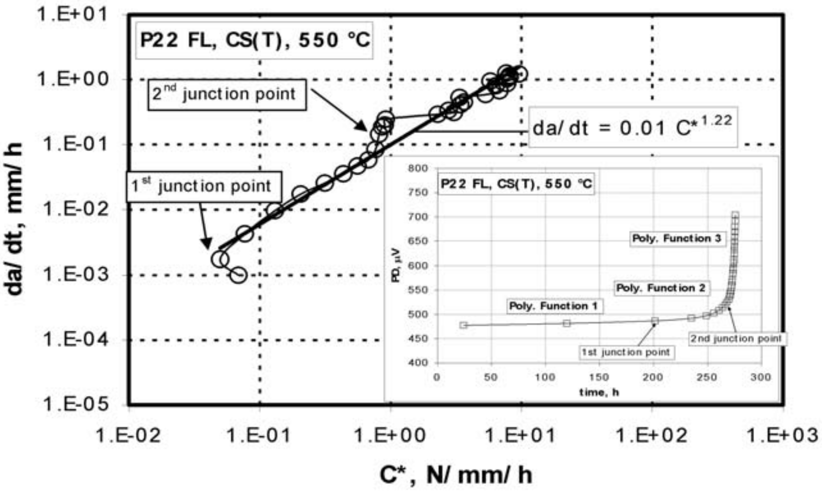

Figure 6.3. Curve fitting of PD data to obtain the crack growth rate, da/dt, with artificial kink at fit function junctions [122].

6.2.3 Test Results

CCI resistances of different weldment zones of P22 and P91 were determined at 550 °C and 600 °C, respectively. The crack growth rate data are correlated with K, K^{c}_{mat} and C^*. It is observed that although P22 WM does not have the highest early CCI resistance, it has the lowest slope of CCI resistance with initiation time, in K correlation (Figure 5.45-5.46). This particular type of CCI resistance behaviour of a material is important for the engineering performance of components made of these materials which is considered as the ultimate goal of these studies. Similarly, the higher CCI resistance and longer initiation times observed in P91 HAZ compared with P91 WM is important and directs attention to lowest CCG resistance determined in P91WM (Figure 5.82). Note also that lower slope of the P91 HAZ obtained at CCI resistance correlations with K and K^{c}_{mat} is worth noting where fracture mode in P91 weldments are usually expected to be type IV in HAZ. Therefore, high temperature deformation and fracture behaviour of P91 WM must be emphasised in defect assessment since it shows the lowest resistance to creep crack initiation and growth. In the light of micromechanical studies of P91 weldment, it is discussed here that the choice of filler material for welding and consecutive treatments of WM strongly affect the WM resistance.

The difference in CCI resistance obtained by using different fracture mechanics parameters directs attention to the validity of fracture mechanics parameters at early (crack initiation) and later (crack growth) stages of crack extension. This issue is addressed by ESIS TC11 WG on testing of weldments which have produced a CoP [6] and by ECCC in the relevant ECCC documents [113]. Increase in scatter by use of C^* correlation for CCI resistance points out that the use of C^* for CCI studies before the steady state creep crack growth conditions at the crack tip have been established, will result in high scatter in correlation. Therefore, the validity criterion of transition time, t_T, must be taken into account before using C^* for CCI correlation. However, the use of K and K^{c}_{mat} for correlation of CCI resistance leads to less scatter in plots where the CCI resistance behaviour of different weldment zones are determined more clearly. The CCI resistance data ranking for the weldment zones by the correlation of data with K^{c}_{mat} is similar to those of K correlation. It is observed that K^{c}_{mat} does not offer any advantage in terms of CCI studies. Therefore, the K correlation suffice for structural assessment purposes.

The use of different highly constrained specimen geometries, e.g. C(T), CS(T) and SEN(B), does not seem to affect the scatter in the data, hence the scatter in CCI and CCG correlations. On the other hand, the use of RNB(T) specimens data may lead to high scatter in CCI and CCG correlations. Therefore, the data from RNB(T) must be always validated by comparison with the data from other type of specimens.

CCG rates of different weldment zones of P22 at 550 °C and P91 at 600 °C are correlated with crack tip parameters K and C^*. The correlations with stress intensity factor, K, are consistent in early crack growth rates. However, they lose their consistency for later crack growth rates with increasing scatter, therefore, they should not be used for correlation of CCG rate in extensive (steady state) creep range. The use of C^*, on the other hand, yields more consistent correlations after the steady state creep crack growth conditions at the crack tip have been established. Comparison of CCG correlations of different weldment zones of P22 and P91 steels at 550 °C and 600 °C, respectively, directs attention to slightly lower resistances of P91 weldment zones than those of P22 weldment zones, which are opposite to the higher CCI resistance of P91 weldment zones.

The predicted plane stress and plane strain bounds using the NSW model are included in the correlation diagrams in order to provide comparison of different methodologies for creep crack behaviour and assessment. The NSW predictions are not consistent for all zones of weldments. Particularly, the predictions of P22 WM CCG behaviour direct attention to the need for revision of the model. This issue is being addressed by NSW authors that led to a modified NSW formula [115]. The NSW model was proposed based on the BM studies. Extension of its applicability to weldments is sought in present study.

It should be noted that increase in scatter in later stage of crack growth rates corresponds to the increasing effect of plastic deformation encountered at final stages of test with advancing crack size (Figure 5.31). Therefore, test durations must be maximised which will minimise the extent of plasticity and the level of crack tip blunting depending on the tensile strength of the material. Otherwise, when using short-term data to assess long term component life, the analysis should be treated with caution.

The scatter of data at moderate crack growth rates where C^* correlation proves reliable, must be related to microstructural deformation and fracture behaviour studied by post-test metallographic observations. The sources of scatter might be due to microstructural differences as in weldments, loading precision, environmental control, and data processing techniques. Confidence in the data will increase with the number of tests performed on any one batch of material. Using small number of tests rather than full set of available tests to characterise the CCG behaviour of a material, may yield unreliable results. This issue is addressed using the Master Curve approach where the data from a high number of tests are used to characterise the crack growth behaviour at high temperatures for a certain material or a set of materials with similar deformation and fracture behaviour.

Master curve concept is applied to the dataset obtained from the high temperature crack growth tests on P22 and P91 weldments, at 550 °C and 600 °C, respectively. The master curve is compared with the individual C^* correlations of crack growth rate of each weldment zone of P22 and P91. The obtained scatter band factor of 30.9 reveals that the master curve may lead to error up to one order of magnitude in the estimated crack growth rate. It is observed that while the master curve fits very well to the C^* correlations of P22 BM, P22 WM and P91 BM, it gives lower values than the correlations of P22 HAZ, P91 HAZ and P91 WM at later crack growth rates. Particularly, the C^* correlation of P91 BM complies excellently with the master curve. However, master curve estimations for both P22 HAZ at 550 °C and P91 HAZ at 600 °C, which are known to be critical weldment zones, are very optimistic compared to the experimental data for a wide range of crack growth rate. However, note that the master curve obtained for P22 and P91 weldments estimates the crack growth rate satisfactorily at earlier crack growth rates, i.e. in the range of $10^{-4} – 10^{-2}$ mm/h. This range of crack growth rate has particular importance for engineering applications, such as component design and life estimation.

6.3. METALLOGRAPHIC STUDIES

Post-test metallographic examinations conducted on specimens show the difference in deformation behaviour of coarse grained ferritic P22 and fine grained martensitic-bainitic P91 steel weldments leading to fracture under creep conditions. Comparison between damage mechanisms controlling the crack initiation and growth reveals an increased CCI resistance of P91 weldments compared to slight increase in CCG resistance of P22 weldments.

Higher crack tip damage seen in P22 BM (Figure 5.112) than that in P91 BM (Figure 5.114) indicates a creep deformation process mainly at grain boundaries. Formation of microvoids either at grain boundaries or in the carbide-rich sub-grains of P22 (Figures. 5.117 to 5.118) leads to microcracks and secondary cracks ahead of the main crack tip. Furthermore, sub-grain formation which has probably occurred during heat treatment leads to increased number of grain boundaries, therefore, increased susceptibility to creep damage. These observations together with smaller CTOD measured at crack initiation (Figure 5.112) explain the reduced CCI resistance determined on P22 weldments (Section 5.2.4). Several secondary cracks observed around the crack tip of the C(T) specimen of P22 BM shows that the coalescence of microvoids at grain boundaries leading to microcracks is more likely to occur for this material. This leads to a lower crack resistance measured in CCI studies.

On the other hand, P91 BM shows significantly less microcracks and secondary cracks on the crack plane (Figure 5.115) which is related to lower susceptibility to pore formation at grain boundaries. The creep damage is mostly seen along prior austenite grain boundaries which are delineated with carbide precipitates and grain boundary failure at hard phases (Figure 5.122). Grain boundary failure is particularly seen around smaller grains. It leads to disintegration of whole sub-grain causing large pore formation along deformation bands following the sequence of 1) grain boundary damage, 2) opening (debonding) of damage particle, 3) Falling of the debonded particle (Figure 5.120). This is a micromechanical process of creep damage in which large grains resist deformation while smaller grains fail. Therefore, it is concluded that large transformed bainitic structure of P91 with less prior austenite grain boundaries leads to much less grain boundary void formation compared to P22. This case also sheds light on the increased CCI resistance of P91 steel, which is given in Section 5.2.4. However, debonding of gradually increasing number of smaller grains will threaten the integrity, hence the performance of P91 in high temperature service. This case directs attention to long-time strength problem of P91, which is pronounced in slightly reduced CCG resistance of P91 compared to P22 (Section 5.2.5).

Determination of CCI and CCG properties of different weldment zones by fracture mechanics tests requires validation by use of post-test metallographic examination of specimens. Advance or even jump of crack into a different weldment zone which differs from the one in which the starter crack has been introduced may lead to acquisition of untargeted data or even to invalidation of the test. Therefore, in crack initiation and growth testing of weldments which exhibit heterogeneous microstructure and interfaces between different weldment zones, starter crack position has utmost importance. It determines the crack tip behaviour by growing on the crack plane, if positioned properly, or leads to crack deviation by forming unbroken ligaments. Crack deviation due to the lower creep resistance of another weldment zone is a common case and it sometimes occurs by separation of crack from initial crack, where new crack propagates independently (Figure 5.124). Note that such a separation cannot be detected by PD crack monitoring method. Hence, post-test metallographic examination is imminent.

Furthermore, directionality of crack propagation encountered during testing of weldments due to heterogeneous solidification dendritic microstructure is an issue to be addressed supported by metallographic evidence (Figures 5.125-127). The C^* correlation of the crack growth rate of the SEN(B) specimen of P22 WM (Figure 5.33) required metallographic evidence (Figure 5.36) for a proper interpretation of fracture behaviour. The correlation has two different stages, namely Stage I and Stage II, where a lower crack growth rate followed by a higher crack growth rate is observed, respectively. Post-test metallographic examination reveals that the shift from Stage I to Stage II corresponds to a sharp change of direction of the crack growth path, following a zigzag route (Figure 5.36). Deviation of crack path following crack initiation is seen to follow weld metal solidification dendrites. Higher deformation is seen in Stage II. Note that, in Stage II, the damage accumulates, similar to Stage I, in the direction of dendrite cooling structure. However, the crack is forced to deviate to main crack plane. Consequently, it propagates perpendicular to dendrite cooling structure by coalescence of microcracks leading to zigzag crack propagation that conforms to the slip line field theory [109].

In most cases, deviation at crack path due to heterogeneous microstructure of weldments is the main source of scatter in early crack growth rate data, which are correlated with crack tip parameters, K or C^*. Additionally, the directionality of crack propagation directs attention to presence of weaker directions (Figure 5.127) in heterogeneous microstructure of weldment. The use of tensile and creep strength properties obtained from bulk deformation of ST test may lead to scatter in calculation of crack tip parameters. This supports the choice of testing of MT specimens sampled from thin weldment zones which yield reliable local material properties.

The metallographic study included behaviour of microstructural constituents as well as the orientation of the crack during crack growth. This is particularly important in interpretation of CCG behaviour when increase or decrease in crack growth rate may be described by local phenomena as reported in Chapter 5. Furthermore, such information is needed in material microstructural design and defect assessment in service components. Note that this industrially vital issue is not considered in the only available high temperature CCG testing standard, ASTM E1457-00 [3], where only testing of base metal is considered.

6.4. FAILURE ASSESSMENT USING DEFECT ASSESSMENT METHODS

The British TDFAD and the German 2CD methods are the most commonly used European methods applied for defect assessment of structures in determining the crack initiation. The TDFAD and 2CD methods are originally developed for determination of CCI in austenitic stainless steels and ferritic steels, respectively. The fundamental principles of both methods rely on fracture behaviour and creep rupture behaviour of a material at a certain temperature. They are both capable of capturing level of contribution of crack tip damage and ligament (farfield) damage for crack initiation. They could be both promoted as a reliable defect assessment of a large number of materials showing ductile fracture behaviour. However, this requires further validation by experimental data, especially for materials and weldment zones which exhibit brittle fracture behaviour.

Specimen geometry effect is observed concerning constraint effect which is noted for C(T), CS(T), SEN(B) and RNB(T) specimens. Notch effect with increased local constraint is seen in C(T) and CS(T) specimens. It is remarkable that both TDFAD (Figure 5.91) and 2CD (Figure 5.98) are able to capture the dominant mode at crack initiation in the RNB(T) specimen of P22 WM tested at 550 °C for 2074 hours where low constraint bulk deformation by pore formation at ferritic grain boundaries with a typical concentration at 0.13 mm distance from the notch is seen (Figure 5.92). These observations indicate that both the TDFAD and 2CD methods can successfully estimate CCI for a wide range of loading and constraint conditions.

However, while the crack initiation in the SEN(B) specimens from P22 WM cannot be determined by the TDFAD (Figure 5.91), the 2CD (Figure 5.98) can capture the crack initiation where crack tip damage mode is more dominant due to high constraint effect of SEN(B) geometry. This case emphasises that the use of TDFAD method for highly constrained defects in engineering components is a concern. This aspect points out the need for further study of applicability of these methods in assessment of materials other than that they are established for.

Higher scatter in the TDFAD estimations than that in the 2CD estimations recalls the use of crack initiation toughness, K^{c}_{mat}, in calculation of crack tip parameter, K_r, of TDFAD (Equation 2.87), which differs from 2CD in which K_{Ii} is used in calculation of crack tip parameter R_K (Equation 2.89). The K_{Ii} of 2CD is the magnitude of the stress intensity factor at the engineering definition of crack initiation (e.g. Δa=0.2 or 0.5 mm) which is obtained from the scattered experimental data. Note that the scatter in stress intensity factor, K, is also inherited during calculation of the K^{c}_{mat}. The use of creep strains in calculation of K^{c}_{mat} (Equation 2.88) introduces additional experimental scatter, which also leads to higher scatter in CCI estimation by TDFAD than by 2CD.

6.5. SENSITIVITY ANALYSIS

Two different approaches, namely deterministic and probabilistic sensitivity analyses are performed in present work. Deterministic sensitivity analysis is performed for a unique input parameter by changing it stepwise in a fictitious variation range and calculating output parameters. The variation given to testing parameters are assumed in realistic ranges, which might have referred to a measurement error and miscalculation. In deterministic sensitivity analysis, the sensitivity of each output parameter to the unit variation of each single input parameter is illustrated by tornado diagrams. On the other hand, the probabilistic approach is applied by use of the Monte Carlo simulation, which is a stochastic technique using random numbers and probability statistics to obtain an answer regarding its probability.

Regardless of the analysis method used, the significance of sensitivity analysis is noted where small variations at input parameters used in calculation of crack tip parameters or the parameters used in defect assessment procedures that might lead to drastic deviations of calculated output parameters. Impact of each single input parameter on the obtained results must be determined and presented accordingly. The effect of variation of creep exponent, n, on C^* correlation of crack growth rate of a C(T) specimen of P22 BM (Figure 5.102) illustrated how crucial the extent of significance of the effect on calculated parameters can be. Therefore, the suggested factors of safety in high temperature defect assessment methods of TDFAD and 2CD are of importance. The application of those methods mainly depends on experimentally determined high temperature crack growth data. Therefore, determination of an optimum safety factor requires the sensitivity analysis of the used high temperature experimental data. The Monte Carlo simulation which is performed to determine the cumulative effect of a row of geometrical parameters and the test load for a CS(T) specimen of P22 BM (Figure 5.107), showed how high the extent of the cumulative effect of slight variations in input parameters on estimations by defect assessment procedures can be.

7. CONCLUSIONS

Deformation and fracture behaviour of similar weldments of P22 and P91 steels at high temperatures were studied. The obtained data and information is used for defect assessment of components made of these materials by using industrial approaches, namely TDFAD and 2CD. MT and fracture mechanics tests were conducted on specimens machined out of different weldment zones (BM, HAZ, WM). The test environment was ambient air and test temperatures were 550 °C and 600 °C for P22 and P91 weldments, respectively. The testing procedures of the recent CoP [6] which was drafted with contribution from present study that introduced novel aspects into high temperature CCI and CCG testing of weldments were used in this study.

The specimen size and complex interactions between different zones of weldments, such as shielding effect, make the use of ST specimens difficult to determine tensile properties of very narrow weldment zones. Therefore, the testing technique which introduces the use of very thin (0.5 mm) MT specimens for high temperature tensile testing of weldments has been used in the reported work. It has been found out that MT specimens with as EDM machined surface conditions could show scatter in data due to possible surface defects introduced during EDM machining. However, enhancement of surface conditions particularly by polishing reduced the scatter in data and produced similar strength and deformation properties where stress and strain are considerably lower than those of ST tests. However, the obtained data followed a similar order of properties for the tested weldment zones as in ST tests. Correction factors were proposed for MT tensile properties to match the ST tensile properties which are taken as material properties. Test loading rate dependency of tensile properties and damage characteristics were reported. Deformation and damage locations were studied by OM and SEM techniques on side surfaces of tested MT specimens. It has been observed that damage and fracture sides in MT specimens are comparable to those sites observed in the vicinity of crack tips of specimens from P22 and P91 weldments. It has been concluded that the use of MT specimen testing method would provide data and information for assessment of components at high temperatures, where complex interactions between different weldment zones and directionality of material properties in weldments, which affect ST results can be eliminated.

The CCI and CCG properties of P22 and P91 steel weldments were determined at 550 °C and 600 °C, respectively. Industrial type specimens of C(T), CS(T), SEN(B) and RNB(T), were used in fracture mechanics tests. Although not standardised yet, use of different specimen geometries enables study of constraints seen in components due to geometry effects and loading mode.

The CCI resistances of different weldment zones of both steel weldments were correlated with crack tip parameters K, K^c_{mat}, and C^*. A higher CCI resistance of P91 steel weldment is seen where the high resistance is correlated with micromechanical aspects during metallographic studies. A reduced susceptibility to grain boundary pore formation was related to the enhanced CCI resistance of P91 weldment. It has also been shown that post-test CTOD measurement on polished side surface of tested specimen, which is developed at GKSS Research Centre with contribution of present work, could be used for determination of CCI resistance of materials.

Comparison of CCI resistance correlations with different loading parameters has shown that the use of C^* as the correlation parameter leads to high scatter, since the steady state creep conditions at the crack tip have not been fully established yet. It has been shown that although reliable correlations with K^c_{mat} can be obtained, which are closer to K correlations, scatter in data is increased. It has been concluded that K^c_{mat} did not offer any advantage in CCI correlations over stress intensity factor, K.

The CCG resistances of P22 and P91 weldment zones were correlated with loading parameters K and C^*, where consistent correlations for earlier and later crack growth rates were obtained with K and C^*, respectively. Very low CCG resistance of P91 WM is of industrial interest that directs attention to the importance of life assessment of welded P91 components at high temperatures. Increased scatter in C^* correlations at later stage of crack growth rates was related to the increasing effect of plasticity during crack growth. Therefore, longer test durations together with increased number of tests are required for more reliable data for assessment.

It has been concluded that the use of different highly constrained specimen geometries, e.g. C(T), CS(T) and SEN(B), did not affect the scatter in both CCI and CCG correlations. On the other hand, the use of RNB(T) specimen in which extensive bulk deformation with little crack extension takes place, might lead to scatter in data. Therefore, the data from RNB(T) specimens relevant to bar shape components should always be validated by comparison with data from conventional (i.e. C(T)) specimen geometries.

The master curve concept has been introduced to the high temperature CCG dataset including all weldment zones of P22 and P91. It has been shown that the master curve fitted to entire data showed good agreement with CCG correlations of P22 BM, P22 WM and P91 BM. For the crack growth range of 10^{-4} to 10^{-2} mm/h, which is important in engineering applications, the master curve yielded satisfactory estimates.

Different CCI and CCG behaviours of P22 and P91 steel weldments were related to micromechanical aspects deduced from post-test metallographic examinations. Higher susceptibility to grain boundary pore formation of P22 is noted. It has been observed that damage in P22 was initiated by excessive pore formation at ferritic grain boundaries indicating a creep weak material compared to P91. On the other hand, despite the creep damage seen along large prior austenite grain boundaries, it has been observed that damage at the crack tip was primarily due to grain boundary failure around smaller sub-grains, which led to debonding of whole sub-grain. It has been concluded that large transformed bainitic structure of P91 with less prior austenite grain boundaries led to much less grain boundary pore formation compared to P22, which explained the higher CCI resistance of P91.

It has been shown that post-test metallographic examinations are of utmost importance among the novel aspects of high temperature testing of weldments. Heterogeneous microstructure of weldments which leads to complex interactions between weldment zones and directionality of material properties requires surely the interpretation of high temperature test results together with metallographic evidence.

Defect assessment procedures, the British TDFAD and the German 2CD have been implemented using the test data from P22 and P91 weldments. The major aim was to check the performance of these methods with the data from weldments which might exhibit complex behaviour. Different types of constraints at crack tip due to specimen geometry effect and weldment zone size are considered. It has been observed that both procedures were consistent with the experimental data including the HAZ's. When constraint effects due to specimen geometry are considered, both methods were able to capture whether the crack initiation was mostly by crack tip or ligament damage controlled. The higher scatter in TDFAD estimations has been related to the use of K^c_{mat}, which is used in calculation of the ratio of K_r for TDFAD.

The sensitivities of high temperature CCG data and defect assessment procedures have been studied by deterministic and probabilistic approaches. It is concluded that even slight variations in input parameters, e.g. geometrical factors and material properties, might lead to an excessive deviation in estimations. Therefore, deterministic and/or probabilistic sensitivity analyses are needed to be performed in order to comprehend the extent of possible error which could be introduced during defect assessment. Thus thoroughly studied materials with reliable data enable defect assessment of engineering structures as in plants for safe operation.

References

[1] EU Project Advanced Creep, WG1, European Creep Collaborative Committee, Coordinator: A. Shibli, European Technology Development (ETD) Ltd., EC Project No: G1RT-CT-2001-05042.

[2] FITNET, EC Thematic Network Project no. GTC1-2001-43049, 2002-2006.

[3] ASTM E1457-00, “Standard test method for measurement of creep crack growth rates in metals”, ASTM 03.01, Philadelphia: ASTM 2000, PA 19103, USA.

[4] European Structural Integrity Society ESIS TC11, Working Group (WG) on High Temperature Testing Weldments, 2001-2005.

[5] EC Project CRETE: Development and Harmonisation of Creep Crack Growth Testing for Industrial Specimens – A Root to a European Code of Practice. EC Project No: GRD2-2000-30021.

[6] Dogan, B., Nikbin, K., Webster, G.A, Ceyhan, U., Petrovski B., Dean, D.W. Ainsworth, R.A., Chapuliot, S. and Holdsworth, S., ESIS TC11 WG on HTTW, “Code of Practice for High Temperature Crack Initiation and Growth Testing of Weldments”, Submitted to IIW SC STAND for ISO Standardisation, IIW 2005.

[7] Tada H., Paris P.C. and Irvin G.R., Stress Analysis of cracks – Handbook, ed. D.r. Co.1985, St. Louis.

[8] Webster, G.A. and Ainsworth, R.A., High Temperature Component Life Assessment, 1st Edition, Chapman & Hall, 1994.

[9] Broek, D., Elementary Engineering Fracture Mechanics, Sitjhoff and Noordholf, Alphen an den Rijn, The Netherlands, 1978.

[10] Larsson, S.G. and Carlsson, A.J., Influence of non-singular stress terms and specimen geometry on small-scale yielding at crack tips in elastic-plastic materials, Journal of Mechanics and Physics of Solids, Vol 21, 1973, pp. 263-277.

[11] O’Dowd N.P. and Shih C.F., Family of Crack Tip Fields Characterised by a Triaxiality Parameter – I Structure of Fields, Journal of Mechanics and Physics of Solids, Vol 39, 1991, pp. 989-1015.

[12] Rice, J.R. “A path independent Integral and the Approximate Analysis of Strain Concentration by Notches and Cracks”, Journal of Applied Mechanics, Vol 35, 1968, pp. 379-386.

[13] Hutchinson, J.W., “Singular Behaviour at the End of Tensile Crack Tip in a Hardening Material”, Journal of Mechanics and Physics of Solids, Vol.16, 1968, pp13-31.

[14] Rice, J.R. and Rosengren, G.F., “Plane Strain Deformation near a Crack Tip in a Power Law Hardening Material”, Journal of the Mechanics and Physics of Solids, Vol. 16, 1968, pp. 1-12.

[15] Anderson T.L., Fracture Mechanics – Fundamentals & Applications, CRC Press, 1991, pp. 254-264.

[16] Landes, J.D. and Begley, J.A., “A Fracture Mechanics Approach to Creep Crack Growth”, ASTM STP, 590, American Society for Testing and Materials, Philadelphia, 1976, pp 128-148.

[17] Saxena, A., Creep Crack Growth under Non-steady State Conditions, ASTM STP 905. American Society for Testing and Materials, Philadelphia, 1986, pp. 185-201.

[18] Ohji, K., Ogura, K., and Kubo, S., Transactions, Japanese Society of Materials Engineers, Vol. 42, 1976, pp 350-358.

[19] Nikbin, K.M., Webster, G.A., and Turner, C.E., ASTM STP 601, American Society for Testing and Materials, Philadelphia, 1976, pp. 47-62.

[20] Hoff, N.J., “Approximate Analysis of Structures in the Presence of Moderately Large Creep Deformations.” Quarterly of Applied Mathematics, Vol.12, 1954, pp 49-55.

[21] Riedel, H., “Creep Crack Growth” ASTM STP 1020, American Society for Testing and Materials, Phiadelphia, 1989, pp 101-126.

[22] Riedel, H., Rice, J.R., Tensile Cracks in Creeping Solids, ASTM STP 700, American Society for Testing and Materials, Philadelphia, 1980, pp. 112-130.

[23] Tan, M., Célard, N. J. C., Nikbin, K. M and Webster, G. A., Comparison of Creep Crack Initiation and Growth in Four Steels Tested in HIDA, International Journal of Pressure Vessels and Piping, 2001, 78(12), pp. 737-747.

[24] Nikbin, K. M., Smith, D.J. and Webster, G.A., An Engineering Approach to the Prediction of Creep Crack Growth, Journal of Engineering Materials and Technology, 1986, 108, pp. 186-191.

[25] Yatomi, M., Factors Affecting the Failure of Cracked Components at Elevated Temperature, Ph.D. and D.I.C. Thesis, Department of Mechanical Engineering, Imperial College London, 2003.

[26] Yatomi, M., Nikbin, K. M., O'Dowd, N. P. and Webster, G. A., Theoretical and Numerical Modelling of Creep Crack Growth in a Carbon-Manganese Steel, Engineering Fracture Mechanics, 73, 2006, pp.1158-1175.

[27] Holdsworth, S.R., “Initiation and early growth of creep cracks from pre-existing defects”, Materials at High Temperatures, Vol.10, No.2, May 1992, pp.127-137.

[28] Dogan, B., Petrovski, B. and Ceyhan, U., “Significance of Creep Crack Initiation for Defect Assessment “U., Proc. Int. Conf. BALTICA VI, VTT Symposium 234, Vol.2, Eds. J.Veivo and P.Auerkari, Espoo, Finland, pp.595-607.

[29] R5, “Assessment procedure for the high temperature response of structures”, BEGL Procedure, British Energy-UK, Issue 3, 2003.

[30] Ewald, J., Sheng, S., The two criteria diagram for creep crack initiation and its application to an ip-turbine, Mater High Temp., 15, 1998, pp. 281-288.

[31] Ainsworth R.A., “The initiation of Creep Crack Growth”, Int. J. Solids Struct., 18, pp.873-881.

[32] Ainsworth, R. A. and Budden, P. J., Design and assessment of components subjected to creep, J. Strain Anal., Vol.29, 1994, pp.201-208.

[33] Austin, T. S. P. and Webster, G. A., Prediction of Creep Crack Growth Incubation Periods, Fatigue and Fracture of Engineering Materials and Structures, 1992, 15(11), pp. 1081-1090.

[34] Davies, C.M., Dean, D.W., Nikbin, K.M. and O’Dowd, N.P., Interpretation of Creep Crack Initiation and Growth Data for Weldments, special issue on Int. Conf. WELDS 2005, Engineering Fracture Mechanics, submitted 2006.

[35] BS7910, "Guidance on methods for assessing the acceptability of flaws in metallic structures", British Standards Institution, 2000.

[36] RCC-MR design and construction rules for mechanical components of FBR nuclear islands. AFCEN, Tour Framatome, F92084 Paris La De´fense Cedex; Edition 2002.

[37] Nikbin, K.M., Proceedings of Int. Conf. CREEP 7, JSME, No:0.1-201, Ed. Y. Asada, 2001,123-129.

[38] Dogan, B., Ceyhan, U., Nikbin, K.M., Petrovski, B. and Dean, D. W., "European Code of Practice for Creep Crack Initiation and Growth Testing of Industrially Relevant Specimens", J.of ASTM Int., Vol.3, No.2, Feb.2006.

[39] Allen, D.J., Proc 6th Int. Conf. PARSONS 2003, Engineering Issues in Turbine Machinery, Power Plant and Renewables, Eds. A Strang et.al., 10 M-UK, 281-294, 2003.

[40] Bicego, V et.al., Proc. Int. Conf. on Plant Life Assessment Santander Ed. R.Hurst and D. Mc. Garry, 211-220, 2001.

[41] Shibli, I.A., Proc 6th Int. Conf. PARSONS 2003, Engineering Issues in Turbine Machinery, Power Plant and Renewables, Eds. A Strang et.al., 10 M-UK, 261-279, 2003.

[42] Brett, S. J., "Cracking experience in Steam Pipework in National Power", Conf. materials and Weld Tech.in Power Plants, Essen, Germany, 1994.

[43] Storesund, J. and Shan, T.T., Geometrical Effect on Creep in Cross Weld Specimens. Int. Journal Vessels & Piping 62 (1995), pp. 179-193.

[44] Chen, W., McQueen, R.L., Princ, J. and Sidey, D., "Metallurgical experience with high temperature piping in Ontario hydro", ASME PVP, 21, Service Experience in Operation Plants, ASME, New York, 1991.

[45] Parker, J. D., Conf. The creep fracture behaviour of thick section multipass welds, "Integrity of High Temperature Welds", Nottingham UK, IOM Communications / Proffesional Eng. Pub. UK, 1998.

[46] Williams, J.A., Hyde T.H and Sun, W., Proc. 9th In. Conf. Creep and Fracture of Engineering Materials and Structures, Ed. J.D. Parker, 10 M-UK, (2001), 499-510.

[47] Ewald, J. and Keienburg, G., "A two criteria diagram for creep crack initiation", Int. Conf. Creep, Tokyo, 173-178, April 1986.

[48] Dean, D.W., Patel, R.D., Klenk A., Müller, F, "Comparison of procedures for the assessment of creep crack initiation", Int. HIDA-4 Conference, Cambridge, UK, September 2004.

[49] Dogan, B., Petrovski, B., and Ceyhan, U., "High Temperature Crack Initiation and Defect Assessment of Power Plant Steel Weldments" Proceedings of ECCC Creep Conference "Creep & Fracture in High Temperature Components – Design and Life Assessment Issues", Eds. I.A. Shibli, S.R. Holdsworth, G. Merckling, London, UK, 12-14 Sept. 2005, pp. 724-743.

[50] Dogan, B., and Ainsworth, R., "Defect assessment procedure for low to high temperature," ASME Conference PVP2003-2032, Vol. 463, ASME, Cleveland, OH, pp. 105–111, 2003.

[51] Dogan, B., "High temperature defect assessment procedures," Int. J. Pressure Vessels Piping, 80, 149–156, 2003.

[52] Auerkari, P. et.al. Int. Seminar Advanced Creep Data for Plant Design and Life Extension, ECCC, Prag, 87, 2003.

[53] Maskell, R., EC PLAN Thematic Network Project CTC2 Doc.98.03 Version III., 1999.

[54] Goodall, I.W. (Ed.), Assessment procedure for the high temperature response of structures, R5 Procedure, Issue 2, British Energy-UK., 1998.

[55] ASME, Boiler and Pressure Vessel Code, Case N-47 (29), Class 1 components in elevated temperature service, Section III, Division I, ASME, New York, 1991.

[56] Drubay, et al., "Defect assessment procedure: a French approach", ASME PVP, Vol. 266, pp. 113-118, 1993.

[57] R6, Assessment of integrity of structures containing defects, Procedure R6, Revision 4, BEGL Procedure, 2001.

[58] Clayton, A. et al., A review of structural integrity in UK industry, HMSO, London, pp. 1-31., 1991.

[59] A16, "Guide for leak before break analysis and defect assessment", Appendix A16, RCC-MR Edition 2002, AFCEN No: 94, 2002.

[60] ASME Boiler and Pressure Vessels Code, “Section XI, Rules for in-service inspection of nuclear power plant components”, The American Society of Mechanical Engineers, 1995.

[61] ASME Section III, Rules for construction of nuclear power plant components, Division 1, Subsection NH , Class 1 components in elevated temperature service, ASME, 1995.

[62] ECCC Recommendations – Vol.3 Part IV (Issue 2), Testing Practices for Creep Crack Initiation, Ed. A. Klenk, 15.08.2005.

[63] Irwin, G.R., Fracture, in: Encyclopedia of Physics, Vol. VI, Ed.: S. Fluegge, Springer, New York, 1958.

[64] Dogan, B., Saxena, A. and Schwalbe, K.-H., "Creep Crack Growth in Creep-Brittle Ti-6242 Alloys", Materials at High Temperatures,Vol 10, No 2, May 1992,pp 138-143.

[65] Holdsworth, S.R. and Cunnane, D.J., 'Lifetime prediction of components containing defects', COST 501-II WP5C-UK5 Final Report, RM93/006, 1993.

[66] Dogan, B. and Ceyhan, U., High Temperature Failure Assessment of Weldments, ECF16 Proceedings of Conference on Failure Analysis of Nano and Engineering Materials and Structures, 3-7 July 2006, Alexandroupolis, Greece.

[67] European Structural Integrity Society, ESIS Procedure for Determining the Fracture Behaviour of Materials, ESIS P2-92, 1992.

[68] British Standards Institution, Fracture Mechanics Toughness Tests. Part 4. Method for Determination of Fracture Resistance Curves and Initiation Values for Stable Crack Extension in Metallic Materials, BS 7448: Part 4: 1997, 1997.

[69] American Society for Testing and Materials, Standard Test Method for J-Integral Characterisation of Fracture Toughness, ASTM E 1737-96, 1996.

[70] Ainsworth, R.A., “The Use of a Failure Assessment Diagram for Initiation and Propagation of Defects at High Temperatures”, Fatigue Fract. Engng. Mater. Struct., 16, 1091-1108, 1993.

[71] Hooton, D.G., Green, D., and Ainsworth, R.A., “An R6 Type Approach for the Assessment of Creep Crack Growth Initiation in 316L Stainless Steel Test Specimens”, Proc. ASME PVP Conf., Minneapolis, 287, 129-136, 1994.

[72] Ainsworth, R.A., Hooton, D.G. and Green, D., “Further Developments of an R6 Type Approach for the Assessment of Creep Crack Incubation”, Proc. ASME PVP Conf., Honolulu, 315, 39-44, 1995.

[73] Ainsworth, R.A., Hooton, D.G. and Green, D., “Failure Assessment Diagrams for High Temperature Defect Assessment”, Engng. Fract. Mech., 62, 95-109, 1999.

[74] Hooton, D.G. and Green, D., The Determination of Fracture Toughness Values for Use with Time-Dependent Failure Assessment Diagrams, AEA Technology Report SPD/D(96)/579, 1996.

[75] Dean, D.W. and Hooton, D.G., “A Review of Creep Toughness Data for Austenitic Type 316 Steels”, BEGL Report E/REP/GEN/0024/00, 2003.

[76] Lamb, M., “A Review of Creep Toughness of Ferritic Steels”, BNFL Magnox Report M/TE/GEN/REP/0171/99, Issue 2, 2002.

[77] Ewald, J., Sheng, S., Klenk, A., Schellenberg, G., “Engineering guide to assessment of creep crack initiation on components by two criteria diagram”, Int. J of Pressure Vessels and Piping, 2001, 78, 937-949.

[78] Ceyhan, U. and Petrovski, B., “Comments about sources of scatter-CRETE CoP contribution”, Internal GKSS document, Sept. 2004.

[79] Jovanovic, A., Colantoni, D., Balos, D., Wagemann G, Le Mat Hamata, N. and Deschanels, H., “Alias-HIDA, A knowldge-based system for probabilistic and sensitivity analysis of creep and fatigue crack growth in high temperature components”, OMMI (www.ommi.co.uk), Vol.3, Issue 2, August 2004.

[80] Yatomi, M. and Nikbin, K., “Life management in creep/fatigue using deterministic and probabilistic modeling, EPRI, Conference on ‘Life Management’, Orlando, March 2002.

[81] Anderson, T.W. and Finn J.D., “The New Statistical Analysis of Data”, 96 Edition, Springer Verlag, December 1996.

[82] Le Mat Hamata, N., “Guidelines and specifications for the implementation of the probabilistic procedure applied to creep and/or fatigue crack growth”, HIDA Applicability Project, Report HA/WP2/2, ETD Ltd UK, September 2003.

[83] British Standards Institution Guide to methods for the assessment of the influence of crack growth on the significance of defects in components operating at high temperatures. PD 6539, 1994.

[84] Ainsworth, R.A., “Sensitivity Analysis in Creep Crack Growth – British Energy Experience”, Int. HIDA - 4 Conf., Cambridge, UK, 20-22 Sept. 2004.

[85] Sensitivity Analysis, Eds. A. Saltelli, K. Chan, E. M. Scott, John Wiley & Sons Ltd., England, 2000.

[86] http://www.visionengineer.com/mech/monte_carlo_simulation.shtml.

[87] EC Project SOTA: SMT 2070, Development of creep crack growth testing and data analysis procedures for welds.

[88] Tan, M., Celard, N.J.C, Nikbin, K.M. and Webster, G.A., “Comparison of creep crack initiation and growth in four steels testes in HIDA”, Int. J. Pres. Vessels and Piping, 78, 2001, pp.737-747.

[89] Dogan, B., Petrovski, B., “Creep Crack Growth of High Temperature Weldments”, International Journal of Pressure Vessels and Piping, 78, 2001, pp. 795-805.

[90] The T91/P91 Book, Vallourec & Mannesmann Tubes, 2nd Edition, 2000.

[91] NRIM Creep Data Sheet on the Elevated Temperature Properties of Grade T/P91 Steel, National Research Institute for Metals, Japan, No.43, 30.09.1996.

[92] http://www.dti.gov.uk/energy/coal/cfft/ccy/pub/pdfs/r2224e.pdf.

[93] EPRI Technical Report, "The Grade 22 Low Alloy Steel Handbook" Draft report, April 2005.

[94] Hainsworth, J. and Tanzosh, J.M., "Welding of 9Cr1MoV Material", Proceedings of Maintenance and Repair Welding in Power Plants, December 9-11, 1991, Orlando, FL, USA, pp. 12-29.

[95] Shibli, A., "P/T91 Fabrication, Welding, Heat Treatment, Oxidation, Damage Mechanisms& Integrity/Life Assessment", Training Course, European Technology Development Ltd., UK, 5-6 December 2005.

[96] King, J., et.al., "Weldability of Mod - 9Cr1Mo Steel", ORNL-6299, September 1986.

[97] Dogan, B., Proc. 2nd Int. Conf. Integrity of High Temperature Welds, Ed. T.H. Hyde, IOM-UK, 2003.

[98] Sekhar, N. C., and Reed, R. C., 6th ASM International-International Trends in Welding Research Conference Proceedings, Pine Mountain GA, April 2002.

[99] Cam, G., Erim S., Yeni, C. and Kocak, M., Welding Journal, 1999, vol. 78(6), pp. 193-201.

[100] Ceyhan, U., Horstmann, M. and Dogan, B., "High Temperature Cross-Weld Characterisation of Steel Weldments by Microtensile Testing", Material at High Temperatures, in print, 2006.

[101] Ceyhan, U. and Dogan, B, "Deformation and Fracture Behaviour of P91 Steel Weldments at High Temperatures", Science and Technology of Welding and Joining, accepted on 25.05.2006, in print, 2006.

[102] Dogan, B. and Horstmann, M., "Laser scanner displacement measurement at high temperatures", Int. J. Pressure Vessels and Piping, 2003, vol.80, pp. 427-434.

[103] Schwalbe, K.-H., Heerens, J., Zerbst, U., Pisarski, H., Kocak, M., "EFAM GTP 02 – The GKSS test procedure for determining the fracture behaviour of materials", ISSN 0344-9629, GKSS Forschungszentrum Geesthacht GmbH, Geesthacht, 2004.

[104] 1100 Series Measurement and Control System, ZYGO Corporation, U.S.A., 1986.

[105] Dogan, B., Martens, H. and Schwalbe, K. H., "Measurement of Displacement by Laser Scanner in Fracture Mechanics Tests", Fifth IITT-International Conference "Laser 5", London, April 1989.

[106] Liu, H. and Dogan, B., " An advanced control concept and algorithm for long-term data acquisition in high temperature fracture mechanics tests", Journal of Testing and Evaluation, SEPT 1993, pp. 351-357.

[107] Davies, C. M., Kourbetis, M., O'Dowd, N. P. and Nikbin, K. M., "Experimental Evaluation of the J or C^* Parameter for a Range of Cracked Geometries", Fifth International ASTM/ESIS Symposium on Fatigue and Fracture Mechanics, Reno, NV, 18-20 May 2005.

[108] Cerjak, H., Hofer, P., Schaffernak, B, ISIJ International , 1999, 39, pp. 874-888.

[109] Dieter, G., "Mechanical Metallurgy", McGraw-Hill Science/Engineering/Math, 1986

[110] Dogan, B. “High Temperature Testing of Weldments”, ESIS TC11, WG: on High Temperature Testing Weldments, 2001-2005.

[111] Dogan, B., Nikbin, K., Ceyhan, U., Petrovski B. and Dean, D.W “Code of Practice for High Temperature Testing of Weldments”, International Journal of Pressure Vessels and Piping, Special Issue for Int. Conf. WELDS 2005, to be published in 2006.

[112] Dogan, B. and Ceyhan, U., Proc. Int. Conf. on Pressure Vessels and Piping - OPE2006, Chennai, India, 7-9. February 2006. http://www.ope2006chennai.com.

[113] ECCC Recommendations – Vol.7 (Issue 1, Draft 1), ECCC Recommendations for Creep Crack Initiation Assessments, 2005.

[114] Saxena, A., "Evaluation of C^* for the Characterisation of Creep Crack Growth Behaviour in 304 Stainless Steel," Fracture Mechanics: Twelfth Conference, 1980 ASTM STP 700, ASTM, pp. 131-151.

[115] Yatomi M., O’Dowd N.P, Nikbin K.M, Webster G.A., “Theoretical and numerical modelling of creep crack growth in a carbon–manganese steel” Engineering Fracture Mechanics 73, 2006, pp. 1158–1175.

[116] McCabe, D.E., Merkle, J.G. and Wallin, K., “An Introduction to the Development and Use of the Master Curve Method”, ASTM International Press, 2005.

[117] Lin, R.C. and Brocks, W., On a finite-strain viscoplastic law coupled with anisotropic damage: theoretical formulations and numerical applications, Arch Appl Mech, 2006, Vol. 75, pp. 315-325.

[118] Ewald, J., “Beurteilung von Risseinleitung und Risswachstum im Kiechbereich mit Hilfe eines Rissspitzen –Fernfeld-Konzeptes”, Mat.-wiss. U. Werkstofftechn. 20, 1989, pp. 195-206.

[119] Ewald, J., “Zwei-Kriterien-Diagramm für Kriechriss einleitung Berücksichtigung des Kriech – Verformungsvermögens (für ferritische Werkstoffe)”, FVW/FVHT, 26. Vortragveranstaltung am 28. November 2003.

[120] Arnswald, Blum, Neubauer, Poulsen, “Application of Structural Surface Examination for the testing of power plant components subjected to creep stress”, reprinted from VGB Kraftwerkstechnik July 1979.

[121] E. Lucon, V. Bicego, D. D’Angelo and C. Fossati: ASTM STP 1204, Philadelphia, PA, 1993.

[122] Dogan, B., Nikbin, K., Ceyhan, U., Petrovski, B., “Code of Practice for creep crack growth testing of industrial specimens” Journal of Strength Fracture and Complexity, accepted on 04.04.2006, in print, 2006.

[123] ASTM E 399-90, “Standard test method for plane-strain fracture toughness of metallic materials”, ASTM 03.01, Philadelphia: ASTM 2000, PA 19103, USA.

[124] BS 5447, Fracture Mechanics Toughness Tests, Part 4. “Method for determination of fracture resistance curves and initiation values for stable crack extension in metallic materials, British Standards Institution, UK, 1997.

[125] JSME Mechanical Engineers’ Handbook Fundamentals. A4, Strength of materials. Tokyo:JSME; 1984. p. 107.

[126] Ohji K, Ogura K, Kubo S. Convenient style of the J integral in the full cross section plasticity and its application to the creep crack problem. Trans Jpn Soc Mech Engrs 1978;44:1831–8.

Nomenclature

2CD	Two-Criteria-Diagram
A	Power law creep material constant
A′	Material constant in $\dot{a}$ correlation with K (Equation 2.47)
ACPD	Alternating Current Potential Drop
a	Crack length
a_o, a_f	Initial and final crack length measurements
Δa	Amount of crack growth
$\dot{a}$, da/dt	Crack growth rate
ASME	American Society of Mechanical Engineers
ASTM	American Society for Testing and Materials
B, B_n, B_e	Specimen thickness, net specimen thickness, effective specimen thickness
b	Ligament size
BM	Base Metal
BS	British Standard
CCI, CCG	Creep Crack Initiation, Creep Crack Growth
CDR	Constant Displacement Rate
CMOD	Crack Mouth Opening Displacement
CTOD, δ	Crack Tip Opening Displacement
CTOA	Crack Tip Opening Angle
C_o	Compliance at time zero
CoP	Code of Practice
C(T)	Compact Tension Specimen
CRETE	EC Project CRETE
CS(T)	C-Shape Specimen in Tension
C(t)	Crack tip parameter for transient creep
C_t	Crack tip parameter for short-term to extensive creep
C^*	Steady state creep fracture mechanics parameter
DCPD	Direct Current Potential Drop
DEN(T)	Double Edge Notch Tensile Specimen
D_c	Creep damage in ASME III Approach (Section 2.2.2.4)
D_f	Fatigue damage in ASME III Approach (Section 2.2.2.4)
D_o	Material constant in $\dot{a}$ correlations with C^* (Equation 2.49)
EC	European Commission
ECCC	European Creep Collaborative Committee
EDM	Electric Discharge Machining
ESIS	European Structural Integrity Society
E	Modulus of elasticity
E′	Effective modulus of elasticity for plane strain
F	Load, test load
F_{const}	Constant test load
f(a/W)	Geometry correction factor for K_I (Equation 2.35)
f_{ij}	Function describing elastic stress variation
FL	Fusion Line
FS	Fracture Surface
$F_c(\theta)$	Shape function for calculation of r_c (Equation 2.38)
g_{ij}	Function describing strain variation

HAZ	Heat Affected Zone
H	Material constant in $\dot{a}$ correlation with σ_{ref}
H^{LLD}	Geometric function to calculate C^* from load line displacement rate
H^{CMOD}	Geometric function to calculate C^* from crack mouth opening displacement rate
I_N	Function of N in HRR field
I_n	Function of n in HRR field
J	J-integral crack tip parameter
J_c	Material fracture toughness value in terms of J
J_{Ic}	Material plain strain fracture toughness value in terms of J
J_s	Analytical estimate of J
K, K_n	Stress intensity factor, Stress intensity factor for net section thickness
K_c	Material fracture toughness value
K_r	Non-dimensional crack tip damage parameter in TDFAD
K_{Ic}	Material plane strain fracture toughness value
K_{Ii}	Value of stress intensity factor at crack initiation (2CD)
K_{Iid0}	Value of stress intensity factor at t=0 h (2CD)
K^c_{mat}	Creep crack initiation toughness
L	Half span length of SEN(B) specimen
L_r	Non-dimensional ligament damage parameter in TDFAD
LLD	Load Line Displacement
LVDT	Linear Variable Displacement Transducer
M	Bending moment
m'	Material constant in $\dot{a}$ correlation with K (Equation 2.47)
MT	Microtensile
M(T)	Middle Crack Tension specimen
N	Plastic exponent
n	Power law creep stress exponent
n	Efficiency coefficient (Section 2.2.4.3)
OM	Optical Microscope
p	Material constant in $\dot{a}$ correlation with σ_{ref}
P_f	Maximum available pre-fatigue load
P22	2.25CrMo Steel in pipe form
P91	Mod-9CrMo Steel in pipe form
PD	Potential Drop
r	Distance from crack tip
r_c	Creep zone size
r_p	Plastic zone size
PWHT	Post Weld Heat Treatment
R_i	Inner radius of CS(T) specimen
R_K	Non-dimensional crack tip damage parameter in 2CD
R_m	Ultimate tensile strength
R_{mt}	Creep rupture strength (2CD)
$R_{p0.2}$	Yield strength calculated from 0.2% plastic strain
R_σ	Non-dimensional ligament damage parameter in 2CD
R_0	Outer radius of CS(T) specimen
RNB(T)	Round Notch Bar in Tension
RT	Room Temperature
SEM	Scanning Electron Microscope

SEN(B)	Single Edge Notch Specimen in Bending
SEN(T)	Single Edge Notch Specimen in Tension
SS	Steady State
SSC	Small Scale Creep
SSY	Small Scale Yielding
ST	Standard Tensile
T	Traction (Equation 2.1)
TC	Technical Committee
TDFAD	Time Dependent Failure Assessment Diagram
WM	Weld Metal
t	Time
t_r	Rupture time
t_i	Time for crack initiation (at $\Delta a=0.2$ mm and 0.5 mm)
t_T	Transition time from primary to steady-state creep
U	Area under load-displacement curve
U_e	Elastic component of area under load-displacement curve
U_p	Plastic component of area under load-displacement curve
U_c	Creep component of area under load-displacement curve
u	Displacement (Equation 2.13)
V_i	Value of the potential drop (PD) measurement at initiation
V_o, V_f	Initial and final values of the potential drop (PD) measurement
W	Specimen width or half width
W_s	Strain energy density
$\dot{W}_s$	Strain energy density rate
Y(a/W)	Geometry factor to calculate K
β	Factor describing plastic zone size
δ_i	Critical crack tip opening displacement
δ_5	Local CTOD measurement at initial crack tip at 5 mm distance
Δ_c	Creep component of load line displacement
$\dot{\Delta}_c$	Creep component of load line displacement rate
$\Delta^{LLD}, \dot{\Delta}^{LLD}$	Load line displacement, load line displacement rate
$\dot{\Delta}_c^{LLD}$	Creep component of the load line displacement rate
$\dot{\Delta}_i^{LLD}$	Instantaneous component of the load line displacement rate
$\dot{\Delta}_{i,e}^{LLD}$	Instantaneous elastic component of the load line displacement rate
$\Delta^{CMOD}, \dot{\Delta}^{CMOD}$	Crack mouth opening displacement, CMOD rate
ε, $\dot{\varepsilon}$	Strain, strain rate
ε_o	Instantaneous strain in creep test
ε^e	Elastic strain
ε_f^*	Multiaxial creep ductility
ε_f	Uniaxial creep ductility
ε_{ref}	Reference strain
$\tilde{\varepsilon}_{ij}$	Non-dimensional function in Equation 2.17
η^{CMOD}	Geometric factor to calculate C^* from CMOD rate
η^{LLD}	Geometric factor to calculate C^* from LLD rate
ϕ	Material constant in $\dot{a}$ correlation with C^* (Equation 2.49)
σ	Stress

σ_b	Nominal bending stress
σ_d	Nominal stress
σ_m	Membrane stress
σ_{n0}	Nominal stress in the farfield of a crack (2CD)
σ_r	Rupture stress
σ_{ref}	Reference stress
σ_Y	Yield stress
$\sigma_{0.2}^{c}$	0.2% inelastic strength; stress corresponding to 0.2% inelastic (plastic and creep) strain
$\tilde{\sigma}_{ij}$	Non-dimensional function in Equation 2.16
θ	Polar coordinate
ν	Poisson's ratio

APPENDIX A – SPECIMEN DETAILS AND GEOMETRICAL FACTORS USED FOR CALCULATION OF FRACTURE MECHANICS PARAMETERS

A.1 COMPACT TENSION SPECIMEN, C(T)

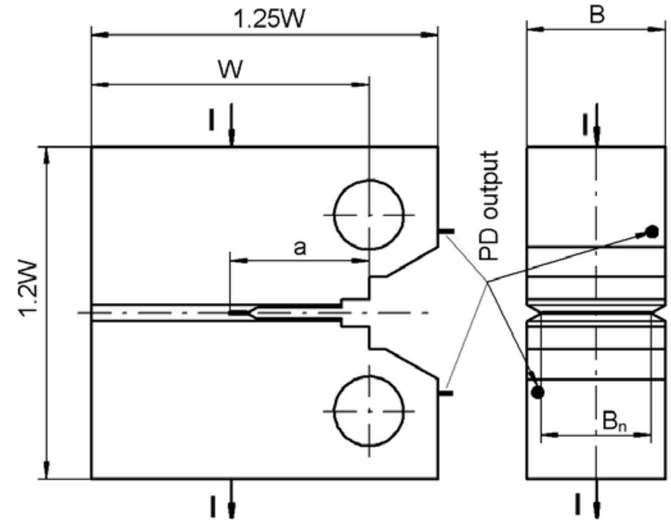

Figure A.1 – Details of the Compact Tension, C(T), specimen

Loading Arrangement: Pin loading tension

Y Function for Stress Intensity Factor, K [3]:

$$Y = \sqrt{\frac{W}{a}}\left[\frac{2 + a/W}{(1 - a/W)^{3/2}}\right]\left\{0.886 + 4.64\left(\frac{a}{W}\right) - 13.32\left(\frac{a}{W}\right)^2 + 14.72\left(\frac{a}{W}\right)^3 - 5.6\left(\frac{a}{W}\right)^4\right\} \qquad \textbf{(A.1)}$$

H Value and η Function for C^* [6]:

$$H^{LLD} = H^{CMOD} = n/(n+1) \qquad (A.2)$$

$$\eta^{LLD} = \eta^{CMOD} = 2.2 \pm 0.1 \qquad 0.45 \le a/W \le 0.7 \qquad (A.3)$$

A.2 C-SHAPE TENSION SPECIMEN, CS(T)

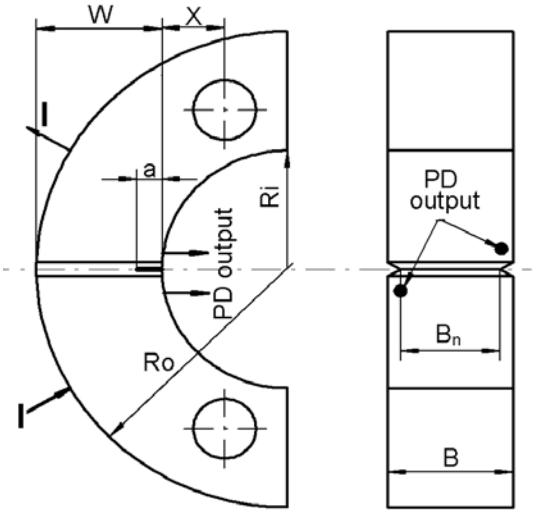

Figure A.2 – Details of the C-Shape Tension, CS(T), specimen

Loading Arrangement: Pin loading tension

Y Function for Stress Intensity Factor, K [123]:

$$Y=\sqrt{\frac{W}{a}}\left[3\frac{a}{W^2}+1.9+1.1\left(\frac{a}{W}\right)\right]\left[1+0.25\left(1-\frac{a}{W}\right)^2\left(1-\frac{R_i}{R_o}\right)\right]$$
$$\times\frac{(a/W)^{1/2}}{(1-a/W)^{3/2}}\left\{3.74-6.30\left(\frac{a}{W}\right)+6.32\left(\frac{a}{W}\right)^2-2.43\left(\frac{a}{W}\right)^3\right\} \tag{A.4}$$

H Value and η Function for C^* [6]:

$$H^{LLD}=H^{CMOD}=n/(n+1) \tag{A.5}$$

$$\eta^{LLD}=(7\frac{a}{W}-0.64)\pm0.6 \qquad 0.2\le a/W\le0.4 \qquad \begin{matrix}R_i/R_0=0.5\\ X/W=0.5\end{matrix} \tag{A.6}$$

$$\eta^{LLD}=(0.4\frac{a}{W}+2)\pm0.15 \qquad 0.4\le a/W\le0.55 \qquad \begin{matrix}R_i/R_0=0.5\\ X/W=0.5\end{matrix} \tag{A.7}$$

$$\eta^{CMOD}=(4.6-1.6\frac{a}{W})\pm0.2 \qquad 0.2\le a/W\le0.55 \qquad \begin{matrix}R_i/R_0=0.5\\ X/W=0.5\end{matrix} \tag{A.8}$$

A.3 DOUBLE EDGE NOTCHED TENSION SPECIMEN, DEN(T)

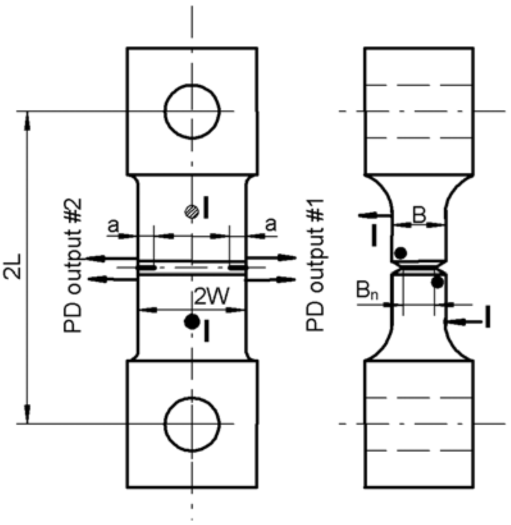

Figure A.3 – Details of the Double Edge Notched Tension, DEN(T), specimen

Loading Arrangement: Pin loading tension

Y Function for Stress Intensity Factor, K [7]:

$$Y = \sqrt{\frac{2W}{a}\tan\left(\frac{\pi a}{2W}\right)}\left[1 + 0.122\cos^4\left(\frac{\pi a}{2W}\right)\right] \qquad \text{(A.9)}$$

H Value and η Function for C^* [6]:

$$H^{LLD} = H^{CMOD} = \tfrac{1}{2}(n-1)/(n+1) \qquad \text{(A.10)}$$

$$\eta^{LLD} = (1.43\frac{a}{W} + 0.15) \pm 0.22 \qquad \begin{array}{l} 0.1 \le a/W \le 0.3 \\ 2 \le L/W \le 4 \end{array} \qquad \text{(A.11)}$$

$$\eta^{LLD} = (0.53\frac{a}{W} + 0.42) \pm 0.22 \qquad \begin{array}{l} 0.3 \le a/W \le 0.7 \\ 2 \le L/W \le 4 \end{array} \qquad \text{(A.12)}$$

$$\eta^{CMOD} = (1.26 - 0.80\frac{a}{W}) \pm 0.20 \qquad \begin{array}{l} 0.1 \le a/W \le 0.5 \\ 2 \le L/W \le 4 \end{array} \qquad \text{(A.13)}$$

$$\eta^{CMOD} = 0.86 \pm 0.20 \qquad \begin{array}{l} 0.5 \le a/W \le 0.7 \\ 2 \le L/W \le 4 \end{array} \qquad \text{(A.14)}$$

A.4 MIDDLE CRACKED TENSION SPECIMEN, M(T)

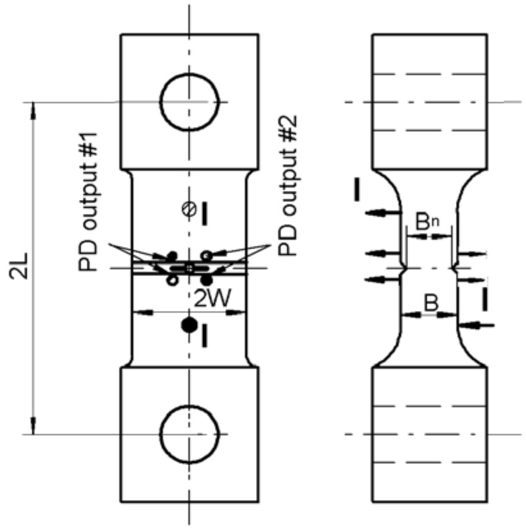

Figure A.4 – Details of the Middle Tension, M(T), specimen

Loading Arrangement: Pin loading tension

Y Function for Stress Intensity Factor, K [7]:

$$Y=\sqrt{\pi\sec\left(\frac{\pi a}{2W}\right)}\left\{1-0.025\left(\frac{a}{W}\right)^{2}+0.06\left(\frac{a}{W}\right)^{4}\right\} \tag{A.15}$$

H Value and η Function for C^* [6]:

$$H^{LLD}=H^{CMOD}=\tfrac{1}{2}(n-1)/(n+1) \tag{A.16}$$

$$\eta^{LLD}=(2.32\frac{a}{W}+0.18)\pm 0.22 \qquad \begin{matrix}0.1\le a/W\le 0.35\\ 2\le L/W\le 4\end{matrix} \tag{A.17}$$

$$\eta^{LLD}=0.99\pm 0.10 \qquad \begin{matrix}0.35\le a/W\le 0.7\\ 2\le L/W\le 4\end{matrix} \tag{A.18}$$

$$\eta^{CMOD}=(1.26-0.36\frac{a}{W})\pm 0.15 \qquad \begin{matrix}0.1\le a/W\le 0.7\\ 2\le L/W\le 4\end{matrix} \tag{A.19}$$

A.5 SINGLE EDGE NOTCHED BEND SPECIMEN, SEN(B)

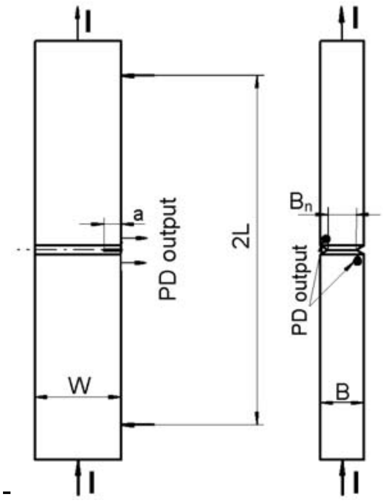

Figure A.5 – Details of the Single Edge Notched Bend, SEN(B), specimen

Loading Arrangement: Three-point bending

Y Function for Stress Intensity Factor, K:

For a span 4W [123]

$$Y = \frac{1}{(1+2a/W)(1-a/W)^{3/2}}\left\{1.99 - \frac{a}{W}\left(1-\frac{a}{W}\right)\left[2.15 - 3.93\left(\frac{a}{W}\right) + 2.7\left(\frac{a}{W}\right)^2\right]\right\} \qquad (A.20)$$

For any span [124]

$$Y = \sqrt{\pi}\cdot\left(1.93\left(\frac{a}{W}\right)^{\frac{1}{2}} - 3.07\left(\frac{a}{W}\right)^{\frac{3}{2}} + 14.53\left(\frac{a}{W}\right)^{\frac{5}{2}} - 25.11\left(\frac{a}{W}\right)^{\frac{7}{2}} + 25.80\left(\frac{a}{W}\right)^{\frac{9}{2}}\right) \qquad (A.21)$$

H Value and η Function for C^* [6]:

$$H^{LLD} = n/(n+1) \qquad (A.22)$$

$$H^{CMOD} = \frac{2L}{W} n/(n+1) \qquad (A.23)$$

$$\eta^{LLD} = (4.06\frac{a}{W} + 0.60) \pm 0.35 \qquad 0.1 \le a/W \le 0.3 \qquad (A.24)$$

$$\eta^{LLD} = (0.56\frac{a}{W} + 1.65) \pm 0.07 \qquad 0.3 \le a/W \le 0.7 \qquad (A.25)$$

$$\eta^{CMOD} = (0.92 - 0.46\frac{a}{W}) \pm 0.06 \qquad 0.1 \le a/W \le 0.7 \qquad (A.26)$$

A.6 SINGLE EDGE NOTCHED TENSION SPECIMEN, SEN(T)

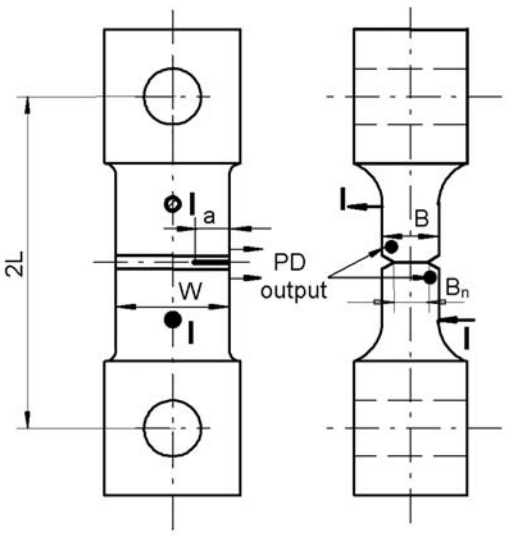

Figure A.6 – Details of the Single Edge Notched Tension, SEN(T), specimen

Loading Arrangement: Pin loading tension

Y Function for Stress Intensity Factor, K [7]:

$$Y = \sqrt{\frac{2W}{a}\tan\left(\frac{\pi a}{2W}\right)}\left\{0.752 + 2.02\left(\frac{a}{W}\right) + 0.37\left(1 - \sin\frac{\pi a}{2W}\right)^3\right\} \Big/ \cos\left(\frac{\pi a}{2W}\right) \tag{A.27}$$

H Value and η Function for C* [6]:

$$H^{LLD} = H^{CMOD} = n/(n+1) \tag{A.28}$$

$$\eta^{LLD} = (5.0\frac{a}{W} - 0.06) \pm 0.38 \qquad \begin{array}{l} 0.1 \le a/W \le 0.5 \\ 1 \le L/W \le 3 \end{array} \tag{A.29}$$

$$\eta^{LLD} = 2.44 \pm 0.38 \qquad \begin{array}{l} 0.5 \le a/W \le 0.7 \\ 1 \le L/W \le 3 \end{array} \tag{A.30}$$

$$\eta^{CMOD} = 1.0 \pm 0.05 \qquad \begin{array}{l} 0.1 \le a/W \le 0.7 \\ 1 \le L/W \le 4 \end{array} \tag{A.31}$$

A.6 ROUND NOTCHED BAR TENSION SPECIMEN, RNB(T)

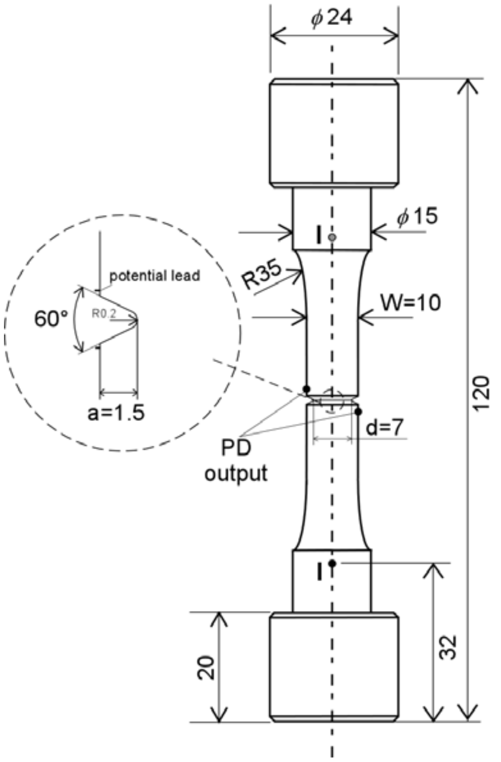

Figure A.7 – Details of the Round Notched Bar Tension, RNB(T), specimen

Loading Arrangement: Shoulder loading tension

Y Function for Stress Intensity Factor, K [125]:

$$Y = \frac{2}{(W-2a)^2}\sqrt{\frac{ad}{W}}\left(1+\frac{1}{2}\lambda+\frac{3}{8}\lambda^2-0.363\lambda^3+0.731\lambda^4\right).\left(1+0.1\sqrt{\frac{2a}{W}}\left(1-\frac{2a}{W}\right)\right) \qquad (A.32)$$

$\lambda = \frac{d}{W}$, where d is the net section diameter and W is the specimen diameter.

Calculation of C* [126]:

$$C^* = \frac{2n+1}{2n-1}.\frac{4P\dot{\Delta}}{\pi(W-2a)^2} \qquad (A.33)$$

APPENDIX B – DETAILS OF TEST MATRICES

B.1. P22 STEEL WELDMENT - TEST SPECIMEN DETAILS

#	Specimen Code	Specimen Type	Crack Plane Position	B(mm)	B_n(mm)	W(mm)	Starter Crack, a_0 (mm)	EDM + Machined Notch Length (mm)	FPC Notch Length (mm)	Aimed a_0/W	Starter Crack Type
1	E22B1A25	C(T)	BM	12.5	10	25	12.5	10	2.5	0.5	FPC
2	E22B2A25	C(T)	BM	12.5	10	25	12.5	10	2.5	0.5	FPC
3	E22B10A35	C(T)	BM	15	12	35	17.5	17.5	0	0.5	EDM
4	E22B10B35	C(T)	BM	15	12	35	17.5	17.5	0	0.5	EDM
5	E22B10C35	C(T)	BM	15	12	35	17.5	17.5	0	0.5	EDM
6	E22F1025	C(T)	FL	12.5	10	25	12.5	10	2.5	0.5	FPC
7	E22F325	C(T)	HAZ	12.5	10	25	12.5	10	2.5	0.5	FPC
8	E22HX135	C(T)	HAZ	15	12	35	17.5	17.5	0	0.5	EDM
9	E22HX235	C(T)	HAZ	15	12	35	17.5	17.5	0	0.5	EDM
10	E22HX335	C(T)	HAZ	15	12	35	17.5	17.5	0	0.5	EDM
11	SENH17	C(T)	HAZ	12.5	10	25	12.5	10	2.5	0.5	FPC
12	SENH18	C(T)	HAZ	12.5	10	25	12.5	10	2.5	0.5	FPC
13	SENH49	C(T)	HAZ	12.5	10	25	12.5	10	2.5	0.5	FPC
14	SENH48	C(T)	HAZ	12.5	10	25	12.5	10	2.5	0.5	FPC
15	SERGHF11	C(T)	HAZ	12.5	10	25	12.5	10	2.5	0.5	FPC
16	SERGHF10	C(T)	HAZ	12.5	10	25	12.5	10	2.5	0.5	FPC
17	SJH63	C(T)	HAZ	12.5	10	25	12.5	10	2.5	0.5	FPC
18	SJH64	C(T)	HAZ	12.5	10	25	12.5	10	2.5	0.5	FPC
19	SJH66	C(T)	HAZ	12.5	10	25	12.5	10	2.5	0.5	FPC
20	SJH65	C(T)	HAZ	12.5	10	25	12.5	10	2.5	0.5	FPC
21	SSPH21	C(T)	HAZ	12.5	10	25	12.5	10	2.5	0.5	FPC
22	SSPH22	C(T)	HAZ	12.5	10	25	12.5	10	2.5	0.5	FPC
23	SSPH27	C(T)	HAZ	12.5	10	25	12.5	10	2.5	0.5	FPC
24	E22W1B25	C(T)	WM	12.5	10	25	12.5	10	2.5	0.5	FPC
25	E22W2B25	C(T)	WM	12.5	10	25	12.5	10	2.5	0.5	FPC
26	E22W735	C(T)	WM	15	12	35	17.5	17.5	0	0.5	EDM
27	E22W835	C(T)	WM	15	12	35	17.5	17.5	0	0.5	EDM
28	E22W935	C(T)	WM	15	12	35	17.5	17.5	0	0.5	EDM
29	E22W435	C(T)	WM	15	12	35	17.5	17.5	0	0.5	EDM
30	E22W535	C(T)	WM	15	12	35	17.5	17.5	0	0.5	EDM
31	E22W635	C(T)	WM	15	12	35	17.5	17.5	0	0.5	EDM
32	SEN8208	C(T)	WM	12.5	10	25	12.5	10	2.5	0.5	FPC
33	SEN9405	C(T)	WM	12.5	10	25	12.5	10	2.5	0.5	FPC
34	SERGHF3	C(T)	WM	12.5	10	25	12.5	10	2.5	0.5	FPC
35	SERGHF5	C(T)	WM	12.5	10	25	12.5	10	2.5	0.5	FPC
36	SERGHF6	C(T)	WM	12.5	10	25	12.5	10	2.5	0.5	FPC
37	SERGHF7	C(T)	WM	12.5	10	25	12.5	10	2.5	0.5	FPC
38	SJW61	C(T)	WM	12.5	10	25	12.5	10	2.5	0.5	FPC
39	SJW62	C(T)	WM	12.5	10	25	12.5	10	2.5	0.5	FPC
40	SJW66	C(T)	WM	12.5	10	25	12.5	10	2.5	0.5	FPC
41	SJW63	C(T)	WM	12.5	10	25	12.5	10	2.5	0.5	FPC
42	SSPS5	C(T)	WM	12.5	10	25	12.5	10	2.5	0.5	FPC
43	SSPS7	C(T)	WM	12.5	10	25	12.5	10	2.5	0.5	FPC
44	SSPS25	C(T)	WM	12.5	10	25	12.5	10	2.5	0.5	FPC
45	E22B4CS	CS(T)	BM	15	12	22.5	4.5	2.5	2	0.2	FPC
46	E22B5CS	CS(T)	BM	15	12	22.5	4.5	2.5	2	0.2	FPC
47	I22F7CS	CS(T)	FL	15	12	22.5	4.5	2.5	2	0.2	FPC
48	I22W5CS	CS(T)	WM	25	20	22.5	4.5	2.5	2	0.2	FPC
49	I22W6CS	CS(T)	WM	15	12	22.5	4.5	2.5	2	0.2	FPC
50	I22W8CS	CS(T)	WM	10	8	22.5	4.5	2.5	2	0.2	FPC

B.1. P22 STEEL WELDMENT - SPECIMEN DETAILS OF TEST MATRIX (Cont'd)

51	E22B7RB	RNB(T)	BM	-	-	D=10	1.5	1.5	0	0.3	EDM
52	E22B8RB	RNB(T)	BM	-	-	D=10	1.5	1.5	0	0.3	EDM
53	E22B9RB	RNB(T)	BM	-	-	D=10	1.5	1.5	0	0.3	EDM
54	I22F1BRB	RNB(T)	FL	-	-	D=10	1.5	1.5	0	0.3	EDM
55	I22W1ARB	RNB(T)	WM	-	-	D=10	1.5	1.5	0	0.3	EDM
56	E22B1ASB	SEN(B)	BM	12.5	10	22	6.6	4.5	2.1	0.3	FPC
57	E22B1BSB	SEN(B)	BM	12.5	10	22	6.6	4.5	2.1	0.3	FPC
58	E22B2ASB	SEN(B)	BM	12.5	10	22	6.6	4.5	2.1	0.3	FPC
59	E22B2BSB	SEN(B)	BM	12.5	10	22	6.6	4.5	2.1	0.3	FPC
60	E22B3ASB	SEN(B)	BM	12.5	10	22	6.6	4.5	2.1	0.3	FPC
61	E22B3BSB	SEN(B)	BM	12.5	10	22	6.6	4.5	2.1	0.3	FPC
62	I22F2ASB	SEN(B)	FL	12.5	10	21	5.3	4	2.3	0.3	FPC
63	I22F3ASB	SEN(B)	FL	12.5	10	20	6	4	2	0.3	FPC
64	I22F4ASB	SEN(B)	HAZ	12.5	10	22	6.6	4.5	2.1	0.3	FPC
65	I22W2BSB	SEN(B)	WM	12.5	10	22	6.6	4.5	2.1	0.3	FPC
66	I22W5BSB	SEN(B)	WM	12.5	10	22	6.6	4.5	2.1	0.3	FPC
67	I22W4BSB	SEN(B)	WM	12.5	10	20	6	4	2	0.3	FPC

ABBREVIATIONS:
BM: Base Material, HAZ: Heat Affected Zone, WM: Weld Metal
FPC: Fatigue Pre-cracked, EDM: Electric Discharge Machined
ERA-UK: ERA Technology Ltd, Cleeve Road, Leatherhead, Surrey. KT22 7SA UK
ISQ-PT: Instituto de Soldadura e Qualidade, Taguspark 2780-994 Porto Salvo Portugal

B.2. P91 STEEL WELDMENT - SPECIMEN DETAILS OF TEST MATRIX

#	Specimen Code	Specimen Type	Crack Plane Position	B(mm)	B_n(mm)	W(mm)	Starter Crack, a_0 (mm)	EDM + Machined Notch Length (mm)	FPC Notch Length (mm)	Aimed a_0/W	Starter Crack Type
1	I91B2A25	C(T)	BM	12.5	10	25	12.5	10	2.5	0.5	FPC
2	I91B3A25	C(T)	BM	12.5	10	25	12.5	10	2.5	0.5	FPC
3	I91B6C25	C(T)	BM	12.5	10	25	12.5	10	2.5	0.5	FPC
4	I91B7A25	C(T)	BM	12.5	10	25	12.5	10	2.5	0.5	FPC
5	I91B7D25	C(T)	BM	12.5	10	25	12.5	10	2.5	0.5	FPC
6	I91B1A35	C(T)	BM	15	12	35	17.5	17.5	0	0.5	EDM
7	I91B4A35	C(T)	BM	15	12	35	17.5	17.5	0	0.5	EDM
8	CTP5	C(T)	BM	25	20	50	25	20	5	0.5	PF
9	PB1T	C(T)	BM	15	12	50	25	20	5	0.5	PF
10	PB2	C(T)	BM	15	12	50	25	20	5	0.5	PF
11	PPB2T	C(T)	BM	15	12	50	25	20	5	0.5	PF
12	I91F7C25	C(T)	FL	12.5	10	25	12.5	10	2.5	0.5	FPC
13	I91F4B35	C(T)	HAZ	15	12	35	17.5	17.5	0	0.5	EDM
14	P91-PHAZ1	C(T)	HAZ	12.5	10	25	12.5	10	2.5	0.5	FPC
15	P91-PHAZ2	C(T)	HAZ	12.5	10	25	12.5	10	2.5	0.5	FPC
16	P91-PTIV1	C(T)	HAZ	12.5	10	25	12.5	10	2.5	0.5	FPC
17	P91-PTIV2	C(T)	HAZ	12.5	10	25	12.5	10	2.5	0.5	FPC
18	I91W7B25	C(T)	WM	12.5	10	25	12.5	10	2.5	0.5	FPC
19	I91W1B35	C(T)	WM	15	12	35	17.5	17.5	0	0.5	EDM
20	I91W3B35	C(T)	WM	15	12	35	17.5	17.5	0	0.5	EDM
21	P91-PW1	C(T)	WM	12.5	10	25	12.5	10	2.5	0.5	FPC
22	P91-PW2	C(T)	WM	12.5	10	25	12.5	10	2.5	0.5	FPC
23	P91-PW3	C(T)	WM	12.5	10	25	12.5	10	2.5	0.5	FPC
24	P91-PW4	C(T)	WM	12.5	10	25	12.5	10	2.5	0.5	FPC
25	P91-PW5	C(T)	WM	12.5	10	25	12.5	10	2.5	0.5	FPC
26	P91-PW6	C(T)	WM	12.5	10	25	12.5	10	2.5	0.5	FPC
27	I91F2CS	CS(T)	HAZ	15	12	25	5	2.5	2.5	0.2	FPC
28	I91W6CS	CS(T)	WM	25	20	25	5	2.5	2.5	0.2	FPC
29	I91F5BRB	RNB(T)	FL	-	-	D=10	1.5	1.5	-	0.3	EDM
30	I91W5ARB	RNB(T)	WM	-	-	D=10	1.5	1.5	-	0.3	EDM

ABBREVIATIONS:
BM: Base Material, HAZ: Heat Affected Zone, WM: Weld Metal
FPC: Fatigue Pre-cracked, EDM: Electric Discharge Machined
ISQ-PT: Instituto de Soldadura e Qualidade, Taguspark 2780-994 Porto Salvo Portugal

B.3. P22 STEEL WELDMENT – SECTIONING OF BLANKS FROM WELDED PIPES

I. P22 Pipe Segment Welded at ISQ-PT

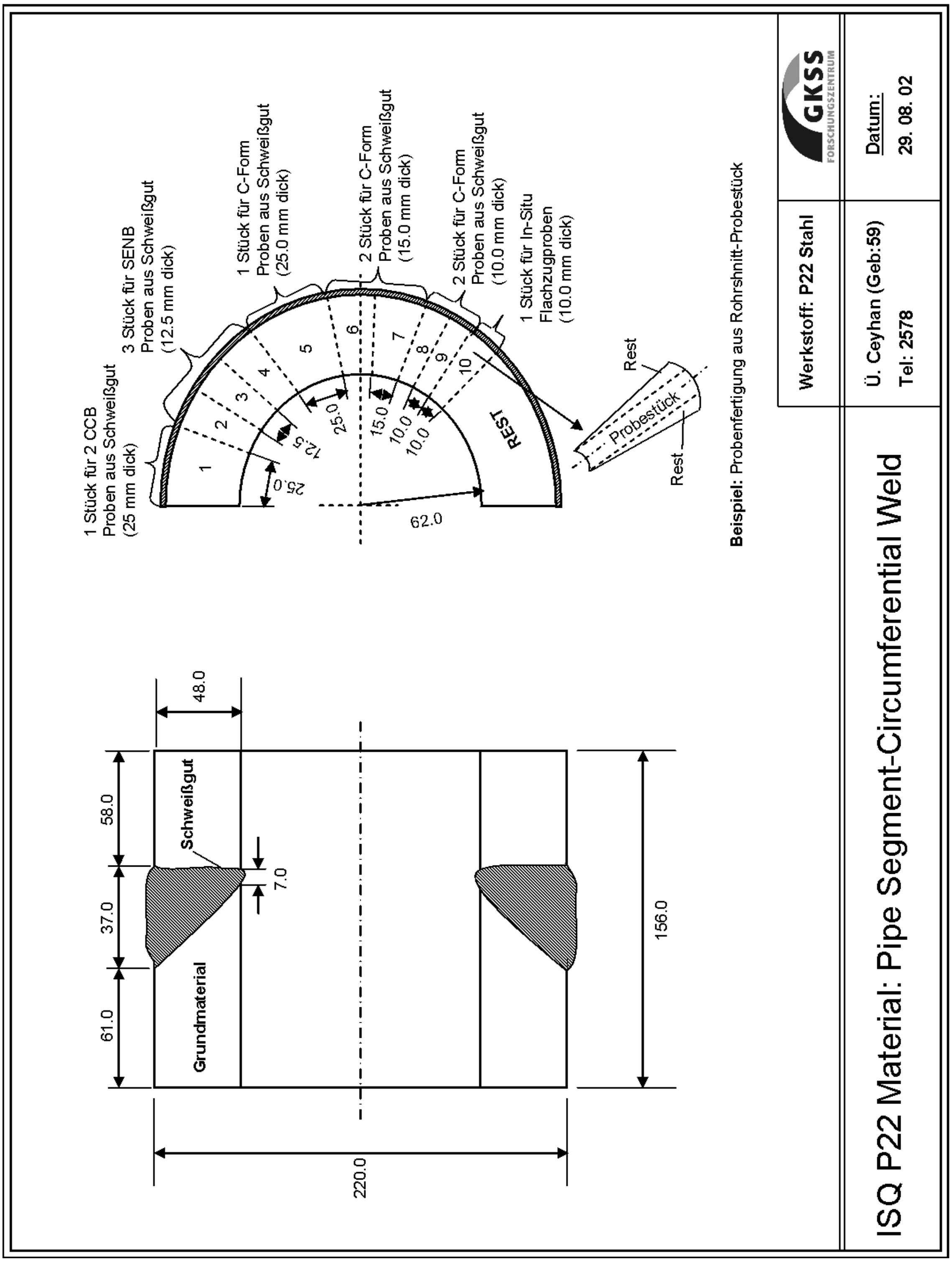

B.3. P22 STEEL WELDMENT – SECTIONING OF BLANKS FROM WELDED PIPES (Cont'd)

II. P22 Pipe Segment Welded at ERA-UK

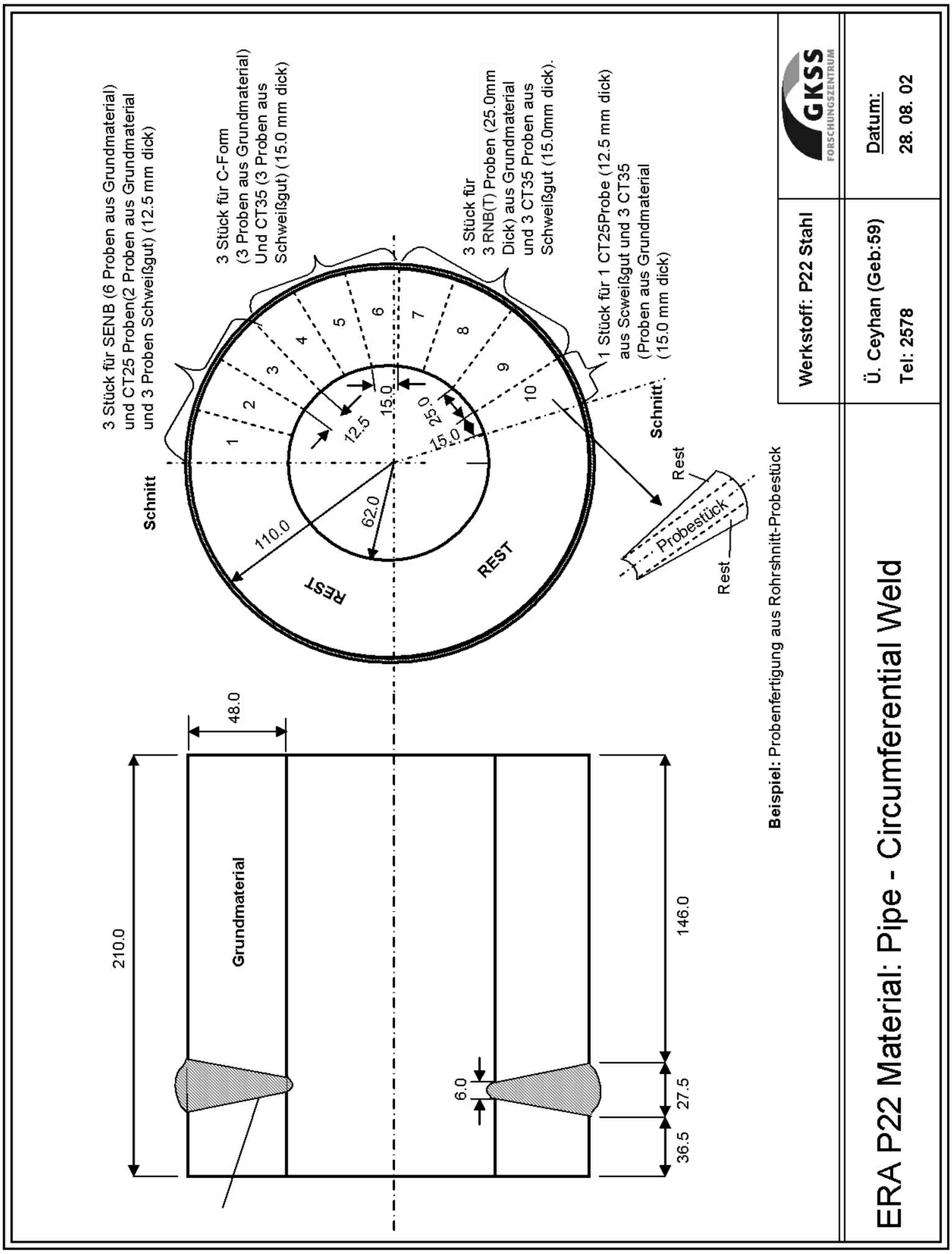

B.4. P91 STEEL WELDMENT – SECTIONING OF BLANKS FROM WELDED PIPES

I. P91 Pipe Segment Welded at ISQ-PT

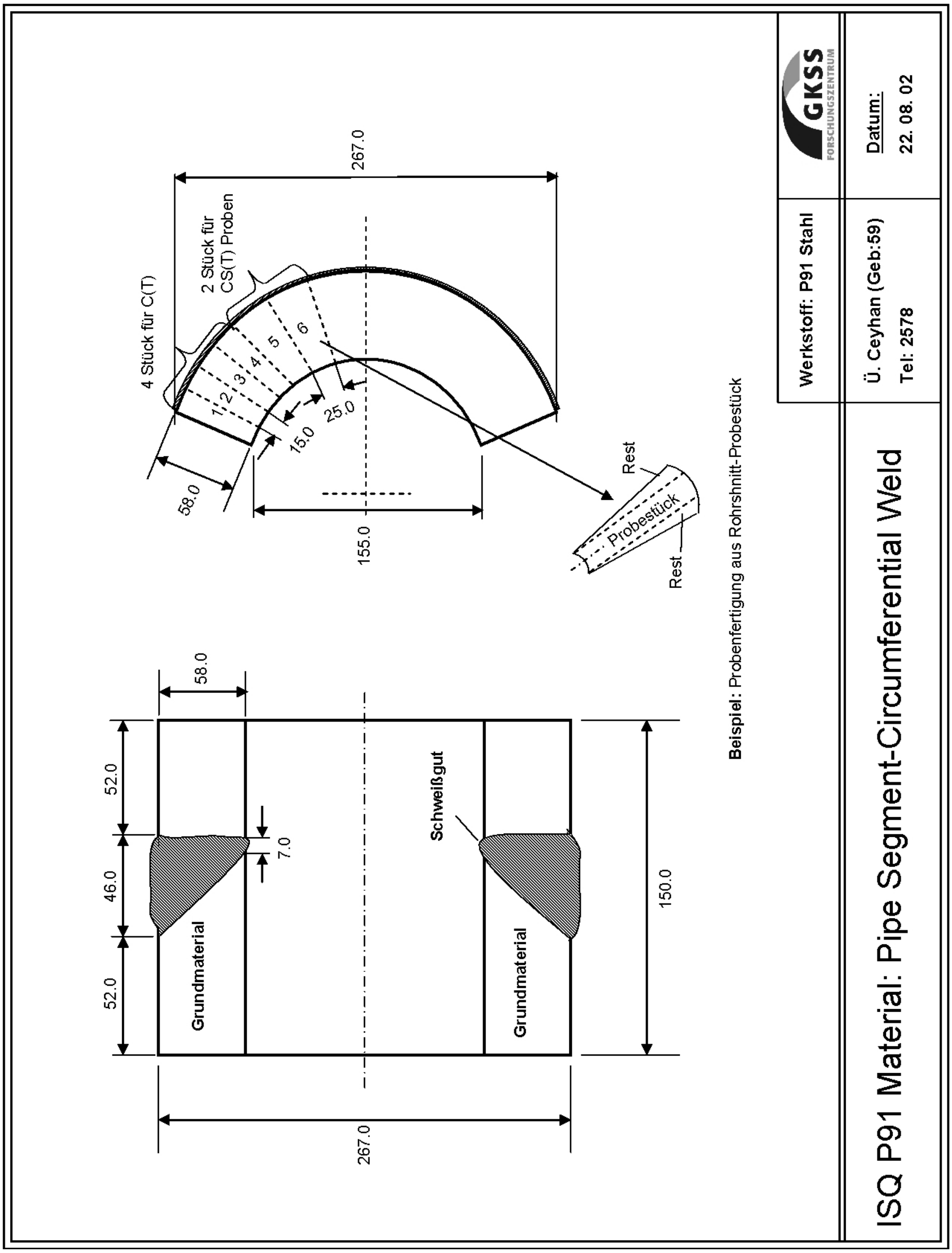

B.5. RECOMMENDED SPECIMEN ALIGNMENT DETAILS

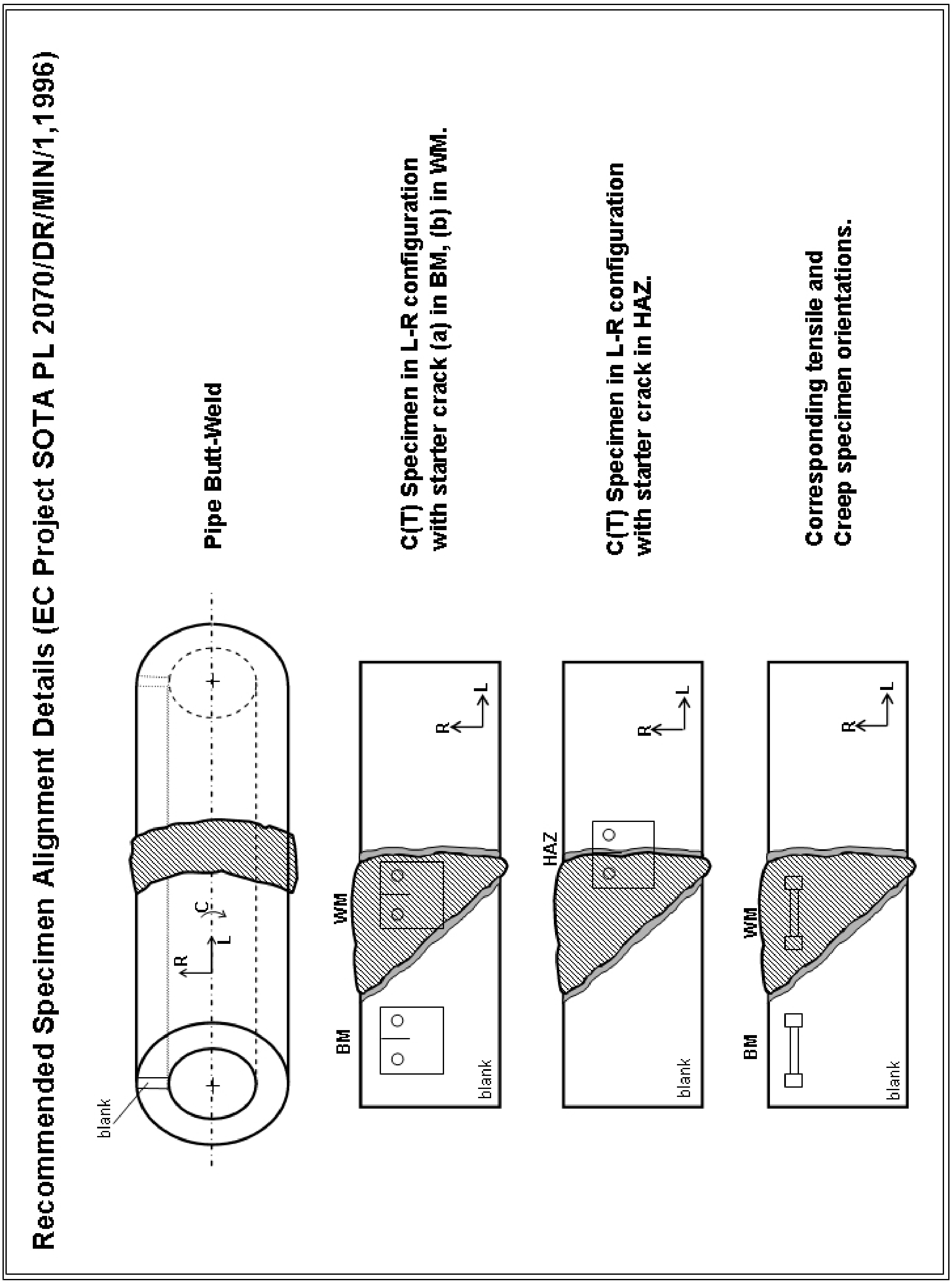

Recommended Specimen Alignment Details (EC Project SOTA PL 2070/DR/MIN/1,1996)

Pipe Butt-Weld

C(T) Specimen in L-R configuration with starter crack (a) in BM, (b) in WM.

C(T) Specimen in L-R configuration with starter crack in HAZ.

Corresponding tensile and Creep specimen orientations.

B.6. TECHNICAL DRAWINGS OF TESTED SPECIMENS

I. Compact Tension, C(T), W=25 mm, B=12.5 mm, B_n=10 mm.

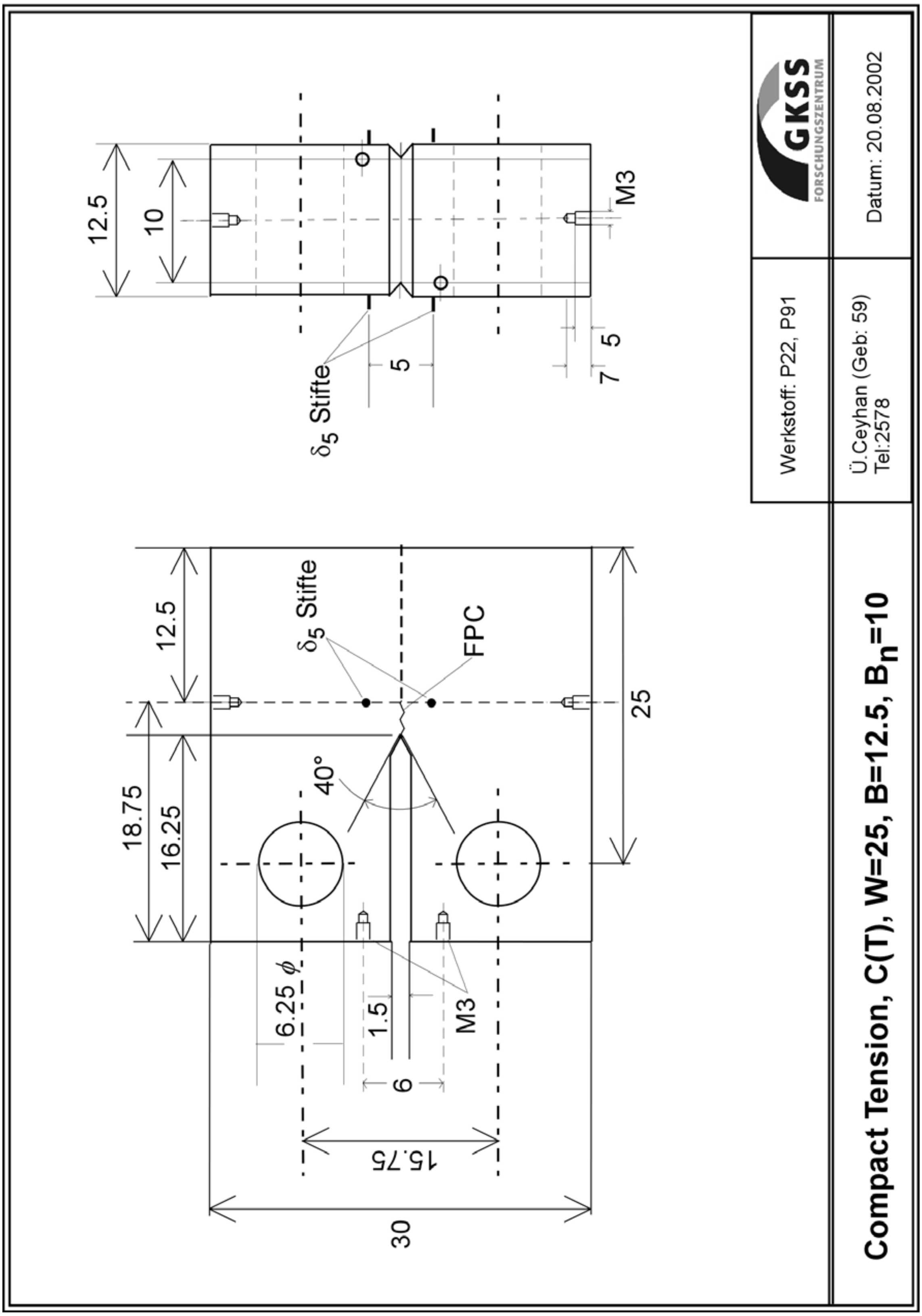

B.6. TECHNICAL DRAWINGS OF TESTED SPECIMENS (Cont'd)

II. Compact Tension, C(T), W=35 mm, B=15 mm, B_n=12 mm.

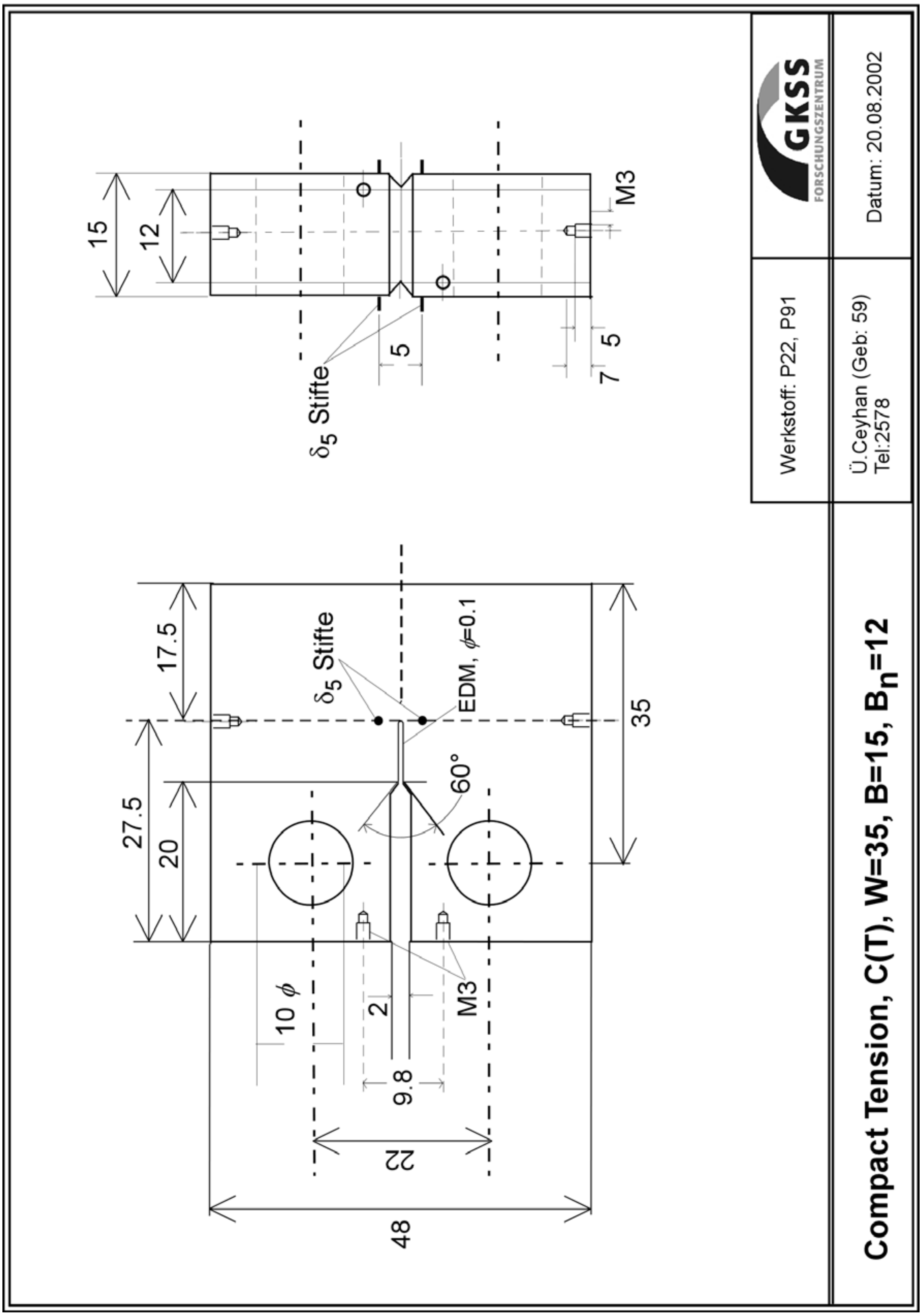

B.6. TECHNICAL DRAWINGS OF TESTED SPECIMENS (Cont'd)

III. C-Shape Tension (for P22 specimens.), CS(T), W=25 mm, B=25, 15 or 10 mm, B_n=20, 12 or 8 mm.

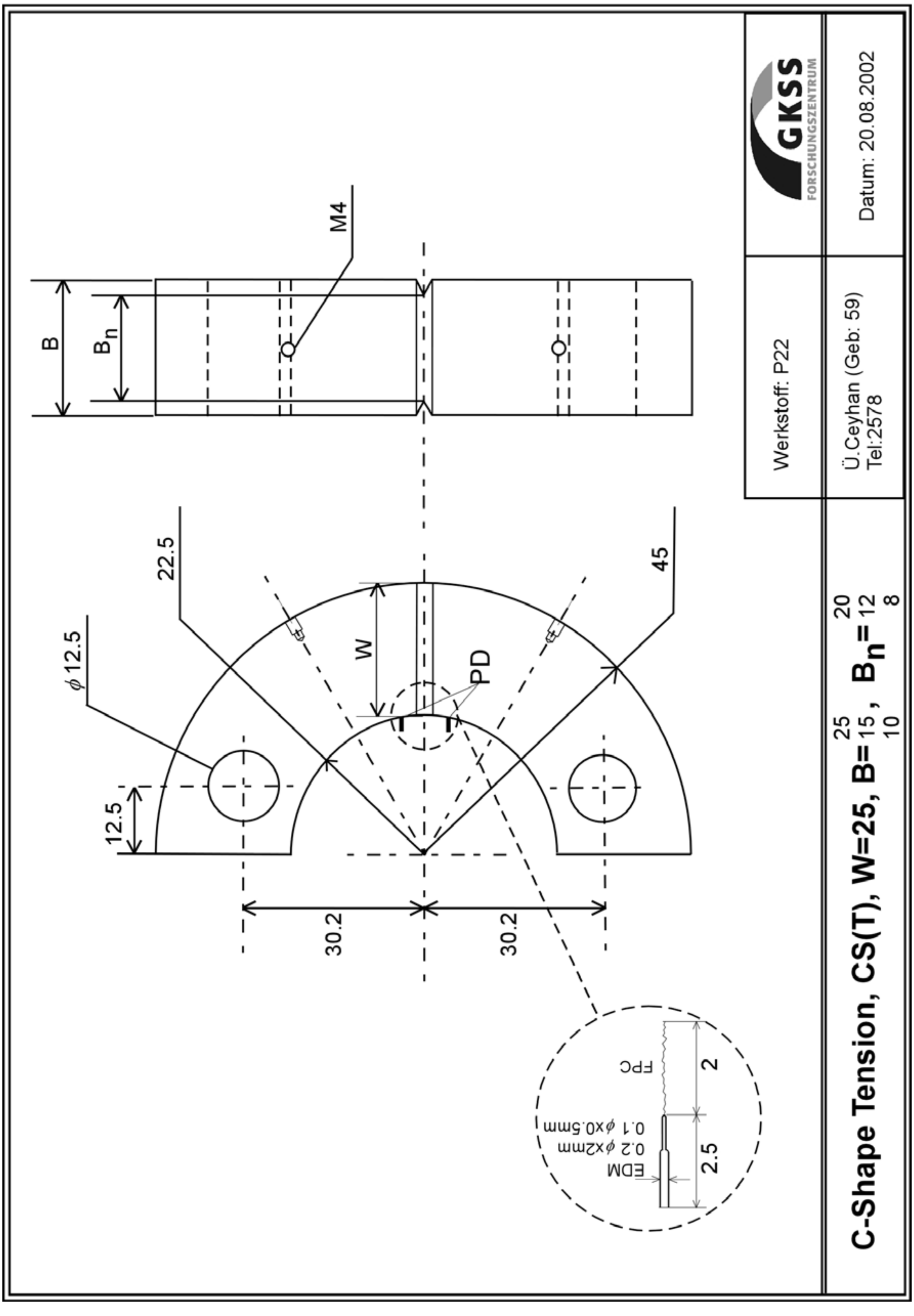

B.6. TECHNICAL DRAWINGS OF TESTED SPECIMENS (Cont'd)

IV. C-Shape Tension (for P91 specimens.), CS(T), W=25 mm, B=25 or 15 mm, B_n=20 or 12 mm

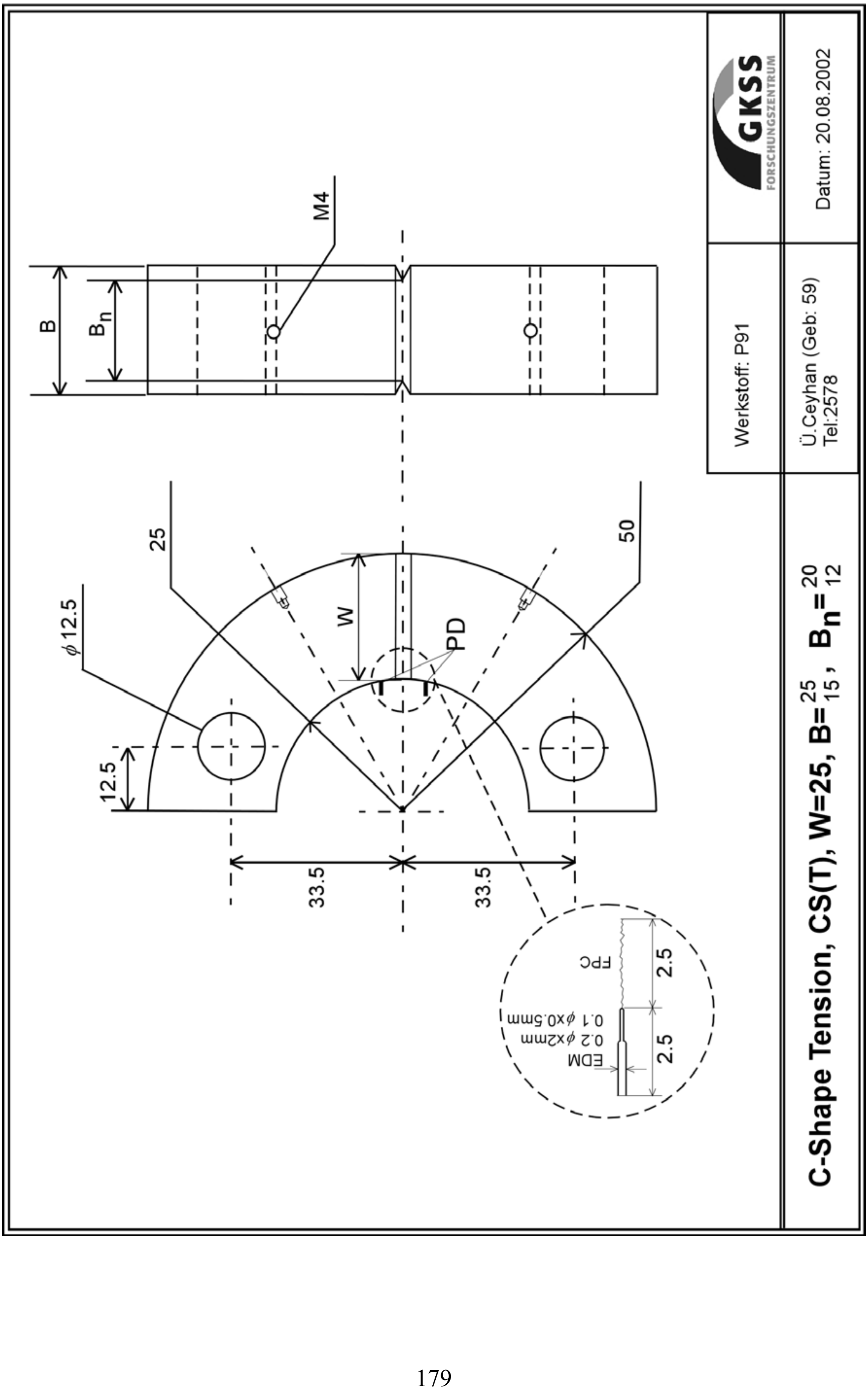

B.6. TECHNICAL DRAWINGS OF TESTED SPECIMENS (Cont'd)

V. Round Notched Bar Tension, RNB(T)

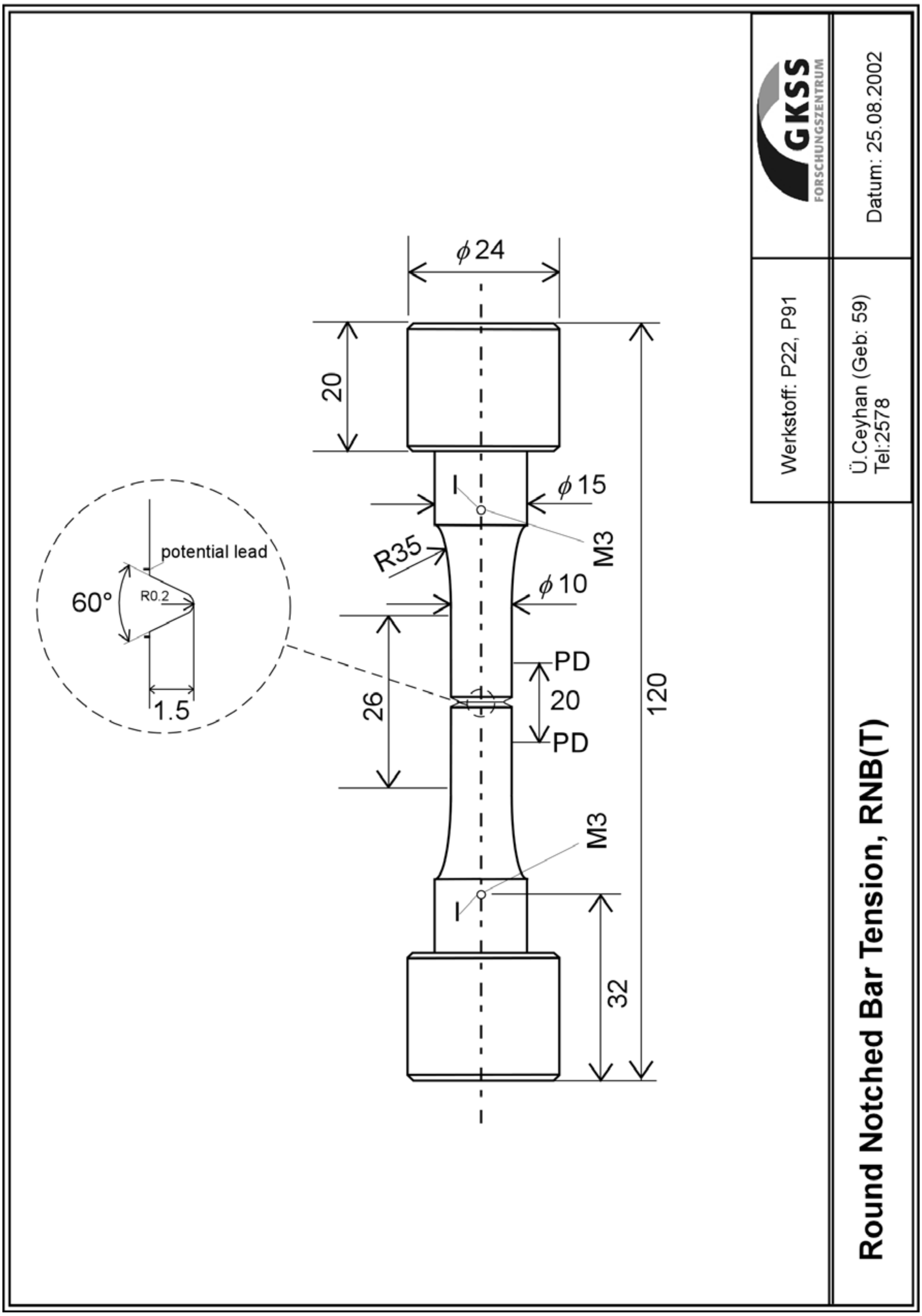

B.6. TECHNICAL DRAWINGS OF TESTED SPECIMENS (Cont'd)

VI. Single Edge Notched Bending, SEN(B), W=25 mm, B=12.5 mm, B_n=10 mm.

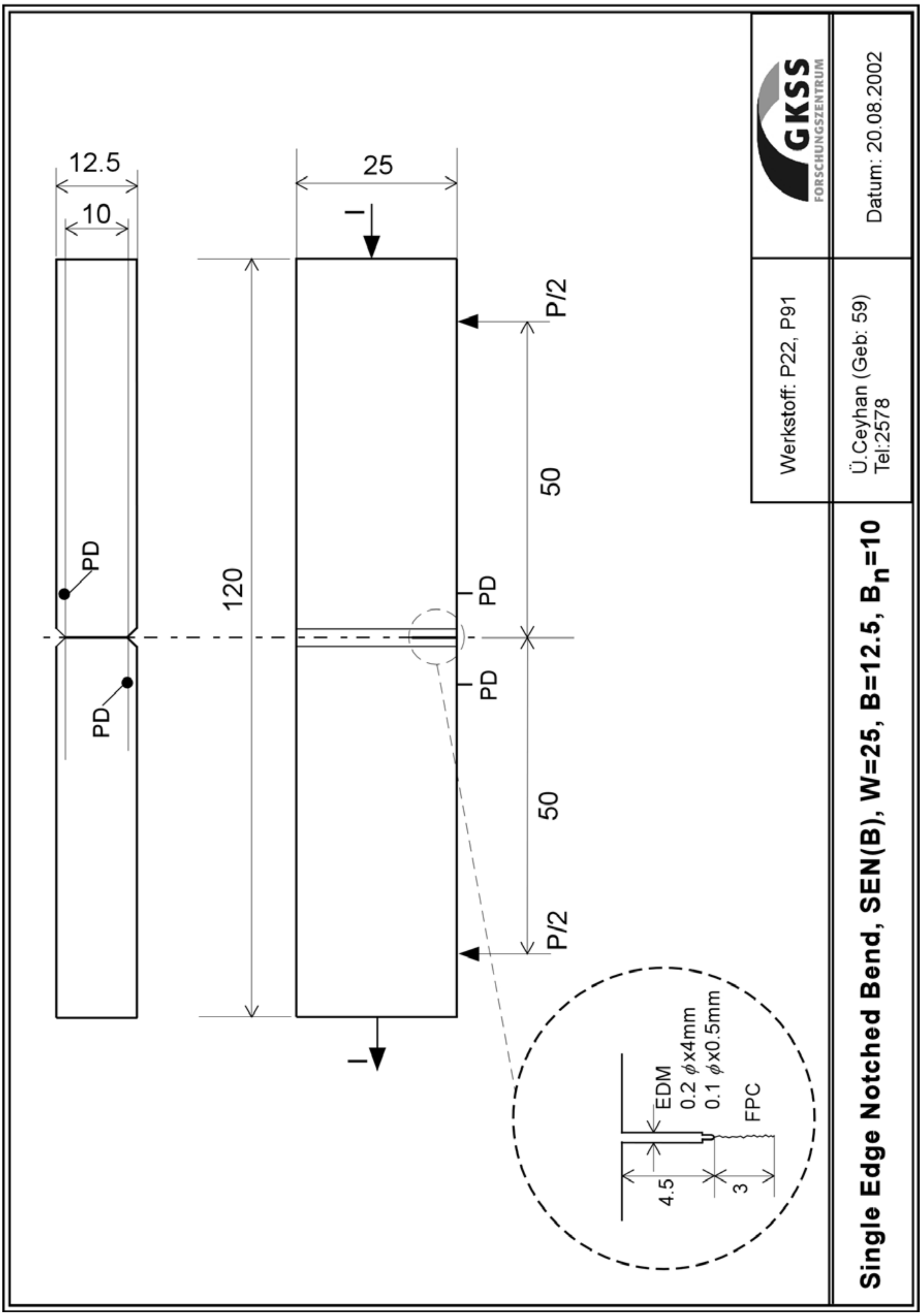

APPENDIX C – TESTING DETAILS

C.1. P22 STEEL WELDMENT

C.1.1. P22 BM

#	Sp. Name	Type	Material	Starter Notch Type	Loading Type	Temp. (°C)	Duration (h)	F D.Rate (kN) mm/ h	K, t=0	C*, t=0	a_o-FS (mm)	a_f-FS (mm)	Δa-FS (mm)
1	E22B10A35	C(T)35-BM	P22BM	EDM	CDR	550	293.6	0.005 mm/ h	32.81	0.367	17.500	18.247	0.747
2	E22B2A25	C(T)25-BM	P22BM	PF	CDR	550	262.5	0.005 mm/ h	22.87	0.275	13.110	13.425	0.315
3	E22B5CS	CS(T)-BM	P22BM	PF	CDR	550	505.0	0.005 mm/ h	18.58	0.224	5.068	5.497	0.429
4	E22B1A25	C(T)25-BM	P22BM	PF	F_{const}	550	428.0	3.8	22.04	0.039	12.978	14.884	1.906
5	E22B4CS	CS(T)-BM	P22BM	PF	F_{const}	550	654.5	5.0	20.00	0.040	5.307	6.774	1.467
6	E22B7RB	RNB(T)-BM	P22BM	EDM	F_{const}	550	182.2	10.0	8.04	1.251	1.500	2.176	0.676
7	E22B9RB	RNB(T)-BM	P22BM	EDM	F_{const}	550	28.0	12.0	15.16	3.619	1.500	2.133	0.633

C.1.2. P22 HAZ

#	Sp. Name	Type	Material	Starter Notch Type	Loading Type	Temp. (°C)	Duration (h)	F D.Rate (kN) mm/ h	K, t=0	C*, t=0	a_o-FS (mm)	a_f-FS (mm)	Δa-FS (mm)
1	I22FL7CS	CS(T)-FL	P22HAZ	PF	F_{const}	550	272.8	4.5	18.70	0.089	5.623	Broken!	NA
2	E22F1025	C(T)25-FL	P22HAZ	PF	F_{const}	550	1377.5	2.5	14.84	0.023	13.120	15.510	2.390
3	SENH17	C(T)25-HAZ	P22HAZ	PF	F_{const}	550	270.0	4.0	20.76	0.170	11.840	15.680	3.840
4	SENH18	C(T)25-HAZ	P22HAZ	PF	F_{const}	550	410.1	3.8	19.41	0.070	11.860	17.990	6.130
5	SENH49	C(T)25-HAZ	P22HAZ	PF	F_{const}	550	439.1	4.0	19.45	0.073	11.850	18.100	6.250
6	SENH48	C(T)25-HAZ	P22HAZ	PF	F_{const}	550	741.1	4.0	17.78	0.068	11.650	16.312	4.662
7	SERGHF11	C(T)25-HAZ	P22HAZ	PF	F_{const}	550	1580.8	2.9	14.74	0.028	11.746	15.190	3.444
8	SERGHF10	C(T)25-HAZ	P22HAZ	PF	F_{const}	550	285.3	3.9	19.56	0.095	11.816	12.947	1.131
9	SJH63	C(T)25-HAZ	P22HAZ	PF	F_{const}	550	429.0	3.8	19.14	0.218	11.776	17.693	5.917
10	SJH64	C(T)25-HAZ	P22HAZ	PF	F_{const}	550	529.7	3.7	19.14	0.091	11.840	13.511	1.671
11	SJH65	C(T)25-HAZ	P22HAZ	PF	F_{const}	550	897.7	2.9	14.62	0.046	11.786	14.815	3.029
12	SJH66	C(T)25-HAZ	P22HAZ	PF	F_{const}	550	1709.4	2.9	14.62	0.028	11.873	14.470	2.597
13	SSPH21	C(T)25-HAZ	P22HAZ	PF	F_{const}	550	641.5	3.6	19.49	0.119	12.283	14.554	2.271
14	SSPH22	C(T)25-HAZ	P22HAZ	PF	F_{const}	550	289.3	3.9	20.68	0.140	12.132	14.240	2.108
15	SSPH27	C(T)25-HAZ	P22HAZ	PF	F_{const}	550	328.8	3.5	19.11	0.104	12.382	14.748	2.366

C.1. P22 STEEL WELDMENT (Cont'd)

C.1.3. P22 WM

#	Sp. Name	Type	Material	Starter Notch Type	Loading Type	Temp. (°C)	Duration (h)	F (kN) D.Rate mm/ h	K, t=0	C*, t=0	a_o-FS (mm)	a_f-FS (mm)	Δa-FS (mm)
1	SERGHF3	C(T)25-WM	P22WM	PF	F_{const}	550	1234.2	4.0	19.25	0.030	11.970	15.839	3.869
2	SERGHF6	C(T)25-WM	P22WM	PF	F_{const}	550	2161.4	3.5	18.16	0.122	11.802	14.843	3.041
3	SEN8208	C(T)25-WM	P22WM	PF	F_{const}	550	1430.6	3.7	19.87	0.037	12.070	15.470	3.400
4	SEN9405	C(T)25-WM	P22WM	PF	F_{const}	550	1619.4	3.8	19.72	0.036	11.960	17.747	5.787
5	E22W1B25	C(T)25-WM	P22WM	PF	F_{const}	550	2261.8	3.0	17.84	0.026	13.169	14.292	1.123
6	E22W2B25	C(T)25-WM	P22WM	PF	CDR	550	414.0	0.005 mm/ h	24.60	0.328	13.210	13.850	0.640
7	SERGHF5	C(T)25-WM	P22WM	PF	F_{const}	550	932.3	4.0	21.41	0.514	12.096	18.877	6.781
8	SERGHF7	C(T)25-WM	P22WM	PF	F_{const}	550	1425.1	3.7	18.11	0.135	11.840	19.297	7.457
9	SSPS25	C(T)25-WM	P22WM	PF	F_{const}	550	1565.9	3.4	19.33	0.037	12.559	14.212	1.653
10	SSPS5	C(T)25-WM	P22WM	PF	F_{const}	550	954.2	3.5	19.22	0.012	12.548	14.552	2.003
11	SSPS7	C(T)25-WM	P22WM	PF	F_{const}	550	1438.9	3.8	20.56	0.022	12.458	13.936	1.478
12	SJW61	C(T)25-WM	P22WM	PF	F_{const}	550	281.0	4.2	21.47	0.132	11.944	18.578	6.634
13	SJW62	C(T)25-WM	P22WM	PF	F_{const}	550	3667.1	3.3	16.66	0.014	11.855	15.826	3.971
14	SJW63	C(T)25-WM	P22WM	PF	F_{const}	550	1369.4	3.8	19.15	0.034	11.865	15.126	3.261
15	SJW66	C(T)25-WM	P22WM	PF	F_{const}	550	1057.5	3.8	18.94	0.058	11.894	14.822	2.928
16	E22W835	C(T)35-WM	P22WM	EDM	F_{const}	550	3002.0	5.5	20.99	0.087	17.500	19.281	1.781
17	I22W5CS	CS(T)-WM	P22WM	PF	F_{const}	550	1613.3	10.0	17.58	0.022	3.689	7.048	3.359
18	I22W6CS	CS(T)-WM	P22WM	PF	F_{const}	550	365.0	5.0	22.02	0.244	6.177	8.564	2.387
19	I22W8CS	CS(T)-WM	P22WM	PF	F_{const}	550	676.2	2.8	20.64	0.062	5.873	7.745	1.872
20	I22W4SB	SEN(B)-WM	P22WM	PF	F_{const}	550	642.6	5.2	22.95	0.114	7.172	9.790	2.618
21	I22W5SB	SEN(B)-WM	P22WM	PF	F_{const}	550	962.0	4.7	20.57	0.054	7.013	9.849	2.836
22	E22W1ARB	RNB(T)-WM	P22WM	EDM	F_{const}	550	2073.8	6.6	8.16	0.010	1.500	1.593	0.093

C.2. P91 STEEL WELDMENT

C.2.1. P91 BM

#	Sp. Name	Type	Material	Starter Notch Type	Loading Type	Temp. (°C)	Duration (h)	F (kN) D.Rate mm/h	K, t=0	C*, t=0	a_o-FS (mm)	a_f-FS (mm)	Δa-FS (mm)
1	I91B1A35	C(T)35-BM	P91BM	EDM	F_{const}	600	2478.9	6.1	23.47	0.014	17.500	19.328	1.828
2	I91B2A25	C(T)25-BM	P91BM	PF	F_{const}	600	1542.9	3.3	19.52	0.056	13.243	14.771	1.528
3	I91B7A25	C(T)25-BM	P91BM	PF	F_{const}	600	766.8	3.8	22.56	0.198	13.211	14.373	1.162
4	I91B7D25	C(T)25-BM	P91BM	PF	F_{const}	600	742.7	3.6	21.70	0.074	13.231	14.200	0.969
5	PB2	C(T)50-BM	P91BM	PF	F_{const}	600	1261.4	7.0	22.89	0.035	25.356	31.233	5.877
6	PPB2T	C(T)50-BM	P91BM	PF	F_{const}	600	1807.4	6.5	21.75	0.019	25.579	33.139	7.560
7	CTP5	C(T)50-BM	P91BM	PF	F_{const}	600	695.4	14.0	27.30	0.052	25.121	31.551	6.430
8	PPB1	C(T)50-BM	P91BM	PF	CDR	600	725.6	1 and 5 mm/h	15.47	0.018	25.860	29.180	3.320
9	PB1T	C(T)50-BM	P91BM	PF	CDR	600	1816.6	6.7 mm/h	13.71	0.016	26.161	35.246	9.085

C.2.2. P91 HAZ

#	Sp. Name	Type	Material	Starter Notch Type	Loading Type	Temp. (°C)	Duration (h)	F (kN) D.Rate mm/h	K, t=0	C*, t=0	a_o-FS (mm)	a_f-FS (mm)	Δa-FS (mm)
1	I91F2CS	CS(T)-HAZ	P91HAZ	PF	F_{const}	600	2157.0	4.8	15.41	0.002	4.200	10.400	6.200
2	SOTA HAZ1	C(T)25-HAZ	P91HAZ	PF	F_{const}	600	1792.6	3.1	16.35	0.008	12.210	14.880	2.670
3	SOTA HAZ2	C(T)25-HAZ	P91HAZ	PF	F_{const}	600	750.1	3.6	19.05	0.013	12.223	12.470	0.247
4	SOTA PTIV1	C(T)25-HAZ	P91HAZ	PF	F_{const}	600	2860.9	3.1	15.79	0.003	11.870	13.069	1.199
5	SOTA PTIV2	C(T)25-HAZ	P91HAZ	PF	F_{const}	600	4852.5	2.6	13.68	0.004	10.692	16.067	5.375

C.2.3. P91 WM

#	Sp. Name	Type	Material	Starter Notch Type	Loading Type	Temp. (°C)	Duration (h)	F (kN) D.Rate mm/h	K, t=0	C*, t=0	a_o-FS (mm)	a_f-FS (mm)	Δa-FS (mm)
1	I91W6CS	CS(T)	P91WM	PF	F_{const}	600	1277.1	9.7	16.73	0.004	4.336	7.263	2.927
2	SOTA PW1	C(T)25-WM	P91WM	PF	F_{const}	600	410.6	3.8	19.33	0.055	11.880	13.618	1.738
3	SOTA PW2	C(T)25-WM	P91WM	PF	F_{const}	600	365.2	3.8	19.33	0.085	11.920	14.682	2.762
4	SOTA PW3	C(T)25-WM	P91WM	PF	F_{const}	600	367.6	3.8	19.10	0.095	11.993	14.434	2.441
5	SOTA PW4	C(T)25-WM	P91WM	PF	F_{const}	600	1463.2	3.1	16.31	0.011	12.210	16.178	3.968
6	SOTA PW5	C(T)25-WM	P91WM	PF	F_{const}	600	1153.1	3.1	16.57	0.011	12.426	16.666	4.240
7	SOTA PW6	C(T)25-WM	P91WM	PF	F_{const}	600	2141.2	3.3	13.04	0.007	11.927	17.422	5.495
8	I91W5ARB	RNB(T)	P91WM	EDM	F_{const}	600	59.1	10.0	13.08	2.058	1.500	1.500	broken!

C.3. DATA SHEET FOR HIGH TEMPERATURE CRACK GROWTH DATA ASSESSMENT – AN EXAMPLE

Spec. & material data		Time (h)	PD (μV)	Δ^{LLD} (mm)	Δ^{CMOD} (mm)	a (mm)	Δa (mm)	da/dt (mm/h)	$d\Delta^{LLD}/dt$ (mm/h)	$d\Delta^{CMOD}/dt$ (mm/h)	a/W	f(a/W)	K (MPa $m^{0.5}$)	ϕ	α	h_1 (a/w,m)	J_p (kJ/m^2)	$d\Delta_c^{LLD}/dt$ (mm/h)	Δ_c^{LLD} (mm)	K^c_{mat} (MPa $m^{0.5}$)	C* (N/mm/h)	t_T (h)	F (kN)	$\frac{(d\Delta_c^{LLD}/dt)}{(d\Delta^{LLD}/dt)}$
Material	P22 BM	235.0	0.000	0.326	0.102	6.894	0.000				0.314	1.875	20.16	0.914	0.245	0.081	6.54E-16	0.00E+00		22.57	0.000	11.18	5.20	0.988
Specimen	E22B2SB	355.6	0.078	0.377	0.130	6.944	0.050	5.60E-04	4.63E-04	2.58E-04	0.316	1.880	20.28	0.924	0.244	0.079	8.09E-16	4.57E-04	2.76E-02	27.83	0.027	13.52	5.20	0.990
W(mm)	21.980	415.0	0.159	0.410	0.148	6.995	0.101	1.03E-03	5.96E-04	3.14E-04	0.318	1.884	20.40	0.934	0.243	0.077	1.00E-15	5.84E-04	5.85E-02	32.74	0.035	16.68	5.20	0.990
B(mm)	12.470	452.3	0.236	0.434	0.161	7.043	0.149	1.46E-03	7.05E-04	3.77E-04	0.320	1.888	20.52	0.943	0.242	0.076	1.24E-15	6.89E-04	8.22E-02	36.08	0.042	20.10	5.20	0.984
B_n(mm)	9.950	482.7	0.315	0.457	0.174	7.093	0.199	1.85E-03	8.09E-04	4.95E-04	0.323	1.893	20.64	0.953	0.241	0.074	1.54E-15	7.88E-04	1.05E-01	38.99	0.048	21.89	5.20	0.975
a_o(mm)	6.894	505.8	0.393	0.478	0.187	7.142	0.248	2.29E-03	9.42E-04	6.20E-04	0.325	1.897	20.76	0.963	0.240	0.073	1.91E-15	9.15E-04	1.24E-01	41.39	0.056	22.69	5.20	0.969
a_f(mm)	9.524	526.8	0.475	0.499	0.201	7.194	0.300	2.60E-03	1.09E-03	7.06E-04	0.327	1.902	20.88	0.973	0.239	0.071	2.37E-15	1.06E-03	1.45E-01	43.77	0.065	23.03	5.20	0.965
P(N)	5.20	544.8	0.553	0.520	0.215	7.244	0.350	2.85E-03	1.24E-03	7.66E-04	0.330	1.906	21.01	0.983	0.238	0.070	2.95E-15	1.21E-03	1.65E-01	46.00	0.075	23.04	5.20	0.962
U_o(mV)	0.000	562.8	0.637	0.544	0.229	7.297	0.403	3.03E-03	1.39E-03	8.01E-04	0.332	1.911	21.14	0.994	0.237	0.068	3.66E-15	1.35E-03	1.88E-01	48.39	0.084	22.78	5.20	0.960
T(°C)	550 °C	578.8	0.716	0.567	0.242	7.347	0.453	3.20E-03	1.53E-03	8.30E-04	0.334	1.916	21.27	1.004	0.236	0.067	4.57E-15	1.49E-03	2.11E-01	50.64	0.092	22.30	5.20	0.958
$R_{p0.2}$ (MPa)	350	592.8	0.789	0.589	0.254	7.393	0.499	3.39E-03	1.66E-03	8.63E-04	0.336	1.921	21.38	1.014	0.235	0.065	5.68E-15	1.62E-03	2.33E-01	52.70	0.101	21.61	5.20	0.956
E (MPa)	157000	606.8	0.866	0.614	0.266	7.442	0.548	3.62E-03	1.79E-03	9.17E-04	0.339	1.926	21.51	1.024	0.234	0.064	7.07E-15	1.74E-03	2.56E-01	54.85	0.109	20.78	5.20	0.955
ν	0.33	620.8	0.950	0.639	0.279	7.494	0.600	3.94E-03	1.92E-03	1.00E-03	0.341	1.931	21.64	1.035	0.232	0.063	8.81E-15	1.87E-03	2.82E-01	57.07	0.117	19.87	5.20	0.952
Y_o(mm)		632.8	1.029	0.663	0.292	7.544	0.650	4.35E-03	2.05E-03	1.12E-03	0.343	1.936	21.77	1.045	0.231	0.062	1.10E-14	2.00E-03	3.05E-01	59.04	0.126	18.92	5.20	0.950
D_1	0.0016	642.8	1.101	0.685	0.304	7.590	0.696	4.87E-03	2.21E-03	1.28E-03	0.345	1.941	21.89	1.055	0.230	0.060	1.38E-14	2.15E-03	3.26E-01	60.75	0.136	18.00	5.20	0.947
m	19.17	652.8	1.183	0.708	0.318	7.642	0.748	5.42E-03	2.33E-03	1.47E-03	0.348	1.946	22.02	1.066	0.229	0.059	1.71E-14	2.25E-03	3.48E-01	62.52	0.144	17.10	5.20	0.944
A_1	7.640E-21	660.8	1.256	0.726	0.330	7.688	0.794	6.11E-03	2.47E-03	1.70E-03	0.350	1.951	22.15	1.076	0.228	0.058	2.15E-14	2.38E-03	3.66E-01	63.99	0.152	16.30	5.20	0.941
n	17.8	668.8	1.337	0.747	0.345	7.739	0.845	6.89E-03	2.74E-03	1.97E-03	0.352	1.956	22.28	1.087	0.227	0.057	2.69E-14	2.65E-03	3.86E-01	65.54	0.170	15.54	5.20	0.938
Δa-difference	2.630	677.1	1.434	0.771	0.363	7.800	0.906	7.67E-03	3.12E-03	2.25E-03	0.355	1.963	22.45	1.100	0.226	0.056	3.37E-14	3.01E-03	4.10E-01	67.33	0.194	14.88	5.20	0.935
ε_f	0.37	683.1	1.511	0.792	0.377	7.849	0.955	8.61E-03	3.66E-03	2.59E-03	0.357	1.969	22.58	1.111	0.225	0.055	4.21E-14	3.55E-03	4.29E-01	68.78	0.230	14.26	5.20	0.932
		689.1	1.597	0.815	0.394	7.903	1.009	9.36E-03	4.16E-03	2.85E-03	0.360	1.975	22.73	1.123	0.224	0.054	5.30E-14	4.03E-03	4.52E-01	70.42	0.262	13.73	5.20	0.928
		693.1	1.659	0.833	0.406	7.943	1.049	1.02E-02	4.79E-03	3.11E-03	0.361	1.979	22.84	1.132	0.223	0.054	6.66E-14	4.64E-03	4.70E-01	71.64	0.303	13.22	5.20	0.925
		697.4	1.731	0.855	0.419	7.988	1.094	1.11E-02	5.50E-03	3.43E-03	0.363	1.984	22.96	1.142	0.222	0.053	8.43E-14	5.34E-03	4.91E-01	73.11	0.350	12.79	5.20	0.922
		703.0	1.834	0.888	0.440	8.053	1.159	1.19E-02	6.20E-03	3.75E-03	0.366	1.992	23.15	1.156	0.221	0.052	1.06E-13	6.03E-03	5.23E-01	75.28	0.397	12.38	5.20	0.919
		707.0	1.913	0.915	0.456	8.103	1.209	1.30E-02	7.13E-03	4.19E-03	0.369	1.998	23.29	1.168	0.220	0.051	1.33E-13	6.94E-03	5.49E-01	76.99	0.460	12.02	5.20	0.916
		711.0	1.998	0.945	0.473	8.157	1.263	1.37E-02	7.78E-03	4.51E-03	0.371	2.005	23.44	1.180	0.218	0.051	1.68E-13	7.58E-03	5.78E-01	78.85	0.504	11.69	5.20	0.913
		713.0	2.043	0.961	0.483	8.185	1.291	1.47E-02	8.74E-03	5.00E-03	0.372	2.008	23.52	1.187	0.218	0.050	2.12E-13	8.52E-03	5.94E-01	79.87	0.568	11.38	5.20	0.910
		717.0	2.138	0.997	0.503	8.245	1.351	1.54E-02	9.42E-03	5.36E-03	0.375	2.016	23.70	1.201	0.217	0.050	2.70E-13	9.18E-03	6.29E-01	82.05	0.615	11.11	5.20	0.906
		720.2	2.217	1.029	0.521	8.295	1.401	1.65E-02	1.06E-02	6.00E-03	0.377	2.022	23.84	1.212	0.216	0.049	3.44E-13	1.03E-02	6.60E-01	83.90	0.693	10.86	5.20	0.903
		724.2	2.324	1.073	0.546	8.363	1.469	1.76E-02	1.17E-02	6.66E-03	0.380	2.030	24.04	1.228	0.214	0.048	4.37E-13	1.14E-02	7.03E-01	86.45	0.771	10.63	5.20	0.900
		728.2	2.439	1.122	0.574	8.436	1.542	1.85E-02	1.27E-02	7.27E-03	0.384	2.040	24.26	1.246	0.213	0.048	5.50E-13	1.24E-02	7.51E-01	89.16	0.843	10.41	5.20	0.897
		730.2	2.500	1.149	0.590	8.474	1.580	1.99E-02	1.41E-02	8.21E-03	0.386	2.045	24.37	1.255	0.212	0.047	7.00E-13	1.38E-02	7.77E-01	90.62	0.942	10.22	5.20	0.894
		734.2	2.628	1.207	0.623	8.555	1.661	2.06E-02	1.49E-02	8.73E-03	0.389	2.056	24.62	1.275	0.210	0.047	9.03E-13	1.45E-02	8.34E-01	93.70	1.001	10.05	5.20	0.891
		736.2	2.696	1.238	0.642	8.598	1.704	2.17E-02	1.61E-02	9.57E-03	0.391	2.062	24.75	1.285	0.209	0.047	1.15E-12	1.57E-02	8.64E-01	95.31	1.086	9.88	5.20	0.888
		738.2	2.766	1.271	0.662	8.642	1.748	2.25E-02	1.69E-02	1.02E-02	0.393	2.068	24.89	1.296	0.208	0.046	1.45E-12	1.65E-02	8.96E-01	96.99	1.148	9.73	5.20	0.885
		740.2	2.838	1.306	0.683	8.688	1.794	2.33E-02	1.78E-02	1.08E-02	0.395	2.074	25.03	1.307	0.207	0.046	1.85E-12	1.74E-02	9.30E-01	98.74	1.212	9.59	5.20	0.882
		742.2	2.913	1.342	0.705	8.735	1.841	2.50E-02	1.97E-02	1.23E-02	0.397	2.081	25.18	1.319	0.206	0.046	2.38E-12	1.92E-02	9.67E-01	100.59	1.346	9.53	5.20	0.879
		748.2	3.154	1.463	0.781	8.888	1.994	2.73E-02	2.22E-02	1.45E-02	0.404	2.103	25.67	1.358	0.203	0.046	2.66E-12	2.17E-02	1.09E+00	106.56	1.540	9.46	5.20	0.877
		756.2	3.517	1.653	0.908	9.117	2.223	0.029149	0.024307	0.01630172	0.415	2.1378	26.4278	1.417	0.199	0.046055	1.75E-12	0.02375319	1.2715674	114.89	1.7198753	9.30	5.20	0.874
		758.2	3.615	1.706	0.944	9.179	2.285	0.031694	0.027129	0.01892375	0.418	2.14763	26.63985	1.434	0.197	0.046242	1.90E-12	0.02651697	1.3218376	117.10	1.9309647	9.18	5.20	0.871
		760.2	3.717	1.762	0.983	9.244	2.350	0.032778	0.028323	0.02009391	0.421	2.15795	26.86174	1.452	0.196	0.046492	2.06E-12	0.02767964	1.3760342	119.44	2.0275968	9.06	5.20	0.869
		762.2	3.823	1.819	1.025	9.310	2.416	0.033893	0.029548	0.02132504	0.424	2.16881	27.09398	1.47	0.195	0.046811	2.21E-12	0.02887082	1.4325846	121.83	2.1278942	8.95	5.20	0.866
		764.2	3.932	1.880	1.069	9.379	2.485	0.035041	0.030803	0.02261886	0.427	2.18022	27.33715	1.489	0.193	0.047204	2.36E-12	0.03008986	1.4915453	124.28	2.2319464	8.83	5.20	0.864
		766.2	4.044	1.943	1.115	9.450	2.556	0.036223	0.032087	0.02397703	0.43	2.19222	27.59186	1.508	0.192	0.047676	2.51E-12	0.03133603	1.5529712	126.79	2.3398454	8.71	5.20	0.861
		768.2	4.161	2.008	1.165	9.524	2.630																	

Figure C1. Data sheet for the assessment of the high temperature crack growth data of a SEN(B) specimen of P22 BM (E22B2CS), tested for 768 hours at 550 °C.

LEBENSLAUF

Angaben zur Person

Name: Ceyhan

Vorname: Ümit

Geburtsdatum, -ort: 10.02.1976, Ankara (Türkei)

Familienstand: verheiratet, 1 Kind

Staatsangehörigkeit: türkisch

Bildungsweg:

1982-1987: Grundschule in Nigde (Türkei)

1987-1994: Gymnasium in Nigde

1994-1998: B.Sc. in Fachrichtung „Ingenieurwesen Maschinenbau“ an der Middle East Technical University (METU) in Ankara

1998-2001: M.Sc. in Fachrichtung „Ingenieurwesen Maschinenbau“mit dem Abschlußarbeit „Optimum design of composite membranes with curved fiber courses“an der METU in Ankara

1998-2002: Wissenschaftlicher Assistent an der METU in Ankara

Seit Juli 2002: Wissenschaftlicher Mitarbeiter am Institut für Werkstoffforschung, GKSS-Forschungszentrum, Geesthacht